
Electronic Thesis and Dissertation Repository

6-9-2022 2:30 PM

Hydration Kinetics, Microstructure, and Mechanical Strength Development of Cement-based Composites Incorporating Phase Change Materials

Afshin Marani, *The University of Western Ontario*

Supervisor: Nehdi, Moncef L., *The University of Western Ontario*

A thesis submitted in partial fulfillment of the requirements for the Doctor of Philosophy degree
in Civil and Environmental Engineering

© Afshin Marani 2022

Follow this and additional works at: <https://ir.lib.uwo.ca/etd>



Part of the [Civil Engineering Commons](#), [Mechanics of Materials Commons](#), [Structural Engineering Commons](#), and the [Structural Materials Commons](#)

Recommended Citation

Marani, Afshin, "Hydration Kinetics, Microstructure, and Mechanical Strength Development of Cement-based Composites Incorporating Phase Change Materials" (2022). *Electronic Thesis and Dissertation Repository*. 8617.

<https://ir.lib.uwo.ca/etd/8617>

This Dissertation/Thesis is brought to you for free and open access by Scholarship@Western. It has been accepted for inclusion in Electronic Thesis and Dissertation Repository by an authorized administrator of Scholarship@Western. For more information, please contact wlsadmin@uwo.ca.

Abstract

The research conducted in this thesis investigates the effects of phase change materials (PCMs) on the hydration kinetics and strength development of cement-based composites using extensive experimental and numerical analyses. Purposefully, the effect of microencapsulated PCMs (MPCMs) on the strength development of cement-based mortars and concretes was evaluated using powerful machine learning models trained with the largest available experimental data. Furthermore, a novel ternary machine learning approach was proposed to optimize the mixture design of mortars and concretes based on the thermo-physical properties of the MPCMs. The results obtained from machine learning simulations suggest the assessment of the effects of MPCMs on the maturity-strength relationship. Multitudinous laboratory experiments were therefore performed to collect data for the calculation of the apparent activation energy. The analysis of isothermal calorimetry and compressive strength measurements at various curing temperatures revealed the reduction of apparent activation energy after the addition of MPCMs, indicating less sensitivity of such composites to curing temperatures. Deep learning proved capable of predicting the hydration kinetics of MPCM-integrated cementitious systems and thus calculating the apparent activation energy of diverse systems. Furthermore, eco-friendly shape-stabilized PCMs (SSPCMs) were fabricated using bio-based PCMs and recycled supporting agents to promote the sustainability of the built environment. Finally yet importantly, a low-carbon latent heat thermal energy storage (LHTES) system was developed based on bio-based MPCMs and limestone calcined clay cement (LC³) binder with lower clinker content. It was shown that utilizing such environmentally friendly construction materials could contribute to lowering the operational and embodied energy and emissions of major infrastructures.

Keywords

Phase change material (PCM); machine learning; deep learning; activation energy; shape-stabilized PCM (SSPCM); limestone calcined clay cement (LC³)

Summary for Lay Audience

Reducing the energy consumption of buildings is an important step toward mitigating climate change and attaining a sustainable and resilient built environment. Researchers have coined brilliant solutions to increase the energy efficiency in the heating and cooling of buildings, very similar to the idea of manufacturing energy-star appliances. One emerging idea is to integrate phase change materials (PCMs) in buildings. PCMs, perform similarly to a battery that can store thermal energy. Using this technology, the change in the indoor temperature of buildings can be narrowed down and major energy savings for heating, ventilation, and air conditioning (HVAC) systems are achieved. PCMs can be added to construction materials, such as concrete, and used for building various elements such as walls, roofs, and envelopes. However, they can cause negative impacts on the mechanical strength of the materials. In this research, advanced experimental and computational tools were employed to evaluate the effects of PCMs on the mechanical performance of concrete and predict its strength after the addition of PCMs. Recommendations are given for proper mixture proportioning of concrete with PCM considering different levels of strength. Furthermore, novel and environmentally friendly materials are developed with PCM inclusion to benefit the sustainability of buildings. The results obtained from this research can better help engineers and policy-makers develop sustainable and resilient frameworks for the construction industry and reduce the impact of the built environment on exacerbating climate change.

Co-Authorship Statement

This thesis is prepared according to the regulation of the integrated-article format stipulated by the Faculty of Graduate Studies at Western University. All the research work in this thesis, including experimental testing, data analysis, and writing draft manuscripts for publication, was carried out by the candidate under the supervision of Dr. Moncef L. Nehdi. Any other co-authors assisted in modeling, conducting the experimental program, and/or revision of the initial draft of the manuscript. The following publications have been either published or submitted to peer-reviewed technical journals or international conferences:

Marani, A., & Nehdi, M. L. (2019). Integrating phase change materials in construction materials: Critical review. *Construction and Building Materials*, 217, 36-49. **Published**

Marani, A., & Nehdi, M. L. (2020). Machine learning prediction of compressive strength for phase change materials integrated cementitious composites. *Construction and Building Materials*, 265, 120286. **Published**

Marani, A., Zhang, L. V., & Nehdi, M. L. (2022), “Design of concrete incorporating microencapsulated phase change materials for clean energy: a ternary machine learning approach” **to be submitted to Journal of Engineering Applications of Artificial Intelligence, Elsevier**

Marani, A., Zhang, L. V., & Nehdi, M. L. (2022), “Activation energy of concrete incorporating phase change materials” **Under review in Cement and Concrete Composites, Elsevier**

Marani, A., Geranfar, E., & Nehdi, M. L. (2022), “Deep learning-assisted calculation of apparent activation energy for cement-based composites incorporating microencapsulated phase change materials” **to be submitted to Construction and Building Materials, Elsevier**

Marani, A., Zhang, L. V., & Nehdi, M. L. (2022), “Multiphysics Study on Cement-Based Composites Incorporating Green Biobased Shape-stabilized Phase Change Materials for Thermal Energy Storage” **Under revision in Journal of Cleaner Productions, Elsevier**

Marani, A., & Nehdi, M. L. (2022), “Hydration Kinetics and Microstructural Development of Ternary Limestone Calcined Clay Cement (LC³) Composites Incorporating Phase Change Materials” In preparation, to be submitted to *Cement and Concrete Research*, Elsevier

Marani, A., & Nehdi, M. L. (2021). “Application of artificial neural networks in prediction of compressive strength of PCM-integrated concretes”. CSCE Materials and Mechanics Specialty Annual Conference, 10 p. Published

Marani, A., Zhang, L. V., & Nehdi, M. L. (2021). Experimental study on effect of micro-encapsulated PCM addition on cement hydration. CSCE Materials and Mechanics Specialty Annual Conference, 9 p. In Press

Dedication

This thesis is dedicated to:

My Beloved Mother

My Beloved brother Iman

My beloved Brother Amin

*And to the Soul of My Beloved
Father ♥*

Acknowledgments

It is always joyful to think of the amazing journey that I have had during my study at Western University. I appreciate this opportunity that was provided by Western and the great support I have received from many outstanding people.

My first and foremost gratitude and sincere appreciation go to my Ph.D. supervisor Dr. Moncef L. Nehdi. No words can describe how wholeheartedly he believed in me and leveraged my confidence to perform impactful research.

I am very grateful to everyone in the Department of Civil and Environmental Engineering for their kind help and support during the last three and a half years. My special appreciation is for Dr. Aiham Adawi who was always a huge help in the structural lab. I also would like to thank Kristen Edwards and wonderful Dr. Wankei Wan (CBE department) for their great help on many occasions.

I have had the privilege to work alongside many amazing students during the past few years. My colleagues in my office SEB 2020, Dr. Lei V. Zhang, Dr. Ahmed Suleiman, Dr. Lui S. Wong, Abdullah Ramadan, Abdul-Aziz Younis, Majdi Flah, Wassim Ben-Chaabene, Amer Sabsabi, and Itzel Nunez.

I am always grateful to my great friends here in London and all over Canada that we shared numerous happy and sad moments, Siamak, Navid, Shayan, Ali, Azadeh, Kamyar, Omid, and so many others!

I cannot think of anyone more important than my whole family. My most precious thing in life is my family, my beloved Mother, and my dear brothers, Iman and Amin. I am sincerely grateful for everything they did for me in all stages of my life, especially the few hard years far from home. I miss them and I wish they were here with me.

I miss my Father in every moment of my life. I am sure no one is proud of me more than he is. I dedicate this piece of work to the beautiful mind and soul of my greatest supporter, my eternal love, my Father ♥.

Table of Contents

Abstract.....	ii
Summary for Lay Audience.....	iii
Co-Authorship Statement.....	iv
Dedication.....	vi
Acknowledgments.....	vii
Table of Contents.....	viii
List of Tables.....	xv
List of Figures.....	xviii
Chapter 1.....	1
1 Introduction.....	1
1.1 Buildings and energy consumption.....	1
1.2 Research on thermal energy storage construction materials.....	2
1.3 Research significance.....	2
1.4 Research objectives.....	3
1.5 Original contributions.....	4
1.6 Thesis structure.....	5
1.7 References.....	5
Chapter 2.....	8
2 Integrating Phase Change Materials in Construction Materials: Critical Review.....	8
2.1 Introduction.....	8
2.2 Microencapsulation techniques.....	11
2.2.1 Physical and mechanical properties.....	11
2.2.2 Thermal properties.....	15
2.2.3 Durability of PCM microcapsule-integrated materials.....	18

2.2.4	Potential applications	19
2.3	Shape-stabilization of PCMs.....	20
2.3.1	Supporting materials.....	21
2.3.2	Fabrication methods.....	23
2.3.3	Characterization of SSPCMs.....	24
2.3.4	Potential applications of SSPCMs	26
2.4	Porous inclusion	27
2.4.1	Lightweight aggregates.....	27
2.4.2	Impregnation method	28
2.4.3	Supporting and coating materials.....	29
2.4.4	Characterization of PCM-LWA concrete	30
2.4.5	Potential applications	31
2.5	Macroencapsulation	31
2.5.1	PCM macroencapsulation through building walls and envelopes	32
2.5.2	PCM macroencapsulation in building roofs	34
2.6	Discussion and recommendations.....	35
2.7	Summary, conclusions, and future work.....	36
2.8	References.....	38
Chapter 3	54
3	Machine Learning Prediction of Compressive Strength for Phase Change Materials Integrated Cementitious Composites	54
3.1	Introduction.....	54
3.2	Machine leaning modeling basis.....	57
3.2.1	Random forest regression (RFR)	58
3.2.2	Extra trees regression (ETR).....	59
3.2.3	Gradient boosting regression (GBR)	60

3.2.4	eXtreme gradient boosting regression (XGBR).....	61
3.3	Model development	62
3.3.1	Data collection, feature extraction, and preprocessing	62
3.3.2	Model development, hyperparameter tuning, and cross-validation.....	63
3.3.3	Model performance evaluation	64
3.4	Results and discussion	65
3.4.1	Hyper-parameter tuning of employed ML models	65
3.4.2	Predictive performance of machine learning models.....	66
3.4.3	Feature importance of machine learning models	72
3.5	Conclusions and recommendations.....	76
3.6	References.....	77
Chapter 4	86
4	Mixture Design of Concrete Incorporating Microencapsulated Phase Change Materials for Clean Energy: A Ternary Machine Learning Approach	86
4.1	Introduction.....	86
4.2	Overview of state-of-the-art.....	88
4.2.1	Knowledge background	88
4.2.2	Machine learning modeling	89
4.3	Methodology	91
4.3.1	Experimental data collection and analysis	93
4.3.2	Model development	94
4.3.3	Model performance evaluation	101
4.3.4	Empirical model.....	102
4.4	Results and discussion	103
4.4.1	Performance of ML models	104
4.4.2	Empirical model.....	113

4.5 Parametric analysis	115
4.6 Mixture optimization	121
4.7 Conclusions, recommendations, and future Work.....	124
4.8 References.....	126
Chapter 5.....	132
5 Activation Energy of Cement-Based Materials Incorporating Microencapsulated Phase Change Materials	132
5.1 Introduction.....	132
5.2 Background knowledge and literature review	134
5.2.1 Apparent activation energy.....	134
5.2.2 Effect of PCMs on cement hydration.....	137
5.3 Materials and methods	138
5.3.1 Materials	138
5.3.2 Experimental program	139
5.3.3 Calculation of apparent activation energy (E_a).....	141
5.4 Results and discussion	144
5.4.1 Effects of MPCM addition on cement hydration.....	145
5.4.2 Calculation of E_a for cement pastes using isothermal calorimetry data	151
5.4.3 Effect of MPCMs on compressive strength.....	157
5.4.4 Calculation of E_a for cement mortars using compressive strength data	160
5.4.5 Microstructural analyses	162
5.5 Concluding remarks	166
5.6 References.....	167
Chapter 6.....	172
6 Deep Learning-Assisted Calculation of Apparent Activation Energy for Cement-based Composites Incorporating Microencapsulated Phase Change Materials.....	172
6.1 Introduction.....	172

6.2	Background knowledge and literature review	174
6.2.1	Hydration kinetics and apparent activation energy	174
6.2.2	Machine learning basis	177
6.3	Model development	178
6.3.1	Data collection	178
6.3.2	Data preparation and partitioning	179
6.3.3	Model development	180
6.3.4	Calculation of apparent activation energy (E_a)	184
6.4	Results and discussion	185
6.4.1	Prediction performance of ML models	186
6.4.2	Calculation of apparent activation energy	194
6.5	Concluding remarks	200
6.6	References	200
Chapter 7		208
7	Multiphysics Study on Cement-Based Composites Incorporating Green Biobased Shape-stabilized Phase Change Materials for Thermal Energy Storage	208
7.1	Introduction	208
7.2	Materials and methods	212
7.2.1	Materials	212
7.2.2	SSPCM Fabrication	212
7.2.3	SSPCM characterization	214
7.2.4	Characterization of SSPCM-integrated mortar	215
7.3	Results and discussion	218
7.3.1	Morphology and leakage analysis of SSPCMs	218
7.3.2	Thermal properties of SSPCM	220
7.3.3	Isothermal calorimetry	222

7.3.4	Mechanical properties	223
7.3.5	Capillary water absorption	226
7.3.6	Micro-computed tomography scan (μ CT scan)	228
7.3.7	Thermoregulating performance	230
7.4	Concluding remarks	233
7.5	References	233
Chapter 8		240
8	Hydration Kinetics, Mechanical, Microstructural, and Thermal Characterization of Low-carbon Limestone Calcined Clay Cement (LC ³) Mortars Incorporating MPCMs	240
8.1	Introduction	240
8.2	Materials and methods	243
8.2.1	Materials	243
8.2.2	Experimental plan	244
8.3	Results and discussion	248
8.3.1	Analysis of hydration kinetics using IC test	248
8.3.2	Effect of MPCMs on compressive strength	251
8.3.3	Microstructural analysis using SEM-EDX	254
8.3.4	Porosity analysis with μ -CT scan	257
8.3.5	Thermo-regulating performance	259
8.4	Concluding remarks	260
8.5	References	261
Chapter 9		267
9	Summary, Conclusions, and Recommendations for Future Work	267
9.1	Summary and conclusions	267
9.2	Contribution to state-of-the-art	269
9.3	Research limitations	270

9.4 Recommendations for future research	270
Appendix A.....	272
Appendix B.....	292
Curriculum Vitae	298

List of Tables

Table 2-1: Various commercial PCM microcapsules used in the literature	12
Table 2-2: Different methods used for measuring thermal conductivity of cementitious composites in the literature	16
Table 2-3: Supporting materials used for fabricating SSPCMs in the literature	21
Table 2-4: Experimental studies on the application of PCM macrocapsules in buildings	34
Table 2-5: Recommendations for the method of PCM incorporation in construction and pavement materials	36
Table 3-1: Examples of ML applications in similar engineering fields.....	58
Table 3-2: Input features of the dataset prepared for modeling.....	63
Table 3-3: Tuned parameters for the employed ML models	66
Table 3-4: Statistical error metrics obtained for employed ML models.....	72
Table 4-1: Sources of collected data points	93
Table 4-2: Input features of dataset prepared for this study	94
Table 4-3: Thermophysical properties of PCM A and PCM B	99
Table 4-4: Upper and lower bonds for optimizing mortar and concrete incorporating MPCM	101
Table 4-5: Parameters and hyperparameters of TGAN model	104
Table 4-6: Comparison on the statistical properties of the real and synthetic data	105
Table 4-7: Tuned hyperparameters of RFR and GBR models.....	107
Table 4-8: Performance accuracy of baseline DNN models.....	110

Table 4-9: Optimization of empirical models	114
Table 4-10: Parametric analysis scenario	116
Table 4-11: Proposed mixture designs for mortar and concrete incorporating MPCMs	122
Table 5-1: Chemical composition of OPC	138
Table 5-2: Thermophysical properties of MPCMs	139
Table 5-3: Mixture components of cement pastes used for isothermal calorimetry tests	139
Table 5-4: Mixture proportions of cement mortars used for compressive strength tests	140
Table 5-5: Hydration parameters extracted from isothermal curves	147
Table 5-6: Reaction rate of cement pastes calculated from the linear approximation of calorimetry data	152
Table 5-7: Hydration parameters and activation energies of cement pastes with En28	155
Table 5-8: Hydration parameters and activation energies of cement pastes with En35	155
Table 5-9: Apparent activation energy of mortars incorporating En28 and En35	161
Table 6-1: Training and testing datasets used for model development	179
Table 6-2: Search space and tuned hyperparameters of GBR and DNN models	183
Table 6-3: Hydration parameters for cement-based systems incorporating En28	197
Table 6-4: Hydration parameters for cement pastes incorporating En35	198
Table 6-5: Apparent activation energy of simulated systems	199
Table 7-1: Thermophysical properties of PCM 23 and PCM 28	212
Table 7-2: Cement paste samples used for isothermal calorimetry	216
Table 7-3: Mixture design of mortars prepared for thermomechanical tests	216

Table 7-4: Melting/freezing temperatures and enthalpies of PCMs and SSPCMs	221
Table 7-5: Thermal properties of some SSPCM systems proposed in the literature	222
Table 8-1: Chemical composition of OPC and metakaolin	244
Table 8-2: Mixture components of LC ³ pastes used for IC tests	245
Table 8-3: Mixture proportions of LC ³ mortars used for compressive strength tests.....	246
Table 8-4: Hydration parameters of LC ³ pastes incorporating En28.....	249
Table 8-5: Hydration parameters of LC ³ pastes incorporating En35.....	249
Table 8-6: EDX analysis of hydration products	257
Table B-1: Collected data for developing machine learning models.....	292

List of Figures

Figure 2-1: Categorization of different methods of PCM incorporation into construction materials and their associated technical considerations.....	10
Figure 2-2: Reasons for strength reduction in concrete incorporating PCM microcapsules. .	14
Figure 2-3: Influential factors in the fabrication of SSPCMs.	20
Figure 2-4: Some of common tests for characterizing SSPCMs.	26
Figure 2-5: Schematic cross-section of PCM macro-encapsulated configurations.	33
Figure 3-1: Simple schematic structure of a random forest model.	60
Figure 3-2: Schematic structure for the 5-fold CV.	64
Figure 3-3: Compressive strength of cementitious composites: observed VS. predicted.....	69
Figure 3-4: Residuals of the predicted output for training and testing data.....	72
Figure 3-5: Feature importance analysis of the proposed models.	76
Figure 4-1: Proposed ternary framework for mixture optimization of MPCM-integrated concrete. TGAN is used to generate synthetic data for training ML models. The models are then fed into the optimization algorithm to find optimum mixtures.....	92
Figure 4-2: Architecture of TGAN model. The generator is fed with random data from the latent space. The discriminator gives the probability of the generated data being fake or real.	96
Figure 4-3: Pearson correlation between attributes of data: real data (left), and synthetic data (right).	106
Figure 4-4: Observed versus predicted compressive strengths for training datasets.	107
Figure 4-5: Observed versus predicted compressive strengths for testing datasets.	108

Figure 4-6: Prediction performance of RFR, GBR, and DNN models using the TSTR approach.....	111
Figure 4-7: Taylor diagram for comparison of models. All three models indicated similar performance with GBR having slightly less error (green lines) and higher correlation (blue lines).....	112
Figure 4-8: Feature importance for GBR-TSTR model.....	112
Figure 4-9: Prediction performance of basic Eq. 4-1 (left) and Eq. 4-10 (right).....	115
Figure 4-10: Effect of fine aggregate replacement with MPCMs on compressive strength.	118
Figure 4-11: Surface response plot of compressive strength (CS)	120
Figure 4-12: Effect of MPCM inclusion on strength development versus time.	121
Figure 4-13: Results of laboratory experiments for mixture design of mortars incorporating MPCM having thermophysical properties similar to that of PCM B.	123
Figure 4-14: Comparison of PCM/C ratio in proposed mixture designs.	124
Figure 5-1: DSC curves of MPCMs.....	138
Figure 5-2: Steps of linear approximation method for calculating apparent activation energy.	142
Figure 5-3: Isothermal curves of pastes incorporating En28 at various temperatures.....	149
Figure 5-4: Isothermal curves of pastes incorporating En35 at various temperatures.....	151
Figure 5-5: Natural logarithm of linear reaction rate versus the inverse of the absolute temperature of pastes incorporating En28 and En35 microcapsules.	153
Figure 5-6: Natural logarithm of hydration time parameter versus the inverse of absolute temperature of pastes incorporating En28 and En35 microcapsules.	156

Figure 5-7: Compressive strength development of mortars cured under different temperatures.	160
Figure 5-8: Natural logarithm of reaction rate versus the inverse of absolute temperature for mortar mixtures using parabolic and exponential functions.	162
Figure 5-9: SEM images of mortar specimens: a) P28T23, b) P28T40, c) P35T23, and d) P35T40. Red arrows show the weak ITZ and gap between MPCMs and cement paste, blue arrows show micro-cracks initiated near MPCMs, and green arrows show cavities related to MPCMs detached from the cementitious matrix.	164
Figure 5-10: Segmentation of μ –CT scan Images for porosity analysis.	165
Figure 6-1: Data collection and partitioning schemes adopted in this study.	180
Figure 6-2: GBR1 model for prediction of hydration heat flow and cumulative heat.....	188
Figure 6-3: Predictions of GBR1 for cement systems incorporating various levels of En28 at 15°C.	188
Figure 6-4: Predictions of GBR1 for cement systems incorporating various levels of En35 at 15°C.	189
Figure 6-5 : DNN1 model for prediction of hydration heat flow and cumulative heat.	190
Figure 6-6: DNN2 model for prediction of hydration heat flow and cumulative heat.	190
Figure 6-7: Predictions of DNN1 for cement systems incorporating various levels of En28 at 40°C.	191
Figure 6-8: Predictions of DNN1 for cement systems incorporating various levels of En35 at 40°C.	192
Figure 6-9: HF and H Predictions of DNN2 for cement systems incorporating 15 wt.% En28 (left) and En35 (right) at various temperatures.	194

Figure 6-10: Heat evolution curves for various cement systems incorporating En28 (left) and En35 (right) obtained from DNN2 model.....	197
Figure 6-11: Variation in the apparent activation energy with MPCM addition of En28. ...	199
Figure 6-12: Comparison of apparent activation energy obtained from experimental measurements and DNN2 predictions.	199
Figure 7-1: Schematic diagram of 4-step vacuum impregnation technique for fabrication of SSPCMs.....	213
Figure 7-2: Physical appearance of PCMs, EG, and SSPCM particles.	214
Figure 7-3: Thermoregulating test setup for evaluation of the TES capacity of mortar specimens.....	218
Figure 7-4: SEM images of the surface of a) EG; b) S23; and c) S28 particles.	219
Figure 7-5: a) Diffusion-oozing circle test of SSPCM particles; b) comparison of the leakage rate of S23 and S28; and c) comparison of theoretical and experimental latent heat of S23 and S28.	220
Figure 7-6: DSC curves of PCM 23 and S23 (left), and PCM 28 and S28 (right).	222
Figure 7-7: Isothermal calorimetry curves of cement pastes in presence of S23 (left) and S28 (right).	223
Figure 7-8: Mechanical strength of mortar specimens incorporating EG and SSPCM: a) and b) compressive strength; c) reduction percentage in compressive strength; and d) tensile strength.	225
Figure 7-9: Optical and binary images of broken surfaces of specimens. Pores are shown with blue arrays, and EG and SSPCM particles are shown with red arrays.	226
Figure 7-10: Capillary water absorption (top) and sorptivity coefficient (bottom) of mortars incorporating EG and SSPCM particles.	227

Figure 7-11: Reconstructed 3D scan and segmentation of the pore structure of mortar samples.	229
Figure 7-12: Correlation between porosity, sorptivity, and compressive strength.	229
Figure 7-13: Temperature history of specimens under slow thermoregulating test.	232
Figure 7-14: Temperature history of specimens under rapid thermoregulating test.....	232
Figure 8-1: Thermo-regulating test setup for evaluation of the TES capacity of mortar specimens.....	247
Figure 8-2: Isothermal hydration curves of LC ³ pastes incorporating En28.	250
Figure 8-3: Isothermal hydration curves of LC ³ pastes incorporating En35.	251
Figure 8-4: Strength development of MPCM-integrated LC ³ mortars at w/b ratios of 0.5 (top) and 0.4 (bottom).	253
Figure 8-5: SEM images of mortars made with w/b ratio of 0.5: a) No MPCM inclusion; b) 20% En28 inclusion; and c) 20% En35 inclusion.....	255
Figure 8-6: SEM images of mortars made with w/b ratio of 0.5: a) No MPCM inclusion; b) 20% En28 inclusion; and c) 20% En35 inclusion.....	256
Figure 8-7: Image segmentation for porosity analysis of mortar samples.....	258
Figure 8-8: 3D pore structure of samples obtained from μ -CT scan analysis.	258
Figure 8-9: Thermo-regulating performance of specimens incorporating En28 (top) and En35 (bottom) inclusion.	260
Figure A-1: Predictions of GBR1 for cement systems incorporating various levels of En28 at 15°C.	272
Figure A-2: Predictions of GBR1 for cement systems incorporating various levels of En28 at 23°C.	273

Figure A-3: Predictions of GBR1 for cement systems incorporating various levels of En28 at 30°C.	274
Figure A-4: Predictions of GBR1 for cement systems incorporating various levels of En28 at 35°C.	275
Figure A-5: Predictions of GBR1 for cement systems incorporating various levels of En28 at 40°C.	276
Figure A-6: Predictions of GBR1 for cement systems incorporating various levels of En35 at 15°C.	277
Figure A-7: Predictions of GBR1 for cement systems incorporating various levels of En35 at 23°C.	278
Figure A-8: Predictions of GBR1 for cement systems incorporating various levels of En35 at 30°C.	279
Figure A-9: Predictions of GBR1 for cement systems incorporating various levels of En35 at 35°C.	280
Figure A-10: Predictions of GBR1 for cement systems incorporating various levels of En35 at 40°C.	281
Figure A-11: Predictions of DNN1 for cement systems incorporating various levels of En28 at 15°C.	282
Figure A-12: Predictions of DNN1 for cement systems incorporating various levels of En28 at 23°C.	283
Figure A-13: Predictions of DNN1 for cement systems incorporating various levels of En28 at 30°C.	284
Figure A-14: Predictions of DNN1 for cement systems incorporating various levels of En28 at 35°C.	285

Figure A-15: Predictions of DNN1 for cement systems incorporating various levels of En28 at 40°C.	286
Figure A-16: Predictions of DNN1 for cement systems incorporating various levels of En35 at 15°C.	287
Figure A-17: Predictions of DNN1 for cement systems incorporating various levels of En35 at 23°C.	288
Figure A-18: Predictions of DNN1 for cement systems incorporating various levels of En35 at 30°C.	289
Figure A-19: Predictions of DNN1 for cement systems incorporating various levels of En35 at 35°C.	290
Figure A-20: Predictions of DNN1 for cement systems incorporating various levels of En35 at 40°C.	291

Chapter 1

1 Introduction

This chapter briefly introduces the background of the research, research motivations and significance, objectives, and the general layout of the thesis.

1.1 Buildings and energy consumption

The drastic worldwide increase in energy demand has raised stern concerns about the depletion of the traditional energy resources, failure of the energy supply infrastructures, and serious environmental problems including global warming and climate change (Santamouris *et al.*, 2001). For instance, between 1984 and 2004, the global energy consumption and CO_2 emissions increased by 49% and 43%, respectively, a growing trend at an average annual rate of 3.2% (Pérez-Lombard *et al.*, 2008). Global energy consumption had been conventionally divided into three groups: industry, transportation, and “other” sections. Nevertheless, more comprehensive analyses revealed that the share of energy consumption in buildings is between 20-40% of the total energy consumption in many developed countries, which is higher than that of industry and transportation sectors (Kingma & van Marken Lichtenbelt, 2015; Pérez-Lombard *et al.*, 2008). For instance, nearly 40% of the total final energy consumption and CO_2 emissions in the European Union (EU) are related to the building sector (Asadi *et al.*, 2012; Soares *et al.*, 2013). Therefore, the energy efficiency of buildings has become a prime goal for energy policies at both national and international levels.

Researchers have attempted to propose new and promising solutions to increase the energy efficiency of buildings. Such strategies include developing new technologies in many related engineering fields, such as electrical engineering, mechanical engineering, civil engineering, and architectural science. Incorporating advanced internet of things (IoT)-based intelligent systems for energy management in buildings, integrating solar energy systems, manufacturing insulating building materials, and promoting passive architectural designs are among the many proposed resolutions (Chen *et al.*, 2019; Good *et al.*, 2015; Marinakis & Doukas, 2018). One compelling solution is to integrate latent heat thermal

energy storage (LHTES) capacity in buildings (Cabeza *et al.*, 2011; De Gracia & Cabeza, 2015). This could be achieved by utilizing phase change materials (PCMs) in different building elements.

PCMs are a type of chemicals that can store/retrieve a significant amount of heat upon their physical phase transition, *e.g.*, from solid to liquid. During the phase transition, the temperature of the PCM remains relatively constant while a huge amount of heat is stored/released owing to their latent heat capacity (Agyenim *et al.*, 2010; Zhang *et al.*, 2021; Zhao & Zhang, 2011). Researchers have proposed the integration of PCMs with phase change temperatures near room temperature for regulating indoor temperature fluctuation and consequently reducing the energy consumption of HVAC systems (Cabeza *et al.*, 2011; Marani & Madhkhan, 2021).

1.2 Research on thermal energy storage construction materials

One interesting approach to integrating LHTES systems in buildings is to incorporate PCMs into building materials. Various techniques have been recommended to add PCMs into construction materials, such as cement-based mortars and concretes, gypsum, etc. (Cabeza *et al.*, 2007; Zhou *et al.*, 2007). Concrete as the most-consumed human-made material has been the most popular host for incorporating PCMs (Berardi & Gallardo, 2019). Extensive research has been devoted to characterizing a wide range of engineering properties of concrete in the presence of PCMs. Most efforts have been directed toward the analysis of the energy-saving aspect of concrete elements (*i.e.*, walls, roofs, etc.) incorporating PCMs (Marani & Madhkhan, 2018; Thiele *et al.*, 2015). Nevertheless, recent findings prompt the multi-physics analysis of the engineering properties of cement-based composites incorporating different types of PCMs.

1.3 Research significance

Despite the improvements in the thermal performance of concrete, PCMs have proven to negatively affect the mechanical properties of concrete. Few studies have investigated the mechanisms related to the decrease of the mechanical strength at the micro-scale. Yet, concerted research is needed to examine the strength development with PCM inclusion.

Furthermore, the effect of the thermo-physical properties of PCMs on the hydration kinetics of cement-based composites needs fundamental assessment to better apprehend their thermal-related properties.

This study aims at investigating the microstructural and mechanical strength development of various cement-based composites incorporating different types of PCMs. The scope of the current study is to optimize the thermal energy storage capacity of structural concrete with respect to required mechanical performance. To further reduce the environmental footprint of the built environment, this study intends to develop low-carbon thermal energy storage composites using emerging eco-friendly and recycled materials. Purposefully, various types of commercially available solid-liquid PCMs in North America were utilized. Extensive numerical simulations and laboratory experiments are carried out to better understand the mechanisms affecting the mechanical strength, hydration kinetics, and microstructure of the PCM-integrated concretes. Understanding these mechanisms allows the efficient design of PCM-integrated systems.

1.4 Research objectives

This research aims at achieving the following specific objectives:

- Compiling an up-to-date dataset of compressive strength measurements of PCM-integrated concrete mixtures from the pertinent studies in the open literature.
- Developing a machine learning framework for the prediction of compressive strength of PCM-integrated concrete.
- Determining the influential factors affecting the strength development of concrete made with PCM inclusion.
- Optimizing the mixture of cement-based mortars and concretes incorporating different types of PCMs.
- Investigating the activation energy and maturity of cement-based composites incorporating PCMs

- Proposing new form-stable PCMs for use in cement-based composites.
- Exploring the effects of PCM addition on the hydration kinetics, microstructure, mechanical, and thermal, performance of green low-clinker cementitious composites.

1.5 Original contributions

This search provides an in-depth discussion and analysis on diverse methods to incorporate PCMs into cementitious composites. It is crucial to find the problems associated with each of the utilized methods. Accordingly, the incorporation of microencapsulated PCMs (MPCMs) was identified as a viable method for adding PCMs to concrete mixtures. Therefore, the most up-to-date dataset of the concrete mixture designs with various types of MPCMs was collected. Developing robust machine learning models enabled the prediction of the compressive strength of MPCM-integrated concretes with desirable accuracies, along with recognizing the influential parameters affecting their mechanical strength development.

Considering the low number of mixture design examples in the open literature, a state-of-the-art synthesized data-generating framework was adopted to create numerous plausible mixture designs. Coupling that framework with metaheuristic algorithms, the mixture design of MPCM-integrated concretes and mortars was optimized such that maximum latent heat capacity and lowest cement consumption are achieved.

Machine learning results suggest that the addition of MPCMs might affect the maturity of concrete. In this regard, the apparent activation energy modeling of the MPCM-integrated mortars confirmed the reduction in the activation energy, while the effect of the melting temperature of MPCMs was found to be insignificant. Furthermore, a deep learning paradigm was also established to calculate the apparent activation energy for more diverse cement-based composites.

To further promote sustainability and reduce the embodied carbon emission of building components, MPCMs were added for the first time to low-carbon calcined clay cement (LC³) mortars. A set of various tests were carried out to characterize the effect of MPCMs on the engineering properties of LC³ mortars. Additionally, a new green bio-based shape

stabilized PCM (SSPCM) with desirable thermo-physical properties was developed based on recycled expanded glass aggregates.

1.6 Thesis structure

The present thesis is formatted according to the integrated-article format predefined by the Faculty of Graduate Studies at Western University, London, Ontario, Canada. The thesis contains nine chapters based on the objectives defined earlier. The main chapters of the current thesis have either been published or submitted for possible publication in peer-reviewed journals and conference proceedings. The chapters are as follows:

Chapter 2 classifies various PCM incorporation methods and provides in-depth discussions on different aspects of each method. Chapter 3 presents a machine-learning model for the prediction of compressive strength of MPCM-integrated concretes. In Chapter 4, a ternary machine-learning paradigm is developed to optimize the mixture design of MPCM concrete. Chapters 5 and 6 investigate the activation energy of cement-based composites incorporating MPCMs using experimental procedures and deep learning models. Chapter 7 proposes the development of leak-free green bio-based SSPCMs for use in concrete materials. Chapter 8 investigates the properties of LC³ mortars incorporating MPCMs. Ultimately, Chapter 9 reviews the major conclusions derived from this research and recommends potential future work.

1.7 References

Agyenim, F., Hewitt, N., Eames, P., & Smyth, M. (2010). A review of materials, heat transfer and phase change problem formulation for latent heat thermal energy storage systems (LHTESS). *Renewable and sustainable energy reviews*, 14(2), 615-628.

Asadi, E., Da Silva, M. G., Antunes, C. H., & Dias, L. (2012). Multi-objective optimization for building retrofit strategies: A model and an application. *Energy and Buildings*, 44, 81-87.

Berardi, U., & Gallardo, A. A. (2019). Properties of concretes enhanced with phase change materials for building applications. *Energy and Buildings*, 199, 402-414.

Cabeza, L. F., Castell, A., Barreneche, C. d., De Gracia, A., & Fernández, A. (2011). Materials used as PCM in thermal energy storage in buildings: A review. *Renewable and sustainable energy reviews*, 15(3), 1675-1695.

Cabeza, L. F., Castellon, C., Nogues, M., Medrano, M., Leppers, R., & Zubillaga, O. (2007). Use of microencapsulated PCM in concrete walls for energy savings. *Energy and Buildings*, 39(2), 113-119.

Chen, X., Huang, J., Yang, H., & Peng, J. (2019). Approaching low-energy high-rise building by integrating passive architectural design with photovoltaic application. *Journal of Cleaner Production*, 220, 313-330.

De Gracia, A., & Cabeza, L. F. (2015). Phase change materials and thermal energy storage for buildings. *Energy and Buildings*, 103, 414-419.

Good, C., Andresen, I., & Hestnes, A. G. (2015). Solar energy for net zero energy buildings—A comparison between solar thermal, PV and photovoltaic–thermal (PV/T) systems. *Solar Energy*, 122, 986-996.

Kingma, B., & van Marken Lichtenbelt, W. (2015). Energy consumption in buildings and female thermal demand. *Nature climate change*, 5(12), 1054-1056.

Marani, A., & Madhkhan, M. (2018). An innovative apparatus for simulating daily temperature for investigating thermal performance of wallboards incorporating PCMs. *Energy and Buildings*, 167, 1-7.

Marani, A., & Madhkhan, M. (2021). Thermal performance of concrete sandwich panels incorporating phase change materials: An experimental study. *Journal of Materials Research and Technology*, 12, 760-775.

Marinakis, V., & Doukas, H. (2018). An advanced IoT-based system for intelligent energy management in buildings. *Sensors*, 18(2), 610.

Pérez-Lombard, L., Ortiz, J., & Pout, C. (2008). A review on buildings energy consumption information. *Energy and Buildings*, 40(3), 394-398.

Santamouris, M., Papanikolaou, N., Livada, I., Koronakis, I., Georgakis, C., Argiriou, A., & Assimakopoulos, D. (2001). On the impact of urban climate on the energy consumption of buildings. *Solar Energy*, 70(3), 201-216.

Soares, N., Costa, J. J., Gaspar, A. R., & Santos, P. (2013). Review of passive PCM latent heat thermal energy storage systems towards buildings' energy efficiency. *Energy and Buildings*, 59, 82-103.

Thiele, A. M., Sant, G., & Pilon, L. (2015). Diurnal thermal analysis of microencapsulated PCM-concrete composite walls. *Energy conversion and management*, 93, 215-227.

Zhang, S., Feng, D., Shi, L., Wang, L., Jin, Y., Tian, L., Li, Z., Wang, G., Zhao, L., & Yan, Y. (2021). A review of phase change heat transfer in shape-stabilized phase change materials (ss-PCMs) based on porous supports for thermal energy storage. *Renewable and sustainable energy reviews*, 135, 110127.

Zhao, C.-Y., & Zhang, G. H. (2011). Review on microencapsulated phase change materials (MEPCMs): fabrication, characterization and applications. *Renewable and sustainable energy reviews*, 15(8), 3813-3832.

Zhou, G., Zhang, Y., Wang, X., Lin, K., & Xiao, W. (2007). An assessment of mixed type PCM-gypsum and shape-stabilized PCM plates in a building for passive solar heating. *Solar Energy*, 81(11), 1351-1360.

Chapter 2

2 Integrating Phase Change Materials in Construction Materials: Critical Review¹

Diverse applications of phase change materials (PCMs) have become of great interest in recent years owing to their beneficial effects on the thermal and durability properties of construction and pavement materials. PCMs can alter the thermal mass and thermal inertia of building materials, thus enhancing thermal energy storage. The effects of PCMs on cement hydration, thermal stress, and shrinkage of concrete have stimulated further applications. Despite various virtues of PCMs in construction and pavement materials, their drawbacks still need concerted research efforts. Among the fundamental problems of PCMs is their risk of leakage in the molten state. Hence, several techniques have been proposed to mitigate this problem. The present chapter examines the potential methods of incorporating PCMs into building materials, including microencapsulation, macroencapsulation, shape-stabilization, and porous inclusion. A critical analysis of PCM applications and stabilization materials and methods in concrete is provided, hence identifying practical recommendations, research needs, and current knowledge gaps.

2.1 Introduction

Rapidly growing energy consumption along with the limitations of energy resources has motivated researchers to seek new methods for energy harvesting and conservation in different sectors. In particular, buildings consume the largest energy share worldwide, exceeding the industry and transportation sectors (Annual Energy Outlook, 2010; Sieminski, 2014). Furthermore, stern climate change implications of the colossal fossil fuel consumption have stimulated the search for novel methods to enhance energy efficiency. For instance, increasing the thermal inertia and thermal mass of buildings has been hailed as a promising method for energy conservation in buildings (Braun *et al.*, 2001; Ruud *et al.*, 1990).

¹ A version of this chapter was published in “*Construction and Building Materials*” journal, 2019.

Phase change materials (PCMs) have been recently introduced to enhance the thermal properties of building materials including thermal mass, thermal inertia, and specific heat capacity (Tyagi *et al.*, 2011; Zalba *et al.*, 2003; Zhou *et al.*, 2012). PCMs are substances capable of storing and releasing a great deal of thermal energy when they undergo phase transitions. They are grouped into three main categories, namely organic, inorganic, and eutectic mixtures (Raoux, 2009; Zalba *et al.*, 2003). Incorporating PCMs in building materials such as concrete and gypsum significantly increases their thermal mass, which contributes to regulating the indoor temperature of buildings. Accordingly, energy conservation in buildings by thermal energy storage (TES) becomes more achievable (Khudhair & Farid, 2004; Schossig *et al.*, 2005; Sharma *et al.*, 2009; Zalba *et al.*, 2003; Zhou *et al.*, 2012).

Not only can PCMs affect the energy efficiency of building elements, but they also may enhance some mechanical and durability features of construction materials. For instance, researchers have explored improving the temperature variations and heat evolution in concrete elements (*e.g.*, mass concrete) during the cement hydration process, crack resistance, and thermal shrinkage of concrete in the presence of PCMs (Fernandes *et al.*, 2014; Kim *et al.*, 2015; Šavija & Schlangen, 2016). Reducing thermal stress and damage due to freezing-thawing cycles or temperature gradients (*i.e.*, curling stresses) in concrete pavements incorporating PCMs has also been studied (Esmaeeli *et al.*, 2018; Pilehvar *et al.*, 2019; Sakulich & Bentz, 2011; Sharifi & Mahboub, 2018).

However, incorporating PCMs into building materials, such as concrete, is associated with drawbacks that need mitigation. For instance, the possible leakage of PCMs in the liquid state has been a concern (Cui *et al.*, 2017; Hunger *et al.*, 2009; Kuznik *et al.*, 2011; Soares *et al.*, 2013). Interference of PCMs with cement hydration and detrimental effects on the mechanical properties of concrete are epitomes of PCM leakage consequences. Hence, researchers have introduced various methods for safer PCM incorporation into building materials to forestall the leakage of PCMs in the melted state. As shown in **Fig. 2-1**, these proposed methods can generally be classified into four groups: microencapsulation, shape-stabilized phase change materials (SSPCMs), porous aggregate inclusions, and macro-encapsulation. Generally, the specific application of PCMs and their influence on the

characteristics of the dissimilar host material are key considerations for selecting the most suitable among these methods. **Figure 2-1** also outlines the main features associated with each incorporation method, which are scrutinized in the current study.

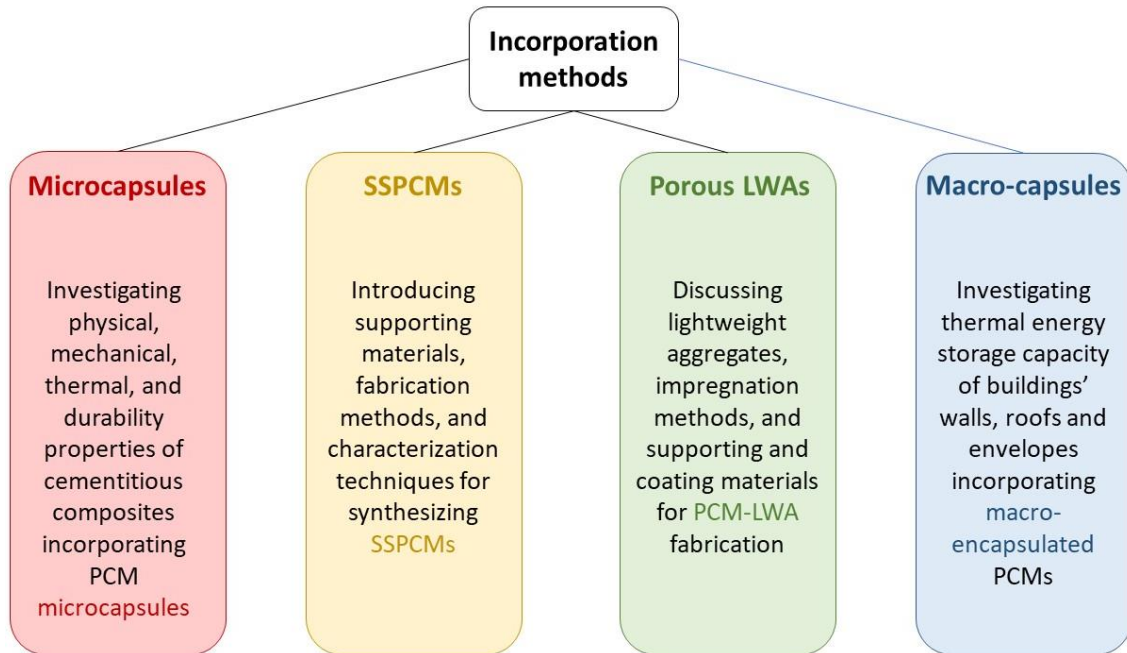


Figure 2-1: Categorization of different methods of PCM incorporation into construction materials and their associated technical considerations.

In the present study, methods for integrating PCMs in construction materials are analyzed and evaluated. The supporting materials and methods are critically reviewed and compared. Moreover, the testing methods for investigating the efficiency of each technique are presented. Finally, the potential applications of each method are outlined. Recognizing the various methods for incorporating PCMs along with their advantages and drawbacks should help engineers and construction materials stakeholders make informed design decisions regarding the most effective approaches for incorporating PCMs in building materials while mitigating any associated risks and side effects, which could yield sustainability and resilience benefits for buildings.

2.2 Microencapsulation techniques

Microencapsulation has been widely used as an effective method for incorporating PCMs into building materials. In addition to the protective effect of microencapsulation against the leakage of PCMs during their melting process, it can further improve the thermal conductivity of PCMs with more efficient performance in melting/freezing cycles. The different methods of PCM microencapsulation can be categorized into three basic groups, namely physical, physic-chemical, and chemical methods (Jamekhorshid *et al.*, 2014; Sánchez-Silva *et al.*, 2010). Several commercial PCM microcapsules have recently been produced for applications in the building industry. **Table 2-1** summarizes different commercial PCM microcapsules used in construction materials. It can be observed that PCM microcapsules have been mostly used in cementitious composites, and several studies have been conducted to characterize PCM-integrated cementitious composites. Generally, PCM microcapsules are used directly in the mixing process of concrete, mostly as a partial replacement for sand. A recent study reported the application of PCM microcapsules in the production of artificial lightweight aggregates (LWAs) using palletization (Jamekhorshid *et al.*, 2014; Sánchez-Silva *et al.*, 2010). Incorporating PCM microcapsules in cementitious composites could induce effects on both thermal and mechanical properties, such as thermal conductivity, specific heat capacity, and compressive strength. Breakage of microcapsules could affect the performance of PCM in cementitious composites. Hence, proper characterization of concrete incorporating PCM microcapsules is of great importance as discussed below.

2.2.1 Physical and mechanical properties

Regardless of the incorporation method, PCMs have considerable effects on both the early- and later-age properties of concrete. The origin and distinctive nature of these effects necessitate a separate discussion of each. The following subsections elaborates the findings relevant to different properties of concrete incorporating PCMs.

Table 2-1: Various commercial PCM microcapsules used in the literature

Material		Ref.	Material		Ref.
Basic	PCM		Basic	PCM	
mortar	Micronal DS 5008	(Lucas <i>et al.</i> , 2013)	concrete	Micronal, Microtek	(Wei, Falzone, Wang, <i>et al.</i> , 2017)
concrete	Micronal DS 5001	(Franquet <i>et al.</i> , 2014)	concrete	Microtek MPCM 24	(Ricklefs <i>et al.</i> , 2017)
mortar	Micronal DS 5001	(Joulin <i>et al.</i> , 2014)	concrete	Microtek MPCM 24	(Falzone <i>et al.</i> , 2016)
mortar	Micronal DS 5001	(Haurie <i>et al.</i> , 2016)	concrete	Microtek MPCM 24	(Wei, Falzone, <i>et al.</i> , 2017a)
concrete	Micronal DS 5001	(Figueiredo <i>et al.</i> , 2016)	concrete	Microtek MPCM 28	(Lecompte <i>et al.</i> , 2015)
concrete	Micronal DS 5001	(Eddhahak-Ouni <i>et al.</i> , 2014)	geopolymer	Microtek MPCM 28	(Shadnia <i>et al.</i> , 2015)
plaster	Micronal DS 5001	(Lachheb <i>et al.</i> , 2017)	concrete	Microtek MPCM 28	(Young, Wei, <i>et al.</i> , 2017)
concrete/LWA	Micronal DS5040X	(Tuncel & Pekmezci, 2018)	mortar	Inertek	(Bahrar <i>et al.</i> , 2018)
concrete	Micronal DS5040X	(Jayalath <i>et al.</i> , 2016)	gypsum	Micronal	(Toppi & Mazzarella, 2013)
concrete	Micronal DS5040X	(Pomianowski <i>et al.</i> , 2014)	polyurethane sandwich panel	Micronal	(Castellón <i>et al.</i> , 2010)
wood and plastic	Micronal, Microtek	(Jamekhorshid <i>et al.</i> , 2017)	mortar	Devan Mikrathermic	(Kheradmand <i>et al.</i> , 2014)

2.2.1.1 Density, compressive strength, and elastic modulus

Incorporating PCM microcapsules into portland cement and geopolymer concrete and mortar tends to decrease their density due to the relatively lower density of PCM microcapsules (Aguayo *et al.*, 2016; Figueiredo *et al.*, 2016; Haurie *et al.*, 2016; Jayalath *et al.*, 2016). For example, the bulk density of Micronal DS 5001 is 250-350 kg/m³, which is far smaller than that of concrete aggregates (Figueiredo *et al.*, 2016). Moreover, PCM microcapsules usually increase the porosity of the matrix, leading to lower density of the composite (Jayalath *et al.*, 2016).

Most studies in the open literature argue that PCM microcapsules addition in concrete is detrimental to its compressive strength. **Figure 2-2** displays the potential reasons for strength reduction of concrete incorporating PCM microcapsules. The inherent softness of PCM microcapsules, which does not provide significant mechanical resistance, has been

reported as a main reason for this behavior (Aguayo *et al.*, 2016; Eddhahak-Ouni *et al.*, 2014; Figueiredo *et al.*, 2016; Haurie *et al.*, 2016; Jayalath *et al.*, 2016). Falzone *et al.* (Falzone *et al.*, 2016) investigated the effect of incorporating soft inclusions on the mechanical properties of cementitious materials. Microtek MPCM24D microcapsules were used as the soft inclusion, while graded quartz sand was used as the stiff inclusion. The modulus of elasticity was evaluated and a critical volume ratio of stiff to soft inclusion was suggested as a design guide for cement mortar mixtures. Likewise, retardation of cement hydration reactions due to the interference of PCM is another factor affecting the compressive strength of concrete (Aguayo *et al.*, 2016; Eddhahak-Ouni *et al.*, 2014; Eddhahak *et al.*, 2014). Rupture of the microcapsules shell during mixing or loading of concrete results in PCM leakage, which can hinder the contact between cement particles and water. Similar effect of PCMs on the geopolymerization of fly ash was also reported (Cao *et al.*, 2017; Shadnia *et al.*, 2015).

Another potential reason for the decrease in the compressive strength of concrete is the increased porosity imparted by PCM addition (Aguayo *et al.*, 2016; Dehdezi *et al.*, 2013; Eddhahak *et al.*, 2014; Haurie *et al.*, 2016; Jayalath *et al.*, 2016; Pilehvar *et al.*, 2017). This was observed for instance by Aguayo *et al.* (Aguayo *et al.*, 2016) who used mercury intrusion porosimetry (MIP), and Pilehvar *et al.* (Pilehvar *et al.*, 2017) who used X-ray tomography imaging to evaluate the porosity of both portland cement and geopolymer concretes. Studies that are more recent assert that the type of shell material of PCM microcapsules can significantly affect the strength of concrete (Aguayo *et al.*, 2016; Liu *et al.*, 2017). For instance, Liu *et al.* (Liu *et al.*, 2017) reported that PCM microcapsules made with cenospheres and strengthened with silica sol could considerably restore strength reduction induced by traditional PCM microcapsules.

Integration of PCM microcapsules into concrete was also reported to reduce its modulus of elasticity (Falzone *et al.*, 2016; Haurie *et al.*, 2016). For instance, Haurie *et al.* (Haurie *et al.*, 2016) investigated the dynamic modulus of elasticity of cement mortars incorporating PCMs via fundamental resonance frequency and propagation of ultrasonic wave methods. Their results substantiated the known effect of reduced elastic modulus due to PCM addition in cement-based materials.

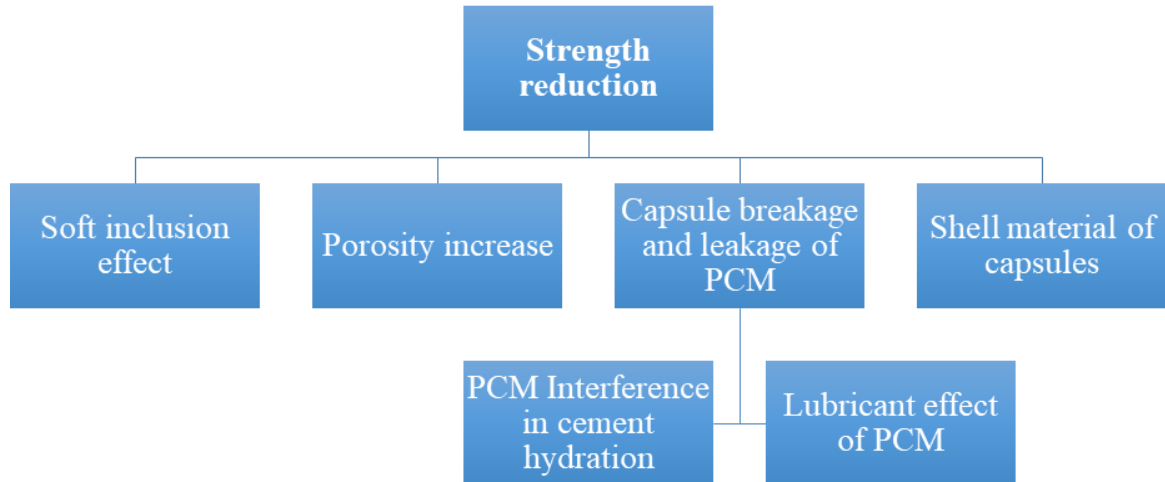


Figure 2-2: Reasons for strength reduction in concrete incorporating PCM microcapsules.

2.2.1.2 Microcapsule breakage

A potential problem associated with incorporating PCM microcapsules in concrete is microcapsule breakage during mixing or loading of concrete, as evidenced by SEM images in various studies (Aguayo *et al.*, 2016; Eddhahak *et al.*, 2014; Hunger *et al.*, 2009; Lecompte *et al.*, 2015; Meshgin & Xi, 2012; Pomianowski *et al.*, 2014). Pomianowski *et al.* (Pomianowski *et al.*, 2014) conducted cryo-scanning electron microscopy (cryo-SEM) analysis to investigate the condition of microcapsules after the mixing process. Results indicated some damage of PCM microcapsules, but this technique did not prove effective for evaluating possible PCM damage during mixing. Nevertheless, some researchers suggested that in order to reduce the occurrence of mechanical damage of PCM microcapsules during the mixing process, it is advantageous to add it as a last component in the mixture. However, Jayalath *et al.* (Jayalath *et al.*, 2016) refuted breakage of PCM microcapsules during mixing and rather attributed it to the loading stage of the hardened concrete. From a chemical point of view, Wei *et al.* (Wei, Falzone, Wang, *et al.*, 2017) attributed the PCM microcapsules damage to chemical reactions of the shell of microcapsules with sulfate ions in cement paste and consequent deformation and rupture of PCM microcapsules. More recently, researchers aimed to introduce new methods such

as the emulsion polymerization technique to produce more resilient PCM microcapsules (D'Alessandro *et al.*, 2018; Stritih *et al.*, 2018).

2.2.2 Thermal properties

Since PCMs have special thermophysical properties, they can impart to construction materials such as concrete immense thermal features, including thermal conductivity, specific heat capacity and thermal diffusivity. Moreover, PCMs can mitigate thermal cracking of concrete and enhance thermal energy storage (Arora *et al.*, 2017; Fernandes *et al.*, 2014; Thiele *et al.*, 2016; Young, Falzone, *et al.*, 2017; Young, Wei, *et al.*, 2017). Other building materials, such as gypsum and geopolymers, are also suitable for incorporation of PCMs, especially for TES applications (Castellón *et al.*, 2010; Jamekhorshid *et al.*, 2017; Shadnia *et al.*, 2015; Toppi & Mazzarella, 2013). For instance, Shadnia *et al.* (Shadnia *et al.*, 2015) evaluated the mechanical and thermal characteristics of geopolymer mortar including microencapsulated PCM. Microtek MPCM 28-D with a melting temperature of 28 °C and a latent heat of 180-195 J/gr was used. Thermal performance testing was conducted on three 305×305×305 mm cubicles to evaluate the performance of PCM integrated into the geopolymer wall in regulating indoor temperature and heat flow. Results indicated that using geopolymer mortar in building walls greatly increased the thermal inertia of the building elements. Hence, energy consumption for heating and cooling of indoor space could be decreased (Shadnia *et al.*, 2015).

2.2.2.1 Thermal conductivity

Several researchers explored the effects of PCM addition on the thermal conductivity of construction materials including cementitious composites and gypsum. The thermal conductivity of bulk materials is typically measured via several methods categorized either as steady-state or transient methods. **Table 2-2** presents methods employed to measure the thermal conductivity of cementitious composites with or without PCM contents. The hot disk and guarded hot disk methods, which are steady-state methods, have been more widely used for the measurement of thermal conductivity of cementitious composites incorporating PCMs (Cao *et al.*, 2017; Cui, Liao, *et al.*, 2015; Eddhahak-Ouni *et al.*, 2014; Haurie *et al.*, 2016; Jayalath *et al.*, 2016; Lecompte *et al.*, 2015; Ricklefs *et al.*, 2017).

Table 2-2: Different methods used for measuring thermal conductivity of cementitious composites in the literature

Material	PCM	Test method	Ref.
cement paste	no	TPS	(Bentz, 2007)
cement paste	no	laser flash	(Xu & Chung, 1999)
cement paste	no	laser flash	(Xu & Chung, 2000)
concrete	no	hot wire	(Demirboğa, 2007)
concrete	no	TPS	(Brown & Javaid, 1970)
concrete	no	hot wire	(Kim <i>et al.</i> , 2003)
concrete	no	hot plate	(Campbell-Allen & Thorne, 1963)
concrete	no	hot wire	(Uysal <i>et al.</i> , 2004)
concrete	paraffin	TPS	(Xu & Li, 2013)
concrete	n-octadecane	TPS	(Zhang <i>et al.</i> , 2013)
concrete	microcapsule	hot wire	(Martin Hunger <i>et al.</i> , 2009)
cement mortar	microcapsule	guarded hot plate	(Ricklefs <i>et al.</i> , 2017)
concrete and mortar	microcapsule	needle probe, C-Therm method	(Jayalath <i>et al.</i> , 2016)
mortar	microcapsule	dynamic measurement	(Haurie <i>et al.</i> , 2016)
concrete	microcapsule	hot disk	(Eddhahak-Ouni <i>et al.</i> , 2014)
cement mortar	microcapsule	hot disk	(Cui <i>et al.</i> , 2015)
concrete	microcapsule	hot disk	(Lecompte <i>et al.</i> , 2015)
geopolymer	microcapsule	guarded hot plate	(Cao <i>et al.</i> , 2017)

Jayalath *et al.* (Jayalath *et al.*, 2016) used two different methods named C-Therm and needle probe methods for measuring the thermal conductivity of both concrete and cement mortar incorporating PCM microcapsules. Results of both methods were in good agreement. Incorporating PCM microcapsules into concrete and mortar generally decreased thermal conductivity. Increased PCM microcapsule dosage resulted in greater reduction of thermal conductivity due to the relatively lower thermal conductivity of PCM microcapsules (Bahrar *et al.*, 2018; Haurie *et al.*, 2016; Jayalath *et al.*, 2016). Moreover, increase in air voids of the cementitious matrix due to PCM microcapsules incorporation led to lower thermal conductivity (Cui, Liao, *et al.*, 2015; Haurie *et al.*, 2016; Jayalath *et al.*, 2016). However, for low PCM microcapsule dosage, the thermal conductivity of concrete may not change significantly (Eddhahak-Ouni *et al.*, 2014).

2.2.2.2 Specific heat capacity

Integrating PCMs into construction materials can dramatically change their specific heat capacity because of PCM's latent heat capacity. Differential scanning calorimetry (DSC) was generally employed for measuring the specific heat capacity of cement pastes and mortars (Eddhahak-Ouni *et al.*, 2014; Haurie *et al.*, 2016; Jayalath *et al.*, 2016). Eddhahak-Ouni *et al.* (Eddhahak-Ouni *et al.*, 2014) used Micronal DS 5001 X as PCM in various concrete mixtures and investigated their specific heat capacity using DSC. The volume ratio of PCMs to concrete was 1%, 3%, and 5%. Integrating PCM into concrete led to significant improvement in the heat storage capacity of the PCM-concrete composite. However, limitations of this method in calculating the specific heat capacity of concrete (*i.e.*, the sample must be homogeneous and very small size) have motivated researchers to propose alternative methods for more accurate measurement of the specific heat capacity of concrete and mortar. For instance, Pomianowski *et al.* (Pomianowski *et al.*, 2014) introduced an experimental technique for assessing the heat capacity of concrete specimens incorporating PCM microcapsules. Micronal type DS 5040X with the latent heat of 100 kJ/kg and melting temperature of 23 °C was used as PCM microcapsules at dosages of 0, 1, 4, and 6 (wt.%). Four methods for calculating specific heat capacity with regards to temperature, $C_p(T)$, including theoretical method, simple method, numerical simple method, and inverse method were discussed. It was argued that the numerical simple method and inverse method were more applicable and appropriate for measuring the specific heat capacity of PCM microencapsulated concrete (Pomianowski *et al.*, 2014).

2.2.2.3 Thermal diffusivity

The thermal diffusivity, α , of materials is affected by the incorporation of phase change materials. It can be defined as:

$$\alpha = \frac{k}{\rho c_p} \quad \text{Eq. 2-1}$$

where k , ρ , and c_p are the thermal conductivity, density, and specific heat capacity, respectively. Since incorporating PCM microcapsules in concrete and mortar reduces the thermal conductivity and significantly increases the specific heat capacity, it is expected

that the thermal diffusivity would be reduced. This was evidenced for instance by experimental findings of Jayalath *et al.* (Jayalath *et al.*, 2016) and Haurie *et al.* (Haurie *et al.*, 2016), which confirm that PCM microcapsules addition reduced the thermal diffusivity of cementitious composites.

2.2.2.4 Heat of hydration

Incorporating PCMs in cementitious composites has considerable influence on portland cement hydration reactions and geo-polymerization of fly ash (Arora *et al.*, 2017; Eddhahak-Ouni *et al.*, 2014; Eddhahak *et al.*, 2014; Fernandes *et al.*, 2014; Hunger *et al.*, 2009; Jayalath *et al.*, 2016). Semi-adiabatic calorimetry and isothermal calorimetry can be utilized to measure the heat of hydration or hydration rate of cement. Jayalath *et al.* (Jayalath *et al.*, 2016) used Micronal DS 5040X as microencapsulated PCM in mortar and concrete mixtures. Isothermal calorimetry and thermogravimetry tests were conducted on mortar specimens to evaluate the effect of PCM microcapsules on heat of hydration and hydration products formation, respectively. Their results indicate that increasing the PCM microcapsules dosage in concrete mixtures caused an increase in the peak of the rate of the heat of hydration associated with a time delay. Eddahhak *et al.* (Eddhahak *et al.*, 2014) used semi-adiabatic calorimetry to measure heat of cement hydration in PCM-integrated mortar. Their results demonstrated that in mortars with broken microcapsules, hydration reactions are delayed compared to that of mortars with intact PCM microcapsules. Such delay in hydration kinetics was attributed to PCM leakage and its interference with the cementitious matrix components.

2.2.3 Durability of PCM microcapsule-integrated materials

A key objective of the application of PCMs in concrete, irrespective of the incorporation method, is enhancing its sustainability and durability (Sakulich & Bentz, 2012). The mitigation of early- and later-age cracks and reducing damage due to freezing-thawing cycles have become focus areas for recent studies. For instance, Wei *et al.* (Wei, *et al.*, 2017) evaluated the durability of cementitious mortars incorporating microencapsulated PCMs. Microtek MPCM6D, MPCM24 D, MPCM43D and Micronal DS 5008X were used as PCM microcapsules. The stability of the phase transition enthalpy of the

microencapsulated PCMs after addition to cement mortar was first examined and it was found that about 25% reduction in the phase change enthalpy occurred. This reduction was not attributed to mechanical damage of PCM microcapsules during the mixing process, but rather to chemical reactions of PCM microcapsules with the sulfate ions. However, the results of this study substantiated that although PCM microcapsules are vulnerable to the reduction of phase change enthalpy due to their chemical reactions with the sulfate-laden environment of cement mortars, they do not detrimentally affect the durability of mortar (Wei, *et al.*, 2017). Moreover, such studies emphasized the essential role of microcapsules to maintain the durability of cementitious composites. In other words, to have adequate durability and sustainability, PCM microcapsules should not be damaged during the host material's lifetime. Accordingly, both mechanical and chemical reasons may account for the deformation and rupture of microcapsules shells, causing leakage of the core PCM. Durability tests, water absorption, and drying shrinkage demonstrated that, in contrast to the vulnerability of PCM capsules in the sulfate environment of cement paste, no harmful effect on the durability of mortars incorporating PCM microcapsules was observed (Wei, *et al.*, 2017).

2.2.4 Potential applications

Researchers have proposed a wide range of potential applications of PCM-incorporated construction materials. Providing TES capability for plasters and mortars was the primary application of PCM microcapsules in construction materials. Lachheb *et al.* (Lachheb *et al.*, 2017) and Kusama and Ishidoya (Kusama & Ishidoya, 2017) reported that PCM plaster for building walls significantly contributes towards indoor thermal comfort and energy consumption reduction in buildings owing to its TES potential. Moreover, various studies on the influence of PCM inclusions on the mechanical, durability and crack behavior of structural concrete have been carried out as discussed earlier. Recently, the application of PCMs to reduce the temperature evolution in concrete at early-ages has been assessed. For instance, Young *et al.* (Young, *et al.*, 2017) reported that PCM inclusion in concrete pavements could reduce the temperature rise induced by cement hydration.

2.3 Shape-stabilization of PCMs

Considering the risk of PCM leakage in its molten state and its interference with the surrounding environment, several researchers have proposed a new form termed shape-stabilized PCM (SSPCMs). Stabilizing PCMs in the molten state is achieved using a supporting material (SM). Shape stabilizing of PCMs, like microencapsulation, not only prevents the leakage of the PCM, but also enhances the thermal conductivity of the phase change composite and improves its thermal behavior in melting/freezing cycles. The selection of SM and fabrication technique of SSPCMs are crucial factors affecting thermal characteristics. Various materials have been used as SM in the fabrication of SSPCMs as outlined in **Table 2-3**. Generally, three principal methods for fabricating SSPCMs are utilized, including direct absorption, vacuum impregnation, and sol-gel methods. The addition of SM could cause an alteration in thermo-physical properties of PCMs. Therefore, characterizing the fabricated SSPCM composites is crucial. Moreover, it is necessary to experimentally evaluate the effects of SSPCMs on thermal and mechanical properties of the host construction material. **Figure 2-3** displays a summarized categorization of influential factors in fabricating SSPCMs.

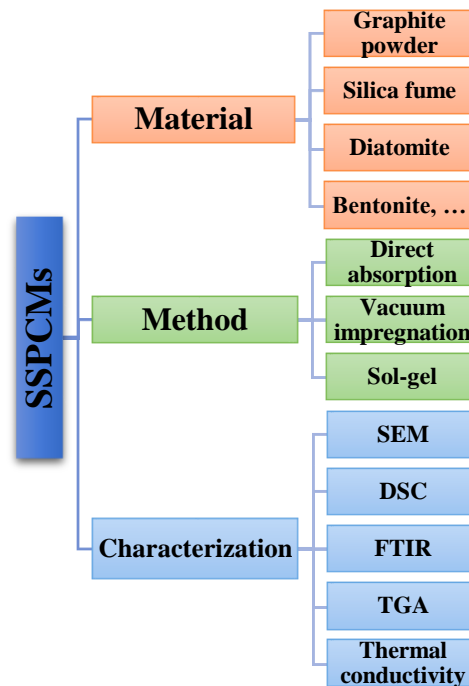


Figure 2-3: Influential factors in the fabrication of SSPCMs.

Table 2-3: Supporting materials used for fabricating SSPCMs in the literature

PCM	Supporting material	Combination method	Ref.
CA-PA	xGnP	direct absorption	(Sayyar <i>et al.</i> , 2014)
n-heptadecane	xGnP	direct absorption	(Biswas <i>et al.</i> , 2014)
n-hexadecane, n-octadecane	xGnP and Na-MMT	Vacuum impregnation	(Jeong <i>et al.</i> , 2015)
PEG	expanded graphite (EG)	direct absorption	(Lv <i>et al.</i> , 2016)
paraffin	expanded graphite (EG)	direct absorption	(Wang <i>et al.</i> , 2016)
n-octadecane	expanded graphite (EG)	direct absorption	(Zhang <i>et al.</i> , 2013)
hexadecane	xGnP	vacuum impregnation	(Kim <i>et al.</i> , 2014)
biobased PCM	silica fume and xGnP	vacuum impregnation	(Kang <i>et al.</i> , 2015)
hexadecane, octadecane	silica fume	vacuum impregnation	(Jeong <i>et al.</i> , 2013)
PEG	SiO ₂	sol-gel	(Xu <i>et al.</i> , 2016)
PEG	diatomite and expanded graphite	vacuum impregnation	(Karaman <i>et al.</i> , 2011)
paraffin RT21	Nano-silica	direct absorption	(Li <i>et al.</i> , 2015)
octadecane	xGnP	vacuum impregnation	(Min <i>et al.</i> , 2017)
stearic acid	silica fume	vacuum impregnation	(Wang <i>et al.</i> , 2011)
paraffin RT21	diatomite	direct absorption	(Li <i>et al.</i> , 2014)
CA and PEG	bentonite	vacuum impregnation	(Sari, 2016)

2.3.1 Supporting materials

The most suitable materials for fabricating shape-stabilized phase change materials are those having a porous structure with desired thermal properties such as high thermal conductivity. A great number of different supporting materials including graphite powder, silica fume, bentonite, diatomite and kaolin have been proposed in recent years. However, graphite powder and silica fume have been more widely used due to their higher absorption capacity and better applicability to integrate into cementitious composites. As outlined in **Table 2-3**, graphite is one of the most prevalent materials for fabricating SSPCM composites, mostly in the form of expanded graphite (EG) and exfoliated graphite nanoplatelets (xGnP), which has porous structure with high thermal conductivity. The high absorption capacity of EG and xGnP facilitates high volume incorporation of PCMs so that up to 90% by mass of composite is achievable (Biswas *et al.*, 2014; Jeong *et al.*, 2015; Kim *et al.*, 2014; Lv *et al.*, 2016; Wang *et al.*, 2016; Zhang *et al.*, 2013). For instance, Zhang *et*

al. (Zhang *et al.*, 2013) and Kim *et al.* (Kim *et al.*, 2014) used n-octadecane/EG and hexadecane/xGnP composites in the fabrication of cementitious thermal energy storage mortars, respectively. According to their results, such SSPCM-incorporated mortars have considerable ability in reducing indoor temperature variations in buildings, as well as providing time lag to reach peak indoor temperature, which are key factors in reducing energy consumption of buildings (Kim *et al.*, 2014; Zhang *et al.*, 2013). SSPCMs fabricated by means of graphite powder were also used in gypsum mortar or wallboard. Similarly, great potential of such PCM composites in regulating the indoor temperature of buildings was observed (Biswas *et al.*, 2014; Cai *et al.*, 2015; Sayyar *et al.*, 2014).

While silica fume has traditionally been used as a microfiller and pozzolanic addition in cementitious composites, its porous structure has made it a proper material for impregnating PCMs. For instance, Jeong *et al.* (Jeong *et al.*, 2013) and Kang *et al.* (Kang *et al.*, 2015) employed silica fume as SM for the fabrication of SSPCM composites. Xu *et al.* (Xu *et al.*, 2016) also introduced a concrete block constructed of PEG/SiO₂ composite SSPCM. Their findings indicate that silica fume is a compatible SM for incorporation of PCMs in terms of maintaining heat storage capacity, thermal and chemical stability. Moreover, silica fume-PCM composites can be added to construction materials such as mortar and concrete to improve their thermal characteristics (Jeong *et al.*, 2013; Kang *et al.*, 2015; Xu *et al.*, 2016). In a different approach, Ma *et al.* (Ma *et al.*, 2013) used Teradecane as the PCM along with carbon and silica as the supporting material to synthesize SSPCMs for highway pavement applications. According to their results, the SSPCM composite made of silica indicated better latent heat capacity compared to that fabricated using carbon.

In general, SSPCMs addition to cement mortar may drastically decrease its compressive strength as reported in (Min *et al.*, 2017; Wang *et al.*, 2016; Xu *et al.*, 2016; Zhang *et al.*, 2013). This reduction is attributed to the fact that SSPCMs do not provide mechanical resistance, especially in the case of using graphite powder as the supporting material (Min *et al.*, 2017; Xu *et al.*, 2016). However, the effect of SSPCM addition on the thermal conductivity of the host material highly depends on the characteristics of the used SSPCM, including thermal conductivity of both PCM and SM, incorporation mass ratio of PCM to

SM, porosity structure of both SSPCM and mortar, and mass ratio of SSPCM to mortar (Kim *et al.*, 2014; Xu *et al.*, 2016; Zhang *et al.*, 2013). For instance, Zhang *et al.* (Zhang *et al.*, 2013) utilized n-octadecane/EG composite with the PCM mass percentage of 90% in the fabrication of different cement mortar specimens in which the mass percentage of SSPCM to mortar was 0, 0.5, 1.2, 1.7, and 2.5%. Their results indicate that thermal conductivity decreased with an increase in the mass percentage of SSPCM to mortar due to porosity induced in the mortar. In contrast, Kim *et al.* (Kim *et al.*, 2014) reported that the incorporation of hexadecane/xGnP composites to the cement mortar increased the thermal conductivity of the cement mortar. According to their results, the percentage of impregnated hexadecane was 48.8%. Therefore, such different findings stipulate that more comprehensive investigations are required to reach conclusive findings regarding the influence of SSPCMs with different types of PCM and SM on the thermal and mechanical properties of construction materials. Nevertheless, the beneficial impact of their addition on providing TES capacity of building materials is well documented (Cai *et al.*, 2015; Jeong *et al.*, 2013; Kim *et al.*, 2014; Sayyar *et al.*, 2014; Zhang *et al.*, 2013).

2.3.2 Fabrication methods

To achieve optimal PCM impregnation into the porous structure of SM, different techniques have been employed including direct absorption, vacuum impregnation, and sol-gel method. The preliminary procedure of SSPCMs fabrication is the direct absorption of PCM into the supporting material. For this purpose, the PCM is usually melted at temperature of 80 to 100 °C. Subsequently, the molten PCM is absorbed into the supporting material (Biswas *et al.*, 2014; Li *et al.*, 2015; Li *et al.*, 2014; Lv *et al.*, 2016; Sayyar *et al.*, 2014; Zhang *et al.*, 2013). For instance, Lv *et al.* (Lv *et al.*, 2016) produced PEG/EG composite with the PEG to EG mass fraction of 96 to 4, 94 to 6, 98 to 2 and 90 to 10. Zhang *et al.* (Zhang *et al.*, 2013) also fabricated n-octadecane/EG composites with PCM mass percentage of 90. The vacuum impregnation method is based on the evacuation of air from the pores of materials. Since, the pore space in porous materials is usually blocked by air, it is required to first remove air that could hinder the PCM path through the pore space to have the greatest amount of molten PCM absorbed in the porous structure of the host material. Hence, vacuum impregnation is applied to achieve the highest ratio of PCM/SM.

Several researchers used this method for fabricating SSPCMs with different porous materials such as graphite powder, silica fume and diatomite (Jeong *et al.*, 2015; Jeong *et al.*, 2013; Kang *et al.*, 2015; Karaman *et al.*, 2011; Kim *et al.*, 2014; Min *et al.*, 2017; Sarı, 2016; Wang *et al.*, 2011).

The sol-gel method is a useful technique for fabricating both organic and inorganic composites (Li *et al.*, 2012; Sakka, 2005; Zhang *et al.*, 2010). Accordingly, researchers proposed shape-stabilized PCMs fabricated by the sol-gel method (Ren *et al.*, 2014; Xu *et al.*, 2016; Zhang *et al.*, 2010). For instance, Xu *et al.* (Xu *et al.*, 2016) used PEG/SiO₂ shape-stabilized PCM and investigated the feasibility of incorporating it in conventional concrete mixtures to enhance its thermal inertia. It was observed that the density, thermal conductivity, and compressive strength of the concrete decreased. However, thermal performance testing using a passive solar chamber showed that adding SSPCM into concrete significantly improved thermal performance as indicated by up to 4.6 °C reduction in peak indoor temperature. Clearly, the characterization of SSPCMs after fabrication using each of the proposed methods in terms of chemical and thermal stability, leakage possibility, etc., plays an essential role in the efficiency of each method.

2.3.3 Characterization of SSPCMs

Experiments should be performed to evaluate the chemical stability and thermal characteristics of the SM/PCM composite, such as assessing the melting/freezing point, latent heat, thermal stability, etc. Scanning electron microscopy (SEM) is commonly used for analyzing the morphology and microstructure of SSPCMs. The absorption pattern of PCM into the pore structure of SM, as well as its possible leakage can also be observed using SEM imaging (Cai *et al.*, 2015; Jeong *et al.*, 2013; Kim *et al.*, 2014; Sayyar *et al.*, 2014; Zhang *et al.*, 2013). For instance, Cai *et al.* (Cai *et al.*, 2015) investigated the absorption mechanism of SSPCM fabricated of nano-silica. It was found that due to the small size of nano-silica particles, the absorption mechanism is immersion as the PCM gets surrounded by nano-silica particles. In this regard, SSPCM would have stability in phase transitions since the PCM is incorporated in the nano-silica particles (Cai *et al.*, 2015). In another study, Li *et al.* (Li *et al.*, 2014) utilized a diffusion-oozing circle test as an

accommodating approach for examining the leakage of the PCM from the SSPCM composites.

Thermal characteristics, phase change behavior and heat storage capacity of the composite SSPCMs are generally evaluated using differential scanning calorimetry (DSC). Melting/freezing temperature, latent heat of fusion/crystallization, and specific heat capacity of SSPCMs can be measured using DSC (Cai *et al.*, 2015; Jeong *et al.*, 2013; Kang *et al.*, 2015; Kim *et al.*, 2014; Sayyar *et al.*, 2014; Zhang *et al.*, 2013). Although the phase change temperature of the SSPCM composite is in most cases equal to that of the PCM (Jeong *et al.*, 2015; Zhang *et al.*, 2013), some studies evidenced that the type of PCM and SM could alter the phase change temperature of the SSPCMs. Lv *et al.* showed that the melting/freezing temperature of the EG/PEG composite reduced compared to pure PEG with the increase of the EG weight percentage due to the drag effect, which prevents perfect crystallization of PEG (Lv *et al.*, 2016). Hence, the chemical analysis of the SSPCM composite has great significance to the thermal characterization. Nevertheless, owing to the large thermal conductivity and high porosity of the SM, the thermal conductivity of the SSPCM composites would strikingly improve in comparison to the pure PCM (Kim *et al.*, 2014; Lv *et al.*, 2016; Zhang *et al.*, 2012).

For the analysis of chemical combination and stability of SSPCMs, Fourier Transform Infrared (FTIR) test has been performed in many studies (Cai *et al.*, 2015; Jeong *et al.*, 2013; Kim *et al.*, 2014). For instance, Cai *et al.* (Cai *et al.*, 2015) and Jeong *et al.* (Jeong *et al.*, 2013) reported that there was no chemical reaction between PCM and SM during the fabrication of SSPCMs. Thermogravimetric analysis (TGA) has also been used to appraise the thermal stability of SSPCMs. For instance, Guan *et al.* (Guan *et al.*, 2015) indicated that no decomposition of paraffin/expanded vermiculite occurred below 169.7 °C, noting that the proposed SSPCM has promising thermal stability within 169.7 °C. **Figure 2-4** summarizes the scope of tests used for characterizing thermal and chemical properties and stability of SSPCMs. SEM, DSC, FTIR, TGA, and thermal conductivity tests are the most commonly used methods for characterizing the thermal properties and thermal stability of SSPCMs.

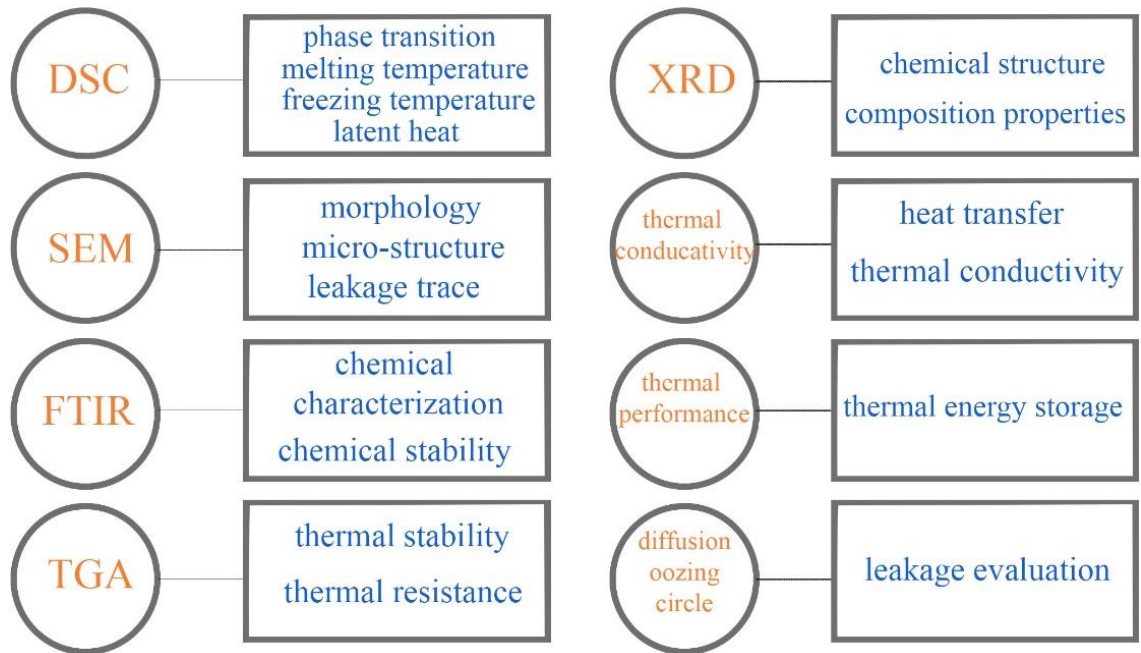


Figure 2-4: Some of common tests for characterizing SSPCMs.

2.3.4 Potential applications of SSPCMs

SSPCMs have been mostly used for TES purposes rather than structural functionality. Several researchers applied different SSPCM composites in non-structural building elements, such as walls and building envelopes in both laboratory and real scale samples to regulate indoor temperature variations and reduce energy consumption (Biswas *et al.*, 2014; Cai *et al.*, 2015; Kim *et al.*, 2014; Sayyar *et al.*, 2014). For instance, Sayyar *et al.* (Sayyar *et al.*, 2014) used a type of SSPCM fabricated from fatty acids eutectic PCM and graphite nanosheets in the construction of a three-layer sandwich panel gypsum wall. Their thermal performance experiment revealed that the utilization of such SSPCM in the composite wall could narrow the indoor temperature variation range from (13-32 °C) to (18.5-26.5 °C). The potential application of SSPCMs in structural concrete has also been explored in recent studies. Min *et al.* (Min *et al.*, 2017) investigated the thermal and mechanical properties of concrete incorporating SSPCMs. Their results indicated that the addition of SSPCMs reduced the compressive strength and elastic modulus of concrete while increasing its specific heat capacity. Nevertheless, they emphasized the need for

more research on the structural, thermal, and energy-saving performance of such cementitious composites.

SSPCMs also stimulated beneficial applications in pavement materials and construction (Ma *et al.*, 2016; Si *et al.*, 2015). In an experimental study, Ren *et al.* (Ren *et al.*, 2014) proposed a type of SSPCM with desirable latent heat and melting temperature to be used in asphalt mixtures. Furthermore, Ma *et al.* (Ma *et al.*, 2013) introduced an SSPCM composite fabricated with Tetradecane as a PCM to be incorporated in highway pavements, which showed a phase transition temperature and enthalpy of 5.8 °C and 178 J/g, respectively.

2.4 Porous inclusion

Another interesting and applicable method of incorporating PCMs into concrete is absorbing liquid PCMs into porous lightweight aggregates (LWAs). This technique is similar to the shape stabilizing method, with some noted differences. For instance, SSPCMs should be added to the concrete mixture as a partial replacement for fine aggregates (Li *et al.*, 2014; Min *et al.*, 2017). Furthermore, SM for preparing PCM-LWA is generally different in comparison with SSPCMs. In SSPCM fabrication, powder materials such as graphite powder or silica fume are generally used as the SM, whereas porous aggregates with larger size and mechanical strength capability are more promising SMs for the PCM-LWA concrete. Various important factors influence the performance of PCM-LWA concrete and should be carefully considered in the mixture proportions. These include the type of LWA and its absorption capacity, the impregnation method, the coating and supporting materials, and characterization and performance testing (Cui, Memon, *et al.*, 2015; Farnam *et al.*, 2017; Kheradmand *et al.*, 2015; Memon, Cui, Lo, *et al.*, 2015; Memon, Cui, Zhang, *et al.*, 2015; Nepomuceno & Silva, 2014; Sakulich & Bentz, 2012; Sharifi & Sakulich, 2015). Researchers proposed various porous aggregates as the host of PCM, different impregnation methods, and various coating and supporting materials.

2.4.1 Lightweight aggregates

The porous structure of LWA makes it suitable as a PCM container in concrete. However, some characteristics of LWAs such as their porosity, pore size, aggregate size, and surface

area, along with the impregnation technique and conditions including the liquid PCM temperature could affect the LWA absorption capacity. Various LWAs have been used as the carrier of the molten PCM in concrete, including expanded clay, expanded shale, expanded perlite, expanded vermiculite, and pumice (Aguayo *et al.*, 2017; Cui, Memon, *et al.*, 2015; Memon, Cui, Lo, *et al.*, 2015; Memon, Cui, Zhang, *et al.*, 2015; Ramakrishnan *et al.*, 2015; Suttaphakdee *et al.*, 2016; Yao *et al.*, 2018). Aguayo *et al.* (Aguayo *et al.*, 2017) used four different types of LWA including pumice, perlite, expanded shale/clay, and expanded slate. They observed that porosity is not the only metric for PCM absorption capacity of LWAs and the pore diameter can affect such properties of LWAs. For instance, pumice with 14% lower porosity than expanded shale/clay had greater PCM absorption due to its larger average pore diameter. Kheradmand *et al.* (Kheradmand *et al.*, 2015) also reported that the aggregate size can impact the PCM absorption capacity of LWAs since the absorption of the smaller size aggregates was higher. Nonetheless, Aguya *et al.* (Aguayo *et al.*, 2017) took the surface adsorption of small particles into account and suggested removing particles finer than 150 μm from LWAs to avoid surface adsorption of PCMs instead of its absorption into the LWAs pores.

Other studies also suggested that LWAs generally could act as SM to incorporate PCMs into structural concrete, while compressive strength remains within structural limits. Memon *et al.* (Memon, Cui, Lo, *et al.*, 2015) proposed an LWA-PCM concrete that had 28-days compressive strength as high as 33.3 MPa to 53.1 MPa, along with 102.5 J/g latent heat capacity. However, providing sufficient mechanical strength may be achieved by adding to the LAW-PCM composites supporting and coating materials, such as epoxy resin, (Cui, Memon, *et al.*, 2015; Memon, Cui, Lo, *et al.*, 2015; Memon, Cui, Zhang, *et al.*, 2015) since leakage of PCM from pores of LWAs can affect cement hydration reactions and consequently the compressive strength of concrete (Bentz & Turpin, 2007; Sakulich & Bentz, 2011, 2012).

2.4.2 Impregnation method

To have greater PCM absorption into LWA, it is essential to deploy an appropriate impregnation method in addition to adequate pore size and pore structure considerations. Generally, two different methods have been introduced: vacuum impregnation and direct

impregnation. Vacuum impregnation of PCMs into LWAs is similar to that for fabricating SSPCMs discussed earlier. However, since the pore structure, the pore size of LWAs, and aggregate size are influential factors on the PCM absorption capacity of LWAs, the effect of the impregnation method is more pronounced in PCM-LWA composites compared to that in SSPCMs. It has been reported that although large LWAs have larger pores, these large voids act as a part of the LWA texture and thus do not contribute as the internal porosity of LWAs (Castro *et al.*, 2011; Kheradmand *et al.*, 2015). In contrast, smaller aggregates have greater total porosity since they have expanded more in comparison to larger particles (Kheradmand *et al.*, 2015). However, due to differences in pore size and pore distribution between SSPCMs' supporting materials and LWAs, the effect of this technique on the absorption capacity of porous materials is more tangible. Generally, in vacuum impregnation, air is removed from the pore space of LWA using a vacuum pump. This enables a better absorption capacity of porous aggregates. For instance, Memon *et al.* (Memon, Cui, Lo, *et al.*, 2015) reported that the absorption capacity of LWA was 18% using direct immersion and could rise to 73.85 % using the vacuum impregnation. Furthermore, the temperature and viscosity of liquid PCM and the duration of mixing can affect the absorption capacity. Yet, this technique is generally considered impractical because of its complexity and time-consuming process (Aguayo *et al.*, 2017).

2.4.3 Supporting and coating materials

Researchers have proposed adding supporting materials to mitigate leakage of molten PCM and improve thermal and mechanical characteristics of the PCM-LWA. For instance, Memon *et al.* (Memon, Cui, Lo, *et al.*, 2015) used a combination of epoxy resin, graphite powder, and silica fume to enhance the mechanical and thermal characteristics of PCM-LWA. Consequently, the thermal conductivity was enhanced significantly and the compressive strength of PCM-LWA concrete increased. Other coatings and resins, such as cement paste, silicone coating, and bituminous emulsion have been used for sealing the PCM-LWA (Cui, Memon, *et al.*, 2015; Kastiukas *et al.*, 2016; Kheradmand *et al.*, 2015). Some of the utilized coating materials brought about some technical problems such as aggregates sticking together or developing a very thin and weak coating layer (Kastiukas *et al.*, 2016). To develop structural PCM-LWA concrete with desirable mechanical,

thermal, and heat storage characteristics, more studies on different coating and supporting materials and their effects on the thermal and mechanical performance of PCM-LWA, along with practical methods for preparing such PCM-LWA composites are required in future research work.

2.4.4 Characterization of PCM-LWA concrete

To understand the effects of incorporating PCM in concrete via lightweight aggregates, it is necessary to characterize both PCM-integrated LWAs and PCM-LWA concrete. SEM, DSC, TGA, and FTIR have been used to investigate the morphology, thermal properties and chemical stability of PCM-LWAs, similar to the characterization of SSPCMs discussed earlier (Chung *et al.*, 2015; Karaipekli & Sarı, 2016; Memon, Cui, Lo, *et al.*, 2015; Memon, Cui, Zhang, *et al.*, 2015; Nepomuceno & Silva, 2014; Ramakrishnan *et al.*, 2015; Ryms *et al.*, 2015; Sakulich & Bentz, 2012; Suttaphakdee *et al.*, 2016; Xu *et al.*, 2015). Moreover, the thermal, mechanical, and durability properties of concrete incorporating PCM-LWA including thermal performance, thermal conductivity, compressive strength, shrinkage strain, and effects of freezing and thawing cycles have been investigated (Aguayo *et al.*, 2017; Cui, *et al.*, 2015; Farnam *et al.*, 2017; He *et al.*, 2014; Kastiukas *et al.*, 2016; Kheradmand *et al.*, 2015; Memon, *et al.*, 2015; Memon, *et al.*, 2015; Nepomuceno & Silva, 2014; Ramakrishnan *et al.*, 2015; Ramakrishnan, *et al.*, 2017; Ramakrishnan, Wang, Sanjayan, & Wilson, 2017; Ryms *et al.*, 2015; Sakulich & Bentz, 2012; Sharifi & Sakulich, 2015; Suttaphakdee *et al.*, 2016). In terms of mechanical properties, while most studies in the literature argue that, regardless of their incorporation method, PCMs decrease the compressive strength; Memon *et al.* (Memon, Cui, Zhang, *et al.*, 2015) reported that the compressive strength of concrete made with epoxy coated PCM-LWA was higher than that of lightweight concrete without coated PCM-LWA. Moreover, the shrinkage strain of coated PCM-LWA concrete decreased compared to that of the control lightweight concrete (Memon, *et al.*, 2015). Consequently, it is widely reported that the compressive strength of LWA-PCM concrete could comply with code requirements for structural LWA concrete (Memon, *et al.*, 2015; Memon, *et al.*, 2015; Suttaphakdee *et al.*, 2016).

In addition to PCMs' effects on mechanical and thermal characteristics of construction materials, a fundamental goal of their use is to impart TES into building materials. Hence,

researchers have performed various tests, for instance, to evaluate the thermal performance of walls and cubic cells made of PCM-integrated concrete. Results show that the incorporation of PCMs into such walls and roofs significantly contributed to the reduction of energy consumption by alleviating temperature fluctuations and reducing/shifting the indoor temperature peak. For instance, Suttaphakdee *et al.* (Suttaphakdee *et al.*, 2016) reported that the maximum indoor temperature of a test room with a PCM-LWA concrete top panel could be reduced by 1.9 °C compared to that of a control room with an ordinary LWA concrete panel. Similar findings reported in the literature evidence the potential of PCM-LWA concrete in regulating the indoor temperature and reducing the energy consumption of buildings (Cui, *et al.*, 2015; Memon, *et al.*, 2015; Memon, *et al.*, 2015; Ramakrishnan *et al.*, 2015; Yao *et al.*, 2018). Numerical simulations on larger scale construction confirmed such experimental results (Cui, *et al.*, 2015; Memon, *et al.*, 2015; Ramakrishnan *et al.*, 2015; Ramakrishnan, *et al.*, 2017; Ramakrishnan; Yao *et al.*, 2018).

2.4.5 Potential applications

Owing to its successful outcomes, integrating PCMs into porous aggregates has attracted many researchers to study various aspects of this inclusion technique. In addition to TES capacity and structural functions discussed earlier, PCM-LWA concrete has provided new insights into deicing pavements. Farnam *et al.* (Farnam *et al.*, 2017) evaluated the application of PCMs incorporated into LWAs in reducing the accumulation of ice and snow on concrete pavements. Accordingly, the heat released during the phase transition of such PCM composites could melt ice and snow on the surface of pavements (Farnam *et al.*, 2017; Farnam *et al.*, 2015; Liston *et al.*, 2016). Another study (Esmaeeli *et al.*, 2018) explored the effects of such PCM-LWA composites on the freezing and thawing performance of concrete, suggesting that PCM-LWA cementitious materials are promising for enhancing the behavior of concrete pavements under freezing-thawing cycles.

2.5 Macroencapsulation

As expressed earlier, a major goal of integrating PCMs in construction materials is providing TES systems via PCM latent heat capacity. Accordingly, PCMs have been incorporated in various building materials, such as concrete and gypsum, and different

building elements, such as walls and roofs. To mitigate the detrimental effects of PCM on mechanical properties, researchers have proposed various techniques to prevent direct contact between PCM and the host construction materials. Macroencapsulation is an effective method to incorporate PCMs into building components, especially prefabricated walls and roofs. In this method, PCM is not mixed with the basic material (concrete, gypsum, etc.). Hence, the mechanical characteristics of the basic material are not hindered. However, the thermal energy storage provided by PCMs could improve the thermal performance of such building components. It should be noted that in some references, macroencapsulation of PCMs might be attributed to other techniques. For instance, PCM impregnation in LWA is sometimes referred to as macroencapsulation (Cui, *et al.*, 2015; Memon, Cui, Lo, *et al.*, 2015; Memon, Cui, Zhang, *et al.*, 2015). Moreover, other types of PCMs, such as PCM microcapsules or SSPCMs, could be employed to prepare macroencapsulated PCM members (Cai *et al.*, 2015; Kim *et al.*, 2017; Sarı, 2014; Zhou *et al.*, 2007). In recent experimental work, researchers used reduced-scale experimental and empirical procedures to assess the thermal response of PCM-integrated building components (Marani & Madhkhan, 2018; Young *et al.*, 2018). Moreover, several numerical investigations have been conducted to assess the effect of PCM inclusion in building components and on the energy consumption of buildings (Han & Taylor, 2016; Stritih *et al.*, 2018). Key aspects of this work are outlined below.

2.5.1 PCM macroencapsulation through building walls and envelopes

Since building walls and envelopes are typically in direct contact with the outdoor boundary conditions and exposed to solar radiation, they are potential candidates for incorporating PCMs. Thus, several research studies have evaluated the effects of PCMs on the thermal performance of such building members (Bastani *et al.*, 2014; Castell & Farid, 2014; Evola *et al.*, 2013; Pagliolico *et al.*, 2015). An applicable method of macroencapsulating PCMs for application in building walls is through panel-shaped PCM containers. For a better thermal performance in charge/discharge cycles, such containers need to have high thermal conductivity. Hence, metal containers are suitable for the macroencapsulation of PCMs. For instance, Shi *et al.* (Shi *et al.*, 2014) used steel containers

for macro encapsulating PCMs in concrete sandwich panel walls. Their results indicate that integrating a PCM layer into the walls of a model room could significantly reduce the maximum indoor temperature as well as increase the minimum indoor temperature. Thus, the indoor temperature variations were greatly flattened (Shi *et al.*, 2014). **Figure 2-5** indicates the schematic of some macro-encapsulated wall and roof configurations utilized in previous studies in the literature.

Generally, the performance of the embedded PCM macrocapsules greatly depends on several factors, such as the location of the PCM macrocapsule (*i.e.*, inner or outer surface or within the central section of the wall), microclimate conditions of the region (*i.e.*, ambient temperature, solar radiation, etc.), the configuration of the building element (*i.e.*, concrete wall, masonry brick wall), thermal properties of the building material and the PCM, etc. Researchers evaluated the performance of such PCM-incorporated building elements under real climatic conditions or using environmental chambers (Marani & Madhkhan, 2018; Shi *et al.*, 2014; Vicente & Silva, 2014). **Table 2-4** presents different experimental configurations used in some recent studies.

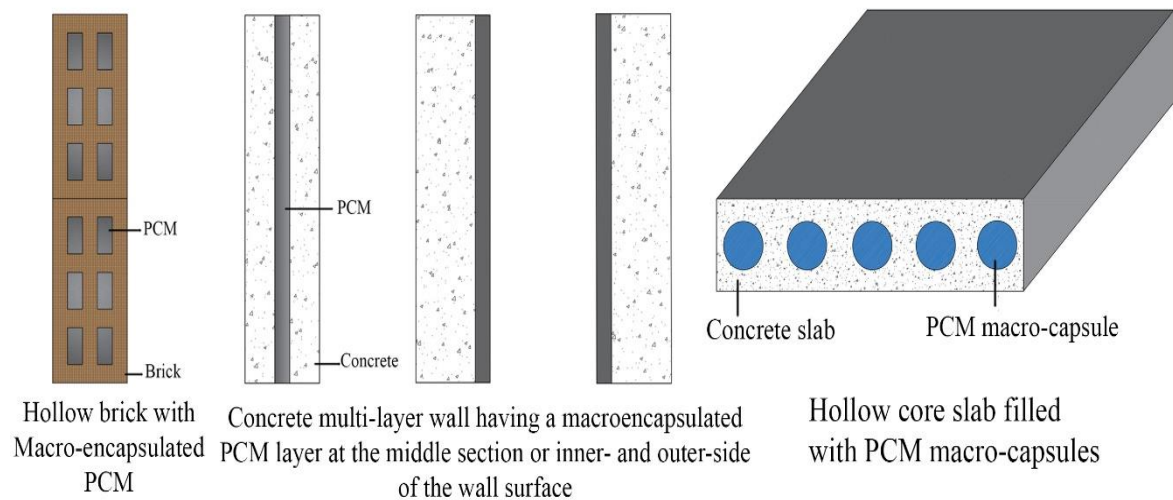


Figure 2-5: Schematic cross-section of PCM macro-encapsulated configurations.

Table 2-4: Experimental studies on the application of PCM macrocapsules in buildings

Experiment Configuration	PCM Inclusion	Test Procedure	Target and Results	Ref.
Small house model	Macro-encapsulated	Real climatic condition	Validation of numerical simulations	(Castell & Farid, 2014)
Cubic test cell	A PCM layer included in multi-layer walls	Experimental test device under real environmental condition	Thermal performance of PCM integrated into multi-layer walls	(Pagliolico <i>et al.</i> , 2015)
Test huts	PCM underfloor heating system and PCM wallboards	Real climatic condition	Evaluation of peak load shifting, energy performance and cost savings	(Barzin <i>et al.</i> , 2015)
Concrete wallboard sample and test rooms	Innovative PCM macrocapsules using hollow steel balls	Self-designed environmental chamber	Evaluation of thermal performance using indoor temperature fluctuations	(Cui <i>et al.</i> , 2017)
Small test room models	Macroencapsulated PCM layer in sandwich concrete walls	Real climatic conditions	Assessment of PCM microcapsule position in concrete wall	(Shi <i>et al.</i> , 2014)
Masonry brick wall	PCM macrocapsules	Climatic chamber	Reducing temperature fluctuations	(Silva <i>et al.</i> , 2012)
Concrete sandwich panel walls	Macroencapsulated PCM layer	Temperature simulator apparatus	Thermal performance evaluations	(Marani & Madhkan, 2018)
Concrete core slab in test cubicles	Macroencapsulated PCM tubes	Real climatic condition	Thermal performance evaluations	(Navarro <i>et al.</i> , 2015)

2.5.2 PCM macroencapsulation in building roofs

Concrete roofs such as hollow core slabs are particularly appropriate for incorporating PCMs macrocapsules. In this technique, PCMs are macro-encapsulated in the form of tubes, cylinder, balls and spheres. For example, Navarro *et al.* (Navarro *et al.*, 2015) examined the thermal performance of PCM macro-capsules in an active hollow core concrete slab. It was concluded that the proposed PCM-concrete slab could perform the charge/discharge process of PCM in almost 70% of summer and winter days. However, the employment of a control system would optimize the charge/discharge process (Navarro *et al.*, 2015). Royon *et al.* (Royon *et al.*, 2014) used a PCM-polymer composite to fill the cavity of hollow-core slabs to provide TES capability. Their results indicate that PCM

incorporation would regulate the indoor temperature and such a floor system could perform as a passive thermal conditioner during hot days (Royon *et al.*, 2014). **Figure 2-5** illustrates the schematic of a hollow-core slab filled with PCM.

In a different approach, Farnam *et al.* (Farnam *et al.*, 2017) used a type of paraffin oil macro-encapsulated in metal pipes to be embedded in concrete pavement slabs. Their results demonstrated the practical possibility of using PCMs to melt ice and snow on concrete pavements by the heat retrieved during the PCM phase change process (Farnam *et al.*, 2017). However, the ambient temperature conditions and melting/freezing temperature of the PCM can be determining criteria for the efficiency of the macro-encapsulation technique compared to using PCM-LWA composites (Farnam *et al.*, 2017; Farnam *et al.*, 2015).

2.6 Discussion and recommendations

Owing to the variety of PCM types, diverse applications in the construction industry have been explored in recent years. Moreover, the potential leakage problem of PCMs during melting/freezing cycles have brought about different incorporation methods as critically discussed earlier. Hence, selecting a proper incorporation method to achieve specific goals of PCM in the host construction material is essential. Moreover, the effect of PCM addition on the host material pivots around the incorporation technique. For instance, the compressive strength of concrete incorporating PCM-LWA composites could be reduced or increased depending on whether supporting and coating materials are used or not (Cui, Memon, *et al.*, 2015; Farnam *et al.*, 2017; Farnam *et al.*, 2015; Memon, Cui, Lo, *et al.*, 2015; Memon, Cui, Zhang, *et al.*, 2015; Sakulich & Bentz, 2011; Sharifi & Sakulich, 2015). By the same token, the improvement of the thermal conductivity and latent heat storage of the SSPCM composites are dependent upon the supporting material and impregnation method (Cai *et al.*, 2015; Kim *et al.*, 2017; Li *et al.*, 2012; Li *et al.*, 2015; Ma *et al.*, 2013; Min *et al.*, 2017; Ramakrishnan, Wang, Sanjayan, & Wilson, 2017; Si *et al.*, 2015; Wang *et al.*, 2016; Wang *et al.*, 2011; Zhou *et al.*, 2007).

Table 2-5 presents some recommendations on the incorporation methods concerning the aimed applications. Yet, more studies are required for each method to enhance its

performance, efficiency, and sustainability as well as to mitigate the associated obstacles and potential detrimental outcomes. It should be noted that each recommendation is provided based on results obtained from studies in the open literature and thus are not a sine qua non. Moreover, the cost analysis of the incorporation method could be an influential factor, which was not taken into account in such recommendations.

Table 2-5: Recommendations for the method of PCM incorporation in construction and pavement materials

Aimed application	Recommended incorporation method
TES	PCM macrocapsules integrated into building walls, floors, envelopes, etc.; SSPCMs
Thermal stress control in concrete Pavements (thermally related stress and damage control)	PCM microcapsules; Porous inclusion
Pavements (ice/snow-melting)	PCM microcapsules; Porous inclusion;
Structural concrete	PCM microcapsules; Porous inclusion; PCM macrocapsules
	PCM microcapsules; Porous inclusion

2.7 Summary, conclusions, and future work

There has been a recent proliferation of studies that incorporate PCMs into construction materials, exploring the benefits of such practice and mitigating the associated drawbacks. In particular, the risk of PCM leakage has been a fundamental problem with deleterious effects on the mechanical, thermal, and durability properties of PCM integrated construction composites. Hence, researchers have proposed various techniques to eliminate such detrimental outcomes of PCM-integrated materials. In the present critical review, such methods have been categorized into four main groups, namely microencapsulation, shape-stabilized phase change materials (SSPCMs), porous aggregate inclusions, and macroencapsulation. The advantages and disadvantages along with the supporting materials for the fabrication and characterization of such composite materials are reviewed and critically discussed. It has been realized that more concerted and dedicated studies are needed to mitigate the detrimental effects of PCMs on the mechanical properties of construction materials by utilizing new chemical or physical incorporation schemes. Accordingly, the following knowledge gaps are recognized and need to be addressed in future work:

- The effect of microencapsulated PCMs on the maturity and strength development of concrete needs to be investigated. Furthermore, the correlation between

physiochemical properties of microencapsulated PCMs and compressive strength should be explored.

- The effect of thermal properties of microencapsulated PCMs together with the curing temperature on the strength development and temperature rise of concrete need to be studied.
- Considering the various mechanism contributing to the reduction of compressive strength after the addition of microencapsulated PCMs, a robust modeling approach should be developed to predict the compressive strength of such types of concrete based on the mixture design proportions.
- SSPCMs offer a promising technique to incorporate PCMs into concrete. Concerted research efforts are required to develop high-performance and efficient SSPCMs for concrete technology applications. Furthermore, comprehensive experiments are needed to elucidate the effects of SSPCMs on various mechanical and thermal properties of concrete.
- With the emergence of eco-friendly and low-carbon concrete technologies, it is of great significance to develop thermal energy storage low-carbon composites to further reduce the carbon emissions of the built environment.
- There is need for the development of new PCM encapsulation techniques that are more compatible with concrete and thus, can further mitigate the negative effect of PCMs on the mechanical performance of concrete.

It should be noted that developing new methods needs to practically enable the PCMs' effect on the energy storage and overall thermal management of buildings in optimal ways. The improved understanding of the different methods and their impact on the performance of the PCM-integrated construction composite material gained in this study should help researchers and engineers in selecting adequate techniques for incorporation of PCMs into desired construction materials and systems, with expected sustainability and resilience outcomes.

2.8 References

- Aguayo, M., Das, S., Castro, C., Kabay, N., Sant, G., & Neithalath, N. (2017). Porous inclusions as hosts for phase change materials in cementitious composites: Characterization, thermal performance, and analytical models. *Construction and Building Materials*, 134, 574-584.
- Aguayo, M., Das, S., Maroli, A., Kabay, N., Mertens, J. C., Rajan, S. D., Sant, G., Chawla, N., & Neithalath, N. (2016). The influence of microencapsulated phase change material (PCM) characteristics on the microstructure and strength of cementitious composites: Experiments and finite element simulations. *Cement and Concrete Composites*, 73, 29-41.
- Arora, A., Sant, G., & Neithalath, N. (2017). Numerical simulations to quantify the influence of phase change materials (PCMs) on the early-and later-age thermal response of concrete pavements. *Cement and Concrete Composites*, 81, 11-24.
- Bahrar, M., Djamai, Z. I., Mankibi, M. E., Larbi, A. S., & Salvia, M. (2018). Numerical and experimental study on the use of microencapsulated phase change materials (PCMs) in textile reinforced concrete panels for energy storage. *Sustainable Cities and Society*, 41, 455-468.
- Barzin, R., Chen, J. J., Young, B. R., & Farid, M. M. (2015). Application of PCM underfloor heating in combination with PCM wallboards for space heating using price based control system. *Applied Energy*, 148, 39-48.
- Bastani, A., Haghghat, F., & Kozinski, J. (2014). Designing building envelope with PCM wallboards: design tool development. *Renewable and Sustainable Energy Reviews*, 31, 554-562.
- Bentz, D. (2007). Transient plane source measurements of the thermal properties of hydrating cement pastes. *Materials and Structures*, 40(10), 1073-1080.
- Bentz, D. P., & Turpin, R. (2007). Potential applications of phase change materials in concrete technology. *Cement and Concrete Composites*, 29(7), 527-532.

Biswas, K., Lu, J., Soroushian, P., & Shrestha, S. (2014). Combined experimental and numerical evaluation of a prototype nano-PCM enhanced wallboard. *Applied energy*, 131, 517-529.

Braun, J. E., Montgomery, K. W., & Chaturvedi, N. (2001). Evaluating the performance of building thermal mass control strategies. *HVAC&R Research*, 7(4), 403-428.

Brown, T., & Javaid, M. (1970). The thermal conductivity of fresh concrete. *Materials and Structures*, 3(6), 411-416.

Cai, Y., Sun, G., Liu, M., Zhang, J., Wang, Q., & Wei, Q. (2015). Fabrication and characterization of capric–lauric–palmitic acid/electrospun SiO₂ nanofibers composite as form-stable phase change material for thermal energy storage/retrieval. *Solar Energy*, 118, 87-95.

Campbell-Allen, D., & Thorne, C. (1963). The thermal conductivity of concrete. *Magazine of Concrete Research*, 15(43), 39-48.

Cao, V. D., Pilehvar, S., Salas-Bringas, C., Szczotok, A. M., Rodriguez, J. F., Carmona, M., Al-Manasir, N., & Kjøniksen, A.-L. (2017). Microencapsulated phase change materials for enhancing the thermal performance of Portland cement concrete and geopolymers concrete for passive building applications. *Energy conversion and management*, 133, 56-66.

Castell, A., & Farid, M. M. (2014). Experimental validation of a methodology to assess PCM effectiveness in cooling building envelopes passively. *Energy and Buildings*, 81, 59-71.

Castellón, C., Medrano, M., Roca, J., Cabeza, L. F., Navarro, M. E., Fernández, A. I., Lázaro, A., & Zalba, B. (2010). Effect of microencapsulated phase change material in sandwich panels. *Renewable Energy*, 35(10), 2370-2374.

Castro, J., Keiser, L., Golias, M., & Weiss, J. (2011). Absorption and desorption properties of fine lightweight aggregate for application to internally cured concrete mixtures. *Cement and Concrete Composites*, 33(10), 1001-1008.

Chung, O., Jeong, S.-G., & Kim, S. (2015). Preparation of energy efficient paraffinic PCMs/expanded vermiculite and perlite composites for energy saving in buildings. *Solar Energy Materials and Solar Cells*, 137, 107-112.

Cui, H., Liao, W., Mi, X., Lo, T. Y., & Chen, D. (2015). Study on functional and mechanical properties of cement mortar with graphite-modified microencapsulated phase-change materials. *Energy and buildings*, 105, 273-284.

Cui, H., Memon, S. A., & Liu, R. (2015). Development, mechanical properties and numerical simulation of macro encapsulated thermal energy storage concrete. *Energy and buildings*, 96, 162-174.

Cui, H., Tang, W., Qin, Q., Xing, F., Liao, W., & Wen, H. (2017). Development of structural-functional integrated energy storage concrete with innovative macro-encapsulated PCM by hollow steel ball. *Applied energy*, 185, 107-118.

D'Alessandro, A., Pisello, A. L., Fabiani, C., Ubertini, F., Cabeza, L. F., & Cotana, F. (2018). Multifunctional smart concretes with novel phase change materials: Mechanical and thermo-energy investigation. *Applied Energy*, 212, 1448-1461.

Dehdezi, P. K., Hall, M. R., Dawson, A. R., & Casey, S. P. (2013). Thermal, mechanical and microstructural analysis of concrete containing microencapsulated phase change materials. *International Journal of Pavement Engineering*, 14(5), 449-462.

Demirboğa, R. (2007). Thermal conductivity and compressive strength of concrete incorporation with mineral admixtures. *Building and Environment*, 42(7), 2467-2471.

Eddhahak-Ouni, A., Drissi, S., Colin, J., Neji, J., & Care, S. (2014). Experimental and multi-scale analysis of the thermal properties of Portland cement concretes embedded with microencapsulated Phase Change Materials (PCMs). *Applied Thermal Engineering*, 64(1), 32-39.

Eddhahak, A., Drissi, S., Colin, J., Caré, S., & Neji, J. (2014). Effect of phase change materials on the hydration reaction and kinetic of PCM-mortars. *Journal of thermal analysis and calorimetry*, 117(2), 537-545.

Esmaeeli, H. S., Farnam, Y., Haddock, J. E., Zavattieri, P. D., & Weiss, W. J. (2018). Numerical analysis of the freeze-thaw performance of cementitious composites that contain phase change material (PCM). *Materials & Design*, 145, 74-87.

Evola, G., Marletta, L., & Sicurella, F. (2013). A methodology for investigating the effectiveness of PCM wallboards for summer thermal comfort in buildings. *Building and Environment*, 59, 517-527.

Falzone, G., Falla, G. P., Wei, Z., Zhao, M., Kumar, A., Bauchy, M., Neithalath, N., Pilon, L., & Sant, G. (2016). The influences of soft and stiff inclusions on the mechanical properties of cementitious composites. *Cement and Concrete Composites*, 71, 153-165.

Farnam, Y., Esmaeeli, H. S., Zavattieri, P. D., Haddock, J., & Weiss, J. (2017). Incorporating phase change materials in concrete pavement to melt snow and ice. *Cement and Concrete Composites*, 84, 134-145.

Farnam, Y., Krafcik, M., Liston, L., Washington, T., Erk, K., Tao, B., & Weiss, J. (2015). Evaluating the use of phase change materials in concrete pavement to melt ice and snow. *Journal of Materials in Civil Engineering*, 28(4), 04015161.

Fernandes, F., Manari, S., Aguayo, M., Santos, K., Oey, T., Wei, Z., Falzone, G., Neithalath, N., & Sant, G. (2014). On the feasibility of using phase change materials (PCMs) to mitigate thermal cracking in cementitious materials. *Cement and Concrete Composites*, 51, 14-26.

Figueiredo, A., Lapa, J., Vicente, R., & Cardoso, C. (2016). Mechanical and thermal characterization of concrete with incorporation of microencapsulated PCM for applications in thermally activated slabs. *Construction and Building Materials*, 112, 639-647.

Franquet, E., Gibout, S., Tittlein, P., Zalewski, L., & Dumas, J.-P. (2014). Experimental and theoretical analysis of a cement mortar containing microencapsulated PCM. *Applied Thermal Engineering*, 73(1), 32-40.

Guan, W.-m., Li, J.-h., Qian, T.-t., Wang, X., & Deng, Y. (2015). Preparation of paraffin/expanded vermiculite with enhanced thermal conductivity by implanting network carbon in vermiculite layers. *Chemical Engineering Journal*, 277, 56-63.

Han, Y., & Taylor, J. E. (2016). Simulating the Inter-Building Effect on energy consumption from embedding phase change materials in building envelopes. *Sustainable Cities and Society*, 27, 287-295.

Haurie, L., Serrano, S., Bosch, M., Fernandez, A. I., & Cabeza, L. F. (2016). Single layer mortars with microencapsulated PCM: Study of physical and thermal properties, and fire behaviour. *Energy and Buildings*, 111, 393-400.

He, Y., Zhang, X., & Zhang, Y. (2014). Preparation technology of phase change perlite and performance research of phase change and temperature control mortar. *Energy and buildings*, 85, 506-514.

Hunger, M., Entrop, A. G., Mandilaras, I., Brouwers, H., & Founti, M. (2009). The behavior of self-compacting concrete containing micro-encapsulated phase change materials. *Cement and Concrete Composites*, 31(10), 731-743.

Jamekhorshid, A., Sadrameli, S., Barzin, R., & Farid, M. (2017). Composite of wood-plastic and micro-encapsulated phase change material (MEPCM) used for thermal energy storage. *Applied Thermal Engineering*, 112, 82-88.

Jamekhorshid, A., Sadrameli, S., & Farid, M. (2014). A review of microencapsulation methods of phase change materials (PCMs) as a thermal energy storage (TES) medium. *Renewable and sustainable energy reviews*, 31, 531-542.

Jayalath, A., San Nicolas, R., Sofi, M., Shanks, R., Ngo, T., Aye, L., & Mendis, P. (2016). Properties of cementitious mortar and concrete containing micro-encapsulated phase change materials. *Construction and Building Materials*, 120, 408-417.

Jeong, S.-G., Chang, S. J., We, S., & Kim, S. (2015). Energy efficient thermal storage montmorillonite with phase change material containing exfoliated graphite nanoplatelets. *Solar Energy Materials and Solar Cells*, 139, 65-70.

Jeong, S.-G., Jeon, J., Cha, J., Kim, J., & Kim, S. (2013). Preparation and evaluation of thermal enhanced silica fume by incorporating organic PCM, for application to concrete. *Energy and buildings*, 62, 190-195.

Joulin, A., Zalewski, L., Lassue, S., & Naji, H. (2014). Experimental investigation of thermal characteristics of a mortar with or without a micro-encapsulated phase change material. *Applied Thermal Engineering*, 66(1), 171-180.

Kang, Y., Jeong, S.-G., Wi, S., & Kim, S. (2015). Energy efficient Bio-based PCM with silica fume composites to apply in concrete for energy saving in buildings. *Solar Energy Materials and Solar Cells*, 143, 430-434.

Karaipekli, A., & Sarı, A. (2016). Development and thermal performance of pumice/organic PCM/gypsum composite plasters for thermal energy storage in buildings. *Solar Energy Materials and Solar Cells*, 149, 19-28.

Karaman, S., Karaipekli, A., Sarı, A., & Bicer, A. (2011). Polyethylene glycol (PEG)/diatomite composite as a novel form-stable phase change material for thermal energy storage. *Solar Energy Materials and Solar Cells*, 95(7), 1647-1653.

Kastiukas, G., Zhou, X., & Castro-Gomes, J. (2016). Development and optimisation of phase change material-impregnated lightweight aggregates for geopolymer composites made from aluminosilicate rich mud and milled glass powder. *Construction and Building Materials*, 110, 201-210.

Kheradmand, M., Azenha, M., de Aguiar, J. L., & Krakowiak, K. J. (2014). Thermal behavior of cement based plastering mortar containing hybrid microencapsulated phase change materials. *Energy and Buildings*, 84, 526-536.

Kheradmand, M., Castro-Gomes, J., Azenha, M., Silva, P. D., de Aguiar, J. L., & Zoorob, S. E. (2015). Assessing the feasibility of impregnating phase change materials in lightweight aggregate for development of thermal energy storage systems. *Construction and Building Materials*, 89, 48-59.

Khudhair, A. M., & Farid, M. M. (2004). A review on energy conservation in building applications with thermal storage by latent heat using phase change materials. *Energy conversion and management*, 45(2), 263-275.

Kim, H. B., Mae, M., & Choi, Y. (2017). Application of shape-stabilized phase-change material sheets as thermal energy storage to reduce heating load in Japanese climate. *Building and Environment*, 125, 1-14.

Kim, K.-H., Jeon, S.-E., Kim, J.-K., & Yang, S. (2003). An experimental study on thermal conductivity of concrete. *Cement and Concrete Research*, 33(3), 363-371.

Kim, S., Chang, S. J., Chung, O., Jeong, S.-G., & Kim, S. (2014). Thermal characteristics of mortar containing hexadecane/xGnP SSPCM and energy storage behaviors of envelopes integrated with enhanced heat storage composites for energy efficient buildings. *Energy and buildings*, 70, 472-479.

Kim, Y.-R., Khil, B.-S., Jang, S.-J., Choi, W.-C., & Yun, H.-D. (2015). Effect of barium-based phase change material (PCM) to control the heat of hydration on the mechanical properties of mass concrete. *Thermochimica Acta*, 613, 100-107.

Kusama, Y., & Ishidoya, Y. (2017). Thermal effects of a novel phase change material (PCM) plaster under different insulation and heating scenarios. *Energy and Buildings*, 141, 226-237.

Kuznik, F., David, D., Johannes, K., & Roux, J.-J. (2011). A review on phase change materials integrated in building walls. *Renewable and Sustainable Energy Reviews*, 15(1), 379-391.

Lachheb, M., Younsi, Z., Naji, H., Karkri, M., & Nasrallah, S. B. (2017). Thermal behavior of a hybrid PCM/plaster: A numerical and experimental investigation. *Applied Thermal Engineering*, 111, 49-59.

Lecompte, T., Le Bideau, P., Glouannec, P., Nortershauser, D., & Le Masson, S. (2015). Mechanical and thermo-physical behaviour of concretes and mortars containing phase change material. *Energy and Buildings*, 94, 52-60.

- Li, M., Wu, Z., & Tan, J. (2012). Properties of form-stable paraffin/silicon dioxide/expanded graphite phase change composites prepared by sol-gel method. *Applied energy*, 92, 456-461.
- Li, X., Chen, H., Li, H., Liu, L., Lu, Z., Zhang, T., & Duan, W. H. (2015). Integration of form-stable paraffin/nanosilica phase change material composites into vacuum insulation panels for thermal energy storage. *Applied energy*, 159, 601-609.
- Li, X., Sanjayan, J. G., & Wilson, J. L. (2014). Fabrication and stability of form-stable diatomite/paraffin phase change material composites. *Energy and Buildings*, 76, 284-294.
- Liston, L. C., Farnam, Y., Krafcik, M., Weiss, J., Erk, K., & Tao, B. Y. (2016). Binary mixtures of fatty acid methyl esters as phase change materials for low temperature applications. *Applied Thermal Engineering*, 96, 501-507.
- Liu, F., Wang, J., & Qian, X. (2017). Integrating phase change materials into concrete through microencapsulation using cenospheres. *Cement and Concrete Composites*, 80, 317-325.
- Lucas, S., Ferreira, V., & de Aguiar, J. B. (2013). Latent heat storage in PCM containing mortars—Study of microstructural modifications. *Energy and Buildings*, 66, 724-731.
- Lv, Y., Zhou, W., & Jin, W. (2016). Experimental and numerical study on thermal energy storage of polyethylene glycol/expanded graphite composite phase change material. *Energy and buildings*, 111, 242-252.
- Ma, B., Adhikari, S., Chang, Y., Ren, J., Liu, J., & You, Z. (2013). Preparation of composite shape-stabilized phase change materials for highway pavements. *Construction and Building Materials*, 42, 114-121.
- Ma, B., Zhou, X.-y., Liu, J., You, Z., Wei, K., & Huang, X.-f. (2016). Determination of specific heat capacity on composite shape-stabilized phase change materials and asphalt mixtures by heat exchange system. *Materials*, 9(5), 389.

Marani, A., & Madhkhan, M. (2018). An innovative apparatus for simulating daily temperature for investigating thermal performance of wallboards incorporating PCMs. *Energy and Buildings*, 167, 1-7.

Memon, S. A., Cui, H., Lo, T. Y., & Li, Q. (2015). Development of structural–functional integrated concrete with macro-encapsulated PCM for thermal energy storage. *Applied Energy*, 150, 245-257.

Memon, S. A., Cui, H., Zhang, H., & Xing, F. (2015). Utilization of macro encapsulated phase change materials for the development of thermal energy storage and structural lightweight aggregate concrete. *Applied Energy*, 139, 43-55.

Meshgin, P., & Xi, Y. (2012). Effect of Phase-Change Materials on Properties of Concrete. *ACI Materials Journal*, 109(1).

Min, H.-W., Kim, S., & Kim, H. S. (2017). Investigation on thermal and mechanical characteristics of concrete mixed with shape stabilized phase change material for mix design. *Construction and Building Materials*, 149, 749-762.

Navarro, L., de Gracia, A., Castell, A., Álvarez, S., & Cabeza, L. F. (2015). PCM incorporation in a concrete core slab as a thermal storage and supply system: proof of concept. *Energy and Buildings*, 103, 70-82.

Nepomuceno, M. C., & Silva, P. D. (2014). Experimental evaluation of cement mortars with phase change material incorporated via lightweight expanded clay aggregate. *Construction and Building Materials*, 63, 89-96.

Outlook, A. E. (2010). Energy information administration. Department of Energy, 92010(9), 1-15.

Pagliolico, S. L., Sassi, G., Cascone, Y., & Bongiovanni, R. M. (2015). A reference device for evaluating the thermal behavior of installed multilayered wall containing a phase change material. *Energy conversion and management*, 106, 1409-1417.

Pilehvar, S., Cao, V. D., Szczotok, A. M., Valentini, L., Salvioni, D., Magistri, M., Pamies, R., & Kjønksen, A.-L. (2017). Mechanical properties and microscale changes of geopolymer concrete and Portland cement concrete containing micro-encapsulated phase change materials. *Cement and Concrete Research*, 100, 341-349.

Pilehvar, S., Szczotok, A. M., Rodríguez, J. F., Valentini, L., Lanzón, M., Pamies, R., & Kjønksen, A.-L. (2019). Effect of freeze-thaw cycles on the mechanical behavior of geopolymer concrete and Portland cement concrete containing micro-encapsulated phase change materials. *Construction and Building Materials*, 200, 94-103.

Pomianowski, M., Heiselberg, P., Jensen, R. L., Cheng, R., & Zhang, Y. (2014). A new experimental method to determine specific heat capacity of inhomogeneous concrete material with incorporated microencapsulated-PCM. *Cement and Concrete Research*, 55, 22-34.

Ramakrishnan, S., Sanjayan, J., Wang, X., Alam, M., & Wilson, J. (2015). A novel paraffin/expanded perlite composite phase change material for prevention of PCM leakage in cementitious composites. *Applied energy*, 157, 85-94.

Ramakrishnan, S., Wang, X., Sanjayan, J., Petinakis, E., & Wilson, J. (2017). Development of thermal energy storage cementitious composites (TESC) containing a novel paraffin/hydrophobic expanded perlite composite phase change material. *Solar Energy*, 158, 626-635.

Ramakrishnan, S., Wang, X., Sanjayan, J., & Wilson, J. (2017). Assessing the feasibility of integrating form-stable phase change material composites with cementitious composites and prevention of PCM leakage. *Materials Letters*, 192, 88-91.

Raoux, S. (2009). Phase change materials. *Annual Review of Materials Research*, 39, 25-48.

Ren, J., Ma, B., Si, W., Zhou, X., & Li, C. (2014). Preparation and analysis of composite phase change material used in asphalt mixture by sol-gel method. *Construction and Building Materials*, 71, 53-62.

Ricklefs, A., Thiele, A. M., Falzone, G., Sant, G., & Pilon, L. (2017). Thermal conductivity of cementitious composites containing microencapsulated phase change materials. *International Journal of Heat and Mass Transfer*, 104, 71-82.

Royon, L., Karim, L., & Bontemps, A. (2014). Optimization of PCM embedded in a floor panel developed for thermal management of the lightweight envelope of buildings. *Energy and buildings*, 82, 385-390.

Ruud, M., Mitchell, J., & Klein, S. (1990). Use of building thermal mass to offset cooling loads. *ASHRAE Transactions (American Society of Heating, Refrigerating and Air-Conditioning Engineers);(United States)*, 96(CONF-9006117--).

Ryms, M., Lewandowski, W. M., Klugmann-Radziemska, E., Denda, H., & Wcisło, P. (2015). The use of lightweight aggregate saturated with PCM as a temperature stabilizing material for road surfaces. *Applied thermal engineering*, 81, 313-324.

Sakka, S. (2005). *Handbook of sol-gel science and technology. 1. Sol-gel processing (Vol. 1)*. Springer Science & Business Media.

Sakulich, A. R., & Bentz, D. P. (2011). Increasing the service life of bridge decks by incorporating phase-change materials to reduce freeze-thaw cycles. *Journal of Materials in Civil Engineering*, 24(8), 1034-1042.

Sakulich, A. R., & Bentz, D. P. (2012). Incorporation of phase change materials in cementitious systems via fine lightweight aggregate. *Construction and Building Materials*, 35, 483-490.

Sánchez-Silva, L., Rodríguez, J. F., Romero, A., Borreguero, A. M., Carmona, M., & Sánchez, P. (2010). Microencapsulation of PCMs with a styrene-methyl methacrylate copolymer shell by suspension-like polymerisation. *Chemical Engineering Journal*, 157(1), 216-222.

Sari, A. (2014). Composites of polyethylene glycol (PEG600) with gypsum and natural clay as new kinds of building PCMs for low temperature-thermal energy storage. *Energy and Buildings*, 69, 184-192.

Sari, A. (2016). Thermal energy storage characteristics of bentonite-based composite PCMs with enhanced thermal conductivity as novel thermal storage building materials. *Energy conversion and management*, 117, 132-141.

Šavija, B., & Schlangen, E. (2016). Use of phase change materials (PCMs) to mitigate early age thermal cracking in concrete: Theoretical considerations. *Construction and Building Materials*, 126, 332-344.

Sayyar, M., Weerasiri, R. R., Soroushian, P., & Lu, J. (2014). Experimental and numerical study of shape-stable phase-change nanocomposite toward energy-efficient building constructions. *Energy and buildings*, 75, 249-255.

Schossig, P., Henning, H.-M., Gschwander, S., & Haussmann, T. (2005). Micro-encapsulated phase-change materials integrated into construction materials. *Solar Energy Materials and Solar Cells*, 89(2), 297-306.

Shadnia, R., Zhang, L., & Li, P. (2015). Experimental study of geopolymer mortar with incorporated PCM. *Construction and Building Materials*, 84, 95-102.

Sharifi, N. P., & Mahboub, K. C. (2018). Application of a PCM-rich concrete overlay to control thermal induced curling stresses in concrete pavements. *Construction and Building Materials*, 183, 502-512.

Sharifi, N. P., & Sakulich, A. (2015). Application of phase change materials to improve the thermal performance of cementitious material. *Energy and Buildings*, 103, 83-95.

Sharma, A., Tyagi, V. V., Chen, C., & Buddhi, D. (2009). Review on thermal energy storage with phase change materials and applications. *Renewable and Sustainable Energy Reviews*, 13(2), 318-345.

Shi, X., Memon, S. A., Tang, W., Cui, H., & Xing, F. (2014). Experimental assessment of position of macro encapsulated phase change material in concrete walls on indoor temperatures and humidity levels. *Energy and Buildings*, 71, 80-87.

Si, W., Zhou, X.-y., Ma, B., Li, N., Ren, J.-p., & Chang, Y.-j. (2015). The mechanism of different thermoregulation types of composite shape-stabilized phase change materials used in asphalt pavement. *Construction and Building Materials*, 98, 547-558.

Sieminski, A. (2014). International energy outlook. Energy Information Administration (EIA).

Silva, T., Vicente, R., Soares, N., & Ferreira, V. (2012). Experimental testing and numerical modelling of masonry wall solution with PCM incorporation: a passive construction solution. *Energy and Buildings*, 49, 235-245.

Soares, N., Costa, J. J., Gaspar, A. R., & Santos, P. (2013). Review of passive PCM latent heat thermal energy storage systems towards buildings' energy efficiency. *Energy and buildings*, 59, 82-103.

Stritih, U., Tyagi, V., Stropnik, R., Paksoy, H., Haghghat, F., & Joybari, M. M. (2018). Integration of passive PCM technologies for net-zero energy buildings. *Sustainable Cities and Society*, 41, 286-295.

Suttaphakdee, P., Dulsang, N., Lorwanishpaisarn, N., Kasemsiri, P., Posi, P., & Chindaprasirt, P. (2016). Optimizing mix proportion and properties of lightweight concrete incorporated phase change material paraffin/recycled concrete block composite. *Construction and Building Materials*, 127, 475-483.

Thiele, A. M., Wei, Z., Falzone, G., Young, B. A., Neithalath, N., Sant, G., & Pilon, L. (2016). Figure of merit for the thermal performance of cementitious composites containing phase change materials. *Cement and Concrete Composites*, 65, 214-226.

Toppi, T., & Mazzarella, L. (2013). Gypsum based composite materials with micro-encapsulated PCM: Experimental correlations for thermal properties estimation on the basis of the composition. *Energy and Buildings*, 57, 227-236.

Tuncel, E. Y., & Pekmezci, B. Y. (2018). A sustainable cold bonded lightweight PCM aggregate production: Its effects on concrete properties. *Construction and Building Materials*, 181, 199-216.

Tyagi, V., Kaushik, S., Tyagi, S., & Akiyama, T. (2011). Development of phase change materials based microencapsulated technology for buildings: a review. *Renewable and Sustainable Energy Reviews*, 15(2), 1373-1391.

Uysal, H., Demirboğa, R., Şahin, R., & Gül, R. (2004). The effects of different cement dosages, slumps, and pumice aggregate ratios on the thermal conductivity and density of concrete. *Cement and Concrete Research*, 34(5), 845-848.

Vicente, R., & Silva, T. (2014). Brick masonry walls with PCM macrocapsules: an experimental approach. *Applied Thermal Engineering*, 67(1-2), 24-34.

Wang, X., Yu, H., Li, L., & Zhao, M. (2016). Experimental assessment on a kind of composite wall incorporated with shape-stabilized phase change materials (SSPCMs). *Energy and buildings*, 128, 567-574.

Wang, Y., Xia, T. D., Zheng, H., & Feng, H. X. (2011). Stearic acid/silica fume composite as form-stable phase change material for thermal energy storage. *Energy and buildings*, 43(9), 2365-2370.

Wei, Z., Falzone, G., Das, S., Saklani, N., Le Pape, Y., Pilon, L., Neithalath, N., & Sant, G. (2017a). Restrained shrinkage cracking of cementitious composites containing soft PCM inclusions: A paste (matrix) controlled response. *Materials & Design*.

Wei, Z., Falzone, G., Das, S., Saklani, N., Le Pape, Y., Pilon, L., Neithalath, N., & Sant, G. (2017b). Restrained shrinkage cracking of cementitious composites containing soft PCM inclusions: A paste (matrix) controlled response. *Materials & Design*, 132, 367-374.

Wei, Z., Falzone, G., Wang, B., Thiele, A., Puerta-Falla, G., Pilon, L., Neithalath, N., & Sant, G. (2017). The durability of cementitious composites containing microencapsulated phase change materials. *Cement and Concrete Composites*, 81, 66-76.

Xu, B., & Li, Z. (2013). Paraffin/diatomite composite phase change material incorporated cement-based composite for thermal energy storage. *Applied Energy*, 105, 229-237.

Xu, B., Ma, H., Lu, Z., & Li, Z. (2015). Paraffin/expanded vermiculite composite phase change material as aggregate for developing lightweight thermal energy storage cement-based composites. *Applied energy*, 160, 358-367.

Xu, T., Chen, Q., Zhang, Z., Gao, X., & Huang, G. (2016). Investigation on the properties of a new type of concrete blocks incorporated with PEG/SiO₂ composite phase change material. *Building and Environment*, 104, 172-177.

Xu, Y., & Chung, D. (1999). Increasing the specific heat of cement paste by admixture surface treatments. *Cement and Concrete Research*, 29(7), 1117-1121.

Xu, Y., & Chung, D. (2000). Effect of sand addition on the specific heat and thermal conductivity of cement. *Cement and Concrete Research*, 30(1), 59-61.

Yao, C., Kong, X., Li, Y., Du, Y., & Qi, C. (2018). Numerical and experimental research of cold storage for a novel expanded perlite-based shape-stabilized phase change material wallboard used in building. *Energy conversion and management*, 155, 20-31.

Young, B. A., Falzone, G., She, Z., Thiele, A. M., Wei, Z., Neithalath, N., Sant, G., & Pilon, L. (2017). Early-age temperature evolutions in concrete pavements containing microencapsulated phase change materials. *Construction and Building Materials*, 147, 466-477.

Young, B. A., Falzone, G., Wei, Z., Sant, G., & Pilon, L. (2018). Reduced-scale experiments to evaluate performance of composite building envelopes containing phase change materials. *Construction and Building Materials*, 162, 584-595.

Young, B. A., Wei, Z., Rubalcava-Cruz, J., Falzone, G., Kumar, A., Neithalath, N., Sant, G., & Pilon, L. (2017). A general method for retrieving thermal deformation properties of microencapsulated phase change materials or other particulate inclusions in cementitious composites. *Materials & Design*, 126, 259-267.

Zalba, B., Marín, J. M., Cabeza, L. F., & Mehling, H. (2003). Review on thermal energy storage with phase change: materials, heat transfer analysis and applications. *Applied thermal engineering*, 23(3), 251-283.

Zhang, H., Wang, X., & Wu, D. (2010). Silica encapsulation of n-octadecane via sol-gel process: a novel microencapsulated phase-change material with enhanced thermal conductivity and performance. *Journal of colloid and interface science*, 343(1), 246-255.

Zhang, L., Zhu, J., Zhou, W., Wang, J., & Wang, Y. (2012). Thermal and electrical conductivity enhancement of graphite nanoplatelets on form-stable polyethylene glycol/polymethyl methacrylate composite phase change materials. *Energy*, 39(1), 294-302.

Zhang, Z., Shi, G., Wang, S., Fang, X., & Liu, X. (2013). Thermal energy storage cement mortar containing n-octadecane/expanded graphite composite phase change material. *Renewable Energy*, 50, 670-675.

Zhou, D., Zhao, C.-Y., & Tian, Y. (2012). Review on thermal energy storage with phase change materials (PCMs) in building applications. *Applied Energy*, 92, 593-605.

Zhou, G., Zhang, Y., Wang, X., Lin, K., & Xiao, W. (2007). An assessment of mixed type PCM-gypsum and shape-stabilized PCM plates in a building for passive solar heating. *Solar energy*, 81(11), 1351-1360.

Chapter 3

3 Machine Learning Prediction of Compressive Strength for Phase Change Materials Integrated Cementitious Composites¹

Incorporating phase change materials (PCMs) into cementitious composites has recently attracted paramount interest. While it can enhance thermal characteristics and energy storage, compressive strength would be decreased. Thus, accurate prediction of the effect of PCM addition on compressive strength is crucial. However, a predictive model for this purpose using physical or chemical features is not feasible at this stage. Thus, machine learning is used for the first time herein to predict the compressive strength of PCM-integrated cementitious composites. A dataset of 154 cement-based mixtures incorporating PCM microcapsules was assembled. Various machine learning regression algorithms including random forest, extra trees, gradient boosting, and extreme gradient boosting were tuned and their prediction accuracy was assessed using several metrics. The models achieved superior prediction accuracy. Exploiting powerful machine learning models to examine the harvested experimental data could provide insights into materials science aspects of this problem and identify pertinent knowledge gaps and needed future research.

3.1 Introduction

The advent of a miscellany of exigencies and constraints including climate change, energy concerns, premature damage of infrastructure, sustainability, and resilience of the built environment have vigorously necessitated the emergence of novel smart materials and systems. For instance, Phase Change Materials (PCMs) can be added into conventional construction materials to bring about enhanced energy efficiency in buildings and sustainability of civil infrastructure (De Gracia & Cabeza, 2015; Ling & Poon, 2013; Rao *et al.*, 2018). Cementitious materials are particularly favorable for incorporating PCMs (Bentz & Turpin, 2007; Hunger *et al.*, 2009; Ling & Poon, 2013). Numerous studies have

¹ A version of this chapter was published in “*Construction and Building Materials*” journal, 2020.

demonstrated the ability of PCM-integrated concrete to store a great deal of thermal energy (Jayalath *et al.*, 2016; Sharifi & Sakulich, 2015; Xu & Li, 2013). Not only do PCMs contribute to thermal energy storage (TES) in cementitious composites, but they also can impart beneficial effects for mitigating thermal shrinkage and cracking (Arora *et al.*, 2017; Fernandes *et al.*, 2014; Pei *et al.*, 2016; Šavija & Schlangen, 2016).

However, PCMs can have deleterious effects on the mechanical properties of cement-based materials (Aguayo *et al.*, 2016; Hunger *et al.*, 2009; Jayalath *et al.*, 2016; Pilehvar *et al.*, 2017; Pilehvar *et al.*, 2019). Copious reasons have been posited to explain such compressive strength reduction, such as the interference of PCM with cement hydration (Hunger *et al.*, 2009; Jayalath *et al.*, 2016; Pilehvar *et al.*, 2017). Hence, researchers have pursued new methods to incorporate PCMs into conventional construction materials to lessen such detrimental effects. Amid proposed techniques (*e.g.* lightweight aggregate inclusion, micro- and macro-encapsulation), PCM microcapsules have been extensively utilized in the fabrication of cementitious composites. Its effects on mechanical and thermal characteristics of cementitious composites have also been extensively assessed over the last decade (Aguayo *et al.*, 2016; Hunger *et al.*, 2009; Jayalath *et al.*, 2016). Diverse features interfere with mechanical strength development of cementitious composites, including the effect of soft PCM microcapsule inclusion, breakage of microcapsules shells during mixing and casting of fresh concrete and loading of hardened concrete, and PCM microcapsule-induced porosity. Hence, designing concrete mixtures with optimum PCM inclusion and desired compressive strength needs accurate predictive tools.

Parallel to the evolution of PCMs and their application in construction materials, soft computing techniques have emerged as powerful tools to model engineering problems and predict the behavior of different engineering systems (Bose & Liang, 1996; Saridakis & Dentsoras, 2008). For instance, the complex fresh and hardened behavior of cementitious composites and its dependency on mixture composition, curing regimes, and environmental exposures have stimulated researchers to deploy numerous modeling techniques to predict fundamental engineering properties, including compressive strength (Ni & Wang, 2000; Snell *et al.*, 1989). The compressive strength of concrete depends upon various parameters and thus, is a convoluted nonlinear phenomenon to analyze and

formulate. Accordingly, numerous studies have attempted to predict the compressive strength of concrete based on its mixture portions using soft computing techniques, such as artificial neural networks (ANN) and fuzzy logic (FL) (Alshihri *et al.*, 2009; Khademi *et al.*, 2017; Nehdi *et al.*, 2001; Ni & Wang, 2000; Topcu & Saridemir, 2008). Such methods have been deployed on a variety of concretes, including self-compacting concrete, lightweight concrete, self-healing concrete, and engineering properties such as mechanical strength, rheology, crack behavior, etc. (Alshihri *et al.*, 2009; Altun *et al.*, 2008; Bilim *et al.*, 2009; Chandwani *et al.*, 2015; Khademi *et al.*, 2017; Nehdi *et al.*, 2001; Ramadan Suleiman & Nehdi, 2017).

Machine learning (ML) has more recently emerged as a powerful technique to predict the compressive strength of concrete using various algorithms (Chou *et al.*, 2010; Chou & Tsai, 2012; Chou *et al.*, 2014; Deng *et al.*, 2018; Yaseen, Deo, *et al.*, 2018; Young *et al.*, 2019). Yaseen *et al.* (Yaseen, Deo, *et al.*, 2018) used extreme learning machine to estimate the compressive strength of foamed concrete. Cement content, foam volume, oven dry density, and water-to-binder ratio were considered as the model attributes. Accordingly, extreme learning machine exhibited most accurate predictions compared to that of other algorithms including multivariate adaptive regression spline, M5 tree model, and support vector machine (SVM). In another study, Ashrafian *et al.* (Ashrafian *et al.*, 2020) used Multivariate Adaptive Regression Splines tuned with Water Cycle Algorithm (MARS-WCA) to estimate the compressive strength of foamed cellular lightweight concrete. They evidenced that their integrative model provided a better prediction accuracy (Ashrafian *et al.*, 2020). Young *et al.* (Young *et al.*, 2019) utilized a large dataset of both laboratory and industry-scale concrete mixture designs to predict the 28-day compressive strength of concrete using ANNs, SVMs and decision trees. The models could predict the compressive strength of laboratory-fabricated concrete more accurately than for industry-scale concrete mixtures. It was proposed that expanding the size of the dataset and taking wider spectrum of input variables are necessary to discern the most weighted patterns in the dataset (Young *et al.*, 2019). In addition to compressive strength, other properties of concrete materials and structures can be modeled using soft computing methods, which has been widely addressed in the literature, including shear strength prediction of concrete beams, bar development

length prediction, etc. (Al-Musawi *et al.*, 2020; Keshtegar *et al.*, 2019; Yaseen, Afan, *et al.*, 2018; Yaseen *et al.*, 2019; Yaseen, Tran, *et al.*, 2018).

Nevertheless, the size of dataset is a crucial factor affecting the performance of ML models. Materials science datasets could be both small or comprehensive, which significantly affects the training of ML models (Zhang & Ling, 2018). Inadequate amount of available data could result in a model with either low prediction accuracy or lack of generalization, *i.e.*, overfitting (Cieslak & Chawla, 2008; Zhang & Ling, 2018). Therefore, effective strategies should be formulated to mitigate the negative impact of small datasets. One versatile approach to overcome the small size of datasets is using ensemble techniques in which multiple learners are aggregated to provide a more robust performance. Among ensemble techniques, tree-based ensembles, such as random forest, gradient boosting, eXtreme gradient boosting, etc. have been extensively proven to achieve promising performance in recent years (Ahmad, Mourshed, *et al.*, 2018; Ahmad, Reynolds, *et al.*, 2018; Torres-Barrán *et al.*, 2019).

Considering the recent extensive use of PCMs in cement-based materials and its effect on the compressive strength of concrete, developing rational predictive tools for the compressive strength of PCM-incorporated concrete is inevitable. Therefore, this study aims to model, for the first time, the compressive strength of PCM-incorporated cement composites using modern ML methods. Since PCM microcapsules have been the most prevalent form of PCM integrated into structural concrete, a dataset containing such concrete mixtures, as well as cement mortar, was created. Tree-based ensembles are favorable tools to develop predictive models based on small datasets as mentioned earlier. Hence different powerful ML algorithms including random forest (RF), extra trees (ET), gradient boosting (GB), and eXtreme gradient boosting (XGB) are used aiming at providing most accurate predictions based on the largest available dataset.

3.2 Machine learning modeling basis

Various machine learning methods can be employed for either regression or classification purposes. For instance, decision trees are appropriate for both regression and classification problems. A decision tree model denoted Classification and Regression Tree (CART) was

proposed as a statistical model by Breiman *et al.* (Breiman, 2017; Breiman *et al.*, 1984). Decision tree is a non-parametric model and does not consider prior parameters. It has two types of nodes, namely decision and leaf nodes. It can pattern complicated relationships between the features of the data to predict the output (*i.e.*, target). The preliminary idea of a decision tree is to split a complex prediction process into some simpler ones. Moreover, the prediction performance of decision tree models can be significantly enhanced in terms of prediction accuracy and over-fitting errors. For this purpose, ensemble models, which are a combination of several decision trees, can be created. Bagging and boosting are mostly used for performing ensemble models, such as the RF model and GB model. Such methods are proper for data having non-linear relationships between features (*i.e.*, attributes). However, each model has some hyper-parameters that need to be tuned (Ahmad, Mourshed, *et al.*, 2018; Pan *et al.*, 2019; Young *et al.*, 2019). In recent years, many researchers used several ensemble models to predict various targets in different civil engineering problems. **Table 3-1** presents some of the recent studies on the application of different tree-based ensembles in the prediction of mechanical properties of concrete. A brief outline of the regression algorithms employed in this study is provided below.

Table 3-1: Examples of ML applications in similar engineering fields

Purpose	Algorithm	Ref.	Purpose	Algorithm	Ref.
Prediction of concrete compressive strength	Random Forest; Gradient-Boosted Tree	(Young <i>et al.</i> , 2019)	Predicting IRI of asphalt pavements	Random Forest	(Gong <i>et al.</i> , 2018)
Prediction of lightweight foamed concrete compressive strength	Extreme Learning Machine;	(Yaseen, Deo, <i>et al.</i> , 2018)	Study of energy use intensity in buildings	Random Forest	(Ma & Cheng, 2016)
Predicting compressive strength of lightweight self-compacting concrete	Random Forest	(J. Zhang <i>et al.</i> , 2019)	Prediction of mechanical properties of concrete	Gradient Boosting	(M. Zhang <i>et al.</i> , 2019)
Prediction of compressive strength of concrete	Random Forest	(Chopra <i>et al.</i> , 2018)	Compressive strength of high performance concrete	Ensemble of decision trees	(Erdal, 2013)

3.2.1 Random forest regression (RFR)

The random forest model is generally developed from the CART method to deliver better performance in predicting the output. Purposefully, it creates a large number of decision

trees to predict the output. The growth of each tree in this model is achieved through a randomized set of features and thus, it is referred to as random forest (Breiman, 1996, 2017; Breiman *et al.*, 1984). The amalgamation of all formed decision trees is done using bagging (*i.e.*, bootstrap aggregation) (Breiman, 1996, 2017; Li *et al.*, 2018; Zahedi *et al.*, 2018). Breiman (Breiman, 1996) introduced bagging as the ensemble model. Bagging can be applied to an RFR model to decrease the associated variance in predictions. In this regard, a subset of features or training data should be randomly sampled for each decision tree, which is called a bootstrap sample. The bagging method applies the decision tree algorithm to selected bootstrap samples to produce predictions (Breiman, 1996; Li *et al.*, 2018; Rodriguez-Galiano *et al.*, 2015). The final output value in RFR model is the average of the output values obtained from all decision trees. Consequently, the outputs of all trees are aggregated and averaged out. Accordingly, the final prediction value can be obtained as follows (Li *et al.*, 2018; Rodriguez-Galiano *et al.*, 2015):

$$\hat{Y} = \frac{1}{N} \sum_{i=1}^N \hat{Y}_i \quad \text{Eq. 3-1}$$

Where \hat{Y}_i is the output value for tree i ($i = 1, 2, 3, \dots, N$). **Figure 3-1** displays a simple schematic of RFR structure. More detailed information on RF models can be found in (Breiman, 1996, 2017; Breiman *et al.*, 1984).

3.2.2 Extra trees regression (ETR)

Extra trees model, also known as extremely randomized trees, is another ML method, which is a tree-based ensemble extended from the random forest algorithm (Ahmad, Mourshed, *et al.*, 2018; Ahmad, Reynolds, *et al.*, 2018; Geurts *et al.*, 2006; John *et al.*, 2015). Like the random forest, the extra trees model uses a subset of features for training estimators with a random selection approach. One of the main differences between such two algorithms is that the extra trees model selects the best feature and its associated value for splitting the node, whilst random forest algorithm employs the most discriminative split. Moreover, the extra trees model, in contrast to the random forest, does not use the bootstrap method for training (Ahmad, Mourshed, *et al.*, 2018; Ahmad, Reynolds, *et al.*, 2018; John *et al.*, 2015).

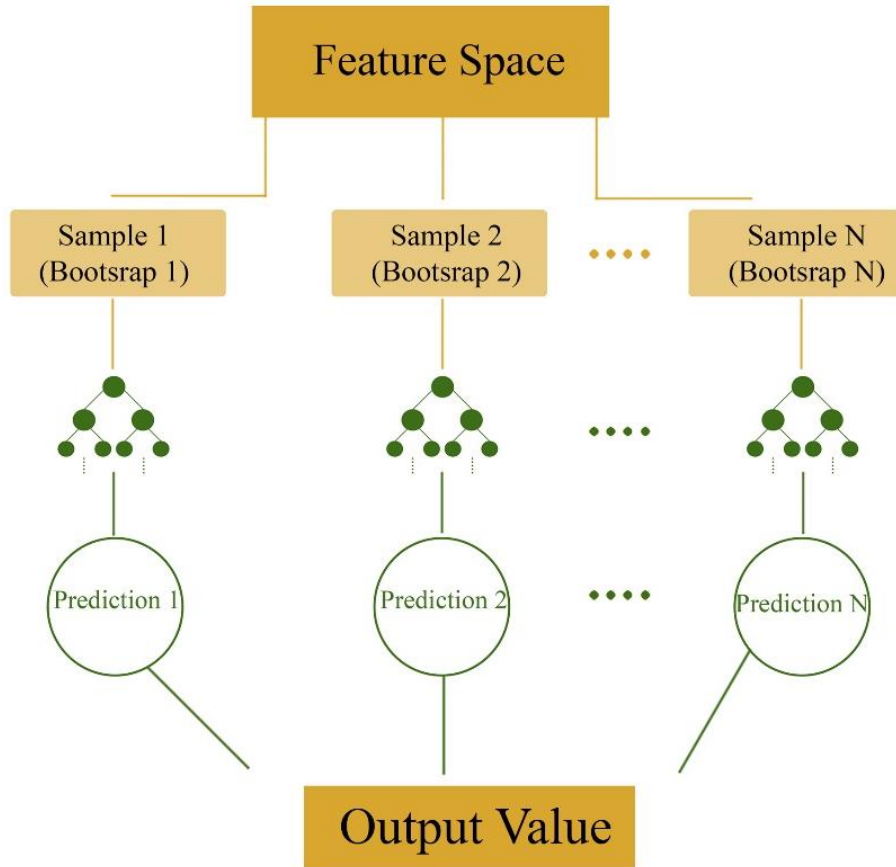


Figure 3-1: Simple schematic structure of a random forest model.

3.2.3 Gradient boosting regression (GBR)

Boosting was mainly developed for classification problems, and then progressed for use in regression models (Hastie *et al.*, 2001; Mason *et al.*, 1999). In this technique, the output values of several weak learners are amalgamated into a robust committee using additive models. Such models are trained in a forward stage-wise procedure as follows:

$$F_m(x) = F_{m-1}(x) + h_m(x) \quad \text{Eq. 3-2}$$

Where $F_m(x)$ is the GBR model and $h_m(x)$ are the weak learners (*i.e.*, basis functions), which are essentially regression trees (Hastie *et al.*, 2001; Persson *et al.*, 2017). In other words, $F_m(x)$ is comprised of m small regression trees where boosting iterations based on functional gradient descent are proceeded until a robust learner is achieved (Mason *et al.*,

1999; Persson *et al.*, 2017). One helpful strategy for mitigating overfitting is to narrow the contribution of each regression tree by applying a scaling factor, α , as follows:

$$F_m(x) = F_{m-1}(x) + \alpha h_m(x) \quad \text{Eq. 3-3}$$

α scales the length of the step for finding the optimum solution in the gradient descent method and is called learning rate (Hastie *et al.*, 2001; Mason *et al.*, 1999; Persson *et al.*, 2017). This parameter plays an important role in optimizing the prediction performance of boosting ensembles. Details on the model parameters can be found in (Hastie *et al.*, 2001; Mason *et al.*, 1999; Persson *et al.*, 2017; Torres-Barrán *et al.*, 2019).

3.2.4 eXtreme gradient boosting regression (XGBR)

XGBR is also an ensemble algorithm in which the boosting process is followed (Chakraborty & Elzarka, 2019a). XGB is an optimized GB model so that the loss function is normalized and thus, the model variances are mitigated. Consequently, the model complexity is reduced and overfitting is much avoided (Chang *et al.*, 2018; Guelman, 2012). Another significant difference between GB and XGB is that XGB employs the Taylor expansion to enhance the loss function, while the GB only considers the first derivative (Chang *et al.*, 2018; Guelman, 2012). In XGB model, the sum of the prediction of each estimator yields the ultimate prediction of the model at each step, t , expressed by the following equation (Fan *et al.*, 2018):

$$f_i^{(t)} = \sum_{k=1}^n f_k(x_i) = f_i^{(t-1)} + f_t(x_i) \quad \text{Eq. 3-4}$$

where x_i is the input vector, and $f_i^{(t)}$ and $f_t(x_i)$ are the predictions and the estimator at step t , respectively. XGB evaluates the “goodness” of the model by implementing a regularization function alongside with the loss function. The regularization parameter is defined as follows (Fan *et al.*, 2018):

$$\Omega(f) = \gamma T + \frac{1}{2} \lambda \|\omega\|^2 \quad \text{Eq. 3-5}$$

where ω is the leaves' score vector, λ is the regularization parameter, and γ is the minimum required loss to partition the leaf node. More details on XGB can be found in (Chen & Guestrin, 2016; Fan *et al.*, 2018).

3.3 Model development

In this study, the various ML models outlined in **Section 3.2** (RFR, ETR, GBR, and XGBR) were developed to estimate the compressive strength of cement composites incorporating PCM microcapsules. The rationale for developing different models is to appraise the performance of each algorithm in modeling this non-linear problem. Fundamental considerations considered to develop such models are elucidated below.

3.3.1 Data collection, feature extraction, and preprocessing

PCM microencapsulation has been a prevalent method for incorporating PCMs into cementitious composites, especially in structural concrete. Commercial PCM microcapsules have been integrated into concrete and its effect on the thermal and mechanical properties of concrete have been widely investigated. The compressive strength of concrete was one of the key parameters measured in such studies. It has been mostly reported that the addition of PCM microcapsules in concrete mixtures led to reduction in compressive strength due to several reasons (Marani & Nehdi, 2019).

To explore this problem systematically, a dataset consisting of 11 attributes (10 input data features and 1 output) and 154 samples was assembled using studies in the open literature (Aguayo *et al.*, 2016; D'Alessandro *et al.*, 2018; Dehdezi *et al.*, 2013; Hunger *et al.*, 2009; Jayalath *et al.*, 2016; Lecompte *et al.*, 2015; Liu *et al.*, 2017; Meshgin & Xi, 2012; Pilehvar *et al.*, 2017; Snoeck *et al.*, 2016). Since only limited studies have been performed in this specific area, mixture proportions for cement mortar and concrete were considered and thereby, the fine and coarse aggregate contents were also used as data features. Furthermore, this study aims at evaluating the influence of those input parameters investigated in previous experimental studies to capture its significance. Hence, thermal properties of PCMs as well as the age and temperature of specimens at the testing time were included as input parameters. Nevertheless, the following assumptions have been made in collecting the data due to the lack of information about the PCM microcapsules in

the literature: i) The chemical and physical properties of the microcapsules such as the shell's material and the percentage of PCM content in microcapsules, the particle size of the microcapsules, etc. are not considered in the dataset; ii) Neither chemical reactions of the microcapsules with concrete nor its potential mechanical damage are considered in the dataset; and iii) It is assumed that there is no leakage of PCM during mixing, curing, and testing of concrete.

Table 3-2 presents the 10 input attributes of the dataset. For model preparation, the dataset was randomly partitioned into two groups, namely “training” and “testing” data. About 80% of the data was allocated to training, while the remaining 20% was used for testing. To have identical training and testing samples for all developed ML models, a unique “random_state” was assigned in each model using the scikit-learn package in Python (Pedregosa *et al.*, 2011). Moreover, the importance of each feature in the prediction performance of the tuned model was evaluated to compare with related findings in the experimental observations. The feature importance explains how much each feature contributes to the prediction of the output (Fisher *et al.*, 2018; Gong *et al.*, 2018; Pedregosa *et al.*, 2011).

Table 3-2: Input features of the dataset prepared for modeling

No.	Attribute	Unit	Subscript	No.	Attribute	Unit	Subscript
1	Melting temperature	°C	T _m	6	Fine aggregate	kg/m ³	FA
2	Latent heat	kJ/kg	L _m	7	Coarse aggregate	kg/m ³	CA
3	PCM dosage	kg/m ³	PCM	8	Superplasticizer	kg/m ³	SP
4	Cement	kg/m ³	C	9	Age	days	Age
5	Water/Cement	-	W/C	10	Curing temperature	°C	T

3.3.2 Model development, hyperparameter tuning, and cross-validation

To optimize the performance of the models used in this study, 5-fold cross-validation (CV) along with a stepwise-randomized searching algorithm were implemented to tune the hyper-parameters of each model using scikit-learn class “RandomizedSearchCV” (Pedregosa *et al.*, 2011). Using a k-fold CV, the data are split into k number of subsets, named folds. Thereupon, the model fits the data k times iteratively so as $k-1$ folds are used

for training, whereas the k th fold is considered as the test data in each iteration. **Figure 3-2** displays the schematic structure of a 5-fold CV. As mentioned earlier, each ML algorithm has specific parameters and thus, the utilization of tuned parameters can contribute towards more accurate predicted outputs.

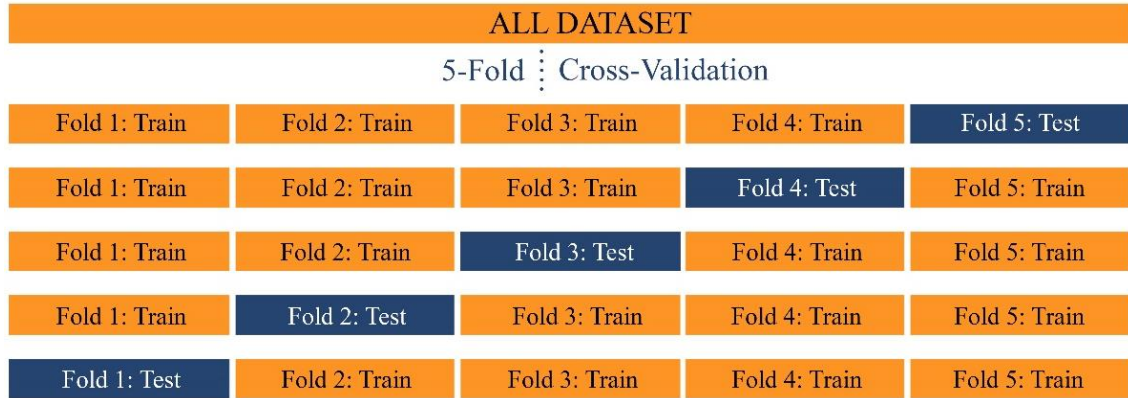


Figure 3-2: Schematic structure for the 5-fold CV.

3.3.3 Model performance evaluation

To assess the accuracy of the applied ML methods, various statistical metrics were utilized. The coefficient of determination (R^2 -value), mean square error (MSE), root mean square error (RMSE), mean absolute error (MAE), as well as the normalized RMSE (nRMSE) and normalized MAE (nMAE) were calculated. Similar metrics were used to assess model predictive performance in many studies in the literature (Yaseen, Deo, *et al.*, 2018; Young *et al.*, 2019). Such metrics are expressed as follows:

$$MSE = \frac{1}{m} \sum_{i=1}^m (Y - \hat{Y})^2 \quad \text{Eq. 3-6}$$

$$RMSE = \sqrt{\frac{1}{m} \sum_{i=1}^m (Y - \hat{Y})^2} \quad \text{Eq. 3-7}$$

$$MAE = \frac{1}{m} \sum_{i=1}^m |Y - \hat{Y}| \quad \text{Eq. 3-8}$$

$$nRMSE = \frac{RMSE}{Y_{mean}} \times 100 \quad \text{Eq. 3-9}$$

$$nMAE = \frac{MAE}{Y_{mean}} \times 100 \quad \text{Eq. 3-10}$$

Where m is the number of observations in the dataset, Y is the observed output (experimental value), \hat{Y} is the predicted output (obtained from ML models), and Y_{mean} is the mean observed output.

3.4 Results and discussion

The predictive performance of the ML models employed in this study (RFR, ETR, GBR, and XGBR), which were outlined in **Section 3.2**, is delineated below. A discussion of the hyper-parameter tuning of each algorithm is provided. Moreover, the prediction accuracy of the tuned algorithms along with their feature importance values are analyzed herein.

3.4.1 Hyper-parameter tuning of employed ML models

The hyper-parameters of each ML model have a significant influence on its prediction accuracy, robustness, as well as its capability to be generalized to new datasets. Accordingly, all models were first tuned to acquire best performance accuracy in predicting the compressive strength, while avoiding overfitting. Moreover, hyper-parameter tuning would significantly influence the computational time of the model. However, considering the rather limited experimental data relevant to the models, the size of the dataset in this study is not considered extensive. Hence, the computational time was not a great concern.

For tuning purposes, the 5-fold CV discussed earlier was implemented along with a stepwise-randomized searching technique. R^2 -value and RMSE were monitored as the criteria for achieving the tuned parameters for each ensemble model. In the case of the RFR and ETR models, the number of trees in the forest ($n_estimators$), the minimum required number of samples to split an internal node ($min_samples_split$), the minimum required number of samples to be at a leaf node ($min_samples_leaf$), the number of features to be randomly considered during the growth of each tree ($max_features$), and the maximum depth of the tree (max_depth) are the most essential parameters to be tuned as demonstrated previously in the literature (Ahmad, Mourshed, *et al.*, 2018; Ahmad, Reynolds, *et al.*, 2018; Pedregosa *et al.*, 2011; Young *et al.*, 2019). Different values for such parameters were assigned during 2000 iterations and subsequently the tuned parameters were extracted as

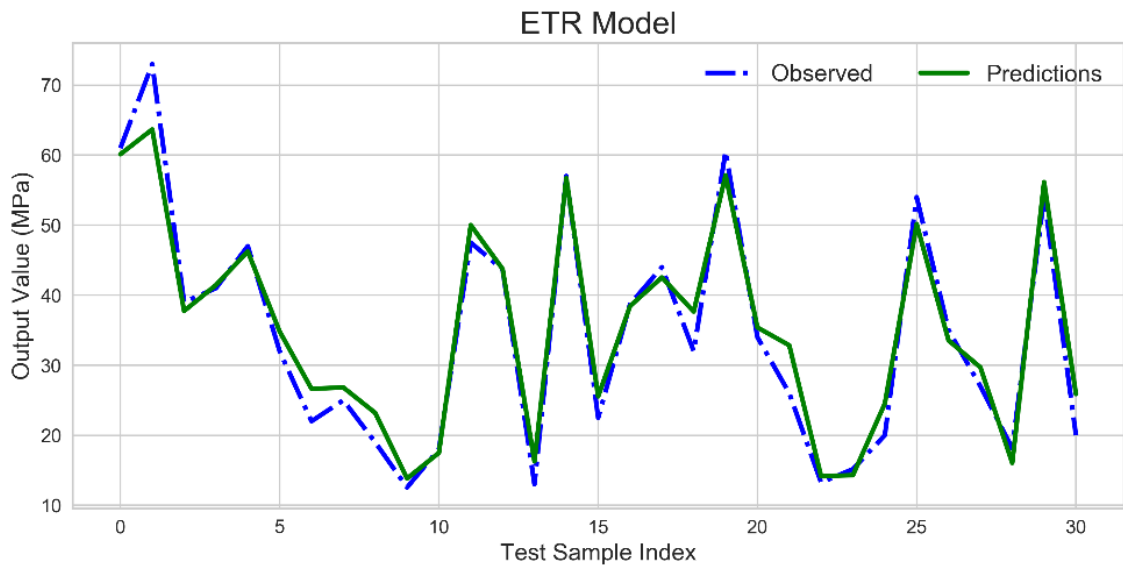
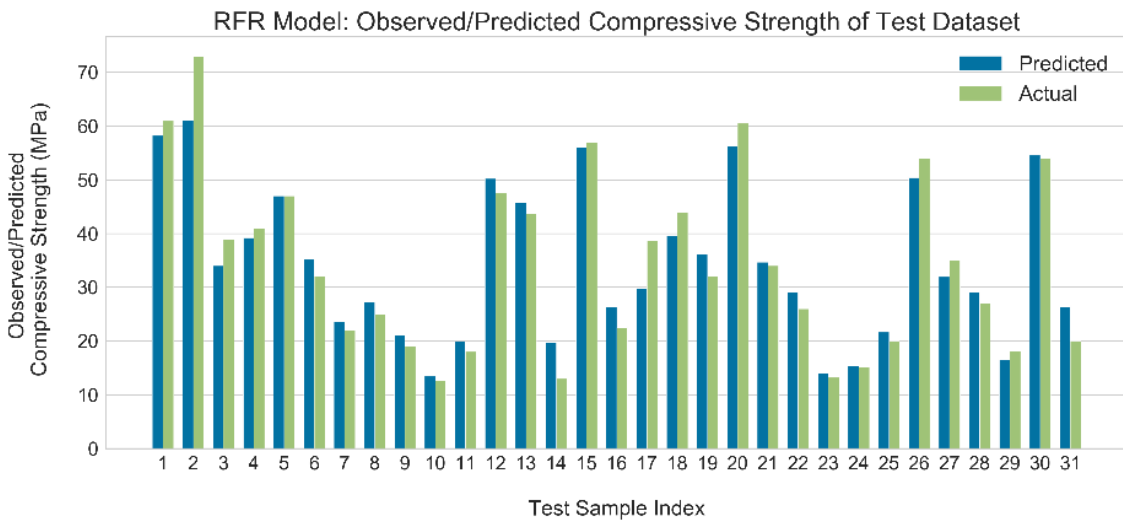
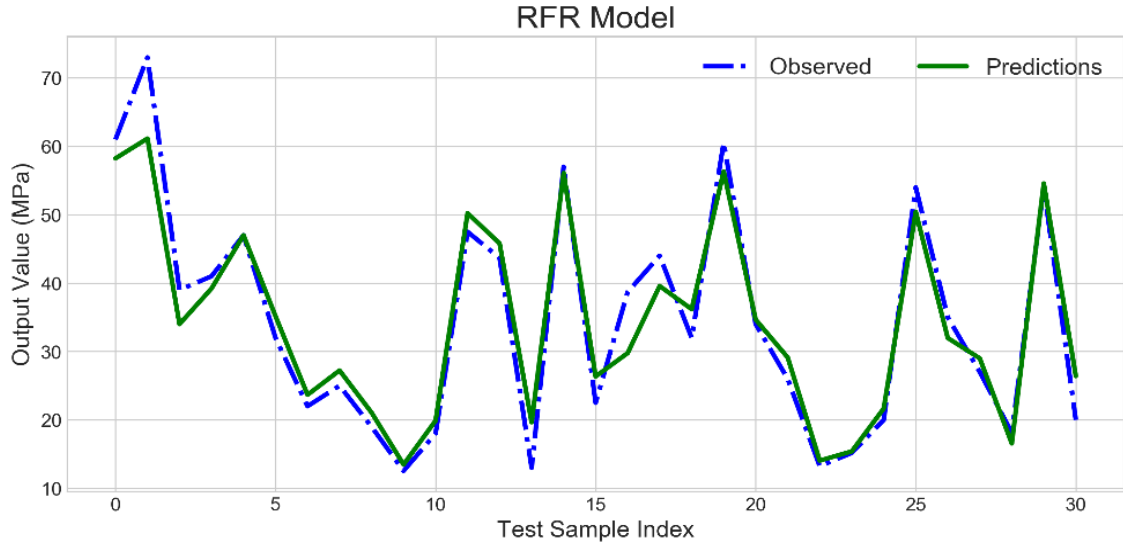
presented in **Table 3-3**. For the GBR model, in addition to the mentioned parameters, the learning rate, which indicates the contribution of each tree, noticeably affects the model performance. Similar observations were reported in (Pan *et al.*, 2019; Persson *et al.*, 2017; Young *et al.*, 2019). In the case of the XGBR model, the “`colsample_bylevel`” and “`colsample_bytree`” perform similar to the “`max_features`” in the GBR model and are important to be tuned. To avoid overfitting, the “`min_child_weight`” should also be optimized (Chakraborty & Elzarka, 2019b; Pedregosa *et al.*, 2011). **Table 3-3** presents the tuned parameters for the four utilized models.

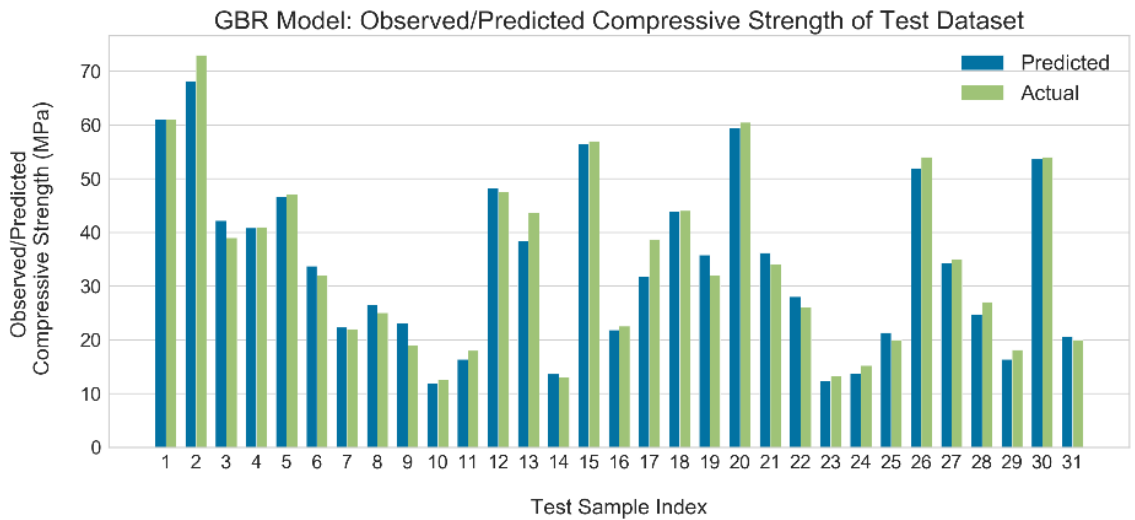
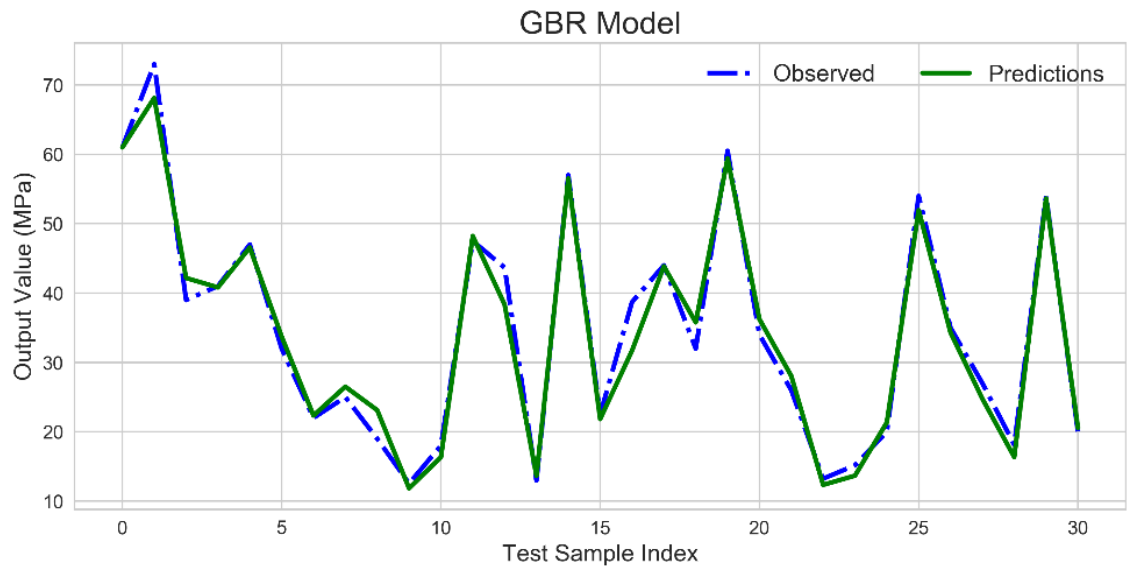
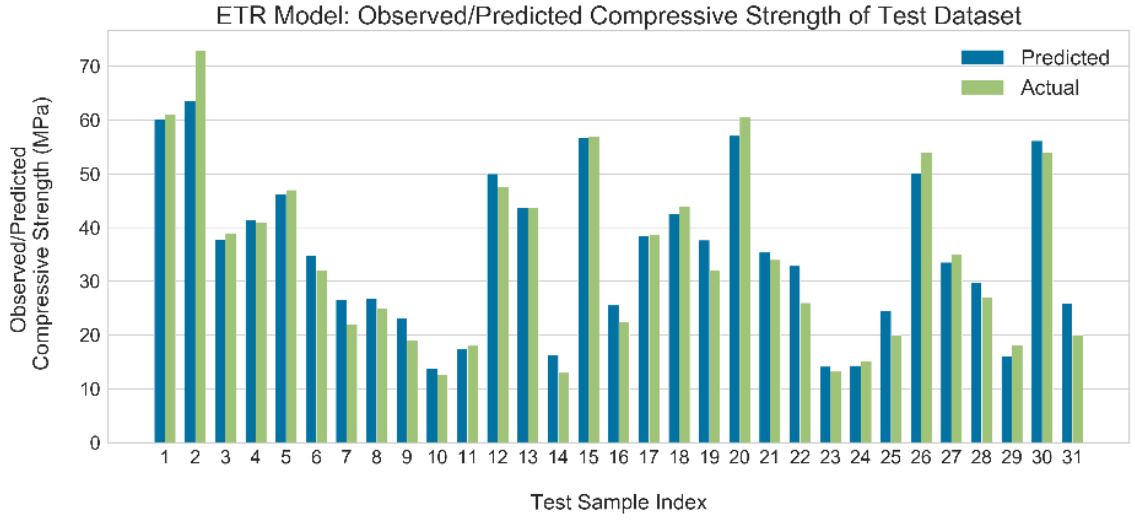
Table 3-3: Tuned parameters for the employed ML models

Model	Tuned Parameters
RFR	<code>n_estimators=50; min_samples_split=2; min_samples_leaf=1; max_depth=17; max_features=5</code>
ETR	<code>n_estimators=130; min_samples_split=2; min_samples_leaf=1; max_depth=10; max_features=7</code>
GBR	<code>n_estimators=220; learning_rate=0.33; min_samples_split=4; min_samples_leaf=2; max_depth=2</code>
XGBR	<code>n_estimators=180; learning_rate=0.50; min_child_weight=7; colsample_bylevel=0.60; colsample_bytree=0.65; max_depth=4</code>

3.4.2 Predictive performance of machine learning models

The accuracy of each ML algorithm in predicting the compressive strength of cement-based materials incorporating phase change materials was assessed through the statistical metrics outlined in **Section 3.3.3**. **Figure 3-3** illustrates the compressive strength values observed in the experimental test data examples versus the corresponding values predicted by the various machine learning models. The experimental values for compressive strength in the testing dataset varied within the range of 12.55 to 73 MPa, for mixtures with and without PCM present in the dataset. It can be observed that all the models were able to learn the non-linear relationship between the features of the dataset (*i.e.*, mixture ingredients) for predicting the compressive strength with a similar trend of predicted versus observed output.





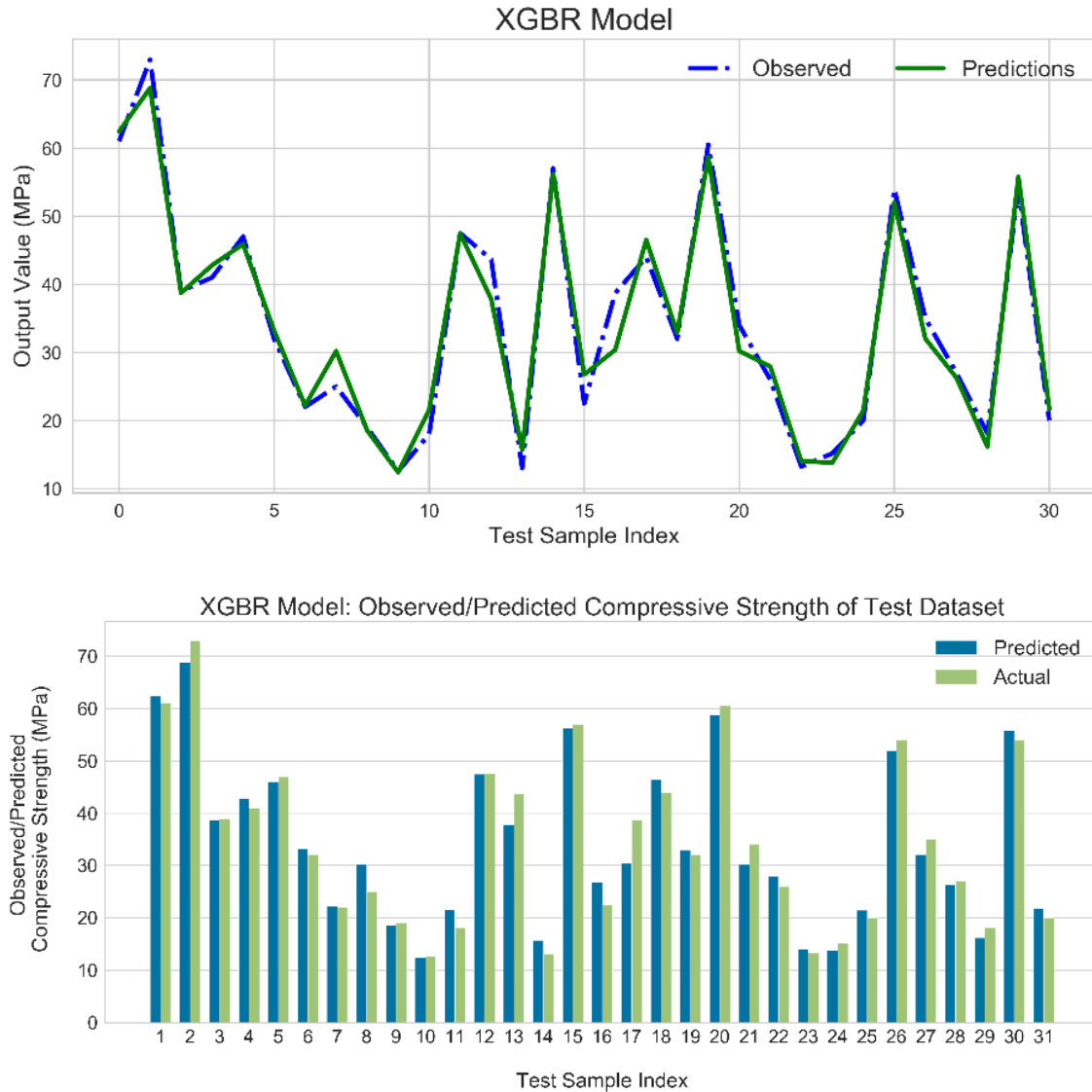
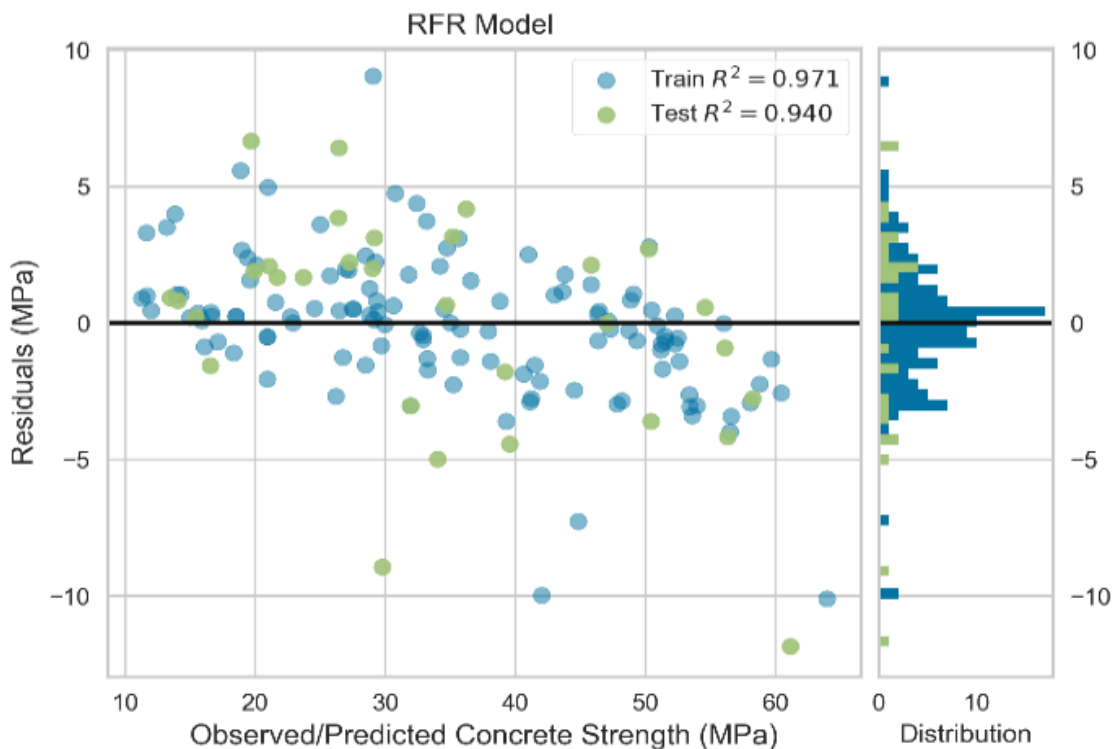


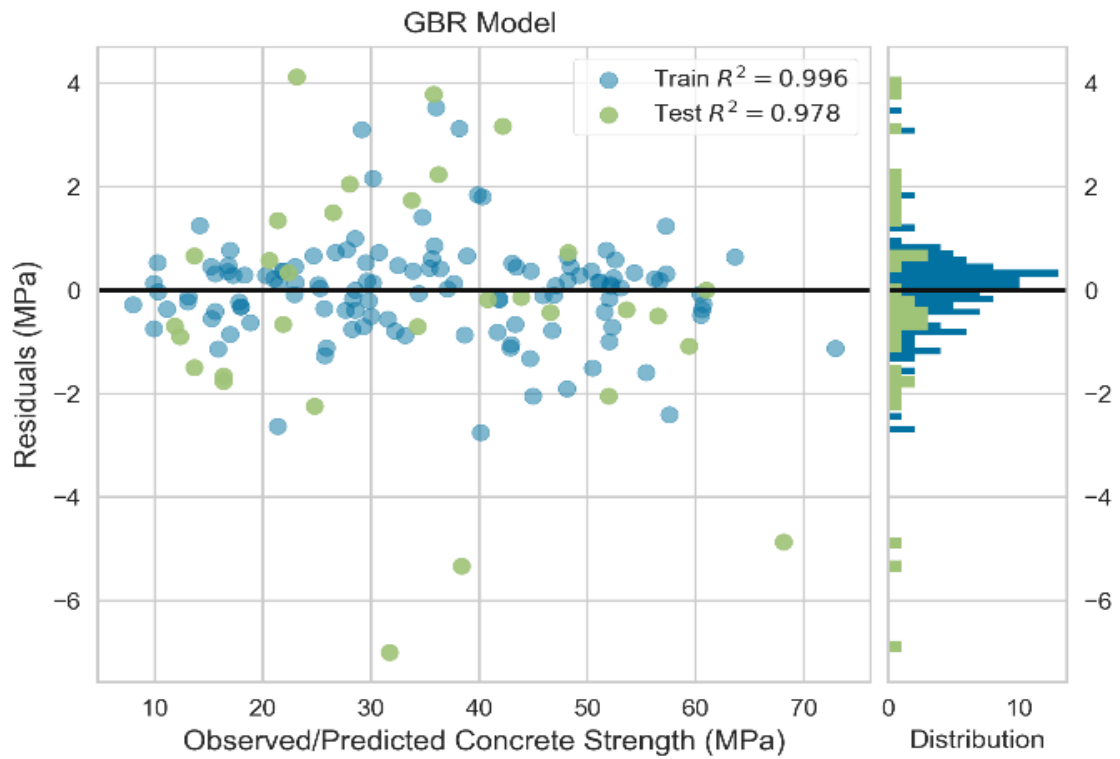
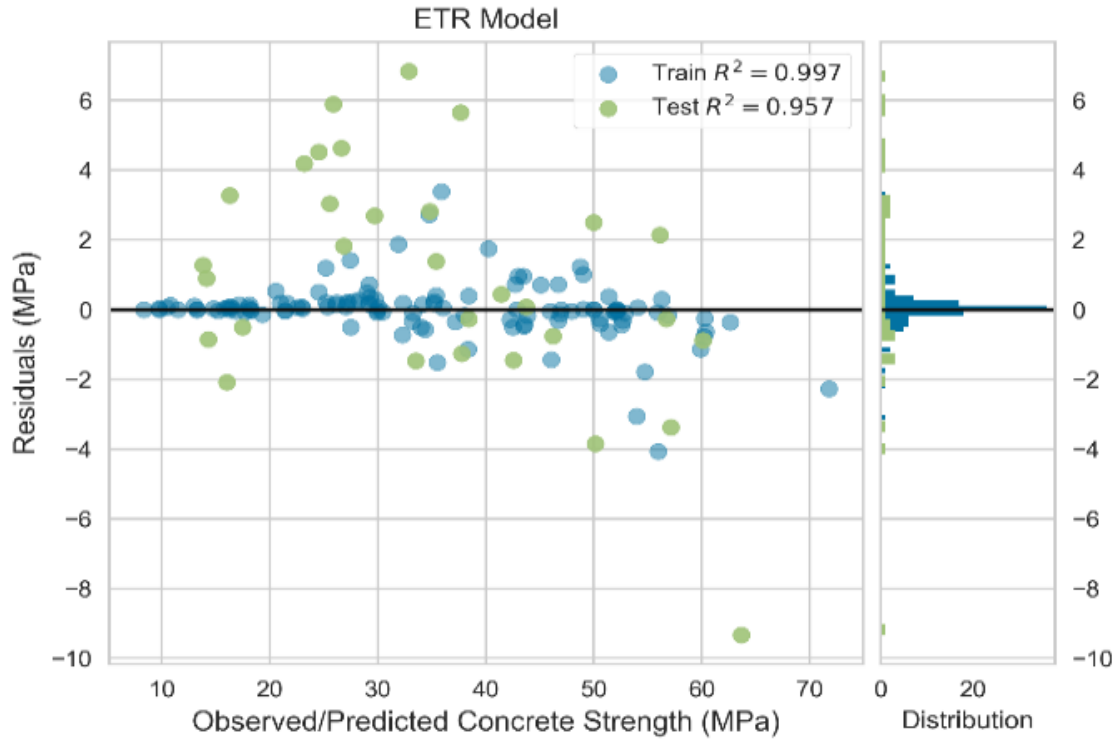
Figure 3-3: Compressive strength of cementitious composites: observed VS. predicted.

Figure 3-4 displays the residuals of the predicted output (*i.e.*, compressive strength) for training and testing datasets. The residual of each training or testing example is the difference between the predicted value and the original observed value of the output for that example. It can be observed that the residuals for the four applied models varied slightly around zero, which denotes excellent prediction performance. Moreover, the R^2 -value of the training and testing datasets are shown in **Fig. 3-4**. All the models had R^2 -values greater than 0.95 for the training and testing datasets, except for the RFR model, which had a testing R^2 -value of 0.94. The residuals along with the R^2 -values of each

predictive model indicate superior predictive ability for the compressive strength of cement-based materials incorporating PCM microcapsules.

It should be noted that due to the relatively limited dataset utilized in developing the models, high R^2 -value for training data (up to 0.99 for ETR, GBR, and XGBR models) was achieved. To avoid model overfitting, the hyper-parameters of each model were tuned in such a way that the difference between the R^2 -value for training and testing datasets is minimized. To better characterize the predictive performance of the models, different statistical metrics introduced in **Section 3** were calculated considering the entire dataset as presented in **Table 3-4**. The RMSE and MAE values for the different models varied between 2.419 and 3.988 MPa and 1.752 to 3.065 MPa, respectively. Such small values indicate that the developed machine learning predictive models had superior accuracy in predicting compressive strength (Ahmad, Mourshed, *et al.*, 2018; Yaseen, Deo, *et al.*, 2018; Young *et al.*, 2019). As evidenced in **Table 3-4**, the GBR model showed best predictive performance as it had the highest R^2 -value (0.977) as well as the lowest RMSE and MAE values (2.419 and 1.752, respectively).





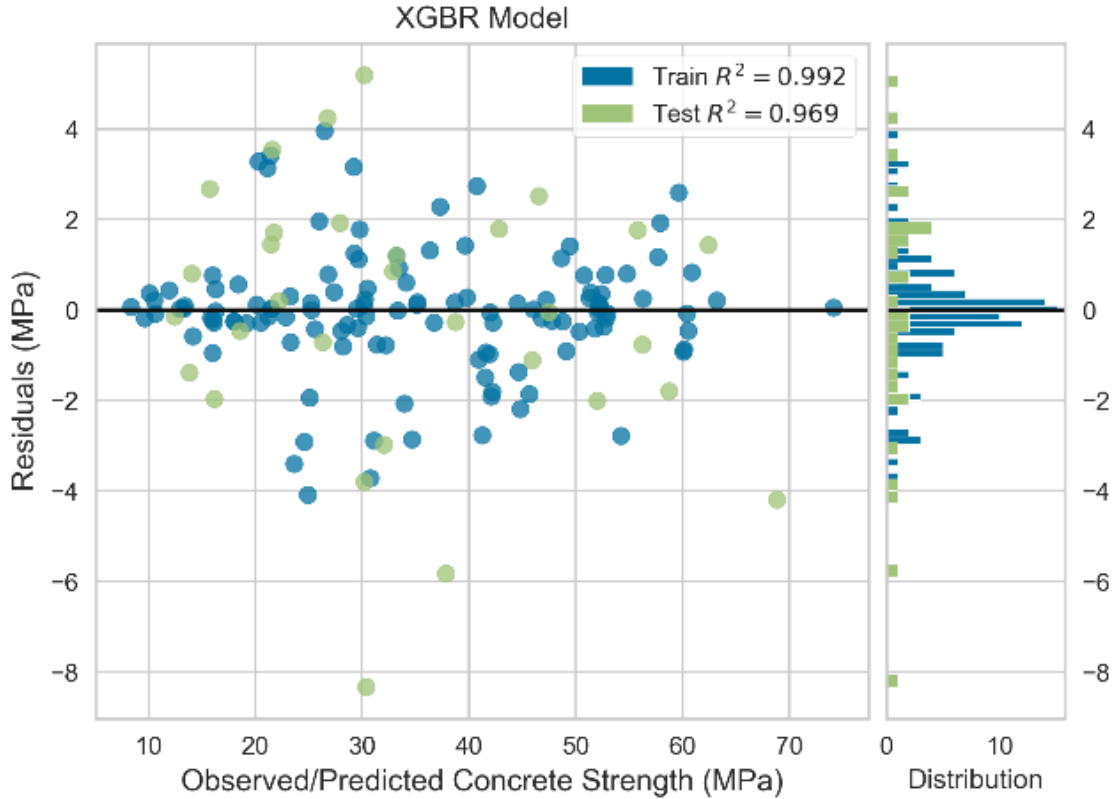


Figure 3-4: Residuals of the predicted output for training and testing data.

Table 3-4: Statistical error metrics obtained for employed ML models

Model	MSE (MPa)	RMSE (MPa)	nRMSE (%)	MAE (MPa)	nMAE (%)	R^2 - Value
RFR	15.904	3.988	11.608	3.065	8.924	0.939
ETR	11.377	3.373	9.818	2.595	7.556	0.957
GBR	5.853	2.419	7.042	1.752	5.100	0.977
XGBR	10.737	2.845	8.283	2.164	6.301	0.969

3.4.3 Feature importance of machine learning models

Feature importance identifies to what extent each feature affects the predictive performance of the model. In other words, it presents a score to indicate how valuable is each feature in the prediction of the output value. Generally, the feature importance in each model highly depends on the configuration of the dataset and the tuning of the hyper-parameters of the model. However, a well-tuned model can distinguish truly high importance features that are consistent with real-world findings. The values of feature importance along with standard deviation error bars for all the developed models are plotted in **Fig. 3-5**. Each

plotted feature importance value is the average of five feature importance values obtained by the execution of five random seeds for the data split. It can be observed that the fine aggregate content “FA” had great feature importance in all the developed models. Previous experimental studies demonstrated that the replacement of stiff fine aggregates by softer PCM microcapsules also alters the particle packing of the aggregates and the porosity and microstructure of the mortar and concrete (Aguayo *et al.*, 2016; Jayalath *et al.*, 2016; Pilehvar *et al.*, 2017), and consequently the compressive strength. Moreover, some studies suggest that the replacement of sand by PCM microcapsules improves the space filling properties of the mortar and thus, has a desirable effect on cement hydration, which needs more experimental investigations (Jayalath *et al.*, 2016). All models successfully distinguished the effect of fine aggregate on the compressive strength development in cementitious materials incorporating PCM microcapsules. Nevertheless, the RFR, ETR, and GBR models yielded higher feature importance values for “FA” compared to XGBR. Furthermore, not only did all the models capture the effect of the fine aggregate content, but also captured the significant effect of the PCM content on compressive strength, as shown in **Fig. 3-5**. This is in consistent with previous findings which showed that PCM inclusion significantly affects the compressive strength of cement mortars and concrete (Aguayo *et al.*, 2016; D'Alessandro *et al.*, 2018; Hunger *et al.*, 2009; Jayalath *et al.*, 2016; Pilehvar *et al.*, 2017). It is noted that among all models, GBR and XGBR had the highest and lowest feature importance for FA, 0.373 and 0.177, respectively. Nevertheless, all models yielded similar feature importance values for PCM within the range of 0.115 to 0.181. This indicates that all models captured the considerable influence of the PCM inclusion on the compressive strength of the cement mortar and concrete.

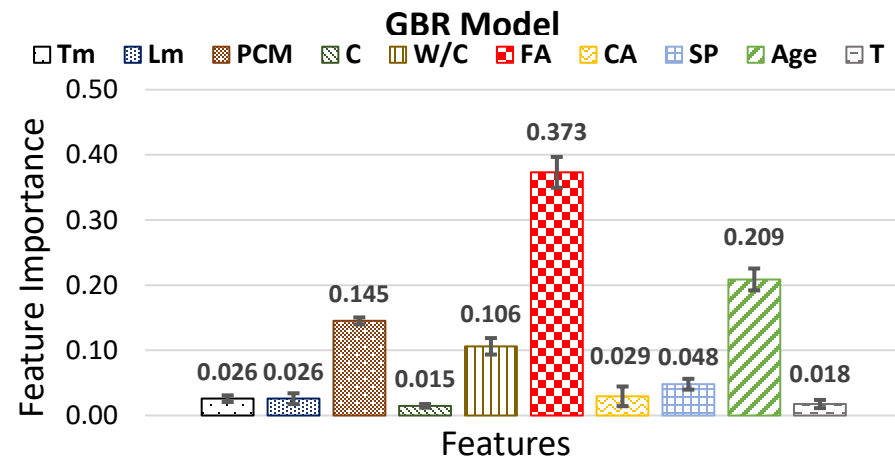
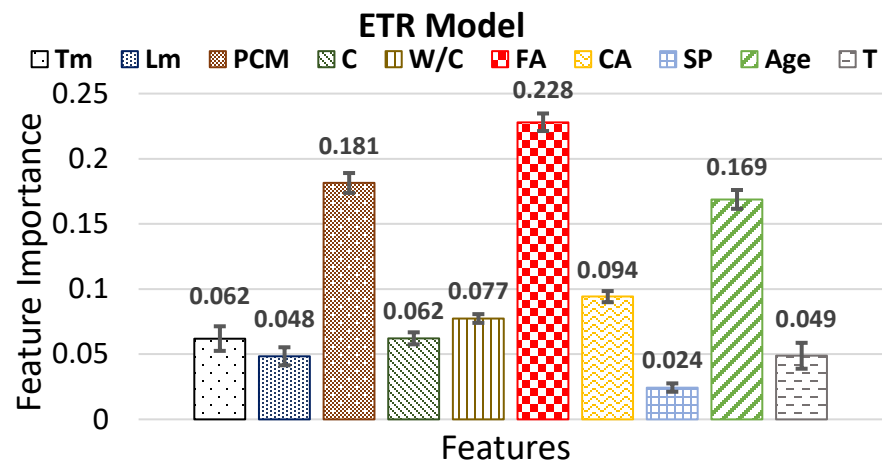
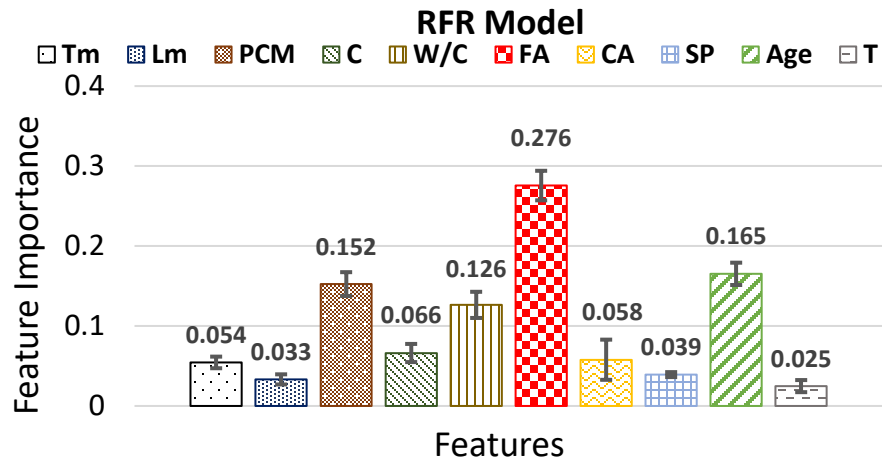
It can be observed in **Fig. 3-5** that the “Age” parameter, which represents the advancement of maturity of the specimen at the time of testing, greatly contributed to the compressive strength, which is expected and widely documented in practice. Furthermore, the addition of the PCM microcapsules to concrete caused a delay in the cement hydration process, and thus, delayed the development of compressive strength over time due to the latent heat capacity of the PCM (Jayalath *et al.*, 2016). Hence, considering the thermal properties of PCM microcapsule (*e.g.*, T_m , and L_m) and the age of specimen at the time of testing is of great importance in developing accurate ML models. This behavior was well captured by

all the developed models since the melting temperature and latent heat of the PCM microcapsules had a high value of feature importance (**Fig. 3-5**). Such high feature importance values suggest the need for a more comprehensive investigation into the effects of PCM inclusion on the maturity and cement hydration of concrete.

Conversely, some features such as “SP” which denotes the superplasticizer dosage did not significantly affect the model prediction. Another parameter with low feature importance in the proposed models was “T”, which is the curing temperature and the temperature of specimens at the testing time. By contrast, in one experimental study, it was found that the temperature of the specimen at the testing time and thus, the solid or liquid state of the PCM, can slightly affect the compressive strength of portland cement concrete due to the microcapsules becoming softer after PCM melting (Pilehvar *et al.*, 2017). As explained in **Section 3.3**, the chemical and physical conditions of the microcapsules were not considered in the data collection in this study. Therefore, the effect of the liquid or solid state of the PCM on the compressive strength was not captured. Moreover, this discrepancy is likely due to insufficient examples in the dataset having a wide range of values of the feature “T”. The obtained results from this study along with the previous experimental findings suggest that the addition of a combined feature such as $\frac{T_m}{T}$ to the dataset to account for the solid or liquid state of the PCM at the testing time may improve the performance of the models in larger datasets. Accordingly, more experimental work and data collection for this feature, as well as the chemical and physical properties of the microcapsules are required to extend the boundaries of the present study.

It can be concluded that in all proposed models, “FA”, “PCM”, and “Age” were the top three input features contributing to the compressive strength prediction. Although the ETR model suggested that the coarse aggregate content is the next input feature having high importance value, the other three models, *i.e.*, RFR, GBR, and XGBR proposed the water-to-cement ratio as the 4th high importance feature. Accordingly, it is highly recommended that the correlation between the aforementioned four input features should be considered in future research to better explore the strength development of PCM-integrated cementitious materials. Furthermore, the consideration of size distribution and particle packing of both PCM microcapsules and aggregates could be highly beneficial in

developing a robust and generalized model based on a larger dataset. Eventually, the thermal properties of PCMs along with the curing temperature of concrete specimens could significantly affect the maturity and cement hydration of concrete, and thus are advantageous in compressive strength prediction.



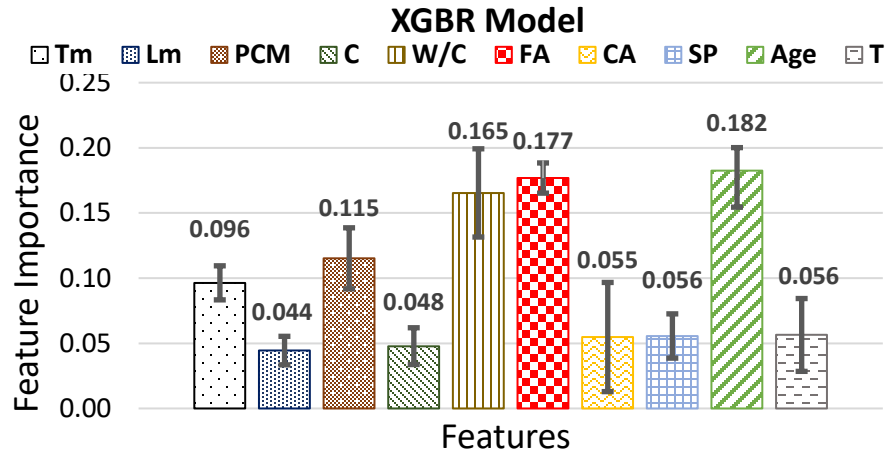


Figure 3-5: Feature importance analysis of the proposed models.

3.5 Conclusions and recommendations

The present study explores the machine learning prediction of the compressive strength of cementitious composites incorporating phase change material microcapsules. Four different machine learning regression algorithms including random forest, extra trees, gradient boosting, and extreme gradient boosting were tuned and applied to the largest experimental dataset that could be currently assembled from the open literature. The dataset had 154 data examples with 10 input features and one output (compressive strength). The following conclusions can be drawn:

- The developed machine learning models achieved superior accuracy in predicting the compressive strength of cementitious composites incorporating phase change materials with R^2 -values within the range of 0.93 to 0.97.
- The gradient boosting model demonstrated the highest accuracy having an R^2 -value of 0.977 along with RMSE and MAE values of 2.419 and 1.752, respectively.
- The feature importance analysis revealed that the proposed models captured the effect of each input feature on the compressive strength of the cementitious materials in consistence with experimental findings in the open literature.
- The fine aggregate and PCM microcapsules content had significant effect on the predicted compressive strength corroborating the significance of their difference in stiffness (since PCM is usually used as partial replacement for sand), along with the associated effect on particle packing density in the cementitious matrix.

- The age of specimen at the testing time as well as the thermal properties PCM including its melting temperature and latent heat capacity also had significant effects on the predicted output value. Taken together, these results suggest that the effect of PCM inclusion on the maturity of concrete and the development of compressive strength over time should be addressed in detailed experimental investigations.
- It appears that more comprehensive experimental studies and larger datasets are needed to better clarify the importance of different features and to get better insight into the key materials science aspects (e.g. chemical and physical properties of PCM microcapsules) that may be shadowed by the limited dataset.

The results indicate that exploiting powerful machine learning models to examine the harvested experimental data can provide insight into current knowledge gaps and the research required in the future to develop more comprehensive and accurate artificial intelligence based predictive tools.

3.6 References

- Aguayo, M., Das, S., Maroli, A., Kabay, N., Mertens, J. C., Rajan, S. D., Sant, G., Chawla, N., & Neithalath, N. (2016). The influence of microencapsulated phase change material (PCM) characteristics on the microstructure and strength of cementitious composites: Experiments and finite element simulations. *Cement and Concrete Composites*, 73, 29-41.
- Ahmad, M. W., Mourshed, M., & Rezgui, Y. (2018). Tree-based ensemble methods for predicting PV power generation and their comparison with support vector regression. *Energy*, 164, 465-474.
- Ahmad, M. W., Reynolds, J., & Rezgui, Y. (2018). Predictive modelling for solar thermal energy systems: A comparison of support vector regression, random forest, extra trees and regression trees. *Journal of Cleaner Production*, 203, 810-821.
- Al-Musawi, A. A., Alwanas, A. A., Salih, S. Q., Ali, Z. H., Tran, M. T., & Yaseen, Z. M. (2020). Shear strength of SFRCB without stirrups simulation: implementation of hybrid artificial intelligence model. *Engineering with Computers*, 36(1), 1-11.

Alshihri, M. M., Azmy, A. M., & El-Bisy, M. S. (2009). Neural networks for predicting compressive strength of structural light weight concrete. *Construction and Building Materials*, 23(6), 2214-2219.

Altun, F., Kişi, Ö., & Aydın, K. (2008). Predicting the compressive strength of steel fiber added lightweight concrete using neural network. *Computational Materials Science*, 42(2), 259-265.

Arora, A., Sant, G., & Neithalath, N. (2017). Numerical simulations to quantify the influence of phase change materials (PCMs) on the early-and later-age thermal response of concrete pavements. *Cement and Concrete Composites*, 81, 11-24.

Ashrafiyan, A., Shokri, F., Amiri, M. J. T., Yaseen, Z. M., & Rezaie-Balf, M. (2020). Compressive strength of Foamed Cellular Lightweight Concrete simulation: New development of hybrid artificial intelligence model. *Construction and Building Materials*, 230, 117048.

Bentz, D. P., & Turpin, R. (2007). Potential applications of phase change materials in concrete technology. *Cement and Concrete Composites*, 29(7), 527-532.

Bilim, C., Atiş, C. D., Tanyildizi, H., & Karahan, O. (2009). Predicting the compressive strength of ground granulated blast furnace slag concrete using artificial neural network. *Advances in Engineering Software*, 40(5), 334-340.

Bose, N. K., & Liang, P. (1996). *Neural Network Fundamentals with Graphs, Algorithms, and Applications* (McGraw-Hill Series in Electrical Computer Engineering).

Breiman, L. (1996). Bagging predictors. *Machine learning*, 24(2), 123-140.

Breiman, L. (2017). *Classification and regression trees*. Routledge.

Breiman, L., Friedman, J., Olshen, R., & Stone, C. (1984). *Classification and regression trees—crc press*. Boca Raton, Florida.

Chakraborty, D., & Elzarka, H. (2019a). Advanced machine learning techniques for building performance simulation: a comparative analysis. *Journal of Building Performance Simulation*, 12(2), 193-207.

Chakraborty, D., & Elzarka, H. (2019b). Early detection of faults in HVAC systems using an XGBoost model with a dynamic threshold. *Energy and Buildings*, 185, 326-344.

Chandwani, V., Agrawal, V., & Nagar, R. (2015). Modeling slump of ready mix concrete using genetic algorithms assisted training of Artificial Neural Networks. *Expert Systems with Applications*, 42(2), 885-893.

Chang, Y.-C., Chang, K.-H., & Wu, G.-J. (2018). Application of eXtreme gradient boosting trees in the construction of credit risk assessment models for financial institutions. *Applied Soft Computing*, 73, 914-920.

Chen, T., & Guestrin, C. (2016). Xgboost: A scalable tree boosting system. *Proceedings of the 22nd acm sigkdd international conference on knowledge discovery and data mining*,

Chopra, P., Sharma, R. K., Kumar, M., & Chopra, T. (2018). Comparison of machine learning techniques for the prediction of compressive strength of concrete. *Advances in Civil Engineering*, 2018.

Chou, J.-S., Chiu, C.-K., Farfoura, M., & Al-Taharwa, I. (2010). Optimizing the prediction accuracy of concrete compressive strength based on a comparison of data-mining techniques. *Journal of Computing in Civil Engineering*, 25(3), 242-253.

Chou, J.-S., & Tsai, C.-F. (2012). Concrete compressive strength analysis using a combined classification and regression technique. *Automation in Construction*, 24, 52-60.

Chou, J.-S., Tsai, C.-F., Pham, A.-D., & Lu, Y.-H. (2014). Machine learning in concrete strength simulations: Multi-nation data analytics. *Construction and Building Materials*, 73, 771-780.

Cieslak, D. A., & Chawla, N. V. (2008). Learning decision trees for unbalanced data. *Joint European Conference on Machine Learning and Knowledge Discovery in Databases*,

D'Alessandro, A., Pisello, A. L., Fabiani, C., Ubertini, F., Cabeza, L. F., & Cotana, F. (2018). Multifunctional smart concretes with novel phase change materials: Mechanical and thermo-energy investigation. *Applied Energy*, 212, 1448-1461.

De Gracia, A., & Cabeza, L. F. (2015). Phase change materials and thermal energy storage for buildings. *Energy and Buildings*, 103, 414-419.

Dehdezi, P. K., Hall, M. R., Dawson, A. R., & Casey, S. P. (2013). Thermal, mechanical and microstructural analysis of concrete containing microencapsulated phase change materials. *International Journal of Pavement Engineering*, 14(5), 449-462.

Deng, F., He, Y., Zhou, S., Yu, Y., Cheng, H., & Wu, X. (2018). Compressive strength prediction of recycled concrete based on deep learning. *Construction and Building Materials*, 175, 562-569.

Erdal, H. I. (2013). Two-level and hybrid ensembles of decision trees for high performance concrete compressive strength prediction. *Engineering Applications of Artificial Intelligence*, 26(7), 1689-1697.

Fan, J., Wang, X., Wu, L., Zhou, H., Zhang, F., Yu, X., Lu, X., & Xiang, Y. (2018). Comparison of Support Vector Machine and Extreme Gradient Boosting for predicting daily global solar radiation using temperature and precipitation in humid subtropical climates: A case study in China. *Energy conversion and management*, 164, 102-111.

Fernandes, F., Manari, S., Aguayo, M., Santos, K., Oey, T., Wei, Z., Falzone, G., Neithalath, N., & Sant, G. (2014). On the feasibility of using phase change materials (PCMs) to mitigate thermal cracking in cementitious materials. *Cement and Concrete Composites*, 51, 14-26.

Fisher, A., Rudin, C., & Dominici, F. (2018). Model Class Reliance: Variable importance measures for any machine learning model class, from the "Rashomon" perspective. arXiv preprint arXiv:1801.01489.

Geurts, P., Ernst, D., & Wehenkel, L. (2006). Extremely randomized trees. *Machine learning*, 63(1), 3-42.

- Gong, H., Sun, Y., Shu, X., & Huang, B. (2018). Use of random forests regression for predicting IRI of asphalt pavements. *Construction and Building Materials*, 189, 890-897.
- Guelman, L. (2012). Gradient boosting trees for auto insurance loss cost modeling and prediction. *Expert Systems with Applications*, 39(3), 3659-3667.
- Hunger, M., Entrop, A. G., Mandilaras, I., Brouwers, H., & Founti, M. (2009). The behavior of self-compacting concrete containing micro-encapsulated phase change materials. *Cement and Concrete Composites*, 31(10), 731-743.
- Jayalath, A., San Nicolas, R., Sofi, M., Shanks, R., Ngo, T., Aye, L., & Mendis, P. (2016). Properties of cementitious mortar and concrete containing micro-encapsulated phase change materials. *Construction and Building Materials*, 120, 408-417.
- John, V., Liu, Z., Guo, C., Mita, S., & Kidono, K. (2015). Real-time lane estimation using deep features and extra trees regression. *Pacific-Rim Symposium on Image and Video Technology*,
- Keshtegar, B., Bagheri, M., & Yaseen, Z. M. (2019). Shear strength of steel fiber-unconfined reinforced concrete beam simulation: Application of novel intelligent model. *Composite Structures*, 212, 230-242.
- Khademi, F., Akbari, M., Jamal, S. M., & Nikoo, M. (2017). Multiple linear regression, artificial neural network, and fuzzy logic prediction of 28 days compressive strength of concrete. *Frontiers of Structural and Civil Engineering*, 11(1), 90-99.
- Lecompte, T., Le Bideau, P., Glouannec, P., Nortershauser, D., & Le Masson, S. (2015). Mechanical and thermo-physical behaviour of concretes and mortars containing phase change material. *Energy and Buildings*, 94, 52-60.
- Li, Y., Zou, C., Berecibar, M., Nanini-Maury, E., Chan, J. C.-W., van den Bossche, P., Van Mierlo, J., & Omar, N. (2018). Random forest regression for online capacity estimation of lithium-ion batteries. *Applied Energy*, 232, 197-210.

- Ling, T.-C., & Poon, C.-S. (2013). Use of phase change materials for thermal energy storage in concrete: an overview. *Construction and Building Materials*, 46, 55-62.
- Liu, F., Wang, J., & Qian, X. (2017). Integrating phase change materials into concrete through microencapsulation using cenospheres. *Cement and Concrete Composites*, 80, 317-325.
- Ma, J., & Cheng, J. C. (2016). Identifying the influential features on the regional energy use intensity of residential buildings based on Random Forests. *Applied Energy*, 183, 193-201.
- Marani, A., & Nehdi, M. L. (2019). Integrating phase change materials in construction materials: Critical review. *Construction and Building Materials*, 217, 36-49.
- Mason, L., Baxter, J., Bartlett, P., & Frean, M. (1999). Boosting algorithms as gradient descent in function space (Technical Report). RSISE, Australian National University.
- Meshgin, P., & Xi, Y. (2012). Effect of Phase-Change Materials on Properties of Concrete. *ACI Materials Journal*, 109(1).
- Nehdi, M., El Chabib, H., & El Naggar, M. H. (2001). Predicting performance of self-compacting concrete mixtures using artificial neural networks. *Materials Journal*, 98(5), 394-401.
- Ni, H.-G., & Wang, J.-Z. (2000). Prediction of compressive strength of concrete by neural networks. *Cement and Concrete Research*, 30(8), 1245-1250.
- Pan, Y., Chen, S., Qiao, F., Ukkusuri, S. V., & Tang, K. (2019). Estimation of real-driving emissions for buses fueled with liquefied natural gas based on gradient boosted regression trees. *Science of The Total Environment*, 660, 741-750.
- Pedregosa, F., Varoquaux, G., Gramfort, A., Michel, V., Thirion, B., Grisel, O., Blondel, M., Prettenhofer, P., Weiss, R., & Dubourg, V. (2011). Scikit-learn: Machine learning in Python. *Journal of machine learning research*, 12(Oct), 2825-2830.

Pei, H., Li, Z., & Li, Y. (2016). Early-age shrinkage and temperature optimization for cement paste by using PCM and MgO based on FBG sensing technique. *Construction and Building Materials*, 117, 58-62.

Persson, C., Bacher, P., Shiga, T., & Madsen, H. (2017). Multi-site solar power forecasting using gradient boosted regression trees. *Solar Energy*, 150, 423-436.

Pilehvar, S., Cao, V. D., Szczotok, A. M., Valentini, L., Salvioni, D., Magistri, M., Pamies, R., & Kjøniksen, A.-L. (2017). Mechanical properties and microscale changes of geopolymer concrete and Portland cement concrete containing micro-encapsulated phase change materials. *Cement and Concrete Research*, 100, 341-349.

Pilehvar, S., Szczotok, A. M., Rodríguez, J. F., Valentini, L., Lanzón, M., Pamies, R., & Kjøniksen, A.-L. (2019). Effect of freeze-thaw cycles on the mechanical behavior of geopolymer concrete and Portland cement concrete containing micro-encapsulated phase change materials. *Construction and Building Materials*, 200, 94-103.

Ramadan Suleiman, A., & Nehdi, M. L. (2017). Modeling Self-Healing of Concrete Using Hybrid Genetic Algorithm–Artificial Neural Network. *Materials*, 10(2), 135.

Rao, V. V., Parameshwaran, R., & Ram, V. V. (2018). PCM-mortar based construction materials for energy efficient buildings: A review on research trends. *Energy and Buildings*, 158, 95-122.

Rodriguez-Galiano, V., Sanchez-Castillo, M., Chica-Olmo, M., & Chica-Rivas, M. (2015). Machine learning predictive models for mineral prospectivity: An evaluation of neural networks, random forest, regression trees and support vector machines. *Ore Geology Reviews*, 71, 804-818.

Saridakis, K. M., & Dentsoras, A. J. (2008). Soft computing in engineering design—A review. *Advanced Engineering Informatics*, 22(2), 202-221.

Šavija, B., & Schlangen, E. (2016). Use of phase change materials (PCMs) to mitigate early age thermal cracking in concrete: Theoretical considerations. *Construction and Building Materials*, 126, 332-344.

Sharifi, N. P., & Sakulich, A. (2015). Application of phase change materials to improve the thermal performance of cementitious material. *Energy and Buildings*, 103, 83-95.

Snell, L. M., Van Roekel, J., & Wallace, N. D. (1989). Predicting early concrete strength. *Concrete International*, 11(12), 43-47.

Snoeck, D., Priem, B., Dubruel, P., & De Belie, N. (2016). Encapsulated Phase-Change Materials as additives in cementitious materials to promote thermal comfort in concrete constructions. *Materials and Structures*, 49(1-2), 225-239.

Topcu, I. B., & Saridemir, M. (2008). Prediction of compressive strength of concrete containing fly ash using artificial neural networks and fuzzy logic. *Computational Materials Science*, 41(3), 305-311.

Torres-Barrán, A., Alonso, Á., & Dorronsoro, J. R. (2019). Regression tree ensembles for wind energy and solar radiation prediction. *Neurocomputing*, 326, 151-160.

Xu, B., & Li, Z. (2013). Paraffin/diatomite composite phase change material incorporated cement-based composite for thermal energy storage. *Applied Energy*, 105, 229-237.

Yaseen, Z. M., Afan, H. A., & Tran, M.-T. (2018). Beam-column joint shear prediction using hybridized deep learning neural network with genetic algorithm. *IOP conference series: earth and environmental science*,

Yaseen, Z. M., Deo, R. C., Hilal, A., Abd, A. M., Bueno, L. C., Salcedo-Sanz, S., & Nehdi, M. L. (2018). Predicting compressive strength of lightweight foamed concrete using extreme learning machine model. *Advances in Engineering Software*, 115, 112-125.

Yaseen, Z. M., Keshtegar, B., Hwang, H.-J., & Nehdi, M. L. (2019). Predicting reinforcing bar development length using polynomial chaos expansions. *Engineering Structures*, 195, 524-535.

Yaseen, Z. M., Tran, M. T., Kim, S., Bakhshpoori, T., & Deo, R. C. (2018). Shear strength prediction of steel fiber reinforced concrete beam using hybrid intelligence models: a new approach. *Engineering Structures*, 177, 244-255.

Young, B. A., Hall, A., Pilon, L., Gupta, P., & Sant, G. (2019). Can the compressive strength of concrete be estimated from knowledge of the mixture proportions?: New insights from statistical analysis and machine learning methods. *Cement and Concrete Research*, 115, 379-388.

Zahedi, P., Parvande, S., Asgharpour, A., McLaury, B. S., Shirazi, S. A., & McKinney, B. A. (2018). Random forest regression prediction of solid particle Erosion in elbows. *Powder Technology*, 338, 983-992.

Zhang, J., Ma, G., Huang, Y., Aslani, F., & Nener, B. (2019). Modelling uniaxial compressive strength of lightweight self-compacting concrete using random forest regression. *Construction and Building Materials*, 210, 713-719.

Zhang, M., Li, M., Shen, Y., Ren, Q., & Zhang, J. (2019). Multiple mechanical properties prediction of hydraulic concrete in the form of combined damming by experimental data mining. *Construction and Building Materials*, 207, 661-671.

Zhang, Y., & Ling, C. (2018). A strategy to apply machine learning to small datasets in materials science. *Npj Computational Materials*, 4(1), 1-8.

Chapter 4

4 Mixture Design of Concrete Incorporating Microencapsulated Phase Change Materials for Clean Energy: A Ternary Machine Learning Approach¹

Inclusion of microencapsulated phase change materials (MPCM) in construction materials is a very promising solution for increasing the energy efficiency of buildings and reducing their carbon emissions. Although MPCMs provide thermal energy storage capability in concrete, they typically decrease its compressive strength. A unified framework for mixture design and optimization of concrete incorporating MPCM is yet to be developed to facilitate practical applications. This study proposes an optimized mixture design approach for concrete incorporating MPCM using a ternary machine learning (ML) framework. For this purpose, a state-of-the-art tabular generative adversarial network (TGAN) was adopted to produce multitudinous synthesized mixture design data based on available experimental mixture examples. The generated data is then employed to construct robust ML predictive models. The best-developed model, which achieved a testing R^2 of 0.963 and MAE of 2.085 MPa, was coupled with a particle swarm optimization (PSO) algorithm to construct a powerful recommendation system for optimizing the mixture design of concrete and mortar incorporating different types of MPCM. Extensive parametric analyses along with the employed optimization procedure accomplished the mixture design of green concrete with maximum MPCM inclusion and minimum cement content for various compressive strength classes. The proposed framework enables clean energy technology in the design of eco-friendly building materials.

4.1 Introduction

Energy consumption of buildings has been recognized as a major environmental concern in recent years. Extensive research has been devoted to recommending solutions for increasing the energy efficiency of the built environment (Chwieduk, 2003). Thermal

¹ A version of this chapter is to be submitted to “*Engineering with Computers*” journal, 2022.

energy storage (TES) systems have emerged as a promising solution to achieve energy-efficient buildings with less carbon footprint. One method to provide TES is by incorporating phase change materials (PCMs) into building components such as walls and roofs (Memon, 2014). PCMs can absorb/retrieve a great deal of thermal energy upon their phase change transition. Accordingly, temperature fluctuations in buildings are significantly hampered and the energy consumption of buildings is significantly decreased (Marani & Madhkhan, 2021). Therefore, the integration of PCMs into building components promotes sustainability of the built environment and leverages clean technology in the construction industry (Qiu *et al.*, 2020).

Since concrete is the world's most consumed construction material, there has been great interest in incorporating PCM in concrete members. Substantial research has explored various techniques to integrate PCM into cementitious materials including PCM microcapsules, porous lightweight aggregates, and shape stabilized PCMs (SSPCMs) (Marani & Nehdi, 2019). Among all proposed methods, the incorporation of microencapsulated PCM (MPCM) has been the most predominant technique owing to its convenient usage and commercial availability. MPCMs are mostly produced in powder form with desirable size and morphological properties. Hence, they can be readily integrated into cementitious mortar/concrete as a partial replacement for fine aggregates (Drissi *et al.*, 2019).

Although the inclusion of MPCM increases the thermal inertia of concrete and provides TES capability, it considerably decreases its mechanical properties (Balapour *et al.*, 2021). Several research studies have posited explanations for the reduction of compressive strength of PCM-integrated cementitious materials as discussed in Chapters 2 and 3. Despite the extensive pertinent research, a robust framework for optimum design of MPCM-integrated concrete is yet to be developed. Therefore, this study aims at introducing a practical design framework for optimized mixture design of concrete incorporating MPCM using state-of-the-art computational intelligence methods, along with extensive data extracted from research studies and commercial MPCM manufacturers. First, a compendious literature review is presented below to identify the knowledge gap in the

design of MPCM-integrated concrete. Thereafter, the proposed methodology is explained, and the outcomes are rigorously scrutinized.

4.2 Overview of state-of-the-art

This section synthesizes concise knowledge from major findings of pertinent research in the open literature and highlights fundamental explanations regarding the interaction between MPCM and the main components of concrete. The fundamentals of the applied methodology, along with the research significance of the current study are also outlined.

4.2.1 Knowledge background

Several types of MPCM with a broad range of thermophysical properties, melting/freezing temperature points, melting/freezing enthalpies, and densities have been incorporated into cement mortar and concrete. All studies reported that the inclusion of MPCM reduced the compressive strength regardless of the thermophysical properties. Nonetheless, explanations postulated for the reduction in compressive strength are not consistent.

According to several studies in the literature, the porosity induced due to MPCM addition, low stiffness of MPCM, breakage of the MPCM shell, and the interference of MPCM with the cement hydration process are the most proposed mechanisms for compressive strength reduction of concrete made with MPCM inclusion. Hunger *et al.* (Hunger *et al.*, 2009) used Micronal DS 5008X in self-compacting concrete and evidenced a significant reduction in compressive strength with increased MPCM dosage. They reported that the destruction of the MPCM shell is the source of the reduction in compressive strength and thus, stronger shells need to be fabricated to withstand both the alkaline environment of concrete and the induced mechanical stress during the mixing of concrete ingredients. Nevertheless, Jayalath *et al.* (Jayalath *et al.*, 2016) refuted the breakage of the MPCM shell during mixing. They used Micronal DS 5040X, which has a significantly lower density compared to that of Micronal DS 5008X.

On the other hand, the increased porosity of cement paste upon MPCM addition has been repeatedly advocated as a major explanation for the decrease in compressive strength. Several researchers evidenced that MPCMs act like air voids and increase the pore diameter

of the cementitious matrix. Pilehvar *et al.* (Pilehvar *et al.*, 2017) studied the inclusion of a type of MPCM fabricated by a spray-drying technique on the compressive strength of portland cement and geopolymer concretes. In addition to the lower stiffness of MPCM compared to sand particles, induced voids and air bubbles were identified as a major reason for mechanical strength reduction. SEM images and X-ray micro-tomography revealed gaps between PCM microcapsules and the cementitious matrix, along with a weak connection between MPCM and the surrounding cement paste, which are caused by the agglomeration of MPCM and poor compatibility of MPCM shells and the matrix. Similar findings were reported in studies conducted by Sanfelix *et al.* (Sanfelix *et al.*, 2020) and Djamai *et al.* (Djamai *et al.*, 2019), which emphasized the weak interface of MPCM and cement matrix and MPCM acting like air voids as potential reasons for strength reduction. Given this analogy, the Bolomey equation has been proposed in two separate studies to estimate the compressive strength of MPCM integrated concrete as follows (Lecompte *et al.*, 2015):

$$f_c = K_B \times \sigma_c \left[\frac{c}{W+W_v+W_{MPCM}} - 0.5 \right] \quad \text{Eq. 4-1}$$

Where f_c is the estimated compressive strength (MPa), K_B is a constant depending on the used aggregates, σ_c is the strength of the cement (MPa), W is the mass of water, W_v is the mass of water corresponding to the volume of the entrapped air voids, and W_{MPCM} is the mass of water equivalent to the volume of the used MPCMs. The compressive strength predicted by the Bolomey equation is highly correlated to the experimental values in the studies of Sanfelix *et al.* (Sanfelix *et al.*, 2020) and Lecompte *et al.* (Lecompte *et al.*, 2015), albeit no study in the open literature has so far evaluated the accuracy of this equation using a large and comprehensive dataset. Overall, the findings from the literature suggest that the prediction of the compressive strength of MPCM-integrated composites is an intricate task, indicating that concerted research effort and advanced modeling tools are needed to better quantify the effects of MPCM inclusion on the compressive strength of concrete.

4.2.2 Machine learning modeling

The compressive strength, favorably benchmarked at the age of 28 days, is the most widely accepted characteristic of the engineering properties of concrete. Not only is compressive

strength an essential structural design parameter but is also widely documented to be proportional to the tensile and flexural strengths of concrete. In normal concrete, the water-to-cement (W/C) ratio is the most correlated parameter to the compressive strength. Yet, different strengths for a given W/C can be obtained due to the effect of other parameters such as the dosage of the other mixture components, physical properties of ingredients, and curing conditions (Young *et al.*, 2019). This is magnified in the case of novel concretes having unique mixture compositions. Furthermore, the stochastic nature of concrete mixing, manpower intervention, and quality control of concrete further affect the resulting compressive strength. Therefore, developing powerful predictive frameworks to model various properties of concrete such as compressive strength can help establish high-throughput mixture optimization (Zhang, Huang, Aslani, *et al.*, 2020).

Several complexities involved in the design of concrete mixtures hinder the accuracy and predictive performance of physical models. Such complexities include the intricacy of modeling cement hydration and the associated microstructure development, time and temperature-dependent nonlinear behavior of cement paste, and the variability and insufficient data regarding the physical, mechanical, and chemical properties of the mixture components. Nevertheless, machine learning (ML) models have demonstrated promising ability to simulate different engineering characteristics of concrete. There have been multiple studies in the recent literature that aspire to propose ML models capable of rigorously modeling the mechanical and durability properties of conventional and modern concretes. Artificial neural networks (AANs) and ensemble models are among the most utilized ML algorithms, having superior predictive performance (Asteris *et al.*, 2021). Additionally, deep learning (DL) models have also been implemented as a promising technique for modeling concrete characteristics and the condition assessment of concrete structures.

Although data-driven modeling methods are accurate and computationally inexpensive, their limitations must be considered to achieve reliable predictive systems with generalized capabilities. The limited number of available data examples for training ML models is one of the major hurdles associated with material science problems, as evidenced in the literature (Zhang & Ling, 2018). Notwithstanding the multiple research studies on ML

modeling of concrete, a dearth of research attempted to address and rectify this obstacle. Young *et al.* (Young *et al.*, 2019) used 10,000 industrial observations of the compressive strength of concrete along with mixture components to compensate for the limited laboratory data. However, there is an utter lack of industrial data on novel concretes. Therefore, the limited number of laboratory data from research studies is the only reliable source for developing predictive models and recommendation systems. In Chapter 3, 154 laboratory mixture examples were extracted from the open literature to estimate the compressive strength of MPCM-integrated cementitious composites. Although the models achieved promising accuracy using ensemble models, the low number of data examples was recognized as a considerable limitation to be addressed in future work.

Meanwhile, the lack of adequate reliable data has been a common problem in diverse areas of artificial intelligence computation. Data augmentation for enhancing the performance of ML models trained on imbalanced datasets or datasets with missing values has attracted vast attention (Antoniou *et al.*, 2017). Furthermore, generative adversarial networks (GAN) has recently emerged as the state-of-the-art technique to generate synthesized image data that resemble real images (Goodfellow *et al.*, 2014). Thereafter, multiple versions of GAN were developed to carry out different ML tasks. Conditional GAN (CGAN) (Mirza & Osindero, 2014), Wasserstein GAN (WGAN) (Arjovsky *et al.*, 2017), and Tabular GAN (TGAN) (Xu & Veeramachaneni, 2018) are examples of such GAN variants. Among these, TGAN was proposed to generate synthesized data having a tabular structure both with continuous and discrete variables. Such types of datasets incorporate a wide range of applications including medical or educational records, material science problems, energy consumption forecasting, etc.

4.3 Methodology

The current study proposes a multi-step data-driven ternary methodology to investigate the effect of MPCM inclusion on the compressive strength of cement mortar and concrete. For this purpose, a comprehensive experimental dataset was first collected from laboratory results reported in the open literature. A smaller dataset was previously developed in Chapter 3 (Marani & Nehdi, 2020). That dataset was further expanded to include recently published data along with some physical properties of the MPCM as model input features.

Considering the limitations of the available experimental data, a state-of-the-art data augmentation technique was employed to compile a large number of synthetic data points for training paramount ML models. Thereafter, the functional ML systems developed herein were used to perform compendious parametric analysis for investigating the effects of MPCM addition on the compressive strength of concrete. Moreover, an empirical model based on a modified version of the Bolomey equation was optimized using the numerous synthesized data to estimate the compressive strength of MPCM-integrated concrete. Ultimately, a mixture optimization for cement mortar and concrete incorporating MPCMs was performed using the best developed ML model coupled with a metaheuristic algorithm. The proposed mixtures were further validated through new laboratory testing. **Figure 4-1** illustrates the scheme of the applied ternary ML model in the present study. The subsections below elaborate on the fundamentals of each aforementioned step.

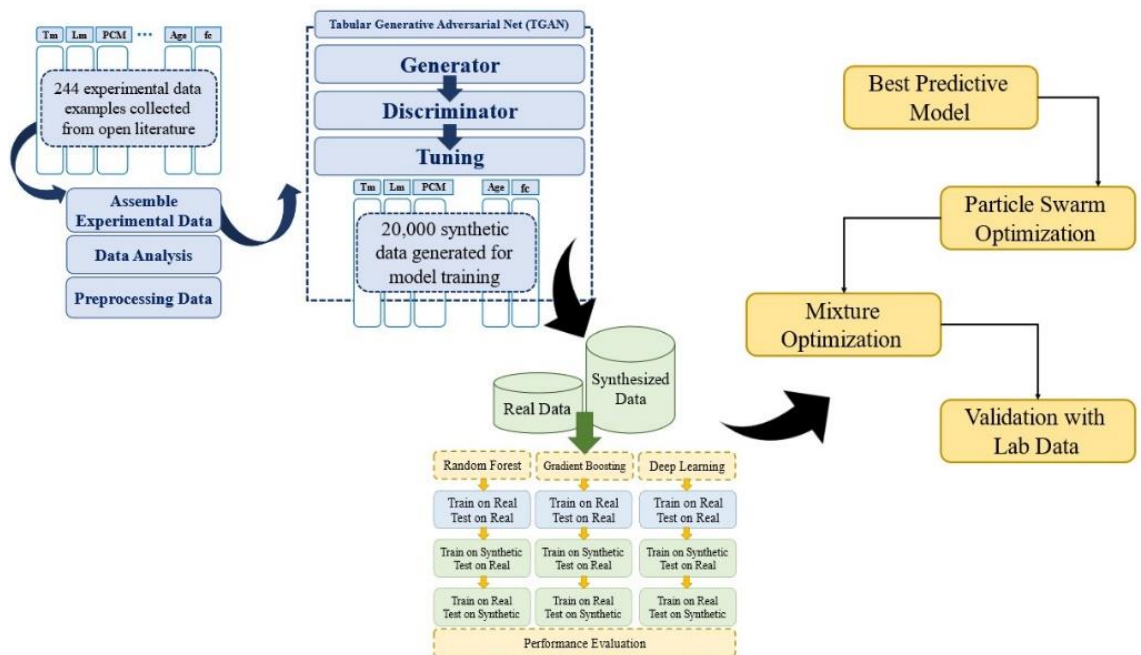


Figure 4-1: Proposed ternary framework for mixture optimization of MPCM-integrated concrete. TGAN is used to generate synthetic data for training ML models. The models are then fed into the optimization algorithm to find optimum mixtures.

4.3.1 Experimental data collection and analysis

The developed dataset in this study updates and extends a previous dataset collected in Chapter 3. Their original dataset included 154 mixture design examples with 10 input features. The new dataset incorporates additional mixture examples from recently published studies, along with key physical properties of MPCM as new model input features. After preprocessing and performing baseline models on this dataset, the final dataset consisting of 244 observations with 12 input features was deployed for modeling and analysis purposes. **Table 4-1** lists the sources of the data points. The compressive strength of each mixture is the only output included in this dataset. According to the findings of Chapter 3, the fine aggregate and MPCM contents exert a significant effect on the compressive strength predictions of ML models, which is also evidenced in several experimental studies. Since fine aggregates are partially replaced by MPCM in the mixture design, the density of MPCM particles is also of great significance. Therefore, the density of MPCM was appended to the dataset in the current study. **Table 4-2** presents the input features of the dataset.

Table 4-1: Sources of collected data points

Data index	Number of data	Ref.	Data indexes	Number of data	Ref.
1-16	17	(Pilehvar <i>et al.</i> , 2017)	131-134	4	(M Hunger <i>et al.</i> , 2009)
17-22	6	(Liu <i>et al.</i> , 2017)	135-154	20	(Meshgin & Xi, 2012)
23-62	40	(Aguayo <i>et al.</i> , 2016)	155-178	24	(Pilehvar <i>et al.</i> , 2020)
63-86	23	(Jayalath <i>et al.</i> , 2016)	179-202	24	(Yang <i>et al.</i> , 2016)
87-91	5	(Dehdezi <i>et al.</i> , 2013)	203-206	4	(Djamai <i>et al.</i> , 2019)
92-95	4	(D'Alessandro <i>et al.</i> , 2018)	207-214	8	(Cunha <i>et al.</i> , 2015)
96-118	23	(Snoeck <i>et al.</i> , 2016)	215-226	12	(Cunha <i>et al.</i> , 2016)
119-130	12	(Lecompte <i>et al.</i> , 2015)	227-244	18	(Fenollera <i>et al.</i> , 2013)

Table 4-2: Input features of dataset prepared for this study

No.	Attribute	Unit	Subscript	No.	Attribute	Unit	Subscript
1	Melting temperature	°C	T_m	7	Water	kg/m ³	W
2	Latent heat	J/kg	L_m	8	Fine aggregate	kg/m ³	FA
3	PCM dosage	kg/m ³	PCM	9	Coarse aggregate	kg/m ³	CA
4	PCM density	kg/m ³	PCM_D	10	Superplasticizer	kg/m ³	SP
5	Cement type	-	C_type	11	Age	days	Age
6	Cement	kg/m ³	C	12	Curing temperature	°C	T

4.3.2 Model development

A major hurdle often facing ML modeling for material science problems is the limited number of available experimental data examples, which are often costly and time-consuming to acquire. On the other hand, providing comprehensive data that encompass the underlying features of the problem is essential when training advanced ML models. Hence, for training ML models in the present study, a novel framework for generating credible mixture proportion data of MPCM-integrated mortar and concrete using a state-of-the-art data generating technique is proposed. For this purpose, tabular generative adversarial networks (TGAN) model is implemented to generate thousands of plausible data examples based on the collected experimental dataset. The synthesized data are further used for multiple tasks such as training paramount ML models, performing parametric analysis, developing empirical models, and mixture optimization. In addition to TGAN, three regression models including gradient boosting regressor (GBR), random forest regressor (RFR), and deep neural network (DNN) are developed herein.

Generating credible synthesized data can be superior to using experimental data alone. Firstly, training ML models with large reliable data enhances the accuracy and generalization capability of the models. Secondly, the models can be tested using the entire experimental data, as opposed to conventional ML modeling in which only 20-30% of the available data is randomly used for testing the model performance, while the majority of the data is used in the model training. Furthermore, reliable models trained with synthesized data can be employed to thoroughly investigate the behavior of concrete with MPCM inclusion considering various design scenarios. Ultimately, it becomes feasible to optimize the mixture design of concrete based on the developed predictive models. In the present study, after validating the quality of the synthesized data using various statistical

tests, mixture optimization of cement mortar and concrete incorporating two different types of commercial MPCM was carried out using the particle swarm optimization (PSO) technique. **Figure 4-1** depicts the overall methodology applied herein. The utilized methods are further described below.

4.3.2.1 Tabular generative adversarial networks (TGAN)

Goodfellow *et al.* (Goodfellow *et al.*, 2014) introduced generative adversarial networks (GANs) for generating “fake images” that resemble given original pictures. GANs discover the patterns in a training dataset and produce plausible data with similar characteristics. After demonstrating the promising capability of GAN, multiple studies have been carried out to improve its functionality by further stabilizing the training process. Generally, a GAN model is comprised of two competing networks called generator (G) and discriminator (D). The task of the generator network is to capture the distribution of the given data for generating synthetic data, while the discriminator is assigned to predict whether the generator’s output is real or fake. Both networks compete in a min-max game in which the generator attempts to fool the discriminator into considering that the synthesized data are real. The discriminator, on the other hand, tries to recognize the fake samples created by the generator. The generator is fed with random input to create fake data, as shown in **Fig. 4-2**. The fake and real data are the inputs for the discriminator to forecast whether they are real or synthesized.

The min-max game with the value function can be expressed as follows:

$$\min_G \max_D V(D, G) = \mathbb{E}_{x \sim p_{\text{data}}(x)} [\log D(x)] + \mathbb{E}_{z \sim p_z(z)} [\log (1 - D(G(z)))] \quad \text{Eq. 4-2}$$

where G and D are the generator and discriminator, x is the real data sampled from $p_{\text{data}}(x)$, and z is the noise (random input) drawn from $p_z(z)$. Early GAN models experienced problems, such as convergence failure, mode collapse, and vanishing gradients upon training. Several versions of GAN have therefore been developed to either mitigate those problems or to fulfill specific tasks. Among the recently developed versions, TGAN was proposed by Xu and Veeramachaneni (Xu & Veeramachaneni, 2018) to generate

TGAN can capture the pattern of the tabular data containing numerical and categorical variables. Therefore, it can generate credible data for training robust models in materials science applications where deficient experimental data hinders developing generalized comprehensive models. The TGAN library in Python, which has demonstrated promising performance in generating synthetic tabular data based on well-known datasets in the open literature, was used for model development (Xu & Veeramachaneni, 2018). TGAN has several parameters and hyperparameters that impact the convergence of the model and the quality of the generated data. A random search optimization was conducted to obtain the tuned parameters and hyperparameters. For this purpose, a baseline GBR model, which was tuned and trained with the real data, was used to evaluate the quality of the generated data for each random search trial.

4.3.2.2 Tree-based ensembles

Classification and regression tree (CART) is a non-parametric ML model which has been widely used for regression and classification purposes. The rationale behind CART is to divide intricate forecasting tasks into decision-making trees with less complexity. This objective is achieved by deriving meaningful relationships and patterns within the input data (Breiman, 2017). The prediction accuracy of the CART algorithm can be further improved through ensemble models. Using this method, several so-called “weak learners” are trained and the predictions are integrated to gain accurate outputs. Purposefully, the bagging and boosting techniques have been implemented to develop paramount ML ensemble models such as random forest (Breiman, 2001), gradient boosting (Ke *et al.*, 2017), and extra trees (Geurts *et al.*, 2006).

In the present study, random forest regression (RFR) and gradient boosting regression (GBR) were selected to model the compressive strength of MPCM-integrated concrete. Random forest is an ensemble model developed using the bagging technique (Breiman, 2001). Therefore, multiple decision tree predictors are independently trained in parallel using multiple datasets, which are randomly sampled with replacements from the original training dataset. The final decision is the equally-weighted average of the predictions made by all base learners. Gradient boosting is a sequential boosting ensemble in which observations are iteratively weighted as per the last prediction to improve accuracy. In

contrast to bagging techniques (*e.g.*, random forest), gradient boosting gives the final output by a weighted average of the base predictors, where more weight is assigned to predictors with better performance on the training data (Ke *et al.*, 2017). The mathematical formulations of these models are widely documented and accessible to the interested reader (Breiman, 2001; Ke *et al.*, 2017). The Scikit-learn package in Python was used to construct the models (Pedregosa *et al.*, 2011). More details about RFR and GBR are given in Chapter 3.

Hyperparameter tuning is a key step in developing robust ML models that are neither overfitted nor under-fitted. A 5-fold cross-validated grid search method was employed herein to obtain optimum hyperparameters of the RFR and GBR models. Accordingly, the data were divided into 5 folds. Thereupon, each model was trained 5 times iteratively so as 4 folds were used for training and the remaining fold was used as the test data in each iteration.

4.3.2.3 Deep neural networks (DNN)

A feed-forward multilayer perceptron deep neural network (DNN) was used in this study to predict compressive strength. The DNN is a fully connected network in which every neuron of one layer is connected to all neurons of the adjacent layers. The major difference between conventional artificial neural networks (ANN) and a truly deep multilayer perceptron network is the number of hidden layers and the number of neurons in the network architecture. Accordingly, DNNs usually have more than one hidden layer with a large number of neurons in each layer (Akanbi *et al.*, 2020). Therefore, tuning DNN to obtain optimized model configuration is a critical step in developing predictive models. In this study, various model architectures were considered by changing the number of hidden layers and neurons. This includes networks having 3 to 5 hidden layers with 64, 128, or 256 neurons in each layer. The rectified linear unit (ReLU) function and Adam optimizer algorithm were used as the activation function and optimization algorithm for all network configurations, respectively. Ultimately, the DNN model was tuned for the number of hidden layers, the number of neurons, learning rate, and kernel initializer as discussed in **Section 4.4.1**.

4.3.2.4 Particle swarm optimization (PSO)

Particle swarm optimization (PSO) is a versatile optimization tool inspired by the flocking behavior of birds (Eberhart & Kennedy, 1995). This technique has been vastly employed in many numerical optimization problems including the optimization of concrete mixture design (Nunez *et al.*, 2020). PSO is constructed upon a randomly initialized population. Each member of the population (*i.e.*, bird) is called a particle that flies at a specific velocity causing momentum. The momentum of each particle is updated by its two so-called memory and current perception variables. Having a sufficient number of iterations, which represents the flying time of birds, particles are capable to reach the optimum position.

PSO was adopted herein to optimize the mixture design of cement mortars and concretes integrating MPCM based on a predictive ML model. Deciding on the dosage of MPCM in concrete is an intricate compromise. This implies that high MPCM content is desired to achieve significant improvement in the thermal performance of concrete. However, it is critical to maintain the required compressive strength of concrete by integrating a low MPCM dosage. Since the cement content is a pivotal parameter to compensate for concrete strength loss, the cement content should be as low as possible to achieve mixtures with the lowest environmental impact. Therefore, the objective of the optimization is to identify the maximum content of different types of MPCM along with the lowest cement content. The optimization was carried out for different classes of compressive strength including 25, 30, 35, 40, and 45 MPa. Purposefully, two commercial MPCMs widely used in research studies, namely Micronal DS 5040 X and Microtek MPCM 28D, were considered for numerical experiments and referred to as PCM A and PCM B, respectively. **Table 4-3** presents the thermophysical properties of these two MPCMs collected from manufacturer datasheets or experimental studies in the open literature.

Table 4-3: Thermophysical properties of PCM A and PCM B

MPCM	Designation	Melting temperature (°C)	Heat of fusion (kg/kJ)	Density (kg/m ³)
Micronal DS 5040 X	PCM A	23	100	350
Microtek MPCM 28D	PCM B	28	190	900

Various design constraints were defined for the optimization problem, the first of which was the target compressive strength as follows:

$$|f'_{C,pred} - f'_{C,target}| \leq 1 \quad \text{Eq. 4-4}$$

where $f'_{C,pred}$ (MPa) is the compressive strength predicted by the ML model based on the input variables presented in the compiled dataset. The $f'_{C,target}$ (MPa) is the desired class of compressive strength for which the optimization is performed. The second type of constraint is the range constraint which specifies the search space for each variable. To enhance the convergence of the optimization process, upper and lower limits for each input variable were narrowed by the analysis of the compiled dataset as presented in **Table 4-4**. The ultimate constraint is the volume of the mixture specifying that the total volume of the mixture proportions should be $1 \pm 0.02 \text{ m}^3$ (Zhang, Huang, Wang, *et al.*, 2020). The two percent tolerance is considered to approximately account for the entrapped air content. In the current study, the volume of each mixture design was calculated by the following equation:

$$\frac{C_c}{\rho_c} + \frac{C_w}{\rho_w} + \frac{C_{PCM}}{\rho_{PCM}} + \frac{C_{FA}}{\rho_{FA}} + \frac{C_{CA}}{\rho_{CA}} + \frac{C_{SP}}{\rho_{SP}} = 1 \quad \text{Eq. 4-5}$$

where C_i and ρ_i are the mass and density of each mixture component. The superplasticizer dosage was considered proportional to the cement dosage and varied based on the water-to-cement ratio and MPCM dosage due to the high-water absorption of MPCM particles (Sanfelix *et al.*, 2020). In the case of mortar mixture design optimization, an additional constraint was implemented to specify a coarse aggregate dosage equal to zero. The optimization was carried out targeting the 28-day compressive strength of concrete and mortar cured at standard temperature (*i.e.*, 23 °C). ASTM C150 Type I standard cement was considered in all scenarios.

To further validate the mixture proportions obtained from the optimization, 50×50×50 mm mortar specimens were cast and tested for compressive strength considering three replicates. For this purpose, Type I cement and natural sand were used. The utilized MPCM was a biobased microencapsulated PCM supplied by CrodaTherm having thermophysical properties similar to PCM B, including a melting temperature of 28 °C, and melting

enthalpy of 185 kJ/kg, and a density of 900 kg/m³. Specimens were covered with a double plastic film upon casting and demolded after 24 hours. Finally, the specimens were moist cured at 23 °C until the testing age.

Table 4-4: Upper and lower bonds for optimizing mortar and concrete incorporating MPCM

Concrete incorporating PCM A											
Input	Unit	25 MPa		30 MPa		35 MPa		40 MPa		45 MPa	
		lower	upper	lower	upper	lower	upper	lower	upper	lower	upper
PCM	kg/m ³	75	125	75	100	50	80	40	60	25	50
C	kg/m ³	350	550	350	550	400	600	400	650	400	650
W	kg/m ³	200	350	180	350	150	350	150	300	130	300
FA	kg/m ³	400	1000	400	1000	500	1300	500	1300	500	1300
CA	kg/m ³	0	400	0	400	100	600	100	800	200	800
SP	kg/m ³	0	8	0	8	2	8	2	8	2	8
Mortar incorporating PCM A											
Input	Unit	25 MPa		30 MPa		35 MPa		40 MPa		45 MPa	
		lower	upper	lower	upper	lower	upper	lower	upper	lower	upper
PCM	kg/m ³	80	125	70	100	50	70	30	50	30	45
C	kg/m ³	300	550	350	550	400	550	400	550	400	600
W	kg/m ³	120	300	100	250	150	275	150	275	150	275
FA	kg/m ³	500	1300	400	1200	600	1500	600	1500	900	1700
SP	kg/m ³	0	15	0	15	0	15	0	15	0	15
Concrete incorporating PCM B											
Input	Unit	25 MPa		30 MPa		35 MPa		40 MPa		45 MPa	
		lower	upper	lower	upper	lower	upper	lower	upper	lower	upper
PCM	kg/m ³	120	140	90	125	50	70	45	60	20	50
C	kg/m ³	450	650	450	650	400	600	350	650	400	750
W	kg/m ³	200	350	200	400	150	350	100	300	140	280
FA	kg/m ³	300	700	300	700	400	800	500	1000	500	1000
CA	kg/m ³	300	700	300	700	400	800	400	900	400	1000
SP	kg/m ³	0	10	0	10	0	15	0	15	0	15
Mortar incorporating PCM B											
Input	Unit	25 MPa		30 MPa		35 MPa		40 MPa		45 MPa	
		lower	upper	lower	upper	lower	upper	lower	upper	lower	upper
PCM	kg/m ³	130	160	90	125	65	80	40	60	30	60
C	kg/m ³	400	600	400	600	450	600	450	600	450	550
W	kg/m ³	150	400	150	450	140	300	130	300	130	300
FA	kg/m ³	200	1200	800	1400	1000	1400	1000	1500	1000	1500
SP	kg/m ³	0	15	0	15	0	15	0	15	0	15

4.3.3 Model performance evaluation

Performance evaluation of the developed models was carried out using a combination of statistical and ML approaches. The synthesized data generated by TGAN was compared with the real experimental data using statistical metrics, such as the mean, standard deviation, minimum, maximum, and quartiles of the continuous input variables and the

output. Moreover, to explore the correlation between the attributes in both synthesized and real experimental datasets, the Pearson correlation covariance was calculated.

However, the principal evaluation of the credibility of the synthesized data was conducted using ML models. A primary objective of the current study is to generate large reliable data for training robust ML models to systematically analyze the compressive strength of MPCM-integrated concrete. Therefore, multiple ML models were trained using the synthesized data and tested with the entire real experimental data. This approach proposed by Esteban *et al.* (Esteban *et al.*, 2017) is referred to as Train on Synthetic; Test on Real (TSTR). They also used Train on Real; Test on Synthetic (TRTS) to complement the quality evaluation of the synthesized data. The conventional Train on Real; Test on Real (TRTR) approach in which 30% of the data is used for testing, was also utilized in this study as a performance benchmark for comparison purposes (Fekri *et al.*, 2020). The predictive performance of each of the models developed using the TRTR, TSTR, and TRTS approaches was assessed using several statistical indicators, including the mean absolute error (MAE), root mean squared error (RMSE), and coefficient of determination (R^2) as follows:

$$MSE = \sqrt{\frac{1}{m} \sum_{i=1}^m (Y_i - \hat{Y}_i)^2} \quad \text{Eq. 4-6}$$

$$MAE = \frac{1}{m} \sum_{i=1}^m |Y_i - \hat{Y}_i|, \quad \text{Eq. 4-7}$$

$$R^2 = 1 - \frac{\sum_{i=1}^m (Y_i - \hat{Y}_i)^2}{\sum_{i=1}^m (Y_i - \bar{Y})^2}, \quad \text{Eq. 4-8}$$

4.3.4 Empirical model

Multiple research studies have reported plausible reasons for the reduction of compressive strength of cementitious mortars made with MPCM inclusion, as discussed earlier. Few studies strove for adopting existing empirical models to estimate the compressive strength of MPCM-integrated concrete. Among these, the Bolomey equation demonstrated propitious performance in two different research studies (Lecompte *et al.*, 2015; Sanfelix *et al.*, 2020). The rationale behind utilizing this equation is to simulate MPCM particles as

air voids due to their low stiffness compared to other ingredients of concrete. Yet, no study has analyzed the performance of this model using a large experimental dataset.

The present study attempts to evaluate the correlation between the compressive strength of MPCM-integrated cementitious composites and predictions carried out by the Bolomey equation using the largest available experimental data. Owing to the large amount of data generated by TGAN along with the most influential parameters recognized by ML models, this equation can be further optimized to offer higher prediction accuracy. For this purpose, a Bayesian optimization algorithm (BOA) is implemented to optimize modified versions of **Eq. 4-1** by fitting the TGAN data. The BOA is based on the Bayes theorem expressed by **Eq. 4-9** below:

$$p(w | D) = \frac{p(D|w)p(w)}{p(D)} \quad \text{Eq. 4-9}$$

where w is the unseen value, $p(w)$ is the preceding distribution, $p(w|D)$ is the posterior distribution, and $p(D|w)$ is the probability. Since the Bayes rule uses prior knowledge to find the posterior possibility, Bayesian optimization similarly employs previous iterations to determine the values for the next iteration. This is a more efficient method to find the optimum point compared to arbitrary selection. Bayesian optimization is a powerful technique to approach the extremum of an objective function that has an unknown structure and depends on less than 20 dimensions. Details on BOA can be found in (Pelikan *et al.*, 1999). In the present study, the TGAN data were fit to different modified versions of the Bolomey equation to estimate the compressive strength. The objective function to be minimized was the error between the observed compressive strength in the TGAN data and the estimated compressive strength by the modified equation. MAE was selected as the error indicator. After optimizing the modified Bolomey equation, its predictive performance was tested using the real experimental data. Hyperopt library in Python was used to implement BOA.

4.4 Results and discussion

This section presents the results and pertinent discussion on the performance of the developed ML models, including tabular generating adversarial networks (TGAN),

gradient boosting regression (GBR), random forest regression (RFR), and deep neural network (DNN).

4.4.1 Performance of ML models

The TGAN model was used to provide an adequate number of credible data for training various predictive models. Due to several parameters affecting the convergence and stability of TGAN, a random search optimization was implemented to determine the tuned parameters and hyperparameters. A baseline GBR model trained with the real experimental data was utilized to test the quality of the generated data using a TRTS approach. Mean absolute error (MAE) was monitored to select the best parameters and hyperparameters. Accordingly, the model corresponding to the data which resulted in the lowest MAE upon testing was selected as the tuned model. **Table 4-5** presents the random search space and optimum values of the TGAN parameters tuned in this study. It is noteworthy that implementing TGAN was computationally expensive and needed powerful GPU resources, therefore Google Colab was used for executing codes.

Table 4-5: Parameters and hyperparameters of TGAN model

Parameters	Search values	Tuned value
Number of RNN cells in generator	[100,200,400]	400
Number of fully connected units in generator	[50,100,200]	100
Number of layers in discriminator	[2,4]	2
Number of units per layer in discriminator	[100,200,400]	200
Learning rate	[0.001,0.01]	0.001
Batch size	[50,100,200]	200
Number of train epochs	[5,10,20,50]	20
Number of steps in epoch	[4000,5000,6000,7000]	6000

Ultimately, 22788 synthetic data points generated by the tuned TGAN were used upon preprocessing. **Table 4-6** compares the statistical properties of the real data with those of the TGAN data. It can be observed that TGAN successfully captured the distribution of the real data points and sampled synthetic data examples with high resemblance to the real data observations since the statistical properties of the synthetic and real data are in great accordance.

Figure 4-3 compares the Pearson correlation matrix of real and synthetic datasets. It is evidenced that the correlation between features of the data generated by the TGAN model

is highly similar to that of the real dataset. For instance, the MPCM content has a high degree of inverse correlation to the compressive strength with a correlation coefficient of -0.52 and -0.53 in real and synthesized data, respectively. This relationship is widely documented in pertinent experimental studies in the literature. Furthermore, the fine aggregate content (FA) has a high degree of positive correlation with the compressive strength and a negative correlation with the MPCM dosage. This reflects the partial replacement of FA with MPCM particles in the concrete mixtures and the contribution of soft MPCM particles to the reduction of compressive strength (Falzone *et al.*, 2016). Such results demonstrate that TGAN was able to generate plausible data with a similar structure to the real data.

Table 4-6: Comparison on the statistical properties of the real and synthetic data

	Tm (°C)		Lm (kJ/kg)		PCM (kg/m ³)		C (kg/m ³)	
	Real	Synthetic	Real	Synthetic	Real	Synthetic	Real	Synthetic
Mean	25.36	25.33	121.95	122.48	48.5	36.96	489.75	495.78
STD	2.88	2.93	42.53	44.38	61	50.77	109.362	109.31
Min	16.1	15.15	55	54.02	0.00	0	255	250.22
25%	23.6	23.06	97.6	97.86	6	4	434	436.38
50%	25	25.99	102	100.67	25.75	17.80	480	483.83
75%	28	27.99	159.25	161.31	64.3	61.25	536	539.11
Max	29.2	29.33	200	203.07	292.9	288.43	721	722.75
	W (kg/m ³)		(kg/m ³)		CA (kg/m ³)		(MPa)	
	Real	Synthetic	Real	Synthetic	Real	Synthetic	Real	Synthetic
Mean	232.17	228.72	958.55	958.2	426.43	455.24	33.26	34.94
STD	39.362	38.58	311.75	313.46	425.86	429.58	15.41	14.98
Min	152.38	144.16	220	298	0.00	0	7.53	7.52
25%	200	197.00	765.60	765.6	0.00	0	19.43	19.71
50%	235.6	232.44	951.30	977.15	598	648.52	31.5	33.84
75%	260	256.61	1119	1133.4	706.7	733.75	46	48.3
Max	377.5	366.91	1673	1600.09	1160	1160	74.05	74.68

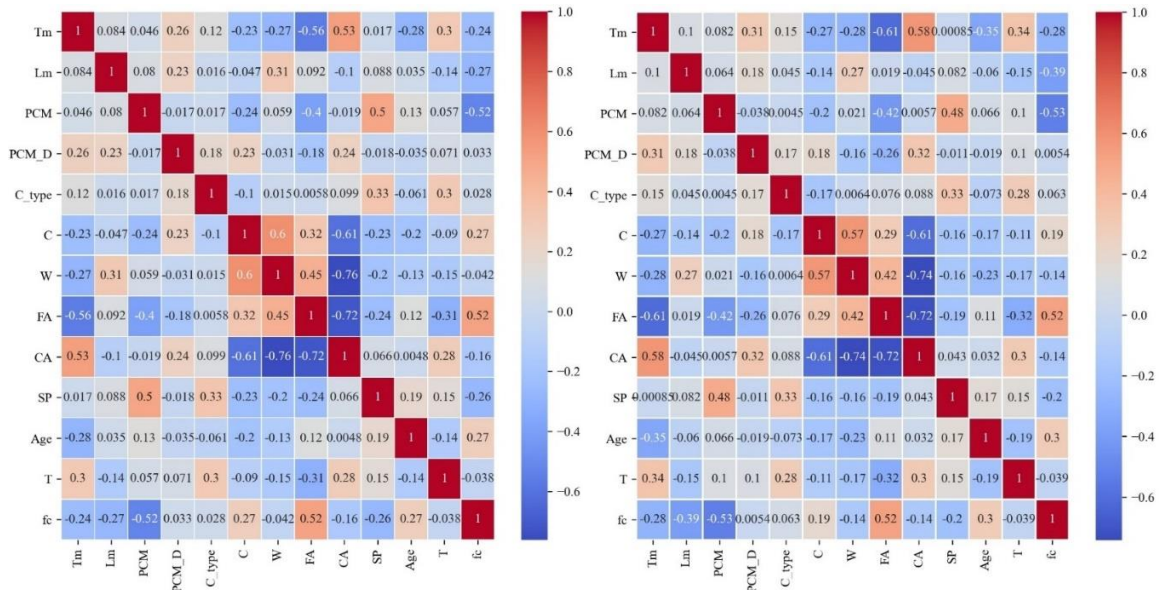


Figure 4-3: Pearson correlation between attributes of data: real data (left), and synthetic data (right).

In addition to the statistical tests, the quality of the generated data can better be assessed by developing ML models using the TRTR, TSTR, and TRTS approaches as explained earlier. Using these methodologies, the predictive performance of models trained with synthetic data is compared to that of models trained with real data and subsequently, the credibility of the synthetic data for training ML models can be appraised (Marani *et al.*, 2020). The performance of the models trained with 70% of the experimental data is thence benchmarked to ascertain the quality of the synthesized data. Three different ML models, including RFR, GBR, and DNN, were tuned with 70% of the real data using a 5-fold cross-validated grid search as explained earlier. **Table 4-7** lists the hyperparameters of RFR and GBR models obtained using a grid search method. To tune the DNN model, 9 various network configurations were considered to establish the baseline architecture of the model as reported in **Table 4-8**. Afterward, a 5-fold cross-validated grid search was performed to obtain the optimum parameters and hyperparameters of the model. Ultimately, a deep network with three hidden layers having 256 neurons in the first layer and 128 neurons in the second and third layers was selected. Adam optimizer with a learning rate of 0.0075 was used to optimize the training process. He_uniform was selected as the kernel weight

initializer. It is noteworthy that the tuned hyperparameters were used to train the models in the TRTR, TSTR, and TRTS approaches.

Table 4-7: Tuned hyperparameters of RFR and GBR models

Model	Tuned Parameters
RFR	n_estimators=150; min_samples_split=2; min_samples_leaf=1; max_depth=19; max_features=11
GBR	n_estimators=140; learning_rate=0.11; min_samples_split=2; min_samples_leaf=5; max_depth=6; max_features=8; subsample=0.48

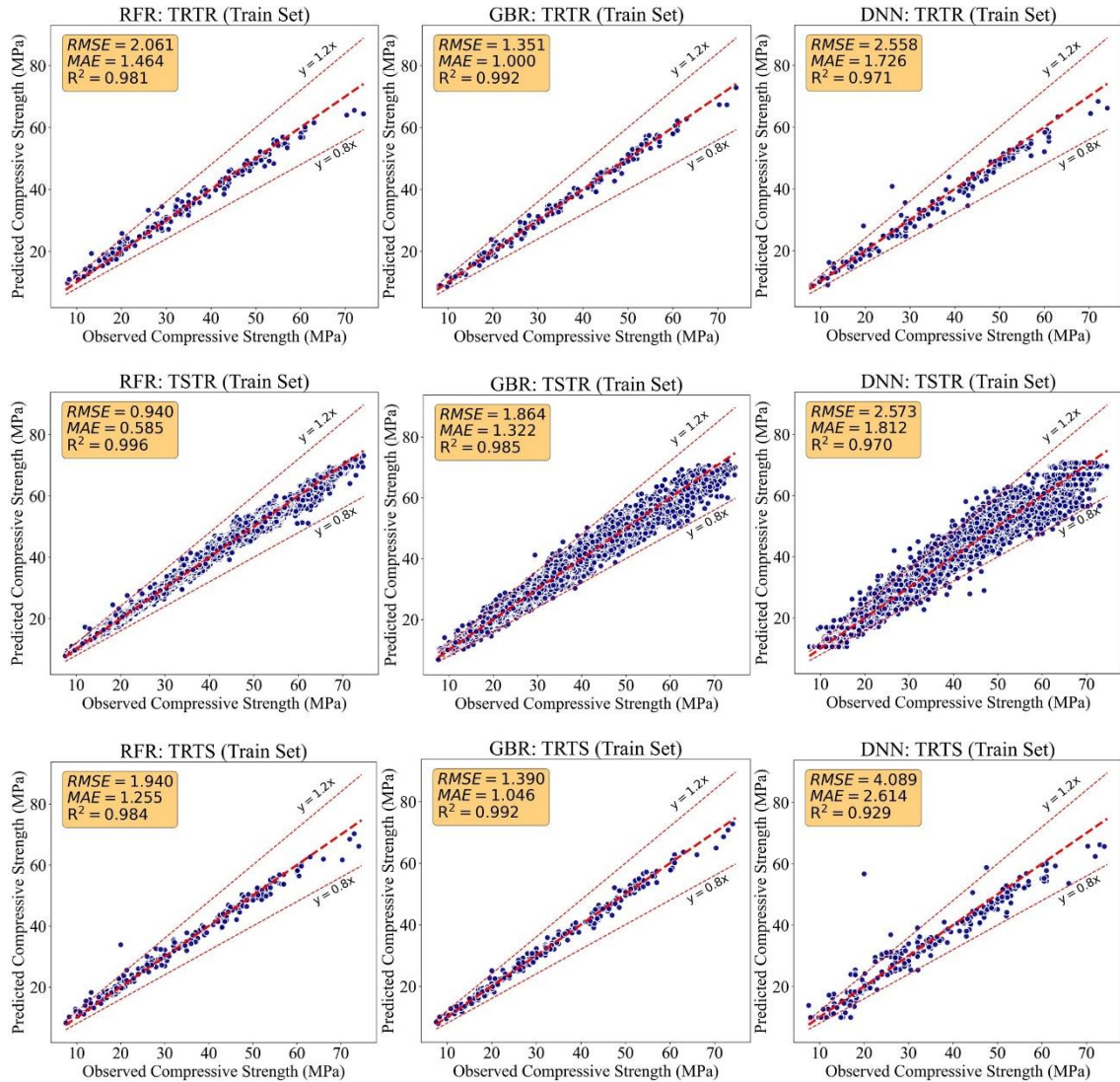


Figure 4-4: Observed versus predicted compressive strengths for training datasets.

Figures 4-4 and 4-5 indicate the observed versus predicted compressive strengths obtained from GBR, RFR, and DNN models for training and testing sets, respectively. Accordingly,

the data generated by the TGAN technique demonstrated supreme reliability in training powerful predictive models. The performance indicators for training sets indicate that different types of ML models can be robustly trained using synthetic data, similar to being trained with real experimental data. Furthermore, what stands out in the testing performance of the models reported herein is the phenomenal improvement in the prediction accuracy of the models trained with the large synthetic dataset. For instance, the test MAE of RFR, GBR, and DNN models in the TRTR approach (*i.e.* trained on 70% of the real data) were 4.142 MPa, 3.276 MPa, and 3.725 MPa, respectively.

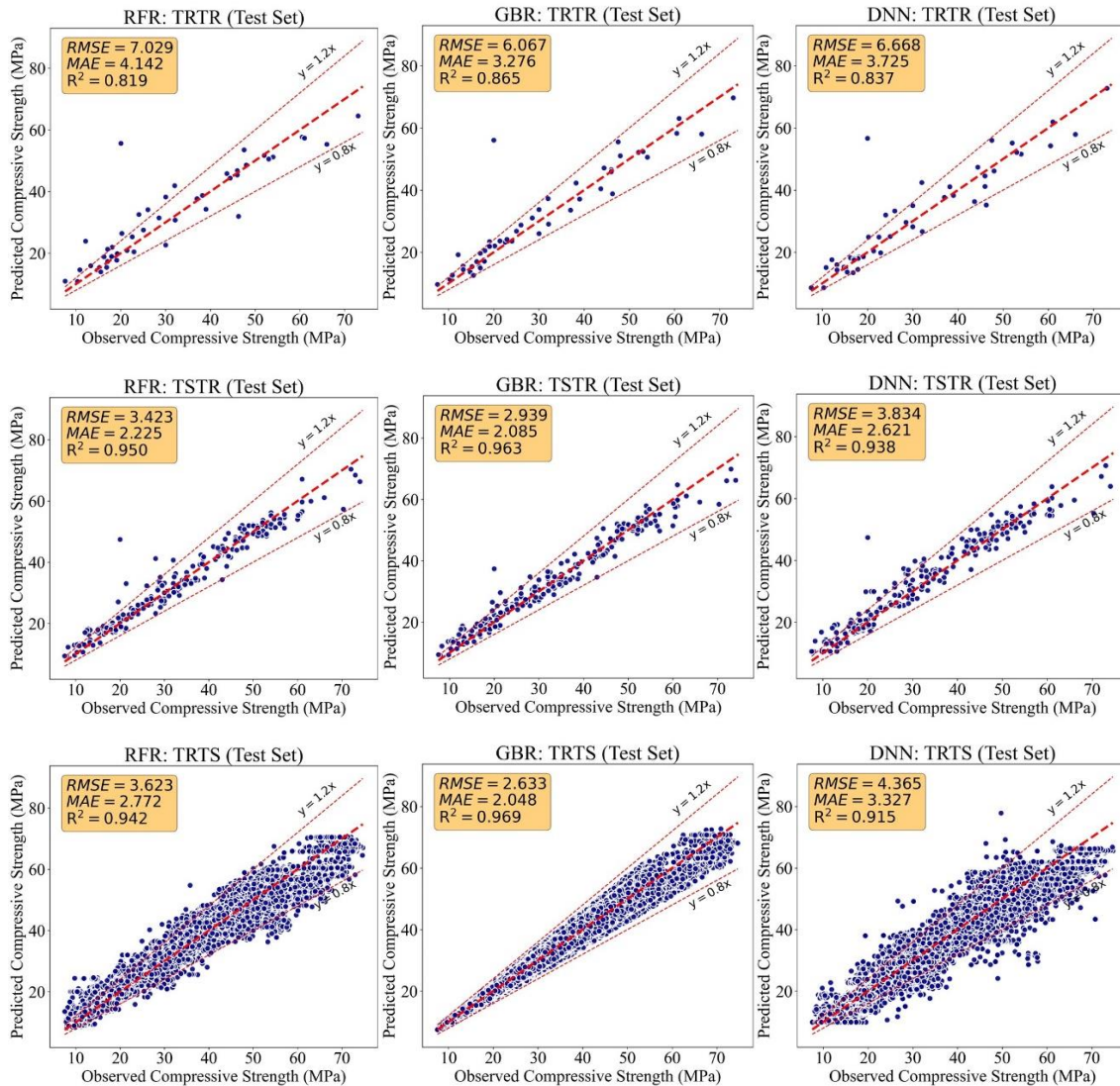


Figure 4-5: Observed versus predicted compressive strengths for testing datasets.

In contrast, MAE values as low as 2.225 MPa, 2.085 MPa, and 2.621 MPa were respectively achieved for RFR, GBR, and DNN models when trained using the synthesized data per the TSTR approach. The higher predictive accuracy of models in the TSTR approach is also evident in other statistical indicators as indicated in **Figs. 4-4** and **4-5**. This demonstrates that the synthesized data had the desirable quality for building successful ML predictive systems. Another striking observation that emerged from the performance comparison was the development of more generalized models with less overfitting in the TSTR approach. Constructing ML models on a limited number of training data can result in overfitted models with poor prediction performance on future unseen data. Nevertheless, as it can be observed in **Fig. 4-5**, models trained with 22,778 plausible data generated by TGAN demonstrated less scatter in their predictions, although being evaluated using a larger testing dataset containing the entire experimental data points. This can be further accentuated by comparing the prediction accuracies of training and testing sets in each approach. For instance, the R^2 of the GBR model in the TRTR approach decreased from 0.992 in the training set to 0.865 in the testing set. Conversely, the R^2 of the GBR model using the TSTR approach was 0.985 and 0.963 in training and testing, respectively, indicating more robust performance. Hence, the ML models strikingly performed better when trained using a large number of credible data generated by the TGAN approach compared to being trained with limited experimental data. It is noteworthy that using the TSTR approach, the performance of each model was tested with the entire real experimental data. This is a remarkably more generalized evaluation of model performance compared to the conventional TRTR approach.

All three powerful ML algorithms adopted herein attained excellent performance in predicting the compressive strength of concrete incorporating MPCM as measured by several statistical indicators. Overall, these results suggest that ML models can be employed to estimate the compressive strength of MPCM-integrated concrete with favorable accuracy. Moreover, the data generated by TGAN highly resembled the real experimental data, and thus, can be used to mitigate the undesirable problems associated with the low number of available laboratory data points. Therefore, the TSTR approach is selected as the main modeling framework for constructing further predictive ML models. **Figure 4-6** illustrates the prediction performance of RFR, GBR, and DNN models trained

with 22,778 synthetic data points and tested using the entire experimental data (*i.e.* TSTR approach).

Figure 4-7 displays a Taylor diagram for statistical comparison of the models' predictive performance. Taylor's diagram is constructed based on RMSE, correlation, and standard deviation of the predictions in comparison with the real observation. Accordingly, the model with lower RMSE and standard deviation and higher correlation has a better performance in forecasting the target with lower error. Albeit models demonstrated comparable accuracy, the GBR-TSTR model attained slightly better performance since it has higher correlation to the real observations along with lower prediction error and scatter. As can be understood from the collective results discussed herein, the GBR-TSTR model outperformed the other models and thus was selected for further analyses (e.g. parametric analysis and mixture optimization) in the current study. The importance of the input features of the GBR-TSTR model is depicted in **Fig. 4-8**. Accordingly, the fine aggregate (FA) and MPCM (PCM) contents had the highest importance, indicating their major contribution to compressive strength prediction. This reflects the fact that the inclusion of low stiffness MPCM as a partial replacement for sand leads to decreasing the compressive strength as evidenced in experimental findings (Jayalath *et al.*, 2016). These results conform with the results observed in Chapter 3 emphasizing the contribution of the MPCM and fine aggregate in the prediction of the compressive strength by various ML models.

Table 4-8: Performance accuracy of baseline DNN models

Model	Number of hidden layers	Number of neurons	MAE		R^2	
			Train	Test	Train	Test
1	3	64	1.905	4.558	0.967	0.770
2	4	64	2.075	4.936	0.955	0.704
3	5	64	2.729	4.204	0.923	0.849
4	3	128	1.618	4.217	0.971	0.801
5	4	128	1.628	4.05	0.970	0.826
6	5	128	2.276	4.553	0.939	0.821
7	3	256	1.665	4.105	0.970	0.786
8	4	256	1.897	4.671	0.961	0.784
9	5	256	2.033	4.275	0.956	0.809

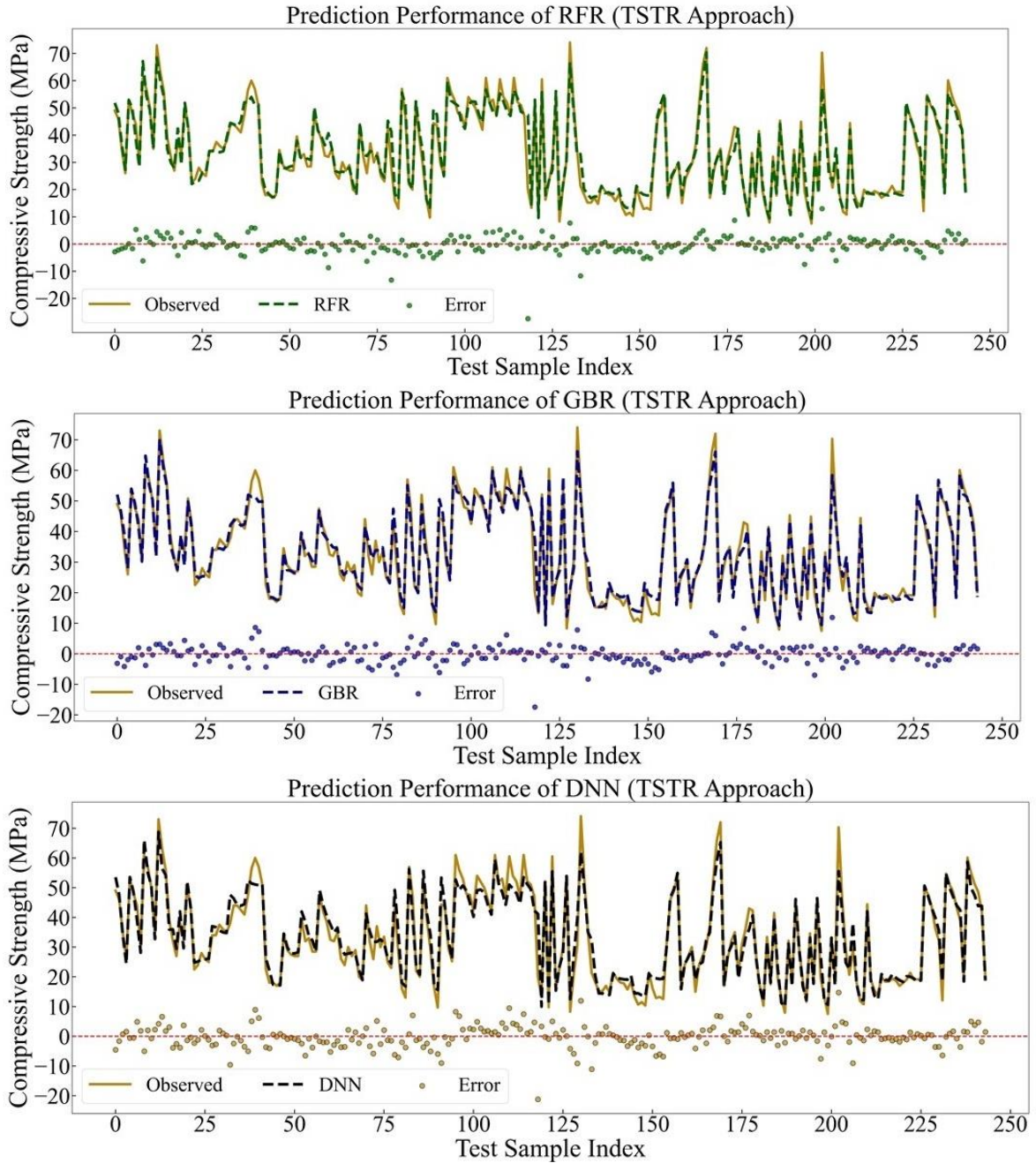


Figure 4-6: Prediction performance of RFR, GBR, and DNN models using the TSTR approach.

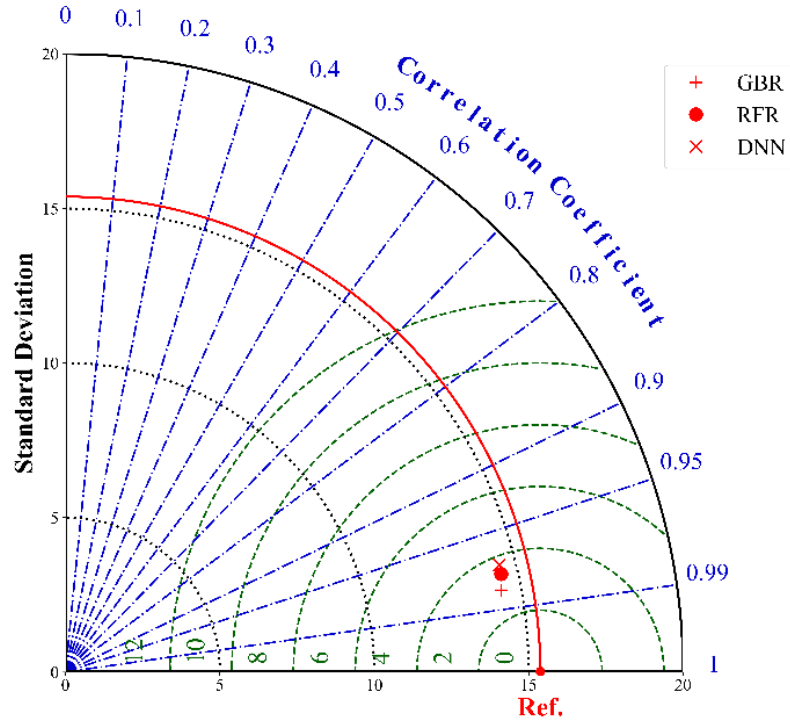


Figure 4-7: Taylor diagram for comparison of models. All three models indicated similar performance with GBR having slightly less error (green lines) and higher correlation (blue lines).

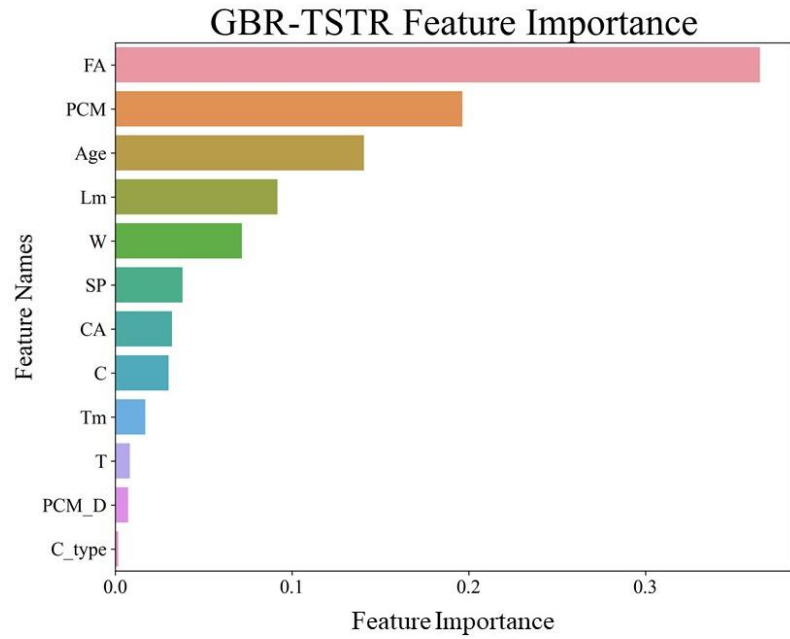


Figure 4-8: Feature importance for GBR-TSTR model.

4.4.2 Empirical model

A Bayesian optimization algorithm (BOA) was implemented to develop an optimized version of the Bolomey equation (**Eq. 4-1**) for estimating the compressive strength of MPCM-integrated concrete. Lecompte *et al.* (Lecompte *et al.*, 2015) and Sanfelix *et al.* (Sanfelix *et al.*, 2020) proposed **Eq. 4-1** to estimate the compressive strength of concrete in which MPCM particles are considered as air voids. Thus, the term W_{PCM} was added to account for that assumption. **Equation 4-1** was previously tested using very little experimental data. Yet, its general predictive performance was so far unexplored since no study evaluated its accuracy using a large and comprehensive dataset. Therefore, the overall performance of this equation on the compiled experimental data is explored as presented in **Table 4-9**. Only data points with MPCM inclusion and 28-day compressive strength were considered. Different versions of this equation were initially considered for optimization using BOA to capture the influential features recognized by the ML model. Accordingly, the fine aggregate content and thermal properties of MPCM had a considerable effect on the compressive strength development as discussed earlier. Therefore, this study attempted to incorporate the fine aggregate content and latent heat of MPCM in the general form of **Eq. 4-1**. Synthetic data generated with TGAN was fitted to the general form of models M1 and M2 in **Table 4-9**. The unknown coefficients C_i were determined by BOA such that the lowest prediction error (MAE) was achieved. The accuracy of the models was tested on 110 real experimental data.

Table 4-9 presents the general and optimized form of the considered equations, along with their prediction error upon testing with the real experimental data. According to the results listed in **Table 4-9**, **Eq. 4-1**, which was not tested on a large experimental dataset before, yielded a relatively low accuracy when tested with the entire experimental data points. However, Models M1 and M2, which include parameters representing the latent heat of MPCM and the fine aggregate content, demonstrated significant improvement in prediction accuracy.

Table 4-9: Optimization of empirical models

Model	Equation	MAE	RMSE	R ²
Eq. 1 General	$f_c = K_B \times \sigma_c \left[\frac{C}{W + W_v + W_{MPCM}} - 0.5 \right]$	11.7	12.16	0.39
General	$f_c = (FA)^{C_2} \times C_3 \times \sigma_c \times \left[\left(\frac{C}{W + W_v + (W_{MPCM})^{C_4}} \right)^{C_5} - C_6 \right]^{C_7}$			
M1 Optimized	$f_{c,28} = 0.4(FA)^{0.05} \sigma_{C,28} \left[\left(\frac{C}{W + W_v + W_{MPCM}} \right)^{0.8} - 0.25 \right]$	9.27	10.8	0.52
General	$f_c = \left(\frac{1}{L_H} \right)^{C_1} \times (FA)^{C_2} \times C_3 \times \sigma_c \times \left[\left(\frac{C}{W + W_v + (W_{MPCM})^{C_4}} \right)^{C_5} - C_6 \right]^{C_7}$			
M2 Optimized	$f_{c,28} = 0.43 \left(FA \frac{1}{L_H} \right)^{\frac{1}{3}} \sigma_{C,28} \left[\left(\frac{C}{W + W_v + W_{MPCM}} \right)^{0.5} - 0.5 \right]$	7.75	9.48	0.63

Model M2 suggests an optimized form similar to **Eq. 4-1** with the inclusion of the latent heat of MPCM (kJ/kg) and dosage of fine aggregate (kg/m³) leading to superior prediction accuracy as follows:

$$f_{c,28} = 0.43 \left(FA \frac{1}{L_H} \right)^{\frac{1}{3}} \sigma_{C,28} \left[\left(\frac{C}{W+W_v+W_{MPCM}} \right)^{0.5} - 0.5 \right] \quad \text{Eq. 4-10}$$

where FA is the fine aggregate content (kg/m³), L_H is the latent heat of MPCM (kJ/kg), C is the cement content (kg/m³), W is the water content (kg/m³), W_v is the mass of water equivalent to the volume of air entrapped in the mixture (kg/m³), and W_{MPCM} is the mass of water equivalent to the volume occupied by MPCM particles in the mixture (kg/m³). 2% air content was assumed to calculate W_v . $\sigma_{C,28}$ is a constant relating to the cement class, which was considered as 55 in the optimization process. In **Eq. 4-1**, K_B is a constant varying between 0.35 to 0.65 depending on the type of aggregate. This constant was determined herein as 0.43 for MPCM-integrated mortars and concretes. **Figure 4-9** compares the prediction performance of **Eq. 4-1** with that of **Eq. 4-10** optimized in this study and tested on 110 real experimental data. Although the optimized version of the Bolomey equation proposed herein demonstrated considerable improvement in the accuracy of predictions, it still has less accuracy and certainty compared to the ML models.

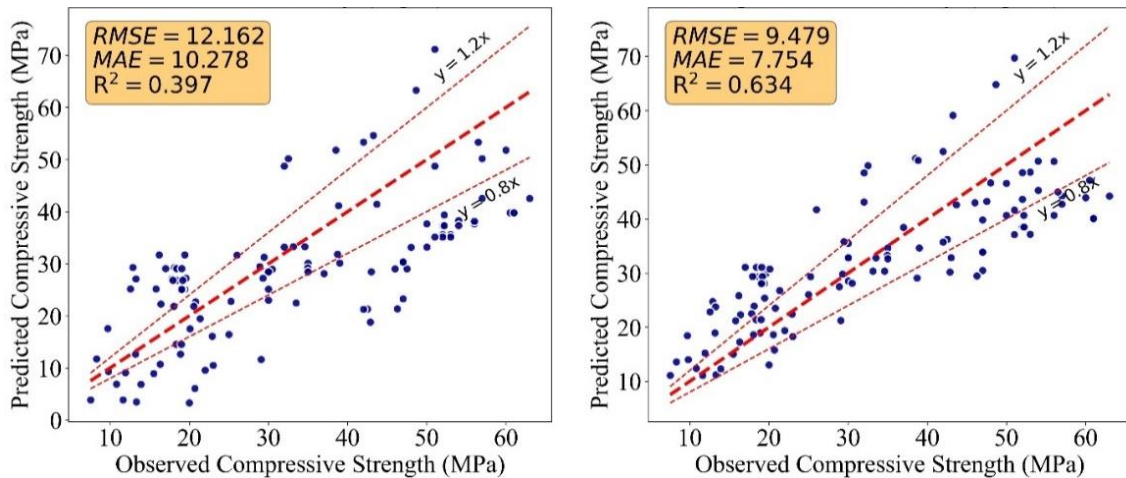


Figure 4-9: Prediction performance of basic Eq. 4-1 (left) and Eq. 4-10 (right).

4.5 Parametric analysis

The intelligent approach developed in this study demonstrated favorable capability in modeling the compressive strength development of cementitious composites integrating MPCM. Therefore, it is feasible to conduct extensive parametric studies to capture the effects of the MPCM content on the compressive strength of mortars and concrete. For this purpose, the two widely available commercial MPCM products considered earlier for mixture optimization, *i.e.* PCM A and PCM B, were deployed here for numerical experiments. Multiple mixture designs having different W/C ratios and cement content were investigated. For each mixture design, MPCM particles were added as a partial replacement for fine aggregates. **Table 4-10** outlines the scenarios considered for the parametric analyses. In each scenario, a control mixture was designed having 1000 kg/m^3 of fine aggregate and no MPCM content. MPCM was then added to the mixture as a partial replacement for fine aggregates. The 28-day compressive strength was investigated assuming a curing temperature of $23 \text{ }^\circ\text{C}$. **Figure 4-10** indicates the changes in compressive strength upon the replacement of fine aggregate with MPCM. It can be observed that a rapid decline in the compressive strength of concrete occurred with the increased addition of MPCM, which concurs with experimental results reported in the literature.

Table 4-10: Parametric analysis scenario

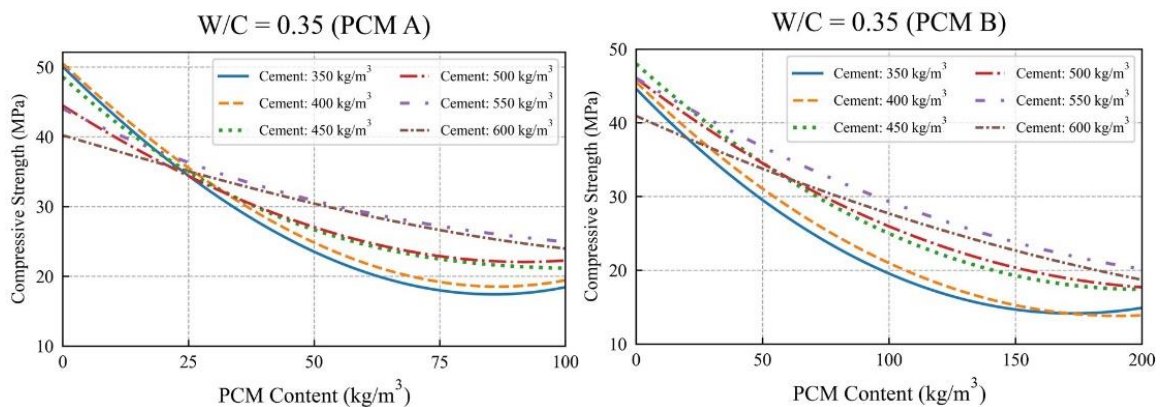
Parametric Study	Constant Parameters	Varying Parameters
Effect of “PCM A” Inclusion with Various Cement Content	Water-to-cement ratio (0.55, 0.5, 0.45, 0.4, 0.35); Cement content (350, 400, 450, 500, 550, 600 kg/m ³)	PCM A dosage
Effect of “PCM B” Inclusion with Various Cement Content	Water-to-cement ratio (0.55, 0.5, 0.45, 0.4, 0.35); Cement content (350, 400, 450, 500, 550, 600 kg/m ³)	PCM B dosage
Effect of PCM A Inclusion at Various Ages	W/C ratio (0.35, 0.45, 0.55); PCM A (0, 25, 50, 75, 100 kg/m ³)	Age
Effect of PCM B Inclusion at Various Ages	W/C ratio (0.35, 0.45, 0.55); PCM B (0, 25, 50, 75, 100 kg/m ³)	Age

This proves that the GBR-TSTR model successfully captured the underlying pattern in the data and thus, can accurately estimate the compressive strength of different mixtures. Furthermore, the extensive parametric analyses reveal new insights into the behavior of MPCM-integrated concrete. Accordingly, the decrease in compressive strength due to MPCM inclusion is less dramatic in mixtures with higher cement content compared to those with an equal W/C ratio and lower cement content. This is more significant when higher levels of MPCM are intended to be added to the concrete. Such a trend was observed for both cases of PCM A and PCM B. This could be related to the fact that with the addition of MPCMs, the nucleation sites for the precipitation and growth of the hydration products are reduced since MPCM particles tend to wrap around the cement grains and prevent their access to water. Increasing the cement content may partially compensate for the decrease in the nucleation sites.

Another striking outcome of the parametric analyses is that different types of MPCM could exert different effects on the compressive strength of concrete due to their different thermophysical properties. PCM A, which has a lower density, caused a steeper rate of compressive strength decrease. For instance, to achieve a 28-day compressive strength of 30 MPa at a W/C ratio of 0.4, the dosage of PCM A is almost half of that of PCM B. This suggests that the physical properties of MPCM should be meticulously involved in the design of MPCM-integrated mixtures. To better illustrate the combined effect of MPCM and cement content on the 28-day compressive strength of concrete, surface response plots are depicted in **Fig. 4-11** for both PCM A and PCM B. It can be observed that the combined effects of cement and MPCM contents were quite similar for different W/C ratios.

However, higher W/C ratios resulted in generally lower compressive strength along with more dramatic drops in the strength upon the addition of MPCM. Using lower W/C ratios probably enhances the porosity of the cement matrix and yields higher compressive strength.

Figure 4-12 explores the strength development of concrete incorporating PCM A and B over 28 days. The effect of MPCM inclusion on the strength development was well captured by the GBR-TSTR model since the compressive strength declined with the increase in MPCM dosage. All mixtures had an equal amount of 500 kg/m^3 cement content. The reduction pattern is similar for different W/C ratios, especially at later ages. It can be again observed that the inclusion of PCM A caused a more dramatic decrease in compressive strength compared to PCM B addition at the same dosage weight. This is another indication of the effect of the low stiffness of MPCM particles. To incorporate a certain dosage of PCM A, more fine aggregates should be deducted from the mixture compared to the inclusion of PCM B and thus, the detrimental effect of soft particles is more pronounced. Surprisingly, the model could capture the delay in strength development at early ages since the strength development curve of mixtures with high MPCM dosage had a lower slope compared to that of the control specimens with no MPCM addition. This delay was more predominant in a lower W/C ratio. The delay in the cement hydration and strength development was previously reported in experimental isothermal calorimetry and compressive strength analysis in the literature (Djamai *et al.*, 2019). However, more comprehensive studies along with additional experimental data are needed to better analyze the delaying effect of MPCM on strength development at early ages.



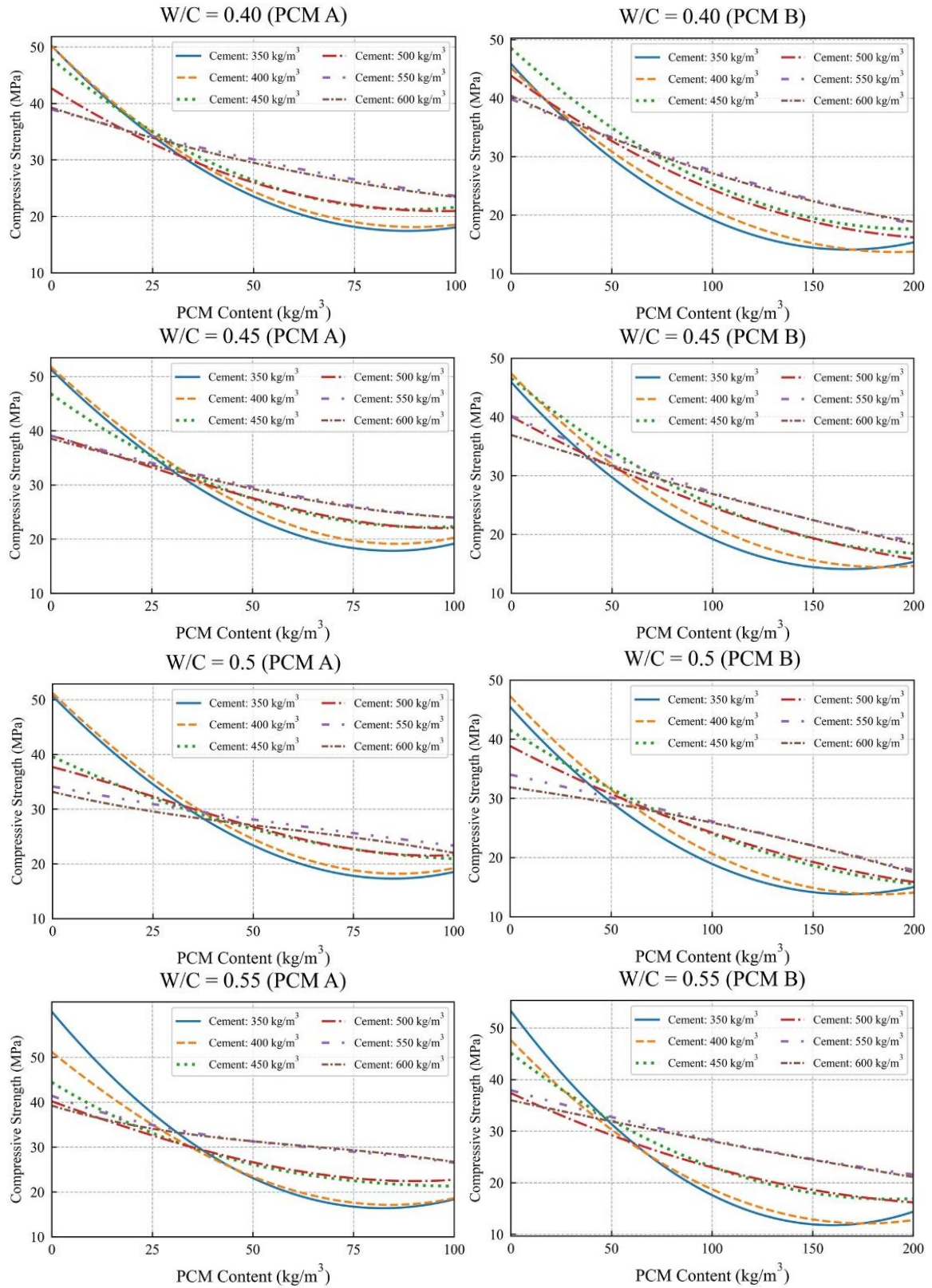
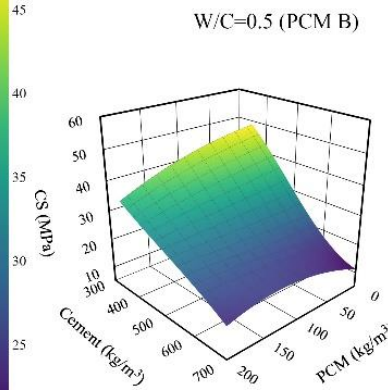
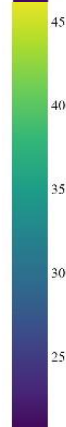
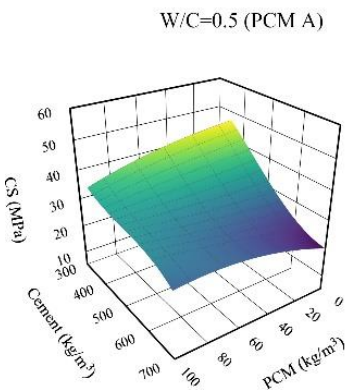
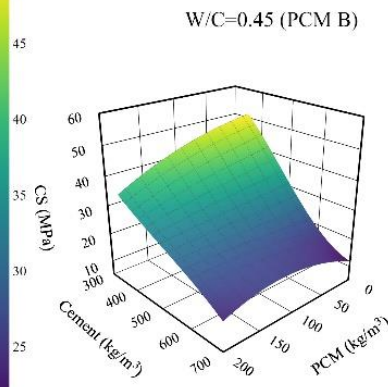
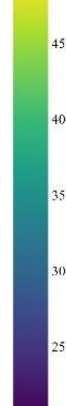
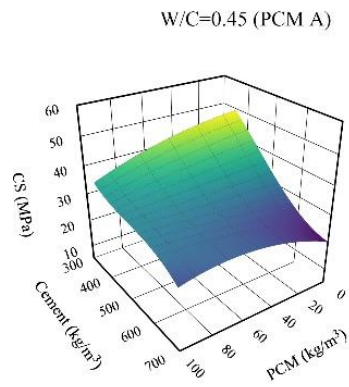
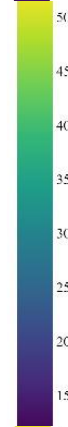
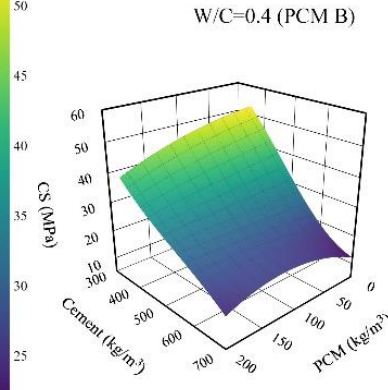
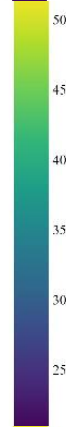
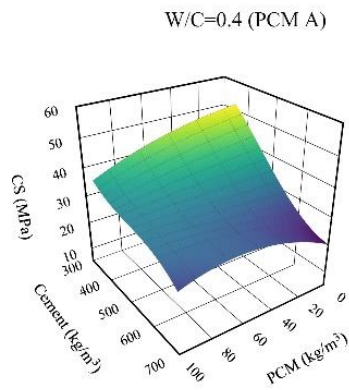
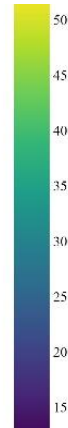
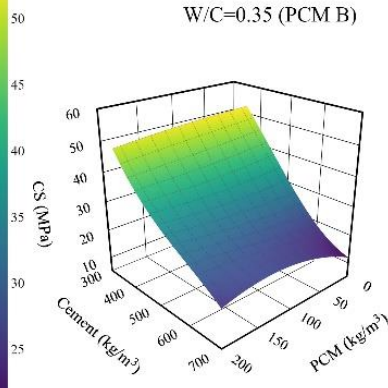
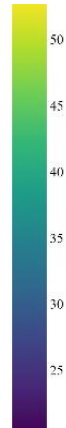
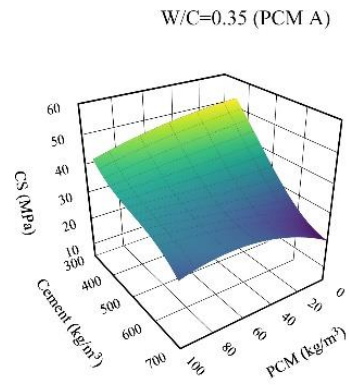


Figure 4-10: Effect of fine aggregate replacement with MPCMs on compressive strength.



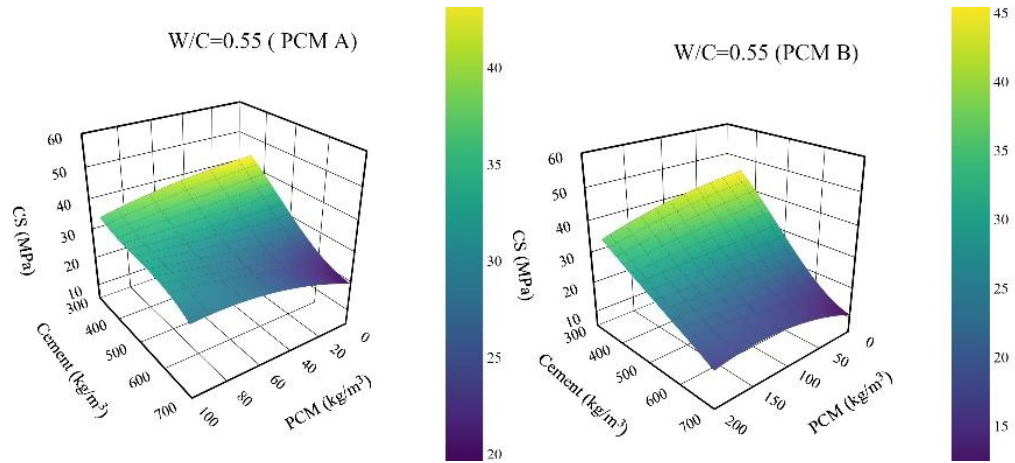
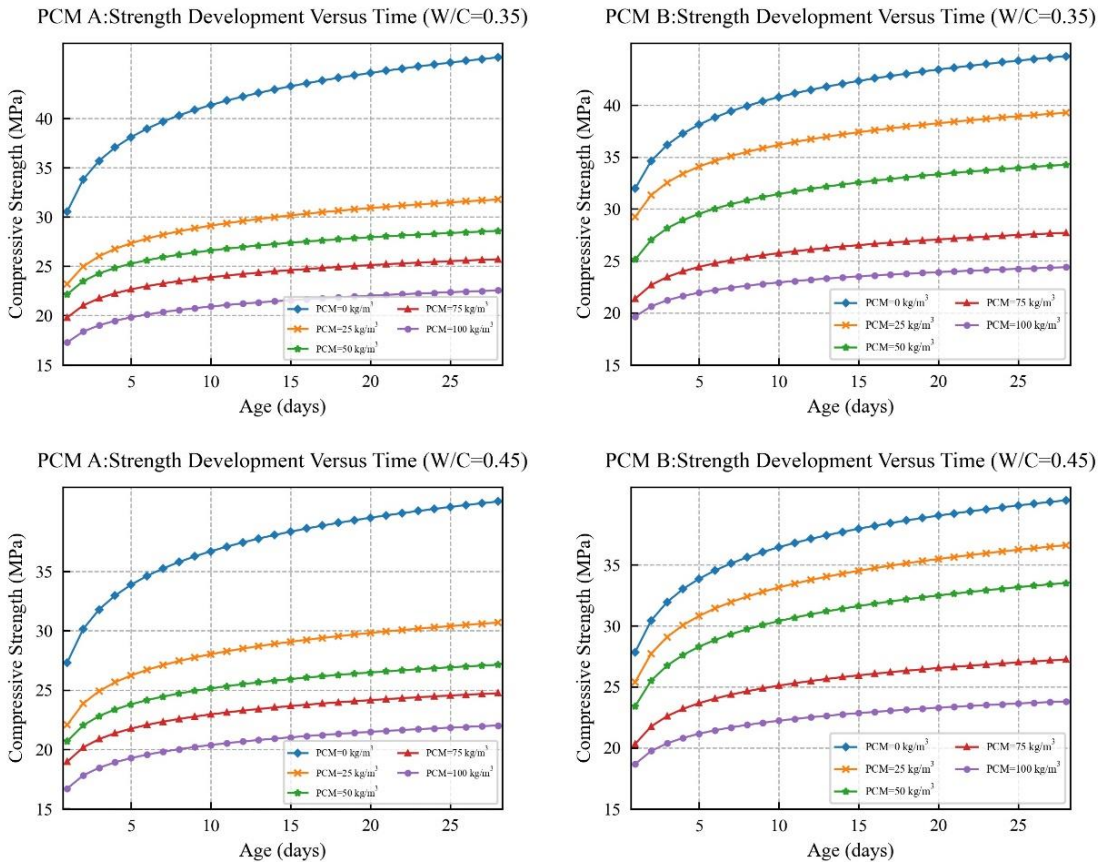


Figure 4-11: Surface response plot of compressive strength (CS)



PCM A: Strength Development Versus Time (W/C=0.35)

PCM B: Strength Development Versus Time (W/C=0.35)

PCM A: Strength Development Versus Time (W/C=0.45)

PCM B: Strength Development Versus Time (W/C=0.45)

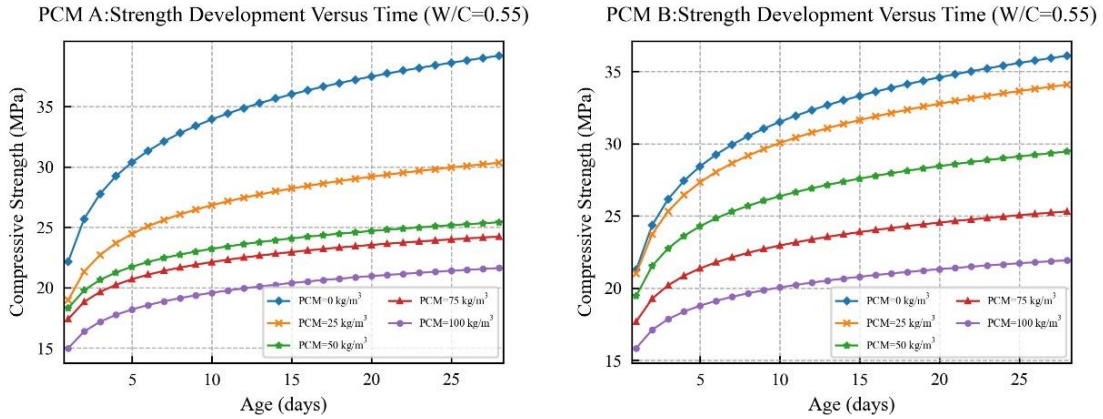


Figure 4-12: Effect of MPCM inclusion on strength development versus time.

4.6 Mixture optimization

The parametric analyses discussed above revealed that optimum mixture proportioning of MPCM-integrated concrete is a convoluted design process due to the involvement and interaction of multiple complex parameters. Therefore, a mixture optimization of cement mortars and concretes incorporating PCM A and B was performed using a hybrid PSO-GBR model. Using this approach, the GBR model trained with synthetic data (*i.e.*, GBR-TSTR) was coupled with a PSO algorithm to design mixtures with maximum MPCM content along with minimum cement content considering the constraints explained earlier. The optimization was conducted for 5 different classes of 28-day compressive strength including 25, 30, 35, 40, and 45 MPa. **Table 4-11** presents the optimum mixture designs obtained from the hybrid PSO-GBR model. The mixture designs were proposed for concrete made with Type I cement and cured at 23 °C.

According to the results, PCM B can be added to concrete at higher dosages compared to PCM A and achieve equal compressive strength owing to its higher density as evidenced in the parametric analysis. In other words, for adding higher weight dosages of PCM A, a larger volume of aggregates should be replaced with PCM microcapsules in comparison with adding PCM B. Therefore, the detrimental effect of the soft microcapsules on the compressive strength is more pronounced in the case of PCM A, especially at high MPCM contents. It can be understood that it is possible to incorporate a high dosage of MPCM into concrete targeting a relatively low compressive strength such as 25 and 30 MPa. In

contrast to normal concrete, much higher cement content (350 to 550 kg/m³) is required for MPCM-integrated concrete having such compressive strengths. This is conforming with the parametric analysis presented earlier.

Table 4-11: Proposed mixture designs for mortar and concrete incorporating MPCMs

Concrete incorporating PCM A						
Strength Class	PCM A (kg/m ³)	Cement (kg/m ³)	Water (kg/m ³)	Fine Agg. (kg/m ³)	Coarse Agg. (kg/m ³)	Superplasticizer (kg/m ³)
25 MPa	91.5	366	180	874	266	6
30 MPa	82.5	484	225.5	814	174.5	6
35 MPa	55	425	170	1015.5	374.5	7
40 MPa	50	430	172	963.75	427.5	7
45 MPa	31.5	460	170.5	861.5	665.5	6
Concrete incorporating PCM B						
Strength Class	PCM B (kg/m ³)	Cement (kg/m ³)	Water (kg/m ³)	Fine Agg. (kg/m ³)	Coarse Agg. (kg/m ³)	Superplasticizer (kg/m ³)
25 MPa	130	541	267.5	524.5	510	11
30 MPa	102	509.5	221.5	636	661	10
35 MPa	73.5	515.5	199.5	779	593.5	10
40 MPa	52	423	191.5	905.5	660.5	5
45 MPa	41	402	190	918	710.2	5
Mortar incorporating PCM A						
Strength Class	PCM A (kg/m ³)	Cement (kg/m ³)	Water (kg/m ³)	Fine Agg. (kg/m ³)	Coarse Agg. (kg/m ³)	Superplasticizer (kg/m ³)
25 MPa	100	345.5	170	1058	0	5.5
30 MPa	90	423	190	995.5	0	3.5
35 MPa	65	430	155	1400	0	7
40 MPa	50	425	167	1417	0	6.5
45 MPa	42	449	165.5	1480.5	0	7
Mortar incorporating PCM B						
Strength Class	PCM B (kg/m ³)	Cement (kg/m ³)	Water (kg/m ³)	Fine Agg. (kg/m ³)	Coarse Agg. (kg/m ³)	Superplasticizer (kg/m ³)
25 MPa	145	581	270	904	0	11
30 MPa	104.5	523	225	1279.5	0	11
35 MPa	76.5	508	214	1400	0	8
40 MPa	60	485	230	1418	0	5
45 MPa	51	460	207	1495	0	5

Furthermore, the proposed mixture proportions can be compared to the results reported in the literature. For instance, Lecompte *et al.* (Lecompte *et al.*, 2015) achieved a compressive strength of 30 MPa for a concrete incorporating 439 kg of cement and 78 kg of MPCM, respectively. The thermophysical properties of the MPCM used are similar to PCM B. The proposed mixture design for concrete made with PCM B and 30 MPa of compressive strength features 102 kg of MPCM and 509.5 kg of cement, respectively. In another study, Snoeck *et al.* (Snoeck *et al.*, 2016) achieved a 28-day compressive strength of 42.5 MPa

for mortar made with 48.3 kg of MPCM having thermophysical properties similar to PCM A. They used 483 kg of cement in their mixture design. The current optimization proposed a mixture with 50 kg of PCM A along with 425 kg of cement to achieve a compressive strength of 40 MPa. Such comparisons demonstrate that the optimization successfully enhanced the mixture design concerning the defined objectives. To further validate the proposed mixture designs, $50 \times 50 \times 50$ mm specimens with mixture proportions listed in **Table 4-11** for mortars incorporating PCM B were cast in the laboratory and tested for 14- and 28-day compressive strength. The used MPCM for casting the specimens were biobased MPCM having thermophysical properties like that of PCM B. Specimens were made with Type I cement and natural sand and cured at 23 °C until testing. The average compressive strength of 3 replicates for each test group is reported in **Figure 4-13**. It can be observed that the experimental 28-day compressive strength was very close to the target strength pursued in the optimization process owing to the high accuracy of the applied ML model.

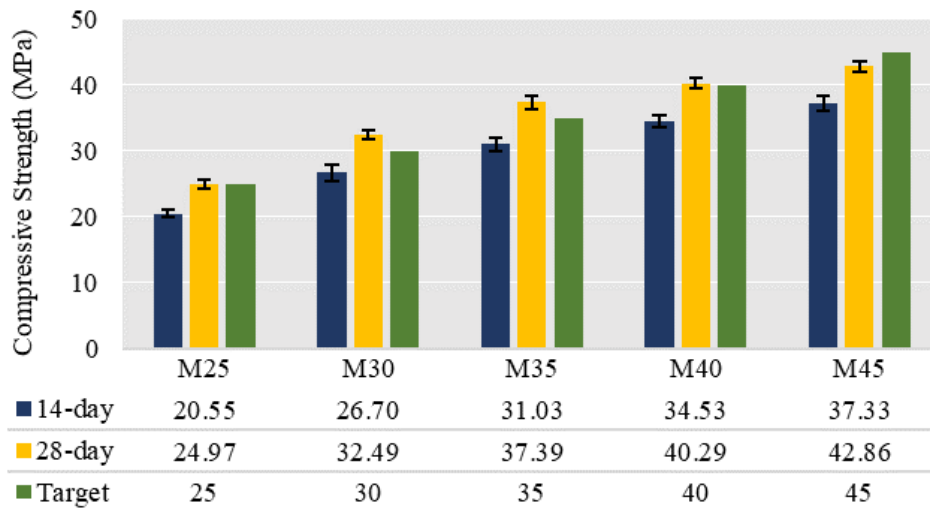


Figure 4-13: Results of laboratory experiments for mixture design of mortars incorporating MPCM having thermophysical properties similar to that of PCM B.

Another striking finding is that the optimization results suggest no clear trend in the cement content or W/C ratio of the mixture concerning the compressive strength. Nevertheless, a continual decline in the MPCM-to-cement (MPCM/C) ratio with an increase in the required compressive strength can be observed. **Figure 4-14** compares the MPCM/C ratio for concretes and mortars incorporating PCM A and PCM B concerning the compressive

strength. Accordingly, to achieve a compressive strength of 25 MPa, the MPCM/C ratio should be approximately 0.25. This ratio is around 0.1 for compressive strength of more than 40 MPa. Overall, the mixture optimization and laboratory tests validate the applied methodology and the developed ML models for predicting the compressive strength of such cementitious composites. The proposed mixture designs can be used as a benchmark for designing concrete mixtures incorporating MPCM with specified compressive strength and thermal energy storage capacity (*i.e.*, dosage and latent heat of MPCM) requirements.

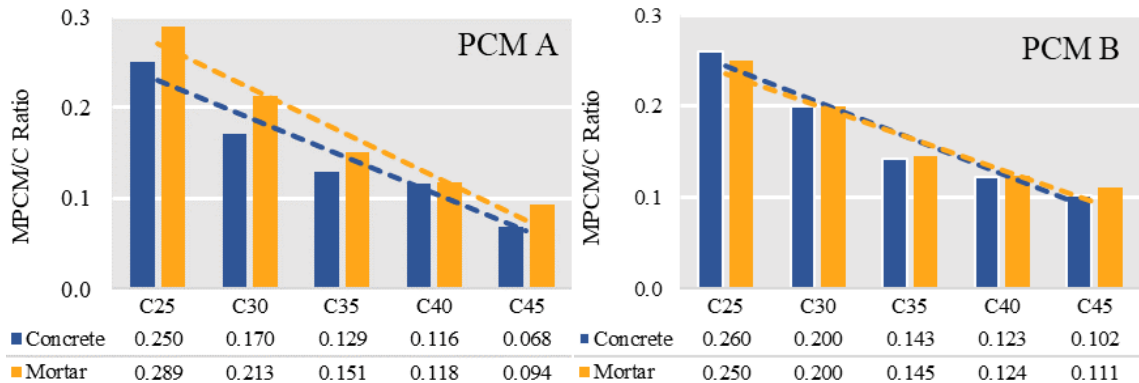


Figure 4-14: Comparison of MPCM/C ratio in proposed mixture designs.

However, the optimization strategy has some limitations that need to be addressed in future work. For instance, the water absorption of MPCMs was not approached in the same manner in experimental studies in the literature. Some studies recommended high dosages of superplasticizer (SP) to mitigate the low workability of concrete made with high MPCM dosage, whereas others attempted to add extra water to account for the absorbed water by MPCM. Given the dearth of data on the slump of MPCM integrated concrete mixtures in the literature, the SP dosage (SP) was not optimized based on workability criteria. Therefore, a multi-objective optimization considering workability along with mechanical requirements can give better SP dosage recommendations.

4.7 Conclusions, recommendations, and future Work

The objective of the present study was to investigate the influence of microencapsulated phase change materials (MPCM) on the compressive strength of concrete along with proposing a robust mixture optimization approach via a ternary machine learning (ML)

model. After collecting the largest available experimental dataset, the state-of-the-art tabular generative adversarial network (TGAN) was implemented to create a large synthetic dataset. Powerful ML models, including random forest regression (RFR), gradient boosting regression (GBR), and deep neural network (DNN), were trained with the synthetic data and tested using the entire collected experimental dataset. Results indicate accurate predictions by the developed models along with promising generalized performance. The best predictive model was coupled with particle swarm optimization to propose an optimized mixture proportions approach for different types of MPCM and compressive strength classes. The findings below could be drawn from this work:

- The results validate the methodology of developing synthetic data for training robust ML models in materials science problems where the available data is insufficient.
- The ML models developed in this study successfully predicted the compressive strength of MPCM-integrated concrete with high accuracy. An R^2 of 0.963 and MAE of 2.085 MPa were achieved using the GBR-TSTR model when tested on the entire experimental dataset.
- Extensive numerical experiments highlighted the significant effect of the cement dosage to compensate for the loss of compressive strength due to MPCM addition.
- Thermophysical properties of MPCM such as density greatly affect the compressive strength of concrete. MPCM with higher density can be added at higher dosages to achieve specific compressive strength values compared to MPCM with lower density.
- Optimized mixture designs allow to the determination of the adequate dosage of MPCM for specific strength grades of mortar and concrete. For instance, to achieve a compressive strength of 25 MPa, 145 and 130 kg/m³ of PCM B can be added to mortar and concrete, respectively. On the other hand, only 60 and 52 kg/m³ of PCM B can be incorporated into mortar and concrete to achieve a compressive strength of 40 MPa.

- Mixture optimizations identified that the PCM to cement mass (PCM/C) ratio is highly correlated to the compressive strength; lower PCM/C is required for higher targeted compressive strength.
- An optimized version of the Bolomey equation was proposed to empirically estimate the compressive strength of concrete. The R^2 of the proposed model increased from 0.39 to 0.63 after the optimization.

The results of the present study can be improved in future research by including other influential parameters and performance indicators not explored in the current study. More experimental research is required to augment the original dataset with other influential features such as the water absorption of MPCM and including performance-based properties of concrete such as the slump of MPCM integrated concrete mixtures. The multi-objective optimization of concrete mixtures concerning both mechanical and thermal performance is an interesting endeavor for future research.

4.8 References

- Aguayo, M., Das, S., Maroli, A., Kabay, N., Mertens, J. C., Rajan, S. D., Sant, G., Chawla, N., & Neithalath, N. (2016). The influence of microencapsulated phase change material (PCM) characteristics on the microstructure and strength of cementitious composites: Experiments and finite element simulations. *Cement and Concrete Composites*, 73, 29-41.
- Akanbi, L. A., Oyedele, A. O., Oyedele, L. O., & Salami, R. O. (2020). Deep learning model for Demolition Waste Prediction in a circular economy. *Journal of Cleaner Production*, 274, 122843.
- Antoniou, A., Storkey, A., & Edwards, H. (2017). Data augmentation generative adversarial networks. arXiv preprint arXiv:1711.04340.
- Arjovsky, M., Chintala, S., & Bottou, L. (2017). Wasserstein generative adversarial networks. *International conference on machine learning*,

Asteris, P. G., Skentou, A. D., Bardhan, A., Samui, P., & Pilakoutas, K. (2021). Predicting concrete compressive strength using hybrid ensembling of surrogate machine learning models. *Cement and concrete research*, 145, 106449.

Balapur, M., Mutua, A. W., & Farnam, Y. (2021). Evaluating the thermal efficiency of microencapsulated phase change materials for thermal energy storage in cementitious composites. *Cement and Concrete Composites*, 116, 103891.

Breiman, L. (2001). Random forests. *Machine learning*, 45(1), 5-32.

Breiman, L. (2017). *Classification and regression trees*. Routledge.

Chwieduk, D. (2003). Towards sustainable-energy buildings. *Applied Energy*, 76(1-3), 211-217.

Cunha, S., Aguiar, J., Ferreira, V., & Tadeu, A. (2015). Mortars based in different binders with incorporation of phase-change materials: Physical and mechanical properties. *European Journal of Environmental and Civil Engineering*, 19(10), 1216-1233.

Cunha, S., Lima, M., & Aguiar, J. B. (2016). Influence of adding phase change materials on the physical and mechanical properties of cement mortars. *Construction and Building Materials*, 127, 1-10.

D'Alessandro, A., Pisello, A. L., Fabiani, C., Ubertini, F., Cabeza, L. F., & Cotana, F. (2018). Multifunctional smart concretes with novel phase change materials: Mechanical and thermo-energy investigation. *Applied energy*, 212, 1448-1461.

Dehdezi, P. K., Hall, M. R., Dawson, A. R., & Casey, S. P. (2013). Thermal, mechanical and microstructural analysis of concrete containing microencapsulated phase change materials. *International Journal of Pavement Engineering*, 14(5), 449-462.

Djamai, Z. I., Salvatore, F., Larbi, A. S., Cai, G., & El Mankibi, M. (2019). Multiphysics analysis of effects of encapsulated phase change materials (PCMs) in cement mortars. *Cement and Concrete Research*, 119, 51-63.

Drissi, S., Ling, T.-C., Mo, K. H., & Eddhahak, A. (2019). A review of microencapsulated and composite phase change materials: Alteration of strength and thermal properties of cement-based materials. *Renewable and sustainable energy reviews*, 110, 467-484.

Eberhart, R., & Kennedy, J. (1995). A new optimizer using particle swarm theory. *MHS'95. Proceedings of the Sixth International Symposium on Micro Machine and Human Science*,

Esteban, C., Hyland, S. L., & Rättsch, G. (2017). Real-valued (medical) time series generation with recurrent conditional gans. *arXiv preprint arXiv:1706.02633*.

Falzone, G., Falla, G. P., Wei, Z., Zhao, M., Kumar, A., Bauchy, M., Neithalath, N., Pilon, L., & Sant, G. (2016). The influences of soft and stiff inclusions on the mechanical properties of cementitious composites. *Cement and Concrete Composites*, 71, 153-165.

Fekri, M. N., Ghosh, A. M., & Grolinger, K. (2020). Generating energy data for machine learning with recurrent generative adversarial networks. *Energies*, 13(1), 130.

Fenollera, M., Míguez, J. L., Goicoechea, I., Lorenzo, J., & Ángel Álvarez, M. (2013). The influence of phase change materials on the properties of self-compacting concrete. *Materials*, 6(8), 3530-3546.

Geurts, P., Ernst, D., & Wehenkel, L. (2006). Extremely randomized trees. *Machine learning*, 63(1), 3-42.

Goodfellow, I., Pouget-Abadie, J., Mirza, M., Xu, B., Warde-Farley, D., Ozair, S., Courville, A., & Bengio, Y. (2014). Generative adversarial nets. *Advances in neural information processing systems*,

Hunger, M., Entrop, A., Mandilaras, I., Brouwers, H., & Founti, M. (2009). The behavior of self-compacting concrete containing micro-encapsulated phase change materials. *Cement and Concrete Composites*, 31(10), 731-743.

Jayalath, A., San Nicolas, R., Sofi, M., Shanks, R., Ngo, T., Aye, L., & Mendis, P. (2016). Properties of cementitious mortar and concrete containing micro-encapsulated phase change materials. *Construction and Building Materials*, 120, 408-417.

- Ke, G., Meng, Q., Finley, T., Wang, T., Chen, W., Ma, W., Ye, Q., & Liu, T.-Y. (2017). Lightgbm: A highly efficient gradient boosting decision tree. *Advances in neural information processing systems*,
- Lecompte, T., Le Bideau, P., Glouannec, P., Nortershauser, D., & Le Masson, S. (2015). Mechanical and thermo-physical behaviour of concretes and mortars containing phase change material. *Energy and Buildings*, 94, 52-60.
- Liu, F., Wang, J., & Qian, X. (2017). Integrating phase change materials into concrete through microencapsulation using cenospheres. *Cement and Concrete Composites*, 80, 317-325.
- Marani, A., Jamali, A., & Nehdi, M. L. (2020). Predicting Ultra-High-Performance Concrete Compressive Strength Using Tabular Generative Adversarial Networks. *Materials*, 13(21), 4757.
- Marani, A., & Madhkhan, M. (2021). Thermal performance of concrete sandwich panels incorporating phase change materials: An experimental study. *Journal of Materials Research and Technology*, 12, 760-775.
- Marani, A., & Nehdi, M. L. (2019). Integrating phase change materials in construction materials: Critical review. *Construction and Building Materials*, 217, 36-49.
- Marani, A., & Nehdi, M. L. (2020). Machine learning prediction of compressive strength for phase change materials integrated cementitious composites. *Construction and Building Materials*, 265, 120286.
- Memon, S. A. (2014). Phase change materials integrated in building walls: A state of the art review. *Renewable and sustainable energy reviews*, 31, 870-906.
- Meshgin, P., & Xi, Y. (2012). Effect of Phase-Change Materials on Properties of Concrete. *ACI Materials Journal*, 109(1).
- Mirza, M., & Osindero, S. (2014). Conditional generative adversarial nets. *arXiv preprint arXiv:1411.1784*.

- Nunez, I., Marani, A., & Nehdi, M. L. (2020). Mixture Optimization of Recycled Aggregate Concrete Using Hybrid Machine Learning Model. *Materials*, 13(19), 4331.
- Pedregosa, F., Varoquaux, G., Gramfort, A., Michel, V., Thirion, B., Grisel, O., Blondel, M., Prettenhofer, P., Weiss, R., & Dubourg, V. (2011). Scikit-learn: Machine learning in Python. *the Journal of machine Learning research*, 12, 2825-2830.
- Pelikan, M., Goldberg, D. E., & Cantú-Paz, E. (1999). BOA: The Bayesian optimization algorithm. *Proceedings of the genetic and evolutionary computation conference GECCO-99*,
- Pilehvar, S., Cao, V. D., Szczotok, A. M., Valentini, L., Salvioni, D., Magistri, M., Pamies, R., & Kjøniksen, A.-L. (2017). Mechanical properties and microscale changes of geopolymer concrete and Portland cement concrete containing micro-encapsulated phase change materials. *Cement and Concrete Research*, 100, 341-349.
- Pilehvar, S., Sanfeliix, S. G., Szczotok, A. M., Rodríguez, J. F., Valentini, L., Lanzón, M., Pamies, R., & Kjøniksen, A.-L. (2020). Effect of temperature on geopolymer and Portland cement composites modified with Micro-encapsulated Phase Change materials. *Construction and Building Materials*, 252, 119055.
- Qiu, F., Song, S., Li, D., Liu, Y., Wang, Y., & Dong, L. (2020). Experimental investigation on improvement of latent heat and thermal conductivity of shape-stable phase-change materials using modified fly ash. *Journal of Cleaner Production*, 246, 118952.
- Sanfeliix, S. G., Zea-García, J. D., Londono-Zuluaga, D., Santacruz, I., Angeles, G., & Kjøniksen, A.-L. (2020). Hydration development and thermal performance of calcium sulphoaluminate cements containing microencapsulated phase change materials. *Cement and Concrete Research*, 132, 106039.
- Snoeck, D., Priem, B., Dubruel, P., & De Belie, N. (2016). Encapsulated Phase-Change Materials as additives in cementitious materials to promote thermal comfort in concrete constructions. *Materials and Structures*, 49(1), 225-239.

Wei, Z., Falzone, G., Wang, B., Thiele, A., Puerta-Falla, G., Pilon, L., Neithalath, N., & Sant, G. (2017). The durability of cementitious composites containing microencapsulated phase change materials. *Cement and Concrete Composites*, 81, 66-76.

Xu, L., & Veeramachaneni, K. (2018). Synthesizing tabular data using generative adversarial networks. *arXiv preprint arXiv:1811.11264*.

Yang, H.-B., Liu, T. C., Chern, J.-C., & Lee, M.-H. (2016). Mechanical properties of concrete containing phase-change material. *Journal of the Chinese institute of engineers*, 39(5), 521-530.

Young, B. A., Hall, A., Pilon, L., Gupta, P., & Sant, G. (2019). Can the compressive strength of concrete be estimated from knowledge of the mixture proportions?: New insights from statistical analysis and machine learning methods. *Cement and concrete research*, 115, 379-388.

Zhang, J., Huang, Y., Aslani, F., Ma, G., & Nener, B. (2020). A hybrid intelligent system for designing optimal proportions of recycled aggregate concrete. *Journal of Cleaner Production*, 273, 122922.

Zhang, J., Huang, Y., Wang, Y., & Ma, G. (2020). Multi-objective optimization of concrete mixture proportions using machine learning and metaheuristic algorithms. *Construction and Building Materials*, 253, 119208.

Zhang, Y., & Ling, C. (2018). A strategy to apply machine learning to small datasets in materials science. *Npj Computational Materials*, 4(1), 1-8.

Chapter 5

5 Activation Energy of Cement-Based Materials Incorporating Microencapsulated Phase Change Materials¹

This study deploys the apparent activation energy concept to explore the reaction kinetics and temperature sensitivity of cement hydration in the presence of microencapsulated phase change materials (MPCMs). Extensive isothermal calorimetry and compressive strength measurements revealed that the addition of MPCMs significantly decreases the apparent activation energy, thus reducing the sensitivity of mechanical strength development to the curing temperature. Furthermore, it was observed that the melting temperature of MPCMs has insignificant effect on cement hydration kinetics and the apparent activation energy. Microstructural analyses suggest that the variation in the effect of MPCMs with different melting temperatures on the compressive strength is likely related to the compatibility of the MPCM shell material with the cementitious matrix, with weaker interfacial transition zone, and resultant more porous structure. The results should allow better evaluation of the heat of hydration stresses and temperature-related properties of MPCM-integrated concrete.

5.1 Introduction

The drastic global energy demand and the advent of a miscellany of environmental exigencies, such as climate change and the need to attain NetZero goals, have entailed determined efforts to carry through sustainable and resilient built environment measures. Resorting to renewable energy resources along with enhancing the energy efficiency of diverse economic sectors have been among the promising solutions to tackle energy-related crises (Chwieduk, 2003). Residential and commercial buildings are responsible for a conspicuous proportion of global energy consumption, a share higher than that of the industry and transportation sectors. According to multiple studies, buildings account for

¹ A version of this chapter is under review in “*Cement and Concrete Research*” journal, 2022.

around 40% of total global energy consumption and over 30% of the CO₂ emissions (Costa *et al.*, 2013; Yang *et al.*, 2014). Therefore, boosting the energy efficiency of buildings is of particularly great concern.

Development and fulfillment of low-carbon energy (LCE) policies alongside thermal energy storage (TES) in buildings are recognized as reassuring solutions toward a low-carbon eco-friendly built environment. TES systems are typically classified into three different categories including sensible heat storage (SHS), latent heat storage (LHS), and thermochemical heat storage (THS) (Lizana *et al.*, 2018). In LHS, thermal energy is conserved or retrieved when the heat storage medium undergoes a phase transition, e.g., solid to liquid, while the temperature of the medium remains constant (Zhang *et al.*, 2004). LHS mediums are commonly referred to as phase change materials (PCMs) and have been widely integrated into building components to provide TES capacity (Cabeza *et al.*, 2011; Pomianowski *et al.*, 2014). Extensive research studies have demonstrated the significant contribution of PCM-integrated building components toward decreasing the energy consumption of buildings (Lizana *et al.*, 2018; Soares *et al.*, 2013).

Concrete is the world's second most-consumed commodity after water and has been predominantly utilized for the incorporation of PCMs. PCMs can be added to concrete mixtures through various incorporation methods such as direct impregnation, lightweight aggregate impregnation, shape-stabilized PCM, macro-encapsulation, and microencapsulation (Marani & Nehdi, 2019). Microencapsulated PCMs (MPCMs) have been widely integrated into cement mortar and concrete owing to their high efficacy and minimum leakage risk. Multiple research studies have explored the influence of MPCM addition on the engineering properties of cement-based mortars and concrete (Drissi *et al.*, 2019). Accordingly, MPCMs favorably impact the thermal performance of concrete owing to their LHS capability. Nevertheless, they can impose negative effects on mechanical properties. In particular, the compressive strength of concrete dramatically decreases after the addition of MPCMs. Several mechanisms have been postulated to explain such a reduction in compressive strength. Low stiffness and strength of polymeric MPCM particles, void-like action, increased concrete porosity induced by MPCMs, breakage of

microcapsules, etc., are among the primary explanations for the reduction of compressive strength in MPCM-integrated cementitious composites.

Sparse research studies also evidenced that the addition of MPCMs could affect the hydration and microstructural development of cement-based composites. Yet, the synergic effect of MPCMs' thermophysical properties and curing conditions on the cement hydration kinetics and strength development of MPCM-integrated concrete remain largely unexplored. Hence the current research aims at proposing a unified experimental methodology to quantify the influence of MPCMs on the cement hydration kinetics and apparent activation energy of MPCM-integrated concrete. Purposefully, an extensive experimental program was carried out to analyze the variation in the apparent activation energy of cement pastes and mortars after MPCM addition. The subsequent section discusses the basis of the apparent activation energy concept and reviews the research on the effect of PCM inclusion on cement hydration. Thereafter, the experimental methodology is elaborated, followed by a profound discussion of the obtained experimental results.

5.2 Background knowledge and literature review

5.2.1 Apparent activation energy

The chemical reaction of cement particles with water in hardening concrete is an exothermic process in which a great deal of heat is generated. The released heat originates a considerable increase in the temperature of the hydrating concrete. Characterization of the changes in the temperature during the placement and curing stages of concrete is of great importance (Poole *et al.*, 2007). The curing temperature of concrete is known to wield an enormous influence on the rate of cement hydration (D'aloia & Chanvillard, 2002). Meanwhile, a precise and rigorous assessment of the hydration process of a cementitious system is required to estimate temperature gradients, the maximum temperature of concrete, thermal stresses and deformations, and related mechanical properties (Assi *et al.*, 2018). The hydration kinetics of a cement-based composite greatly depends on the chemical and physical properties of the cementitious materials (Bogner *et al.*, 2020; Zajac *et al.*, 2018). Additionally, the incorporation of reactive or nonreactive additives to the

binder along with the curing temperature can exert dominant effects on the hydration kinetics (Tafesse & Kim, 2019; Yan *et al.*, 2020).

The concept of activation energy of cementitious materials represents the minimum energy that cement particles need to trigger their chemical reactions with water. During the cement hydration process, several phases simultaneously react with water, while the reaction products continuously change with time. Notwithstanding that the activation energy concept is not technically applicable to cement hydration, the Arrhenius theory employs the “apparent activation energy” (E_a) to apprehend the temperature sensitivity of portland cement hydration (Saadoon *et al.*, 2019). According to the Arrhenius theory, the temperature-related variations in the specific rate of a given reaction can be described as follows:

$$k = A \cdot e^{-\frac{E_a}{RT}} \quad \text{Eq. 5-1}$$

where R is the universal gas constant (8.314 J/mol/K), T is the temperature (K) at which the reaction occurs, k is the rate of reaction (W), A is the proportionality constant, and E_a is the activation energy (J/mol). The proportionality constant (A) is typically not considered in cement hydration since the ratio of the reaction rates is used in maturity calculations and thus, E_a is calculated independent of A. The measurements of the reaction rates at different isothermal temperatures can be utilized to quantify the experimental E_a . Therefore, isothermal calorimetry data can be used to investigate the rates of the hydration heat at various temperatures and compute the apparent activation energy based on the Arrhenius theory (Kada-Benameur *et al.*, 2000; Pang *et al.*, 2021; Thomas *et al.*, 2017).

The degree of hydration (DOH) of cement, α , quantifies the proportion of cement particles that have hydrated, and is typically employed to represent the cement hydration progress. The DOH of cement at any time t, $\alpha(t)$ can be calculated using the following equation:

$$\alpha(t) = H(t)/H_{cem} \quad \text{Eq. 5-2}$$

where H(t) is the cumulative heat released from the cement reaction at time t (J/g) and H_{cem} is the total heat of hydration of cement (J/g). H_{cem} can be obtained using the

proportion of phases and chemical compositions of the cement based on the Bogue's equation as per **Eq. 5-3**, where P_i denotes the mass fraction of the i^{th} chemical composition:

$$H_{cem} = 500 \cdot P_{C_3S} + 260 \cdot P_{C_2S} + 866 \cdot P_{C_3A} + 420 \cdot P_{C_4AF} + 624 \cdot P_{SO_3} + 1186 \cdot P_{FreeCa} + 850 \cdot P_{MgO} \quad \text{Eq. 5-3}$$

After computing the DOH at every time step of the isothermal calorimetry test, the cement hydration progress can be mathematically expressed using several hydration models. Among the proposed models, a three-parameter exponential function has been widely utilized to quantify the hydration progress with time as follows:

$$\alpha(t) = \alpha_u e^{-\left(\frac{\tau}{t}\right)^\beta} \quad \text{Eq. 5-4}$$

where α_u is the maximum DOH, τ is the hydration time parameter, and β is the hydration shape parameter (Poole *et al.*, 2007). Determining these hydration parameters can provide useful information about the hydration development of cementitious systems. For instance, a decrease or increase in the hydration time parameter (τ) denotes an accelerated or decelerated reaction along with lower or greater time to reach the peak of hydration rate, respectively. The setting behavior of the cement-based mixture is highly correlated to the maximum rate of the hydration and thus, the hydration time parameter could represent the setting time of the mixture. β characterizes the slope of the DOH curve as the higher values indicate greater slopes of the heat evolution and DOH curves. A decrease in the β (the slope of the heat evolution curve) denotes a higher DOH of the mixture at earlier stages of hydration. Conversely, an increase in β represents lower DOH at the initial stages of the hydration process (Sargam & Wang, 2021).

Another approach to calculating the apparent activation energy of concrete is to use compressive strength or setting time measurements of mixtures at various temperatures. Researchers have calculated the activation energy of concrete incorporating supplementary cementitious materials (SCMs), retarding admixtures, rapid hardening agents, etc., using strength or setting time measurements (Han & Han, 2010; Pinto & Schindler, 2010; Saadoon *et al.*, 2019). The apparent activation energy can be further used in the maturity

method to estimate the compressive strength of the concrete from its curing temperature history as specified in ASTM C1074 standard (ASTM, 2004). Various prediction models can be employed to obtain the strength development parameters and subsequently calculate the apparent activation energy as will be explained later in **Section 5.3**.

5.2.2 Effect of PCMs on cement hydration

There have been several recent research studies on the effect of MPCM inclusion on the hydration kinetics and strength development of cementitious systems. As mentioned earlier, the compressive strength of concrete significantly decreases after the addition of MPCMs. Although the major reason for the reduction of compressive strength is the low strength of MPCM particles compared to other components of concrete, the effects of MPCM particles on the cement hydration, microstructural development, and pore structure of the cementitious matrix are also significant (Drissi *et al.*, 2021; Marani & Nehdi, 2019). For instance, Djamaï *et al.* (Djamaï *et al.*, 2019) evidenced that accessible pore volume and critical pore diameter of MPCM-integrating specimens were much higher compared to that of control samples due to the unbound water attributed to the interaction of MPCMs with cement particles. Comparable findings were reported in studies by Pilehvar *et al.* (Pilehvar *et al.*, 2017) and Sanfelix *et al.* (Sanfelix *et al.*, 2019), demonstrating the adverse effect of MPCMs on the porosity of cementitious matrices.

MPCMs can also impact the hydration kinetics of portland cement and geopolymer concrete. Eddhahak *et al.* (Eddhahak *et al.*, 2014) found that the addition of 5% MPCMs to cement paste led to 10% decrease in the heat of hydration in a 5-day hydration period. Additionally, a delay in the hydration process due to the latent heat of MPCMs was identified. Pilehvar *et al.* (Pilehvar *et al.*, 2020) observed that the addition of MPCMs decreased and delayed the hydration rate of geopolymer and Portland cement paste. Various mechanisms have been postulated regarding the change in the hydration kinetics, such as the relatively high water absorption of MPCMs, MPCMs wrapping around cement particles and blocking their access to water, reduction in available nucleation sites with the addition of MPCMs, etc. (Djamaï *et al.*, 2019; Pilehvar *et al.*, 2017). Furthermore, the curing temperature can affect the hydration kinetics, microstructural and strength development of cementitious composites. Pilehvar *et al.* (Pilehvar *et al.*, 2020) noted that

at higher curing temperatures, hydration reactions of cement pastes containing MPCMs were faster and the compressive strength was higher at the early stages.

5.3 Materials and methods

5.3.1 Materials

Ordinary ASTM C150 Type I portland cement (OPC) was used for paste and mortar specimen preparation. **Table 5-1** presents the chemical composition of OPC. Two types of non-formaldehyde biobased MPCMs having melting temperatures of 28 and 35°C, referred to as En28 and En35, respectively, supplied by Encapsys LLC were used. Natural river sand and a polycarboxylate-based superplasticizer were also used for making mortar specimens. The thermophysical properties of En28 and En35 are listed in **Table 5-2**. **Figure 5-1** illustrates differential scanning calorimetry (DSC) curves of MPCMs.

Table 5-1: Chemical composition of OPC

Components	Proportion (%)	Components	Proportion (%)
Silicon oxide (SiO ₂)	19.6	Free Calcium	1
Aluminum oxide (Al ₂ O ₃)	4.8	Other oxides	-
Ferric oxide (Fe ₂ O ₃)	3.3	Tricalcium silicate (C ₃ S)	55
Calcium oxide (CaO)	61.5	Dicalcium silicate (C ₂ S)	15
Magnesium oxide (MgO)	3	Tricalcium aluminate (C ₃ A)	7
Sulfur trioxide (SO ₃)	3.5	Tetracalcium aluminoferrite (C ₄ AF)	10

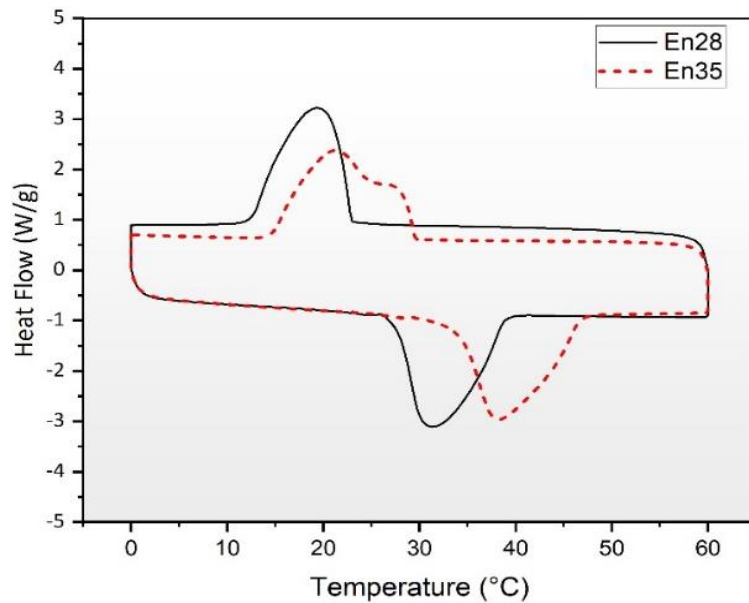


Figure 5-1: DSC curves of MPCMs

Table 5-2: Thermophysical properties of MPCMs

MPCM	Melting point (°C)	Melting enthalpy (kJ/kg)	Mean particle size (µm)
En28	28	175	22.6
En35	35	180	25.4

5.3.2 Experimental program

In this research, the cement hydration kinetics, strength development, and apparent activation energy of cement pastes and mortars incorporating MPCMs were calculated using isothermal calorimetry and compressive strength measurements. The microstructure and porosity of the mortars were further analyzed using scanning electron microscopy (SEM) and 3D X-ray micro-computed tomography (μ -CT) scans as explained below.

5.3.2.1 Isothermal calorimetry of cement pastes

Isothermal calorimetry was employed to study the hydration kinetics and calculate the activation energy of cement pastes incorporating En28 and En35. A water-to-cement (w/c) ratio of 0.5 was selected and MPCMs were added at dosages of 0, 5, 10, 15, 20, and 25 % by cement weight. **Table 5-3** summarizes the mixtures prepared for the isothermal calorimetry test. The heat of hydration of cement pastes was measured in an eight-channel microcalorimeter (TAM air, TA Instruments) at five different temperatures including 15, 23, 30, 35, and 40 ± 0.02 °C. Collectively, 55 isothermal calorimetry tests (11 mixtures at 5 testing temperatures) were conducted to obtain the rate of hydration data. The calorimetry measurements were performed using an ex-situ mixing procedure of approximately 5 grams of cement paste for 96 h. It is noteworthy that opening the cover and putting the ampoule into the channel can cause a drastic increase in the heat flow for the initial few minutes of the experiments. Thus, the measurements were considered from 0.75 h after the placement of the sample to minimize this error.

Table 5-3: Mixture components of cement pastes used for isothermal calorimetry tests

Designation	Cement (g)	Water (g)	En28 (g)	Designation	Cement (g)	Water (g)	En35 (g)
P0En28	3	1.5	0	P0En35	3	1.5	0
P05En28	3	1.5	0.15	P05En35	3	1.5	0.15
P10En28	3	1.5	0.3	P10En35	3	1.5	0.3
P15En28	3	1.5	0.45	P15En35	3	1.5	0.45
P20En28	3	1.5	0.6	P20En35	3	1.5	0.6
P25En28	3	1.5	0.75	P25En35	3	1.5	0.75

5.3.2.2 Compressive strength of cement mortars

Three different mortar mixtures were considered for the compressive strength measurements including a control mixture without MPCM, a mixture incorporating En28, and a mixture incorporating En35. MPCMs were added as partial replacement for sand particles. **Table 5-4** presents the mixture design of the mortars. The apparent activation energy of cement mortars was calculated based on ASTM C1074 (ASTM, 2004), which suggests a minimum three replicates of mortar specimens per mixture that are moist cured at three different temperatures and tested at seven testing ages. Furthermore, it is recommended that the first test should be performed when the compressive strength is approximately 4 MPa. Subsequent compressive strength tests must be carried out at ages that are approximately twice the previous testing age. Accordingly, in this study, 50-mm mortar cubes were moist cured in temperature-controlled water baths or a moist room at 5 different curing temperatures including 15, 23, 30, 35, and 40 ± 1 °C. The compressive strength was measured at least at 8 different ages using three specimen replicates.

Table 5-4: Mixture proportions of cement mortars used for compressive strength tests

Mixture	Cement (kg/m ³)	Water (kg/m ³)	Sand (kg/m ³)	MPCM (kg/m ³)	Superplasticizer (kg/m ³)	Type of MPCM
R	500	225	1598	0	10	-
En28	500	225	1358	75	10	En28
En35	500	225	1358	75	10	En35

5.3.2.3 Microstructure of cement mortars

Microstructure and porosity of hardened cement mortars were investigated using scanning electron microscopy (SEM) and X-ray micro-computed tomography (μ -CT scan). SEM imaging was performed by a Hitachi TM3030Plus electron microscope at an accelerating voltage of 15 kV. A Nikon XT H 225 ST (Nikon Corporation) was used for μ CT scans. High-resolution 2D X-ray images were captured while specimens were rotating 360° to construct the 3D CT volume. The 3D volumetric representation of the scans and the image analysis were carried out via the Dragonfly software.

5.3.3 Calculation of apparent activation energy (E_a)

5.3.3.1 Calculation of E_a using isothermal calorimetry

Different methods have been proposed to determine the apparent activation energy, E_a of cement-based systems using the isothermal calorimetry (Bentz, 2014; D'aloia & Chanvillard, 2002; Kada-Benameur *et al.*, 2000). In a comparative study, Poole *et al.* (Poole *et al.*, 2007) proposed three methods for calculating E_a including single linear approximation, incremental, and modified ASTM C1074 methods. In this research, the linear approximation and modified ASTM C1074 methods were used to investigate the apparent activation energy of cement pastes incorporating MPCMs.

5.3.3.1.1 Linear approximation method

The linear approximation of the hydration rate is a simple technique to estimate the apparent activation energy. This method calculates E_a based on the slope of the acceleratory segment of the cumulative released heat curve. The procedure for obtaining the apparent activation energy using the linear method is summarized below and schematically illustrated in **Fig. 5-2**.

- i) The released heat rate measurements along with the cumulative released heat data are obtained from the isothermal calorimetry test for each cement mixture (**Fig. 5-2a**).
- ii) The acceleratory region of the reaction rate, which contains the peak of the hydration curve (R_{max}), is determined (**Fig. 5-2b**). The reaction rate (k) is calculated as the linear slope of the cumulative released heat in the acceleratory region using a least-squares linear regression (**Fig. 5-2c**). It is noteworthy that the hydration rate curve is used to determine the acceleratory region, but the cumulative released heat curve is deployed to obtain the reaction rate.
- iii) The natural logarithm of the reaction rate (k) is plotted versus the inverse of the absolute temperature (in Kelvin) for each mixture (**Fig. 5-2d**).
- iv) Using **Eq. 5-1**, the activation energy for each mixture is calculated by multiplying the negative of the slope of $\ln(k) - 1/T$ linear line with the universal gas constant R ($8.314 \text{ J} \cdot (\text{mol} \cdot \text{K})^{-1}$).

Although the linear approximation method is a straightforward scheme to acquire the apparent activation energy, it has some drawbacks. The determination of the peak point, and thus the linear portion in the hydration curve, could be subjective depending on the peaks related to C_3S and C_3A hydration. Furthermore, only limited hydration data points, including the acceleratory segment and peak of the hydration curve, are utilized to calculate the activation energy in the linear method. Another disadvantage of this method is that the start of the acceleratory region cannot be easily distinguished for experiments conducted at low temperatures. This judgment is further thwarted in the case of MPCM-integrated cement pastes due to the delaying effect of MPCMs on the hydration peak as will be discussed later.

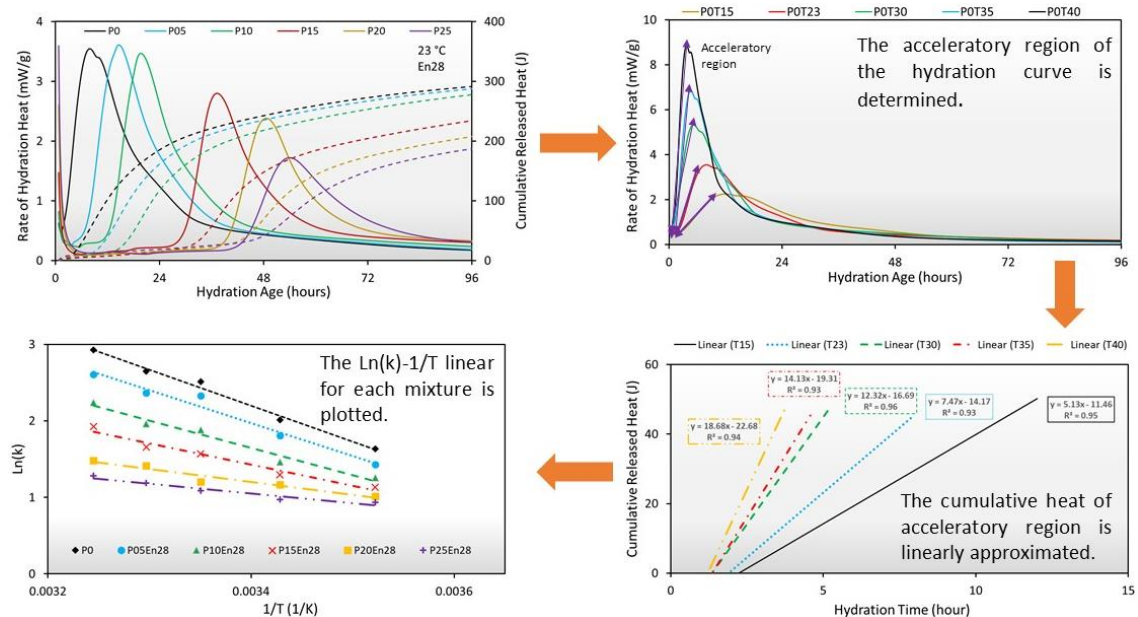


Figure 5-2: Steps of linear approximation method for calculating apparent activation energy.

5.3.3.1.2 Modified ASTM C1074

A unified methodology is described in ASTM C1074 (ASTM, 2004) to calculate the apparent activation energy of concrete based on the compressive strength data and equivalent age concept. Researchers have proposed a similar procedure to calculate E_a using the isothermal calorimetry data. A three-parameter exponential function expressed in Eq. 5-4 is utilized to model the cement hydration and obtain the hydration parameters

based on the DOH (Poole *et al.*, 2007; Schindler, 2004; Wirquin *et al.*, 2002). In this method, instead of using the equivalent time in the Arrhenius equation, the hydration time parameter is employed to calculate E_a using the following equation:

$$E_a = \frac{-\ln\left(\frac{\tau_{ref}}{\tau_c}\right)}{\left(\frac{1}{T_{ref}} - \frac{1}{T_c}\right)} \cdot R \quad \text{Eq. 5-5}$$

where τ_{ref} and τ_c are respectively the hydration time parameters at the reference and a given temperature, T_{ref} and T_c are respectively the temperatures of the mixture at the reference and a given temperature, and R is the universal gas constant. The following steps are required to obtain E_a based on the modified ASTM C1074 procedure and isothermal calorimetry data.

- i) The variation in the DOH of the hydrating cement paste versus time is calculated using **Eqs. 5-2** and **5-3**. The DOH at time t is determined by dividing the cumulative released heat at time t by the total heat of hydration of the cement paste obtained from **Eq. 5-3**.
- ii) The degree of hydration of the cementitious system is modeled with the three-parameter hydration model given in **Eq. 5-4**. For this purpose, the DOH data is fitted to the exponential function to solve for α_u , τ , and β using a least-squares method. Firstly, for each mixture, α_u , τ , and β values are computed for every test temperature. Afterward, the average values of α_u and β for each mixture are calculated. Using the average values of α_u and β , the value of τ at each isothermal temperature is recalculated.
- iii) The natural logarithm of the hydration time parameter (τ) is plotted versus the inverse of the absolute temperature (in Kelvin) for each mixture.
- iv) Using **Eq. 5-5**, the activation energy for each mixture is calculated by multiplying the negative of the slope of $\ln(\tau) - 1/T$ linear line with universal gas constant R (8.314 J.(mol.K)⁻¹).

5.3.3.2 Calculation of E_a using compressive strength

In addition to using the calorimetry data, E_a can also be calculated using the compressive strength data according to ASTM C1074 (ASTM, 2004). Accordingly, the strength development of concrete over the curing time can be modeled using the following hyperbolic equation:

$$S(t_e) = S_u \frac{k(t_e - t_0)}{1 + k(t_e - t_0)} \quad \text{Eq. 5-6}$$

where $S(t_e)$ is the strength at a given time (MPa), S_u is the ultimate strength at the infinite time (MPa), k is the reaction rate (1/days), t_e is the age for the predicted strength (days), and t_0 is the time at the start of strength development (days). The strength development could also be estimated using an exponential model as follows:

$$S(t_e) = S_u \cdot e^{-\left(\frac{\tau_s}{t_e}\right)^\beta} \quad \text{Eq. 5-7}$$

where τ_s is the strength time constant (days) and β is the strength shape constant (Saadoon *et al.*, 2019). Similar to using hydration data, a least-square program should be deployed to find the strength gain parameters. E_a of mixtures can be calculated by multiplying the slope of the $\ln(k) - 1/T$ curve by the universal gas constant (Zhang *et al.*, 2008). In the current study, the compressive strengths of the three replicates of mixtures listed in **Table 5-4** measured at 9 different ages were used to estimate the apparent activation energy.

5.4 Results and discussion

This section examines the effect of MPCM addition on the hydration kinetics and apparent activation energy of cement pastes and mortars. Firstly, the effect of MPCMs' dosages on the hydration heat evolution is analyzed. Thereafter, the results of apparent activation energy calculation are investigated to quantify the effect of the MPCMs on the temperature sensitivity of cement hydration. Furthermore, the compressive strengths of mortar specimens incorporating MPCMs are investigated. Microstructural analyses are performed to complement the observations inferred from hydration and strength experiments.

5.4.1 Effects of MPCM addition on cement hydration

Figures 5-3 and **5-4** illustrate the rate of hydration heat together with the cumulative released heat of the plain cement pastes and cement pastes incorporating En28 and En35, respectively, during the first 96 hours. Cement hydration is initiated with a first peak mainly due to the dissolution, followed by an induction period related to the slow-down stage of the dissolution process (Juilland *et al.*, 2010; Scrivener *et al.*, 2015). The major peaks related to the hydration of C_3S of the Portland cement was observed after the acceleration period. However, what stands out in the results is that the addition of MPCM to the cement paste exerted two notable influences on the hydration progress: (1) it prolonged the dormant period of the cement hydration resulting in a delay in the time to reach the hydration peak, known as the retarding effect; and (2) it caused a decrease in the peak of hydration rate, which is referred to as the depressing effect (Yan *et al.*, 2020; Yan *et al.*, 2021). Such alterations in the hydration process were substantiated in both types of MPCMs regardless of their melting temperature. Therefore, the inclusion of MPCMs in the cement pastes resulted in a reduction in the rate and degree of hydration reactions. It is noteworthy that low dosages of MPCM, *i.e.*, 5-10 wt.% of the cement, imposed a slight effect on the hydration kinetics of the cement paste. Nevertheless, with increasing the MPCM content in the cement paste, longer delays and more drastic reductions in the maximum rate and degree of hydration were evidenced.

The changes in the cement hydration kinetics can be linked to different physical origins. One probable reason for such a reduction in the intensity of hydration reactions is the dilution of the plain cement paste compared to pastes with MPCM inclusion, *i.e.*, reduction in the cement paste volume in the test sample (Fernandes *et al.*, 2014; Lawrence *et al.*, 2003). The dilution effect is further aggravated considering the significant water absorption of MPCM particles due to their polar polymeric shells. The water absorption of En28 and En35 was found to be approximately 40 and 48 wt.%. The water absorption of MPCMs has a complex effect on the cement hydration process. The water retained by MPCMs reduces the effective water content in the cement paste and thus, increases its viscosity. Consequently, the higher viscosity of the MPCM-integrated cement paste slows down the movement of the reactants and consequently the reaction rate (Pilehvar *et al.*, 2018;

Pilehvar *et al.*, 2017; Pilehvar *et al.*, 2020; Sanfelix *et al.*, 2019). Moreover, the lower water content can reduce the number of reactive agents that are dissolved before the saturation of the sample. Hence, the period of the low undersaturation due to the lesser amount of available water is extended, causing the retarding behavior. This mechanism is consistent with the pattern captured from increasing the MPCM dosages where the dormant period becomes longer at higher of MPCMs dosages, *i.e.*, 15-25 wt.%. The MPCM particles also enclose the cement particles and hinder the accessibility of water to the anhydrous cement grains (Djamai *et al.*, 2019). Another adverse consequence of MPCMs wrapping around cement particles is that the enclosed cement particles can no longer serve as surface nucleation sites for the growth of hydration products. Hence the duration of the dormant period is prolonged, and the rate of hydration is declined.

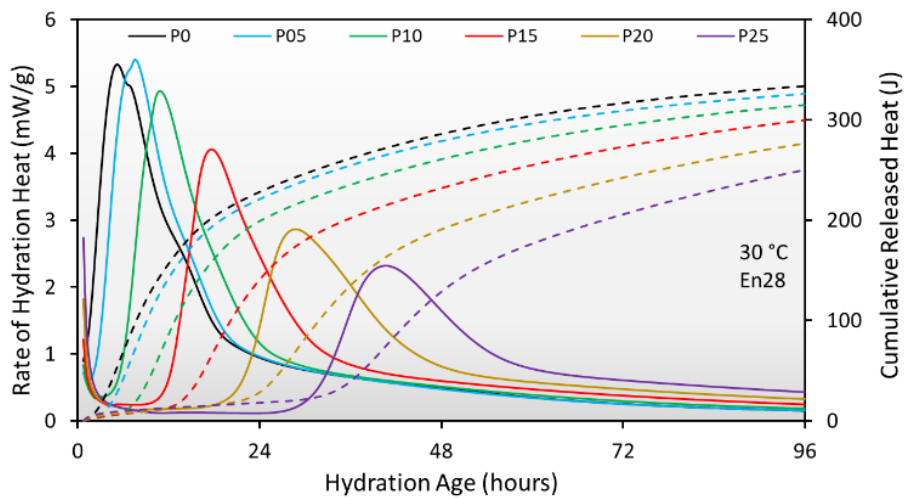
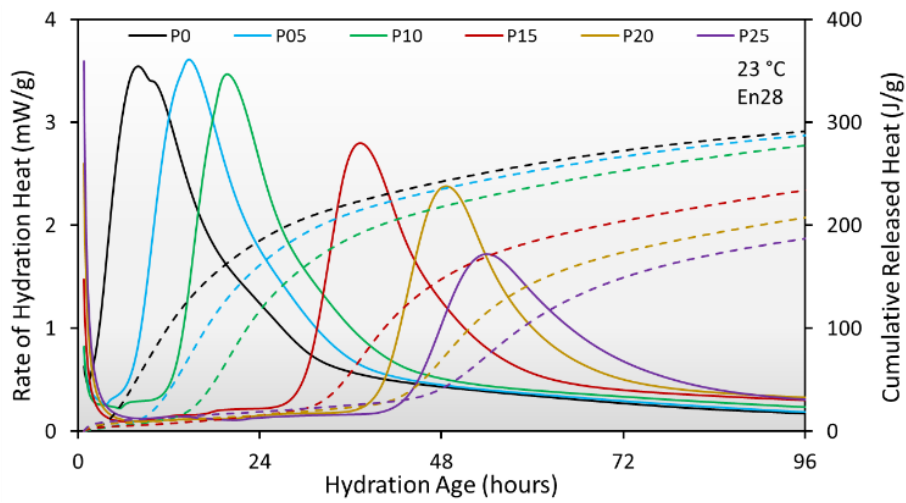
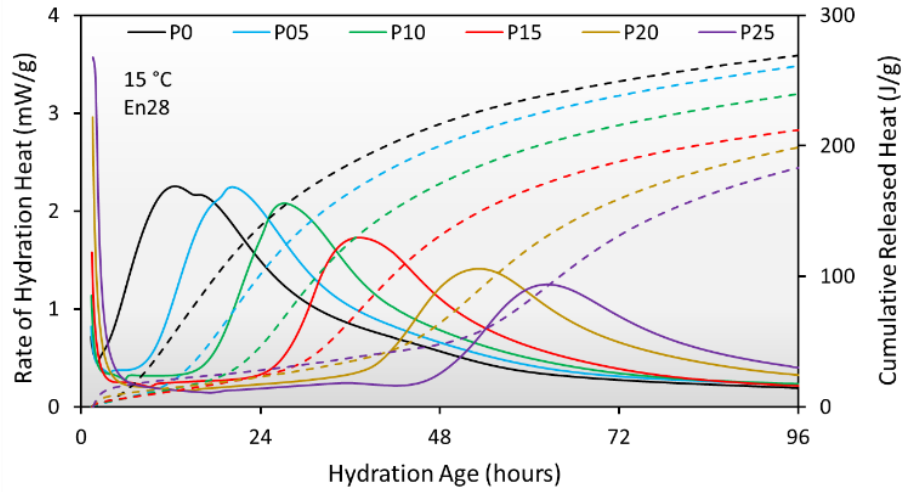
Ultimately, the delay in the hydration of the cement is intensified by the sensible and latent heat capacity of the MPCM particles as evidenced in isothermal and semi-adiabatic calorimetry experiments in the literature (Djamai *et al.*, 2019; Fernandes *et al.*, 2014; Pilehvar *et al.*, 2018; Pilehvar *et al.*, 2017; Pilehvar *et al.*, 2020). Nonetheless, the extent of the effect of the latent heat storage capability highly depends on the melting temperatures and enthalpies of the MPCMs along with the operating temperature of the experiments. To further investigate the effect of MPCM addition on the hydration kinetics, several parameters were extracted from the isothermal curves including the maximum hydration rate (R_{max}) and the time to reach the maximum hydration rate ($T_{R_{max}}$) as presented in **Table 5-5**. Accordingly, the reduction of the reaction rate and the delay in the hydration process with MPCM inclusion can be identified. For instance, $T_{R_{max}}$ of P05 and P15 mixtures containing En28 and tested at 15°C increased by 63.83 and 204.91%, respectively compared to corresponding values for the control mixture (*i.e.*, P0), respectively. With increasing the test temperature, this parameter significantly decreased, indicating a lower delay in the hydration process at higher temperatures. Notwithstanding, what is striking in the results presented in **Table 5-5** is the longer delays in all mixtures integrating En28 tested at 35°C compared to 30°C where the MPCM particles undergo a complete phase transition, causing an excessive delay in the hydration of cement. A similar trend was observed in mixtures containing En35 where $T_{R_{max}}$ for specimens tested at 40°C

is higher or immensely close to that of pastes tested at 35°C. Hence, it can be concluded that the synergic effect of the melting point of MPCMs and curing temperature impact the hydration process, in particular, the time to reach the maximum rate of hydration. This is of particular significance since $T_{R_{max}}$ is likely correlated to the setting time of the mixture.

The isothermal results discussed herein suggest that MPCMs can exert fundamental effects on the hydration process of cement and thus, the strength gain and microstructural development of the cement matrix. It is, therefore, crucial to further quantify the hydration parameters to better understand the strength development of MPCM-integrated cementitious composites over time and under various curing temperatures. Purposefully, the apparent activation energy and hydration parameters of cement pastes with and without MPCM particles were calculated as discussed below.

Table 5-5: Hydration parameters extracted from isothermal curves

En28												
Temp. (°C)	R_{max}						$T_{R_{max}}$					
	P0	P05	P10	P15	P20	P25	P0	P05	P10	P15	P20	P25
15	2.25	2.23	2.07	1.72	1.40	1.2	12	19.66	26.64	36.59	52.54	61.69
23	3.54	3.50	3.46	2.79	2.38	1.72	7.93	14.65	19.71	37.27	48.59	54.04
30	5.4	5.32	4.93	4.05	2.86	2.31	5.2	7.6	10.88	17.65	28.77	40.67
35	6.83	6.76	6.41	5.78	3.45	3.07	4.57	8.4	12.98	22.54	30.63	50.53
40	8.83	8.67	8.17	6.1	3.65	3.26	3.73	6.57	10	16.49	24.24	28.41
En35												
Temp. (°C)	R_{max}						$T_{R_{max}}$					
	P0	P05	P10	P15	P20	P25	P0	P05	P10	P15	P20	P25
15	2.25	2.25	1.91	.65	1.26	1.15	12	20.96	30.34	43.1	53.28	65.46
23	3.64	3.59	3.03	2.37	2.09	1.75	7.98	12.66	23.96	47.74	59.51	70.31
30	5.33	5.25	4.85	4.37	3.38	3.17	5.2	8.77	14.39	22.53	33.32	23.17
35	6.83	6.47	6.46	5.44	4.55	4.05	4.57	6.55	9.34	16.52	26.09	33.37
40	8.93	8.37	7.40	6.72	5.13	4.06	3.73	5.95	8.99	18.62	24.05	29.42



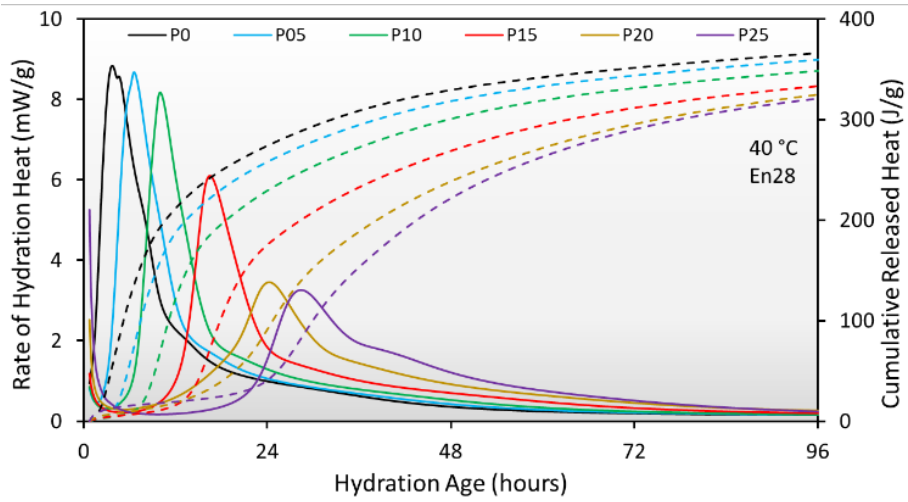
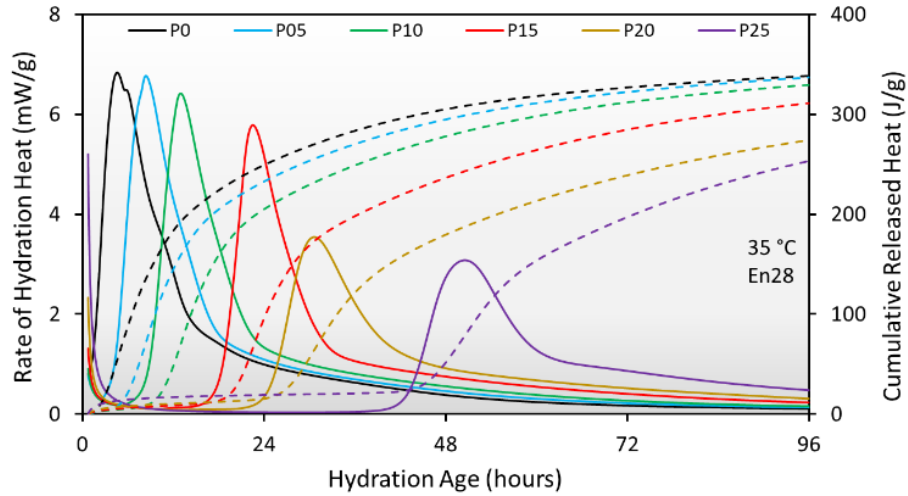
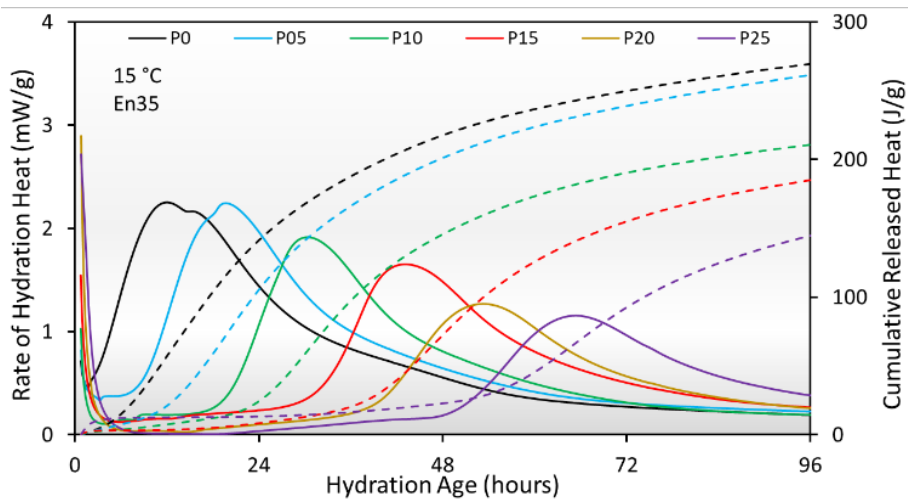
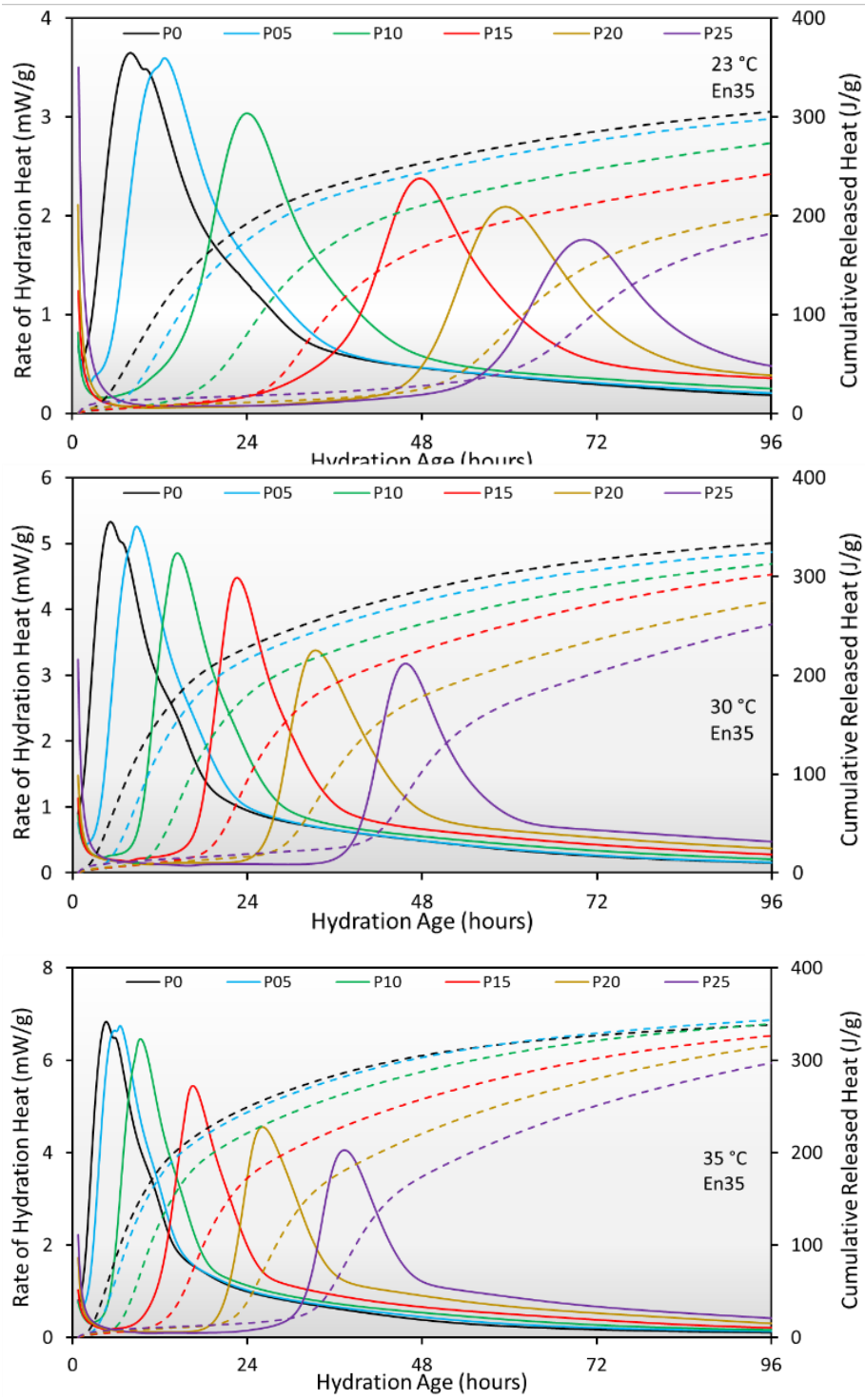


Figure 5-3: Isothermal curves of pastes incorporating En28 at various temperatures.





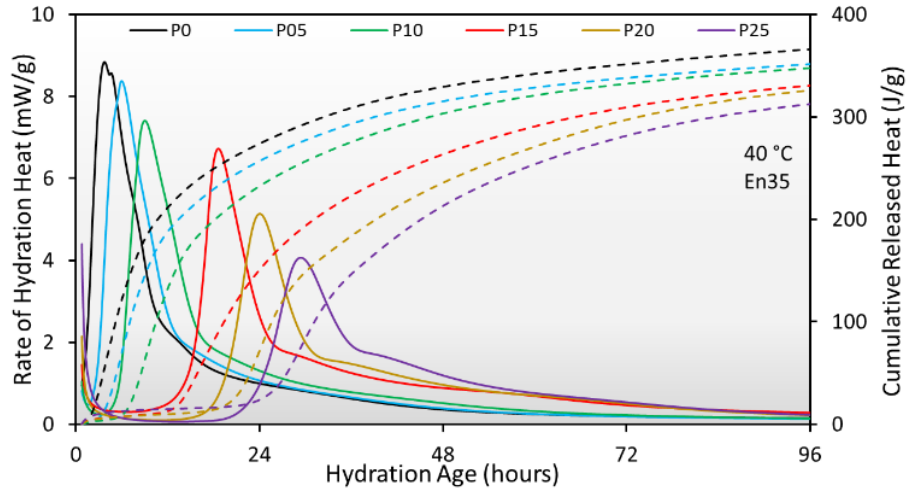


Figure 5-4: Isothermal curves of pastes incorporating En35 at various temperatures.

5.4.2 Calculation of E_a for cement pastes using isothermal calorimetry data

5.4.2.1 Linear approximation method

The reaction rate of each cement mixture was calculated at different isothermal temperatures using the linear slope of the cumulative heat curve in the acceleratory region as explained earlier and illustrated in **Fig. 5-2**. **Table 5-6** presents the reaction rate of all mixtures at various test temperatures. The results indicate that the reaction rate decreased after the addition of MPCMs, whereas it raised with the increase in the test temperature. Interestingly, the rate of increase in the reaction rate with respect to temperature declined with higher levels of MPCM inclusion. For instance, in the case of En28, the reaction rate of the P0 mixture (*i.e.*, plain cement paste) hydrated at $T=40^{\circ}\text{C}$ was increased by 264.6% compared to that at $T=15^{\circ}\text{C}$. In contrast, it increased by 167.2% and 69.7% for mixtures P10 and P20, respectively, indicating a less drastic change in the reaction rate with respect to temperature. The variation in the reaction rate can be better quantified using the apparent activation energy concept. Purposefully, the natural logarithm of the reaction rate was plotted versus the inverse of the absolute temperature, and a linear least-squared line was fitted to obtain the apparent activation energy of each mixture as displayed in **Figure 5-5**.

Table 5-6: Reaction rate of cement pastes calculated from the linear approximation of calorimetry data

En28					
	T=15 °C	T=23 °C	T=30 °C	T=35 °C	T=40 °C
P0	5.12	7.46	12.32	14.13	18.67
P05	4.17	6.09	10.24	10.63	13.57
P10	3.51	4.31	6.57	7.1	9.38
P15	3.11	3.65	4.79	5.24	6.86
P20	2.76	3.21	3.33	4.12	4.41
P25	2.55	2.65	2.96	3.28	3.6
En35					
	T=15 °C	T=23 °C	T=30 °C	T=35 °C	T=40 °C
P0	5.12	7.46	12.32	14.13	18.67
P05	4.09	7.21	9.76	12.41	14.08
P10	3.42	5.32	6.7	9.83	10.46
P15	2.76	4	4.75	6.56	7.74
P20	2.16	2.88	3.58	4.91	5.34
P25	1.85	2.17	2.9	3.65	3.89

According to **Eq. 5-1**, E_a can be computed by multiplying the negative of the slope of the fitting line by the universal gas constant, R . **Tables 5-7** and **5-8** report the apparent activation energy of cement pastes incorporating various dosages of En28 and En35 microcapsules, respectively. It can be observed that the inclusion of the MPCMs resulted in considerable reduction in the apparent activation energy of the cement mixtures for both En28 and En35 microcapsules, especially at higher levels of MPCM inclusion.

The activation energy is computed based on the relative variations of the reaction rate at different temperatures. It was observed that the inclusion of MPCMs led to reduction in the hydration rate of the cement along with reduction in the apparent activation energy. Therefore, the incorporation of MPCMs in cement paste decreased the sensitivity of the hydration process to temperature. This implies that higher ambient temperatures could not bring about as much acceleration in setting and strength gain in MPCM-integrated concrete as would be expected in normal concrete without MPCM inclusion. However, the adverse impact of the thermal stresses or shrinkage may be lower in MPCM-integrated concrete (Jayapalan *et al.*, 2014; Pinto & Schindler, 2010; Poole *et al.*, 2007; Sargam & Wang, 2021).

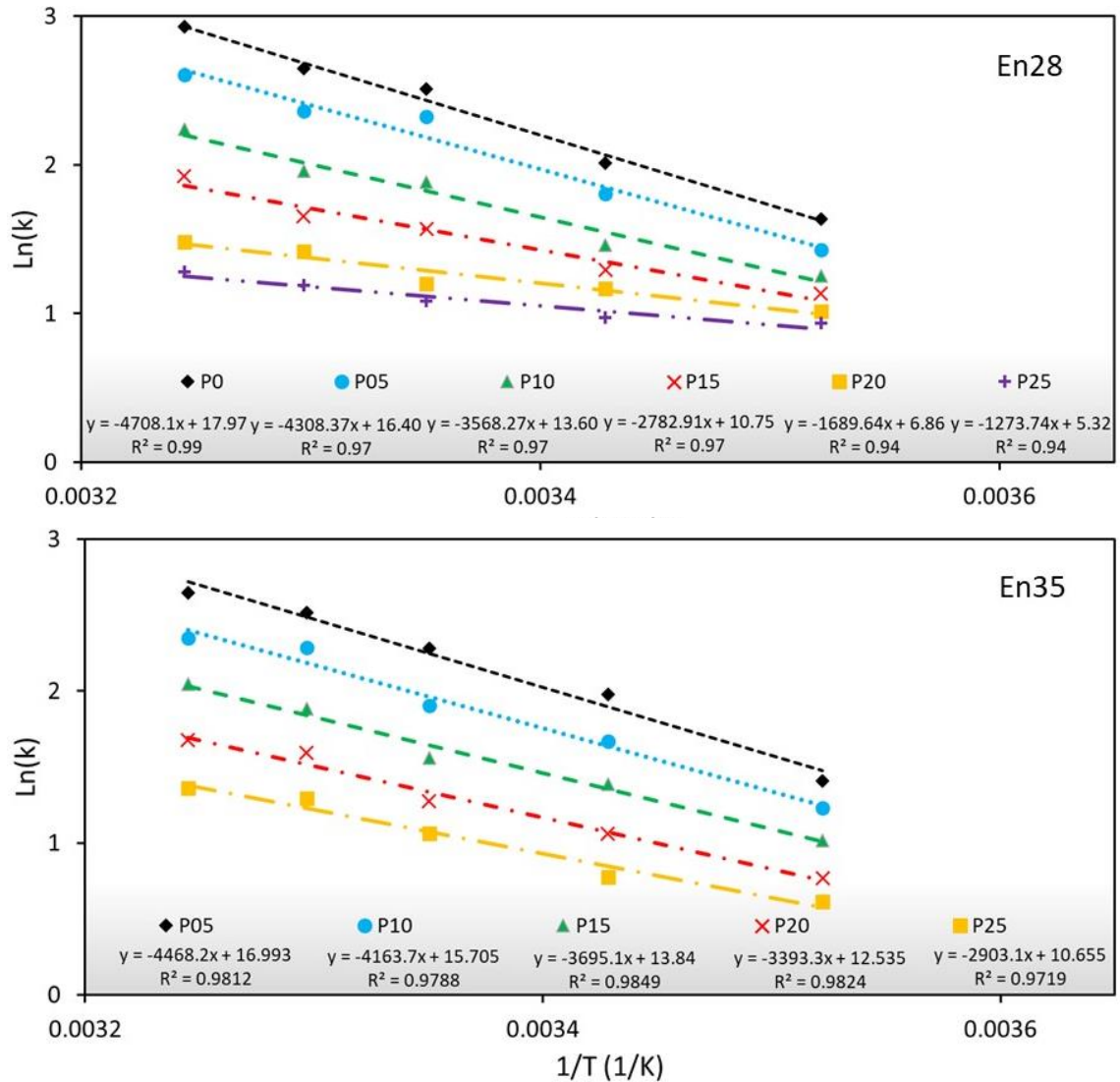


Figure 5-5: Natural logarithm of linear reaction rate versus the inverse of the absolute temperature of pastes incorporating En28 and En35 microcapsules.

It should be noted that the determination of the linear portion of the hydration curve is relatively subjective due to several reasons. Firstly, the addition of the MPCMs prolongs the dormant period and slows down the hydration rate in the acceleratory stage. Therefore, the determination of the start of the acceleratory phase is not consistent between all mixtures. Moreover, there may be more than one best linear fit to the acceleratory region in some mixtures, especially when the maximum rate of hydration is difficult to detect. An example is when the peaks related to C_3S and C_3A hydration overlap. Consequently, utilizing the modified ASTM C1074 is beneficial for acquiring more accurate results as

suggested in the literature (Jayapalan *et al.*, 2014; Poole *et al.*, 2007; Sargam & Wang, 2021). Yet, the results obtained from the linear approximation method provide initial insights into the comparison of the apparent activation energy of various mixtures.

5.4.2.2 Modified ASTM C1074 method

E_a can be calculated after estimating the hydration parameters using the three-parameter model expressed in **Eq. 5-4**. **Tables 5-7** and **5-8** report the hydration parameters obtained from a least-squares regression fit for mixtures incorporating En28 and En35, respectively. It could be understood that the incorporation of MPCMs decreased the apparent activation energy of the mixtures, showing a similar trend to the results obtained from the linear analysis. Nevertheless, the results obtained from the three-parameter model tend to be more accurate since it accounts for all calorimetry data in contrast to the linear method which only considers the acceleratory region. **Figure 5-6** depicts the linear fit of the natural logarithm of the hydration time parameter versus the inverse of the absolute temperature.

It is noteworthy that the apparent activation energy does not represent the potential energy to trigger a reaction as classically defined by the Arrhenius theory. Alternatively, it characterizes the sensitivity of the reaction to changes in temperature. The reaction of portland cement with water is a coupled nucleation and growth mechanism in the initial stages of hydration along with diffusion-controlled reactions in the later stages of hydration. It is believed that at the very early stages of hydration ($\alpha < 0.05$), the reaction is directed by a mode of diffusion (Kada-Benameur *et al.*, 2000). The addition of MPCM particles reduces the nucleation sites for CSH growth and precipitation primarily due to their morphology and particle size, and the fact that they wrap around cement particles. Therefore, the nucleation and growth mechanism in hydration of cement in the presence of MPCM particles is probably less dominant compared to that for plain cement pastes, leading to the lower apparent activation energy. In other words, the initiation of the nucleation-controlled phase of hydration is delayed upon MPCM addition.

Table 5-7: Hydration parameters and activation energies of cement pastes with En28

Mix	T (°C)	Modified ASTM C1074				Linear			
		α_u	β	τ (h)	R^2	E_a (kJ/mol)	Ln(k)	E_a (kJ/mol)	R^2
P0	15	0.784	0.892	24.452	0.996	43.13	1.635	39.143	0.99
	23			17.618	0.991		2.010		
	30			10.456	0.996		2.511		
	35			8.365	0.996		2.648		
	40			5.884	0.960		2.927		
P05En28	15	0.729	1.194	29.326	0.994	39.759	1.428	35.820	0.97
	23			21.056	0.992		1.806		
	30			11.932	0.993		2.326		
	35			10.820	0.989		2.363		
	40			7.951	0.954		2.607		
P10En28	15	0.665	1.763	43.369	0.954	38.583	1.255	29.666	0.97
	23			24.470	0.984		1.460		
	30			15.493	0.985		1.882		
	35			15.110	0.981		1.960		
	40			11.648	0.944		2.238		
P15En28	15	0.608	2.319	59.103	0.971	36.865	1.134	23.137	0.97
	23			43.098	0.988		1.294		
	30			21.792	0.989		1.566		
	35			24.056	0.972		1.656		
	40			17.711	0.932		1.925		
P20En28	15	0.583	2.480	67.507	0.953	31.189	1.015	14.048	0.94
	23			53.374	0.984		1.166		
	30			32.062	0.994		1.203		
	35			34.261	0.992		1.415		
	40			23.240	0.924		1.483		
P25En28	15	0.56172	2.833	78.690	0.958	26.470	0.936	10.59	0.94
	23			59.748	0.971		0.947		
	30			43.663	0.992		1.085		
	35			47.870	0.937		1.187		
	40			29.130	0.976		1.280		

Table 5-8: Hydration parameters and activation energies of cement pastes with En35

Mix	T (°C)	Modified ASTM C1074				Linear			
		α_u	β	τ (h)	R^2	E_a (kJ/mol)	Ln(k)	E_a (kJ/mol)	R^2
P0	15	0.747	0.892	24.452	0.996	43.124	1.635	39.143	0.99
	23			17.618	0.991		2.010		
	30			10.456	0.996		2.511		
	35			8.365	0.996		2.648		
	40			5.884	0.960		2.927		
P05En28	15	0.740	1.120	29.358	0.995	40.613	1.408	37.148	0.98
	23			18.738	0.995		1.975		
	30			12.862	0.996		2.278		
	35			9.056	0.989		2.518		
	40			7.929	0.977		2.644		
P10En28	15	0.672	1.609	45.289	0.966	39.552	1.229	34.617	0.97
	23			28.583	0.994		1.671		

				30	18.053	0.994		1.902		
				35	14.464	0.970		2.285		
				40	12.704	0.940		2.347		
P15En28				15	59.819	0.974		1.015		
				23	39.052	0.973		1.386		
		0.624	2.167	30	25.302	0.991	37.004	1.558	30.720	0.98
				35	18.564	0.969		1.880		
				40	19.364	0.951		2.046		
P20En28				15	68.826	0.937		0.77		
				23	62.800	0.984		1.057		
		0.597	2.623	30	36.711	0.994	33.693	1.275	28.211	0.98
				35	27.759	0.968		1.591		
				40	25.383	0.973		1.675		
P25En28				15	76.715	0.950		0.615		
				23	70.406	0.955		0.774		
		0.566	3.005	30	47.212	0.985	29.565	1.064	24.136	0.97
				35	37.236	0.963		1.294		
				40	30.252	0.939		1.358		

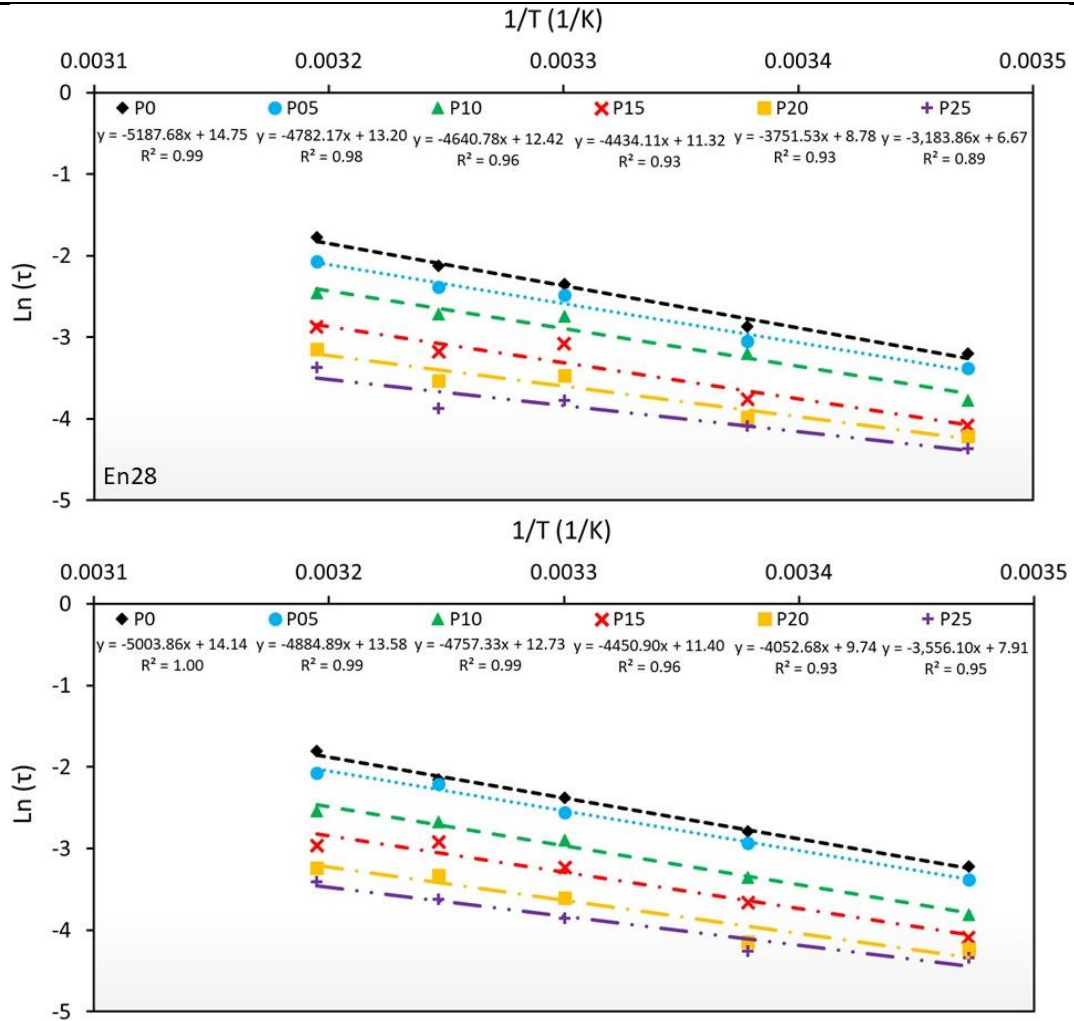


Figure 5-6: Natural logarithm of hydration time parameter versus the inverse of absolute temperature of pastes incorporating En28 and En35 microcapsules.

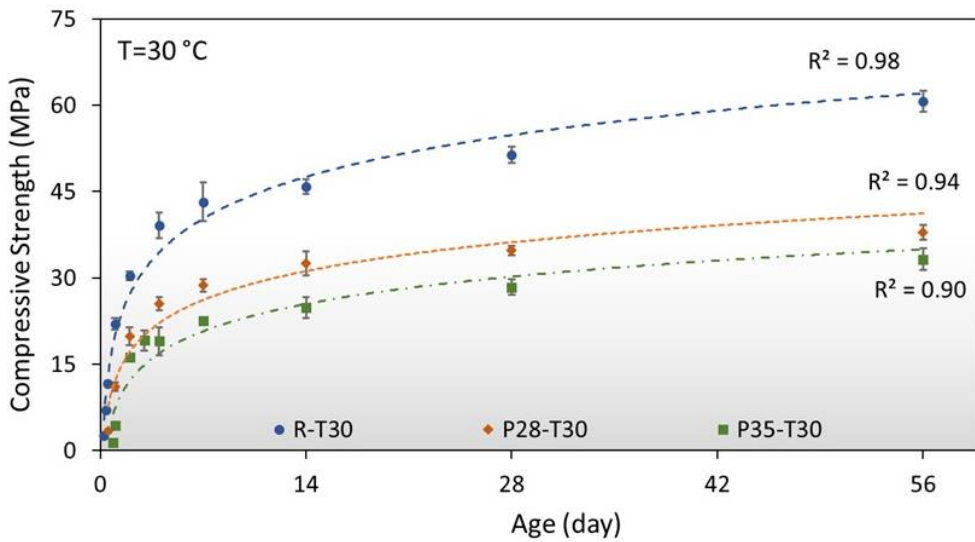
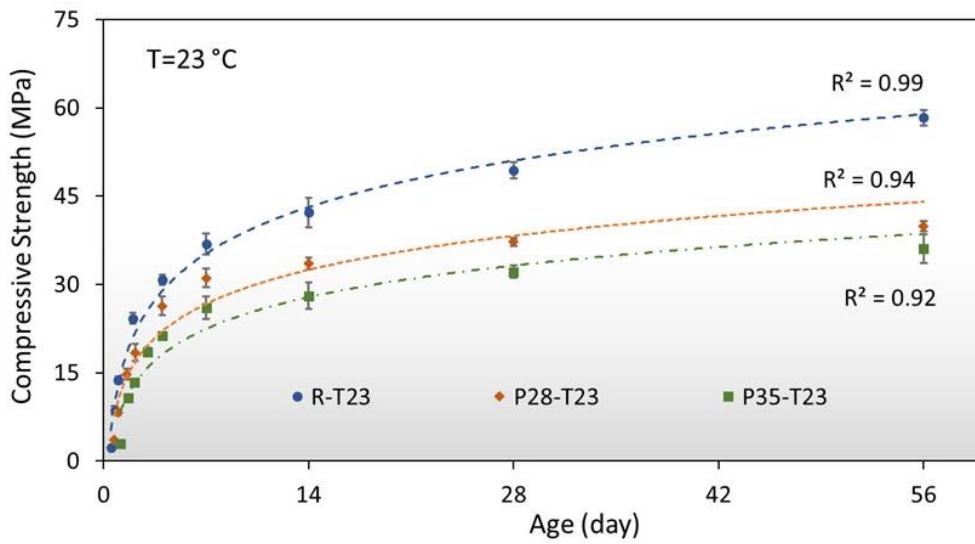
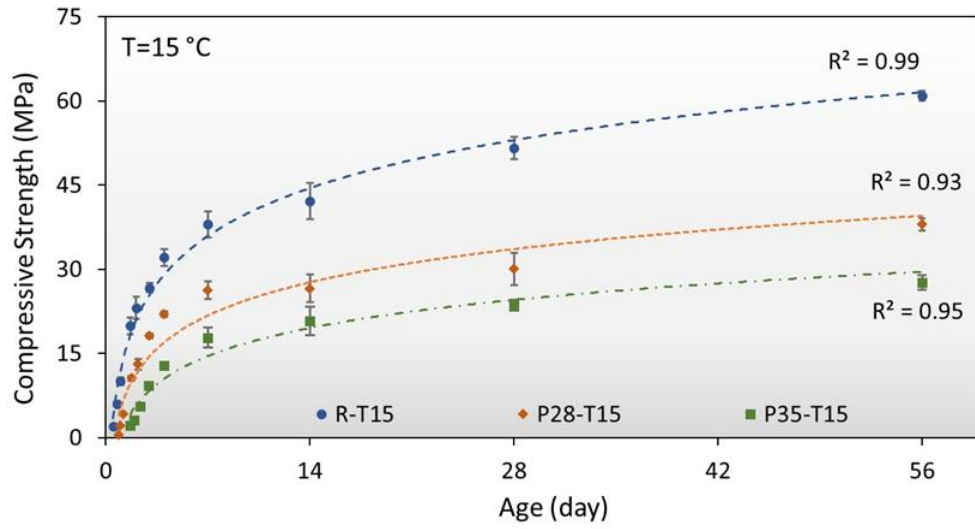
Previous research has demonstrated that the activation energy of nucleation-controlled reactions is higher (D'aloia & Chanvillard, 2002; Kada-Benameur *et al.*, 2000). For instance, the activation energy of cement hydration increased with the incorporation of nano-particles that act as seeds for nucleation growth and CSH precipitation (Jayapalan *et al.*, 2014; Sargam & Wang, 2021). The diffusion-controlled hydration of MPCM-integrated cement pastes is further related to the significant water absorption of the MPCMs along with their wrapping around anhydrous cement particles. The desorption of water from MPCM particles and the free water in macro-pores permeate towards the anhydrous cement grains to progress the reactions. Hence contrary to plain cement hydration, the reaction of water with the MPCM-cement system becomes less nucleation-controlled during the early stages of hydration. This is in remarkable conformity with the longer dormant period in MPCM-integrated cement pastes as discussed earlier.

5.4.3 Effect of MPCMs on compressive strength

Figure 5-7 illustrates the compressive strength development of mortars with and without MPCMs over time for various mixtures cured at different temperatures. More than 135 distinct compressive strength measurements were collected to monitor the strength development pattern of the mortars. Several trends can be detected in the strength development curves of mortars. Generally, the MPCM inclusion significantly decreased the compressive strength compared to that of the control mortar both at early and later ages. The reduction in the compressive strength is related to several mechanisms. MPCM particles were incorporated as a partial replacement for fine aggregates. However, they have a significantly lower stiffness compared to that of sand particles and the cementitious matrix. Therefore, it is expected that the strength of the mortars is limited by the strength of polymeric MPCM particles in the matrix (Aguayo *et al.*, 2016; Pilehvar *et al.*, 2017). In addition to the void-like behavior, polymeric MPCM particles have weak interfaces with the surrounding matrix compared to that for sand particles, resulting in weaker bonds and lower compressive strength of the mortar. As evidenced in SEM images in **Fig. 5-8**, MPCM particles notably deform and wrinkle during the mixing and hardening stages of the mortar. These deformations lead to increased porosity and a weaker interfacial bond with the cementitious matrix. It can be observed in the SEM images (see **Section 5.4.5**), that the

fracture of the cement paste mostly occurred at the MPCMs' interface where there is a weak bond with the surrounding matrix (Aguayo *et al.*, 2016; Cao *et al.*, 2018). The microstructure of the mortars is further discussed in **Section 5.4.5**.

Another pattern recognized in the strength development data is the delay in the strength gain of the MPCM-integrated mortars. The lower strengths at early ages along with the delay in the setting behavior of mortars incorporating MPCMs can be attributed to the hydration process as thoroughly discussed in **Sections 5.4.1** and **5.4.2**. The addition of MPCMs at the level of 15 wt.% by cement weight, significantly decreased and delayed the hydration peak, as observed in **Figs. 5-3** and **5-4**. Hence, the rate of strength gain in MPCM-integrated mortars is lower than for the control mortar. It was also evidenced that samples incorporating En35 achieved lower compressive strengths compared to those integrating En28. As discussed in **Section 5.4.1**, both types of MPCMs imposed comparable effects on the hydration kinetics of the cement paste. Therefore, the difference in the compressive strength of mortars containing different types of MPCMs is mainly related to the pore structure of the mortar and the bond strength of MPCMs with the cement matrix rather than the hydration kinetics. The curing temperature promoted the strength development of mortars at earlier ages. This is related to the accelerated cement hydration at higher temperatures as discussed earlier. However, it should be noted that higher curing temperatures can affect the microstructure development and the porosity of the cementitious matrix. Therefore, the compressive strength of specimens cured at higher temperatures may be lower at later ages. The apparent activation energy of mortars was computed based on the compressive strength to better analyze the effect of the curing temperature on the strength development of mortars.



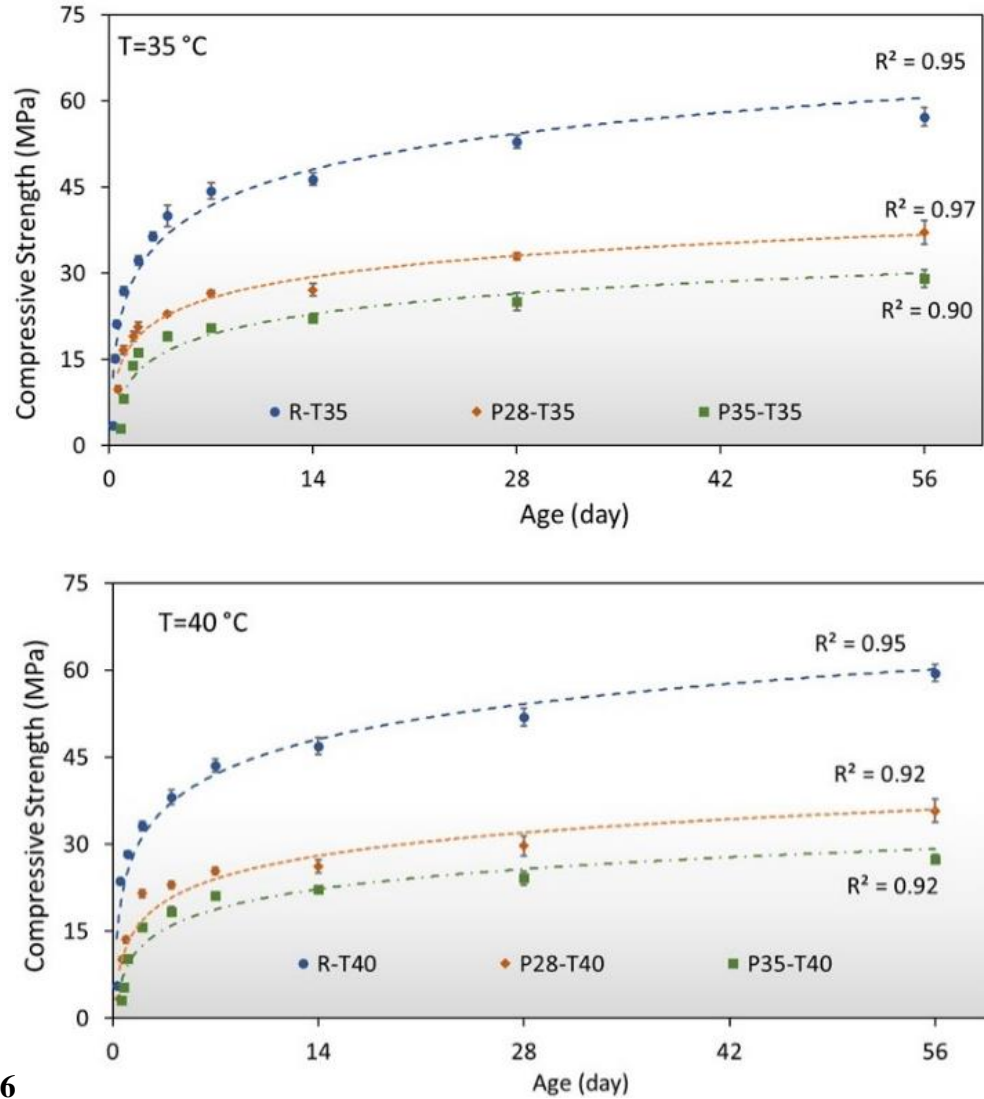


Figure 5-7: Compressive strength development of mortars cured under different temperatures.

5.4.4 Calculation of E_a for cement mortars using compressive strength data

To further investigate the synergic effect of the MPCM inclusion and curing temperature on the strength development of mortars, the apparent activation energy was further calculated based on the compressive strength measurements using **Eqs. 5-5** and **5-6**. **Table 5-9** presents the strength parameters of the mixtures after a least-square regression fit to the collected compressive strength data based on the parabolic and hyperbolic models. It could be understood that similar to the trend observed in the apparent activation energy of

cement pastes calculated based on the calorimetry data, E_a of mortars decreased with the addition of MPCM particles. Therefore, it could be concluded that the temperature sensitivity of the strength gains decreased with MPCM inclusion. This should be noted that compressive strength measurements suggest slightly lower apparent activation energy compared to the calorimetry data at the same MPCM inclusion level, *i.e.*, 15 wt.%. This is related to the age of the mixtures considered in the calculations. Accordingly, the calorimetry data were collected for the first 96 h of the hydration in which the nucleation and growth mechanism is predominant, and the apparent activation energy is typically higher. In contrast, the compressive strengths were measured over a 56-day period in which the diffusion becomes the major hydration mechanism after the first few days, and thus the apparent activation energy slightly decreased. The obtained strength development parameters suggest that the reaction rate (k) was increased with the rise in the curing temperature, while the addition of MPCMs decreased the reaction rate. It is also evident that increasing the curing temperature generally decreased the strength time constant, which is correlated to the setting behavior of mortars. Similar findings were evidenced in the calorimetry data analysis. Furthermore, curing the mortars at higher temperatures led to typically lower ultimate strength parameter, S_u . This is attributed to the synergic effect of the curing temperature and MPCM inclusion on the microstructure development and porosity of mortar specimens as will be discussed in the subsequent section.

Table 5-9: Apparent activation energy of mortars incorporating En28 and En35

Mix	Eq. 5-5				Eq. 5-6			
	S_u	k	t_0	E_a (kJ/mol)	S_u	τ_s	β	E_a (kJ/mol)
R-T15	58.62	0.3154	0.3383	37.19	66.82	2.5803	0.615	39.83
R-T23	50.22	0.4991	0.3433		64.78	2.3607	0.5798	
R-T30	55.78	0.6228	0.1255		64.43	1.3599	0.5647	
R-T35	53.72	0.8621	0.0183		62.19	0.8521	0.5147	
R-T40	52.82	1.1282	0.1134		61.7	0.8049	0.5268	
P28-T15	35.13	0.4352	0.8516	28.01	35.07	2.259	1.093	28.2
P28-T23	40.03	0.5254	0.5173		40.7	1.727	0.932	
P28-T30	37.39	0.6136	0.3578		37.34	1.3123	0.8559	
P28-T35	32.75	0.9705	0.3162		35.63	0.9753	0.7147	
P28-T40	31.38	1.0519	0.2903		34.24	0.9379	0.6591	
P35-T15	26.67	0.3614	1.5234	30.24	27.8	3.4072	1.1213	32.2
P35-T23	34.71	0.5325	0.9289		33.73	2.04	1.1616	
P35-T30	30.4	0.6595	0.7637		30.74	1.766	1.0465	
P35-T35	26.17	0.9818	0.5808		27.42	1.26	0.8761	
P35-T40	25.54	0.9164	0.4406		26.21	1.1598	0.9016	

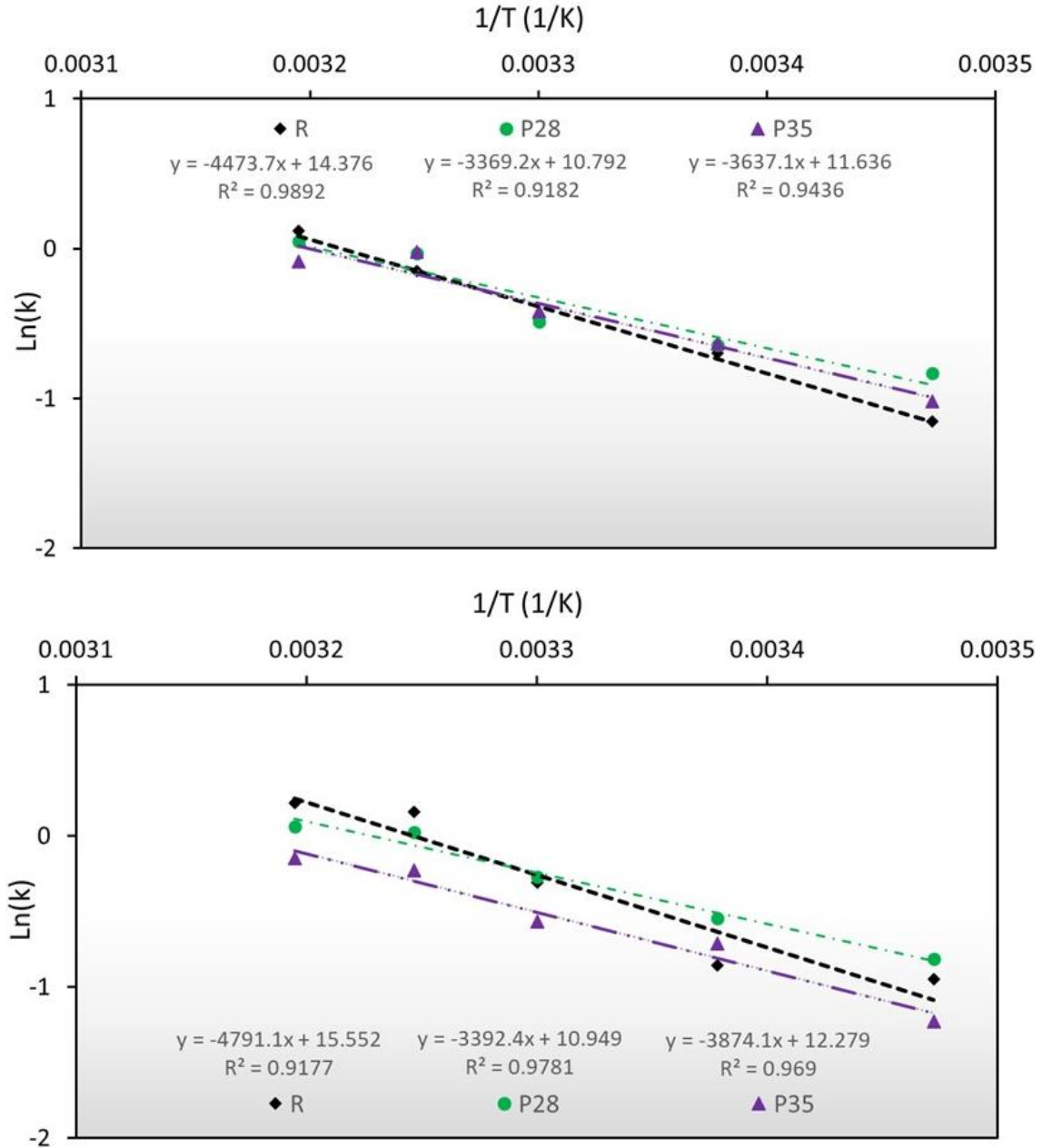


Figure 5-8: Natural logarithm of reaction rate versus the inverse of absolute temperature for mortar mixtures using parabolic and exponential functions.

5.4.5 Microstructural analyses

This section analyzes the SEM images and micro-CT images of mortar samples cured at 23 and 40°C. **Figure 5-9** displays the SEM images of the failure surface of mortar samples at different locations. It can be observed that MPCMs in all samples are drastically deformed and wrinkled, which could result in the reduction of compressive strength.

Furthermore, a weak interfacial transition zone (ITZ) is evident between the cement matrix and MPCM particles (see red arrows in the SEM images). A gap between the MPCMs and the surrounding cement matrix is also distinguishable. The weak bond between MPCM particles and cement paste in the ITZ demonstrates the potential initiation of micro-cracks that provoked the reduction in compressive strength and failure of specimens. The development of micro-cracks near MPCM affirms the contribution of the MPCMs to the failure of specimens (see blue arrows in the SEM images). Interestingly, En35 tended to have weaker interaction with the cement matrix compared to En28. As it is depicted with green indicators in the SEM images, several spots were identified in which MPCMs were detached from the surrounding cement paste. Conversely, no such cavities were pinpointed in numerous SEM images of samples containing En28 investigated herein. This is correlated with the lower compressive strength of mortar specimens incorporating En35 compared to those containing En28 as discussed earlier. In fact, the void-like effect of MPCMs in the mortar is more evident in the case of En35 particles which in turn may be attributed to the lower compatibility of the microcapsule shell with the surrounding cementitious matrix. The influence of the MPCMs addition on the porosity of the samples can be better examined using micro-CT images.

Figure 5-10 depicts the two-dimensional (2D) X-ray microtomography slices of specimens from mortar mixtures investigated in this study. Specimens cured at 23 and 40°C were selected for the analysis. Due to the low level of X-ray attenuation of organic materials fabricating MPCMs along with the low density of the MPCM particles, the discrimination between air voids and MPCM particles is relatively strenuous. However, air voids tend to form spherical shapes, whereas MPCMs have irregular morphology. After the image segmentation, it was observed that MPCM inclusions increased the porosity of cement mortars. The image analysis suggests a total volume of air voids of 6.32, 8.16, and 10.42% for RT23, En28T23, and En35T23 samples, respectively. The percentage of air voids in samples cured at 40°C, *i.e.*, RT40, En28T40, and En35T40, was 7.33, 9.01, and 11.66 %, respectively. This demonstrates that the MPCM inclusions resulted in increased porosity of the cementitious matrix and thus, a decrease in compressive strength. Interestingly, image analysis confirmed that En35 particles had aggravated the negative impact on the pore structure of the samples, which conforms with compressive strength data.

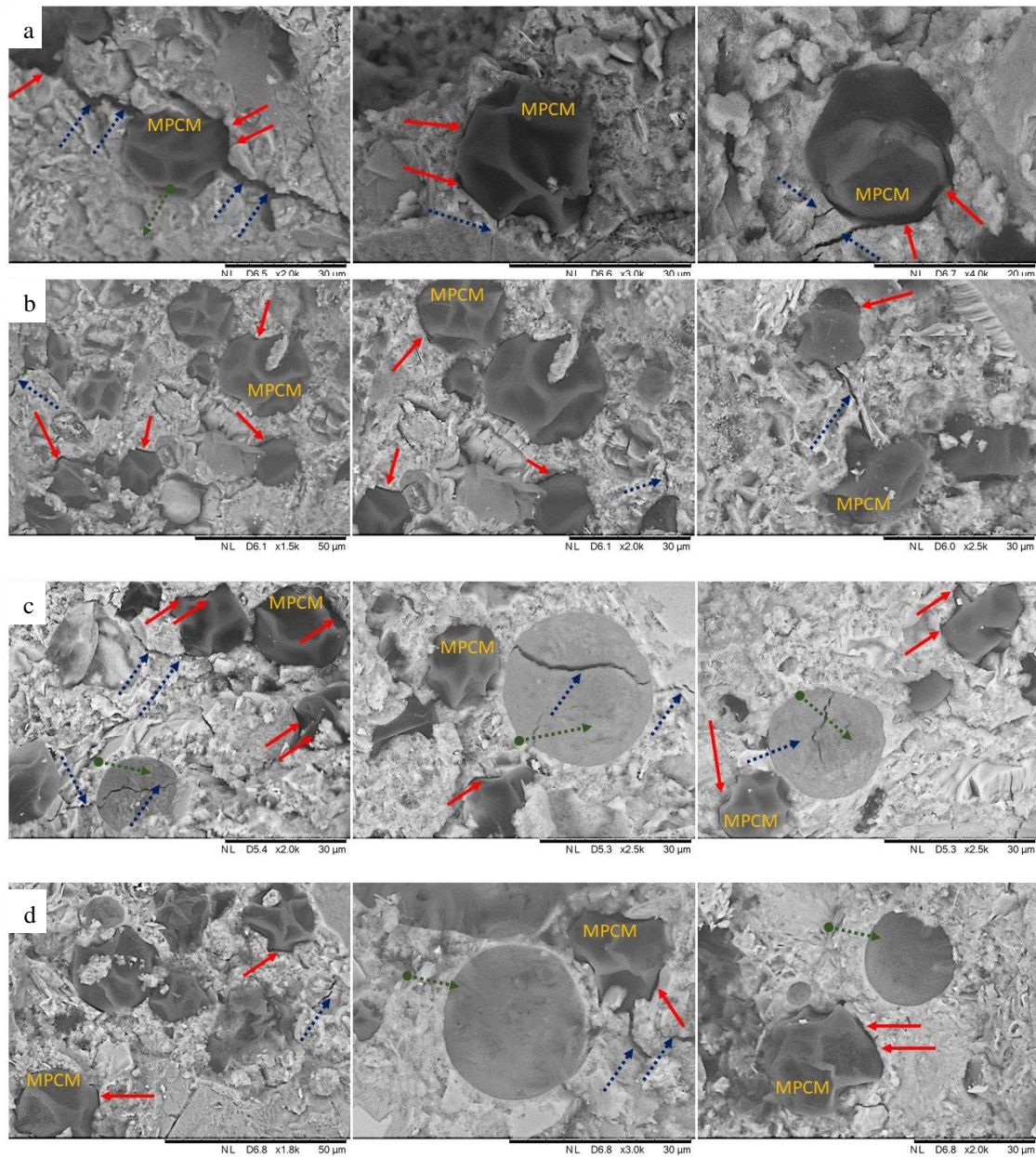


Figure 5-9: SEM images of mortar specimens: a) P28T23, b) P28T40, c) P35T23, and d) P35T40. Red arrows show the weak ITZ and gap between MPCMs and cement paste, blue arrows show micro-cracks initiated near MPCMs, and green arrows show cavities related to MPCMs detached from the cementitious matrix.

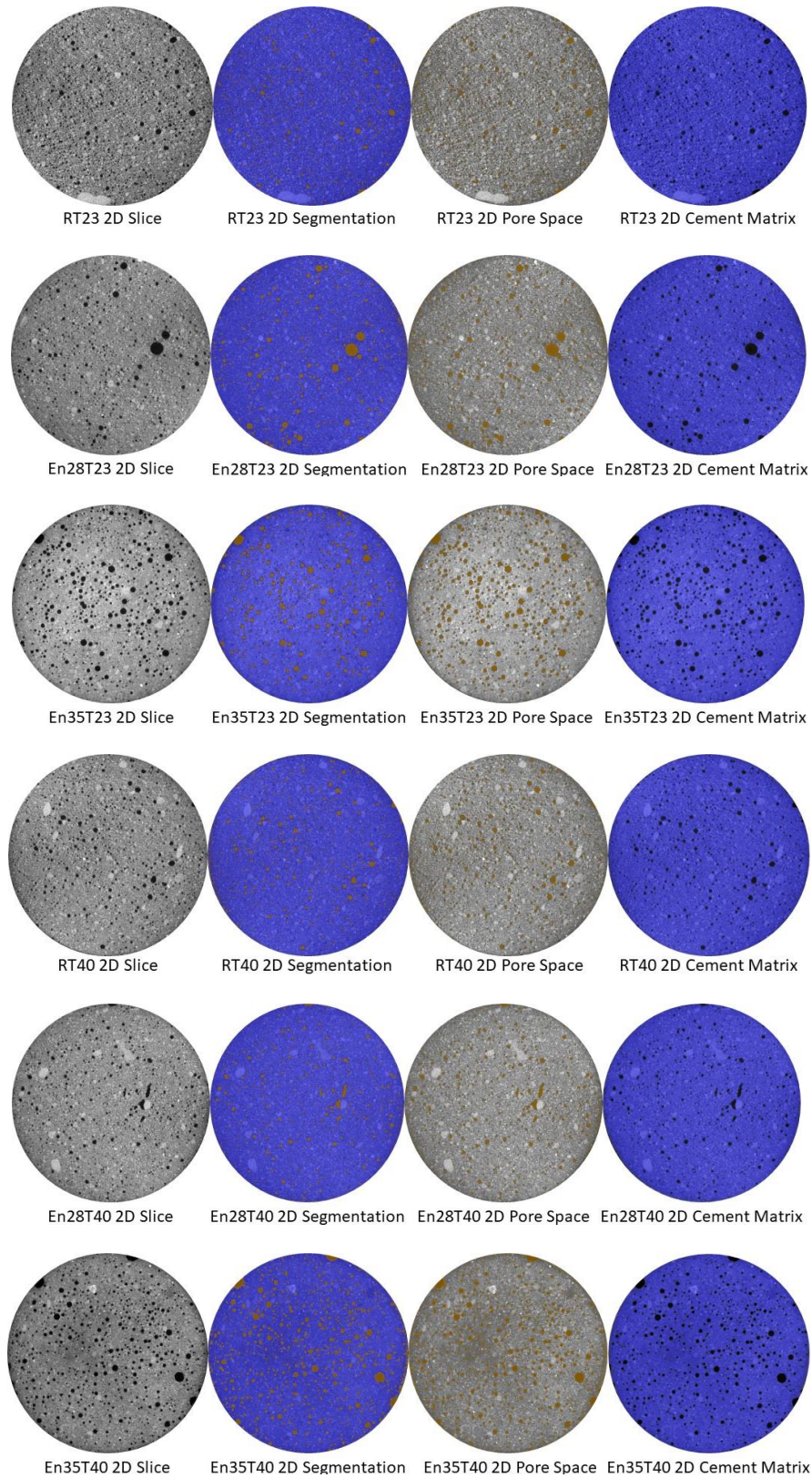


Figure 5-10: Segmentation of μ –CT scan Images for porosity analysis.

5.5 Concluding remarks

This study explored the apparent activation energy of cement pastes and mortars incorporating MPCMs using isothermal calorimetry and compressive strength measurements. Two types of non-formaldehyde biobased MPCMs with melting temperatures of 28 and 35°C were used to prepare test samples. Isothermal calorimetry and compressive strength tests were conducted at 5 curing temperatures including 15, 23, 30, 35, and 40 °C. SEM and X-ray μ CT analyses were performed to complement the findings from the hydration kinetics analysis. The following conclusions are drawn:

- MPCM addition to cement paste prolonged the dormant period of the cement hydration reactions and decreased the maximum rate of hydration. A delay in the time to reach the maximum rate of hydration was also evident.
- Increasing the temperature accelerated the hydration rate. However, this increase was less significant in cement pastes made with higher MPCM content.
- The latent heat of MPCMs further affected the delay in the maximum rate of hydration reactions for specimens tested at temperatures close to the melting temperature of the MPCMs.
- The apparent activation energy of cement pastes significantly decreased with the addition of MPCMs, indicating less temperature sensitivity of MPCM-integrated cement pastes.
- The inclusion of MPCMs in cement mortar led to significant reductions in compressive strength.
- The apparent activation energy of cement mortars decreased after the addition of MPCMs, indicating reduced sensitivity of the strength development to the curing temperature.
- SEM images and μ CT scans demonstrated the weak bond between MPCMs and the surrounding cementitious matrix, along with increased porosity induced by MPCM particles.

5.6 References

- Aguayo, M., Das, S., Maroli, A., Kabay, N., Mertens, J. C., Rajan, S. D., Sant, G., Chawla, N., & Neithalath, N. (2016). The influence of microencapsulated phase change material (PCM) characteristics on the microstructure and strength of cementitious composites: Experiments and finite element simulations. *Cement and Concrete Composites*, 73, 29-41.
- Assi, L., Soltangharai, V., Anay, R., Ziehl, P., & Matta, F. (2018). Unsupervised and supervised pattern recognition of acoustic emission signals during early hydration of Portland cement paste. *Cement and Concrete Research*, 103, 216-225.
- ASTM, S. (2004). Standard practice for estimating concrete strength by the maturity method. *ASTM C, 1074*, 1074-1093.
- Bentz, D. P. (2014). Activation energies of high-volume fly ash ternary blends: Hydration and setting. *Cement and Concrete Composites*, 53, 214-223.
- Bogner, A., Link, J., Baum, M., Mahlbacher, M., Gil-Diaz, T., Lützenkirchen, J., Sowoidnich, T., Heberling, F., Schäfer, T., & Ludwig, H.-M. (2020). Early hydration and microstructure formation of Portland cement paste studied by oscillation rheology, isothermal calorimetry, ¹H NMR relaxometry, conductance and SAXS. *Cement and Concrete Research*, 130, 105977.
- Cabeza, L. F., Castell, A., Barreneche, C. d., De Gracia, A., & Fernández, A. (2011). Materials used as PCM in thermal energy storage in buildings: A review. *Renewable and sustainable energy reviews*, 15(3), 1675-1695.
- Cao, V. D., Pilehvar, S., Salas-Bringas, C., Szczotok, A. M., Valentini, L., Carmona, M., Rodriguez, J. F., & Kjøniksen, A.-L. (2018). Influence of microcapsule size and shell polarity on thermal and mechanical properties of thermoregulating geopolymer concrete for passive building applications. *Energy conversion and management*, 164, 198-209.
- Chwieduk, D. (2003). Towards sustainable-energy buildings. *Applied Energy*, 76(1-3), 211-217.

Costa, A., Keane, M. M., Torrens, J. I., & Corry, E. (2013). Building operation and energy performance: Monitoring, analysis and optimisation toolkit. *Applied energy*, 101, 310-316.

D'aloia, L., & Chanvillard, G. (2002). Determining the “apparent” activation energy of concrete: Ea—numerical simulations of the heat of hydration of cement. *Cement and Concrete Research*, 32(8), 1277-1289.

Djamai, Z. I., Salvatore, F., Larbi, A. S., Cai, G., & El Mankibi, M. (2019). Multiphysics analysis of effects of encapsulated phase change materials (PCMs) in cement mortars. *Cement and Concrete Research*, 119, 51-63.

Drissi, S., Ling, T.-C., Mo, K. H., & Eddhahak, A. (2019). A review of microencapsulated and composite phase change materials: Alteration of strength and thermal properties of cement-based materials. *Renewable and sustainable energy reviews*, 110, 467-484.

Drissi, S., Mo, K. H., Falchetto, A. C., & Ling, T.-C. (2021). Understanding the compressive strength degradation mechanism of cement-paste incorporating phase change material. *Cement and Concrete Composites*, 124, 104249.

Eddhahak, A., Drissi, S., Colin, J., Caré, S., & Neji, J. (2014). Effect of phase change materials on the hydration reaction and kinetic of PCM-mortars. *Journal of thermal analysis and calorimetry*, 117(2), 537-545.

Fernandes, F., Manari, S., Aguayo, M., Santos, K., Oey, T., Wei, Z., Falzone, G., Neithalath, N., & Sant, G. (2014). On the feasibility of using phase change materials (PCMs) to mitigate thermal cracking in cementitious materials. *Cement and Concrete Composites*, 51, 14-26.

Han, M.-C., & Han, C.-G. (2010). Use of maturity methods to estimate the setting time of concrete containing super retarding agents. *Cement and Concrete Composites*, 32(2), 164-172.

Jayapalan, A. R., Jue, M. L., & Kurtis, K. E. (2014). Nanoparticles and apparent activation energy of Portland cement. *Journal of the American Ceramic Society*, 97(5), 1534-1542.

Juilland, P., Gallucci, E., Flatt, R., & Scrivener, K. (2010). Dissolution theory applied to the induction period in alite hydration. *Cement and Concrete Research*, 40(6), 831-844.

Kada-Benameur, H., Wirquin, E., & Duthoit, B. (2000). Determination of apparent activation energy of concrete by isothermal calorimetry. *Cement and Concrete Research*, 30(2), 301-305.

Lawrence, P., Cyr, M., & Ringot, E. (2003). Mineral admixtures in mortars: effect of inert materials on short-term hydration. *Cement and Concrete Research*, 33(12), 1939-1947.

Lizana, J., Chacartegui, R., Barrios-Padura, A., & Ortiz, C. (2018). Advanced low-carbon energy measures based on thermal energy storage in buildings: A review. *Renewable and sustainable energy reviews*, 82, 3705-3749.

Marani, A., & Nehdi, M. L. (2019). Integrating phase change materials in construction materials: Critical review. *Construction and Building Materials*, 217, 36-49.

Pang, X., Sun, L., Sun, F., Zhang, G., Guo, S., & Bu, Y. (2021). Cement hydration kinetics study in the temperature range from 15° C to 95° C. *Cement and Concrete Research*, 148, 106552.

Pilehvar, S., Cao, V. D., Szczotok, A. M., Carmona, M., Valentini, L., Lanzón, M., Pamies, R., & Kjøniksen, A.-L. (2018). Physical and mechanical properties of fly ash and slag geopolymer concrete containing different types of micro-encapsulated phase change materials. *Construction and Building Materials*, 173, 28-39.

Pilehvar, S., Cao, V. D., Szczotok, A. M., Valentini, L., Salvioni, D., Magistri, M., Pamies, R., & Kjøniksen, A.-L. (2017). Mechanical properties and microscale changes of geopolymer concrete and Portland cement concrete containing micro-encapsulated phase change materials. *Cement and Concrete Research*, 100, 341-349.

Pilehvar, S., Sanfeliu, S. G., Szczotok, A. M., Rodríguez, J. F., Valentini, L., Lanzón, M., Pamies, R., & Kjøniksen, A.-L. (2020). Effect of temperature on geopolymer and Portland cement composites modified with Micro-encapsulated Phase Change materials. *Construction and Building Materials*, 252, 119055.

Pinto, R., & Schindler, A. (2010). Unified modeling of setting and strength development. *Cement and Concrete Research*, 40(1), 58-65.

Pomianowski, M., Heiselberg, P., Jensen, R. L., Cheng, R., & Zhang, Y. (2014). A new experimental method to determine specific heat capacity of inhomogeneous concrete material with incorporated microencapsulated-PCM. *Cement and Concrete Research*, 55, 22-34.

Poole, J. L., Riding, K. A., Folliard, K. J., Juenger, M. C., & Schindler, A. K. (2007). Methods for calculating activation energy for Portland cement. *ACI Materials Journal*, 104(1), 303-311.

Saadoon, T., Gómez-Meijide, B., & Garcia, A. (2019). New predictive methodology for the apparent activation energy and strength of conventional and rapid hardening concretes. *Cement and Concrete Research*, 115, 264-273.

Sanfeliix, S. G., Santacruz, I., Szczotok, A. M., Belloc, L. M. O., Angeles, G., & Kjøniksen, A.-L. (2019). Effect of microencapsulated phase change materials on the flow behavior of cement composites. *Construction and Building Materials*, 202, 353-362.

Sargam, Y., & Wang, K. (2021). Hydration kinetics and activation energy of cement pastes containing various nanoparticles. *Composites Part B: Engineering*, 216, 108836.

Schindler, A. K. (2004). Effect of temperature on hydration of cementitious materials. *Materials Journal*, 101(1), 72-81.

Scrivener, K. L., Juilland, P., & Monteiro, P. J. (2015). Advances in understanding hydration of Portland cement. *Cement and Concrete Research*, 78, 38-56.

Soares, N., Costa, J. J., Gaspar, A. R., & Santos, P. (2013). Review of passive PCM latent heat thermal energy storage systems towards buildings' energy efficiency. *Energy and Buildings*, 59, 82-103.

Tafesse, M., & Kim, H.-K. (2019). The role of carbon nanotube on hydration kinetics and shrinkage of cement composite. *Composites Part B: Engineering*, 169, 55-64.

Thomas, J. J., Ghazizadeh, S., & Masoero, E. (2017). Kinetic mechanisms and activation energies for hydration of standard and highly reactive forms of β -dicalcium silicate (C2S). *Cement and Concrete Research*, 100, 322-328.

Wirquin, E., Broda, M., & Duthoit, B. (2002). Determination of the apparent activation energy of one concrete by calorimetric and mechanical means: Influence of a superplasticizer. *Cement and Concrete Research*, 32(8), 1207-1213.

Yan, Y., Ouzia, A., Yu, C., Liu, J., & Scrivener, K. L. (2020). Effect of a novel starch-based temperature rise inhibitor on cement hydration and microstructure development. *Cement and Concrete Research*, 129, 105961.

Yan, Y., Wang, R., Liu, J., Tang, J., & Scrivener, K. L. (2021). Effect of a liquid-type temperature rise inhibitor on cement hydration. *Cement and Concrete Research*, 140, 106286.

Yang, L., Yan, H., & Lam, J. C. (2014). Thermal comfort and building energy consumption implications—a review. *Applied energy*, 115, 164-173.

Zajac, M., Durdzinski, P., Stabler, C., Skocek, J., Nied, D., & Haha, M. B. (2018). Influence of calcium and magnesium carbonates on hydration kinetics, hydrate assemblage and microstructural development of metakaolin containing composite cements. *Cement and Concrete Research*, 106, 91-102.

Zhang, D., Li, Z., Zhou, J., & Wu, K. (2004). Development of thermal energy storage concrete. *Cement and Concrete Research*, 34(6), 927-934.

Zhang, J., Cusson, D., Monteiro, P., & Harvey, J. (2008). New perspectives on maturity method and approach for high performance concrete applications. *Cement and Concrete Research*, 38(12), 1438-1446.

Chapter 6

6 Deep Learning-Assisted Calculation of Apparent Activation Energy for Cement-based Composites Incorporating Microencapsulated Phase Change Materials¹

Sustained efforts have been directed towards understanding the effects of microencapsulated phase change materials (MPCMs) on the microstructure and mechanical strength development of portland cement-based composites. Yet, the effects of temperature on the kinetics of hydration reactions of MPCM-integrated cementitious systems remain largely unexplored. This study proposes a deep learning framework to simulate the hydration process and calculate the apparent activation energy of such cementitious composites. Extensive isothermal calorimetry tests were carried out in this study to compile a robust time-dependent dataset for developing various pertinent machine learning models. It was demonstrated that the deep neural network outperformed the gradient boosting ensemble in predicting the hydration rate and cumulative heat. Furthermore, the apparent activation energy of diverse cement-based systems incorporating MPCMs was calculated based on the predictions of the deep learning model. It was found that the addition of MPCMs decreased the activation energy of the cementitious systems, indicating less sensitivity of the hydration reactions to temperature.

6.1 Introduction

The growing world population and urbanization have created a colossal demand in contemporary societies for energy. Considering the rapid depletion of non-renewable energy resources and the associated climate change threats, developing sustainable energy-saving practices is paramount. A promising solution to mitigate imminent shortages in energy supply is coining novel efficient energy storage systems. Latent heat thermal energy storage (LHTES) has been proposed as an attractive technology to tackle the intermittent

¹ A version of this chapter is under review in “Cement and Concrete Composites” journal, 2022.

mismatch between energy demand and supply (Xu *et al.*, 2021). Owing to their high energy storage density, latent heat energy storage systems require a smaller mass and volume of materials compared to sensible heat energy storage media (Agyenim *et al.*, 2010). For instance, phase change materials (PCMs) can absorb/release a considerable amount of heat energy when they undergo a phase transition, *e.g.*, from solid to liquid. Therefore, they can be employed to store thermal energy at a constant temperature and retrieve it at a later time (Huang *et al.*, 2019).

PCMs have been utilized as non-polluting, sustainable, and efficient energy storage materials in various relevant industries, such as waste heat recovery (Li *et al.*, 2019) textiles and fabrics (Li *et al.*, 2018), and buildings (Faraj *et al.*, 2020). Buildings are responsible for nearly one-third of the global energy consumption (Pan *et al.*, 2018). A significant share of this energy consumption is used for heating and cooling indoor spaces (Hassan *et al.*, 2022). Integrating LHTES systems in buildings can narrow the indoor temperature fluctuations and thus, decrease the energy consumption, as widely reported in the literature (Lizana *et al.*, 2017). Purposefully, several PCM-based systems have been developed for building applications including PCM-based heat exchangers and HVAC systems (Maccarini *et al.*, 2018), PCM-based photovoltaics (Fayaz *et al.*, 2019), and PCM-integrated building envelopes (Akeiber *et al.*, 2016; Boussaba *et al.*, 2018).

To integrate LHTES capacity in buildings, PCMs can be incorporated in cement-based composites used for the construction of structural elements such as walls, roofs, and envelopes. Among the diverse methods proposed in the pertinent research, polymeric microencapsulated PCMs (MPCMs) have been predominantly utilized for fabricating PCM-integrated cement mortars and concretes (Marani & Nehdi, 2019). Accordingly, the addition of MPCMs can lead to significant improvements in the thermal performance and energy saving of cement-based composites. Nonetheless, several adverse effects of MPCMs on the hydration, setting behavior, and microstructural development of cementitious matrices have been identified (Drissi *et al.*, 2019; Drissi *et al.*, 2021). Several experimental studies explored the potential effects of polymeric MPCMs on the hydration kinetics of cement pastes and postulated relevant mechanisms such as the dilution of the cement paste after MPCM addition (Aguayo *et al.*, 2016) and the reduced available water

needed for cement hydration reactions due to high water absorption of MPCMs (Aguayo *et al.*, 2016; Pilehvar *et al.*, 2017). A potential benefit of using PCMs in cement-based composites is the control of hydration heat evolution in the hardening cementitious system and therefore, possibly mitigating early-age thermal cracking (Fernandes *et al.*, 2014). It has been theoretically demonstrated that MPCM inclusion in concrete can reduce the internal temperature and thermal stresses in massive concrete placements (Šavija & Schlangen, 2016). However, rigorous studies on the hydration kinetics of MPCM-integrated cementitious systems are needed to better understand the temperature-related stresses and strains.

The promising yet deficient findings in the open literature denote the need for comprehensive investigations to capture the effects of MPCMs on the temperature sensitivity and hydration process in MPCM-integrated cementitious systems. For this purpose, a robust modeling approach based on a machine learning (ML) framework is proposed for the first time to calculate the apparent activation energy, which is representative of the temperature sensitivity of the hydration reactions. Multiple isothermal calorimetry tests were performed on diverse MPCM-integrated systems at 5 different temperatures to extract time-dependent cement hydration heat. The isothermal calorimetry data were employed to establish the ML framework for the prediction of the hydration heat evolution. The subsequent section elucidates the fundamental knowledge in the study of cement hydration and ML modeling, followed by a description of the data collection and model development. Ultimately, the apparent activation energy for diverse cement-based systems is calculated based on the predictions of the best ML model, and in-depth discussions are presented.

6.2 Background knowledge and literature review

6.2.1 Hydration kinetics and apparent activation energy

During the exothermic chemical reactions of cement particles with water, a great amount of heat is released, which is referred to as hydration heat. This generated heat brings about a significant increase in the temperature of the hydrating cementitious system. From a practical point of view, it is essential to characterize the temperature gradients along with

the maximum temperature of the mixture during the pouring and curing stages (Bentz, 2014; Poole *et al.*, 2007). The evaluation of the hydration kinetics of a given cementitious system is pivotal to investigate other thermal-related characteristics such as thermal stresses, strains, and potential cracking (Assi *et al.*, 2018; Zajac *et al.*, 2018). The setting behavior, microstructural development, and mechanical properties of cement-based systems are also closely related to the development of the hydration process (Bogner *et al.*, 2020; Zou *et al.*, 2021).

Several environmental and material parameters are known to affect the cement hydration process. The chemical compositions and physical properties (e.g. particle size and specific surface area) of the cementitious materials, along with the curing temperature, are among the most influential parameters (D'aloia & Chanvillard, 2002; Zajac *et al.*, 2018). Furthermore, the incorporation of reactive or nonreactive additives into the binder can exert a dominant influence on the hydration kinetics (Tafesse & Kim, 2019; Yan *et al.*, 2020). For instance, Sargam and Wang (Sargam & Wang, 2021) reported an increase in the rate of cement hydration after the addition of nanoparticles, while Yan *et al.* (Yan *et al.*, 2021) evidenced that the addition of liquid-type temperature rise inhibitor prolonged the dormant period and reduced the maximum hydration rate.

There have been few studies in the open literature that explored the effects of MPCM addition on the hydration process of cement pastes. In a study conducted by Eddhahak *et al.* (Eddhahak *et al.*, 2014), it was observed that the addition of MPCMs to the cement paste decreased the heat of hydration and delayed the accelerating phase of the hydration process. They mainly attributed such changes to the latent heat of MPCMs. Additionally, Pilehvar *et al.* (Pilehvar *et al.*, 2017) postulated that various mechanisms are related to the change in the hydration kinetics of MPCM-integrated cement and geopolymer pastes. These include MPCMs covering the cement grains and preventing their contact with water, and partial loss of nucleation sites for the growth of hydration products. The relatively high water absorption of MPCMs and the change in the dilution of the cement paste are other potential reasons for the change in the hydration kinetics (Aguayo *et al.*, 2016).

In addition to the physiochemical properties of MPCMs, the curing temperature can affect the hydration kinetics and microstructural development of cement-based composites. For instance, Pilehvar *et al.* (Pilehvar *et al.*, 2020) observed that similar to plain cement pastes, the hydration reactions of cement pastes incorporating MPCMs are faster at higher temperatures. Meanwhile, the thermal properties of MPCMs, such as melting/freezing temperatures and enthalpies, may exert additional influence on the hydration rate and heat evolution of cement paste.

The sensitivity of cement hydration to temperature change can be better captured using the activation energy concept. Activation energy is not directly applicable to cement hydration, however, the Arrhenius theory utilizes the “apparent activation energy” (E_a) to measure the effect of temperature on the hydration kinetics of cementitious composites (Saadoon *et al.*, 2019). Accordingly, the reaction rate of cement hydration is dependent on temperature and can be expressed as follows:

$$k = A \cdot e^{-\frac{E_a}{RT}} \quad \text{Eq. 6-1}$$

where R is the universal gas constant (8.314 J/mol/K), T is the temperature (K) at which the reaction occurs, k is the rate of the reaction (W), A is the proportionality constant, and E_a is the apparent activation energy (J/mol). The proportionality (pre-exponential) factor, A, is typically excluded in the cement hydration since the ratio of the reaction rates is utilized in the concrete maturity calculations. Therefore, E_a is calculated independent of A for cementitious systems (Sakai & Koga, 2022).

Isothermal calorimetry is widely used to measure the released heat of hydration for cement-based systems (Carette & Staquet, 2016; Chen *et al.*, 2022). To calculate the apparent activation energy based on **Eq. 6-1**, measurement of the reaction rates at several isothermal temperatures is required. Various methods have been proposed by Poole *et al.* (Poole *et al.*, 2007) to calculate E_a based on the isothermal calorimetry data, including linear approximation, modified ASTM C1074, and incremental method. They computed E_a for multiple cement-based systems incorporating supplementary cementitious materials (SCMs). Accordingly, it was found that the modified ASTM C1074 gives an accurate

characterization of E_a to account for the effect of the curing temperature on the hydration rate of cementitious materials. In other pertinent studies, the effect of nanoparticles on the apparent activation energy and thus, the temperature sensitivity of cement-based systems have been studied (Jayapalan *et al.*, 2014; Sargam & Wang, 2021).

6.2.2 Machine learning basis

In recent decades, data-driven techniques have emerged as promising alternative approaches to model various engineering properties of a broad range of smart and multifunctional materials and systems (He *et al.*, 2021; Jose *et al.*, 2021; Li *et al.*, 2021). In particular, the mechanical, thermal, and durability properties of cement-based composites have been accurately predicted using various types of ML algorithms (Gomaa *et al.*, 2021; Nunez *et al.*, 2021; Tanyildizi, 2021). Findings in the literature suggest that powerful ML models coupled with analytical parametric studies can reveal profound insights into the design of complex multicomponent materials. This is of great significance in the performance analysis of modern cement-based composites, where the diversity of components and their makeups, large combinatorial spaces, nonlinear interactions, and time-dependent chemical reactions convolute the design process.

Despite improvements in thermal characteristics, MPCM addition to cementitious composites has proven to affect microstructural development. Chapters 2 and 3 (Marani & Nehdi, 2020) proposed ML models to investigate the effect of MPCM addition on the strength development of cementitious mortars and concrete. They evidenced that the strength development slows down after the addition of MPCM, which may be related to the physicochemical properties of MPCM particles. However, their model only considered the interaction of mixture components and overlooked the influence of MPCMs on the kinetics of cement hydration reactions.

It has been recently demonstrated that ML algorithms can contribute to high-fidelity predictions and optimization of chemical reactions (Hein, 2021; Meuwly, 2021). Consequently, a dearth of studies explored the ability of ML models to estimate the hydration kinetics of cementitious systems based on isothermal calorimetry data. Cook *et al.* (Cook *et al.*, 2021) predicted the heat-evolution profiles of blended cementitious

systems using 300+ data entries. The model training set encompassed 7800 data records along with 8 input features. The heat flow rate and cumulative heat during 24 hours of hydration were collected as the output. A random forest model was trained to predict the time-dependent hydration progress of the plain and blended cement-based systems. They demonstrated that the properly trained model could accurately predict the long-time hydration behavior of cementitious systems (Cook *et al.*, 2021). In a similar study performed by Lapeyre *et al.* (Lapeyre *et al.*, 2021), a random forest model was used to formulate the optimal design of multicomponent systems based on the hydration kinetics criteria. Such findings highlight the potential ability of computational intelligence to simulate the hydration heat evolution and temperature sensitivity of cement-based systems incorporating MPCMs.

6.3 Model development

This section describes the experimental data collection and preprocessing steps along with the fundamentals of the applied models. The procedure of apparent activation energy calculation based on the hydration heat predicted by the best-developed ML paradigm is also expounded.

6.3.1 Data collection

The isothermal calorimetry results of the cement pastes tested in Chapter 5 were utilized as the experimental data for the model development. The tests were performed at 5 different isothermal temperatures including 15, 23, 30, 35, and 40°C. MPCMs were added to the cement pastes at various dosages including 0, 5, 10, 15, 20, and 25 wt.% of cement.

The heat of hydration of cement pastes was recorded using an eight-channel microcalorimeter (TAM air, TA Instruments) for 96 hours. Collectively, 55 isothermal calorimetry data entries corresponding to 11 mixtures tested at 5 different temperatures were extracted. The data entry corresponding to each mixture and testing temperature is designated as PxTy where x denotes the inclusion percentage of MPCM, and y indicates the testing temperature. The rate of hydration was recorded every 5 minutes and normalized per gram of cement (mW/g). The final dataset was compiled by concatenating data entries to establish more than 60000 time-dependent observations of hydration heat flow and

cumulative heat. The dataset contains one continuous input feature, time (hour), along with three discrete features including MPCM dosage (%), MPCMs' melting point (°C), and test temperature (°C). Heat flow rate (mW/g) and cumulative heat (J/g) were the outputs to be predicted by the trained models and are referred to as HF and H, respectively.

6.3.2 Data preparation and partitioning

Two different data split schemes were considered in this study as schematically illustrated in **Figure 6-1**. In the first approach, the entire dataset was randomly divided into training and testing subsets as per conventional approach in ML modeling. 70% of the data were used for training and the remaining 30% were allocated to the testing set. In another approach, all the data observations with 15 wt.% MPCM inclusion were considered as the testing set, while all other data observations (*i.e.*, corresponding to 0, 5, 10, 20, and 25 wt.% MPCM inclusions) were used for the training purpose. This approach was implemented to assess the generalization capability of the trained models to predict the hydration kinetics for cement-based systems with MPCM levels not included in the training dataset, e.g., 7.5%, 12.5%, etc. **Table 6-1** summarizes the datasets used for training and testing purposes. Input data was normalized before fitting to the models using **Eq. 6-2** below:

$$x'_i = \frac{x_i - \min(x)}{\max(x) - \min(x)} \quad \text{Eq. 6-2}$$

where $x = (x_1, x_2, \dots, x_n)$ is the input vector and x'_i is the normalized data.

Table 6-1: Training and testing datasets used for model development

Dataset	Number of observations	Split method
Train-1	44,433	Random (70%)
Test-1	19,044	Random (30%)
Train-2	52,932	MPCPM levels of 0, 5, 10, 20, and 25 wt.%
Test-2	10,545	MPCPM level of 15 wt.%

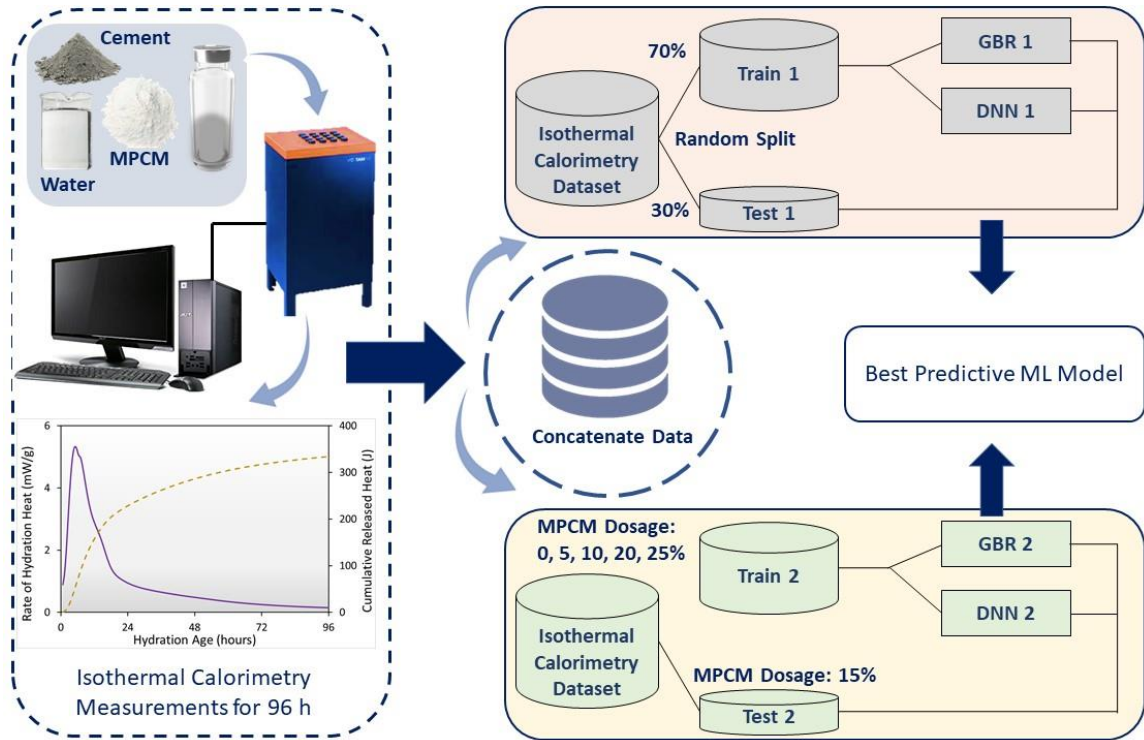


Figure 6-1: Data collection and partitioning schemes adopted in this study.

6.3.3 Model development

Gradient boosting regressor (GBR) and deep neural network (DNN) models were developed to predict the isothermal hydration curves. The models were trained and tested with both training datasets described in **Table 6-1**. The details of each model are explained below.

6.3.3.1 Gradient boosting regressor (GBR)

GBR is established based on the classification and regression tree (CART) which is a non-parametric algorithm for regression and classification problems. CART algorithm breaks down an intricate prediction problem into several simple decision-making trees by extracting meaningful patterns in the input data (Breiman, 2017). Furthermore, ensemble algorithms can be implemented to improve the prediction accuracy of the CART model. Using ensembles, multiple “weak learners” are aggregated to construct a single “strong” consensus estimator. Gradient boosting is a powerful ensemble algorithm developed based on the statistical boosting technique (Friedman, 2002; Ke *et al.*, 2017).

In the GBR algorithm, the additional base estimators are appended in sequence without the further change in the former model's parameters. The objective of GBR is to reach the function $F(X)$ which minimizes the loss of function $\mathcal{L}(F(X), y)$ where X and y are the inputs and output of a given dataset, $\{(X_1, y_1), (X_2, y_2), \dots, (X_N, y_N)\}$. The loss function indicates the deviation of the predictions from the actual outputs. Various error functions, such as the least squared error and least absolute error, can be used as the loss function (Yang *et al.*, 2020). GBR predictions are initiated using a constant function that grows in a greedy way as described below:

$$F_0(X) = \arg \min_{\gamma} \sum_{t=1}^N \mathcal{L}(y', y) \quad \text{Eq. 5-3}$$

where y' are the predictions. GBR model approaches the optimum function by weighting weak learners, $h(x_t)$, which are the basic decision tree estimators trained with the input data. The model progresses with adding additional trees in a greedy manner as follows:

$$F_m(\mathbf{x}) = F_{m-1}(\mathbf{x}) + h_m(\mathbf{x}) \quad \text{Eq. 6-4}$$

$$y' = F_m(X) = \sum_{m=1}^M h_m(X) \quad \text{Eq. 6-5}$$

where the constant m represents the number of weak estimators usually referred to as “ $n_estimators$ ”. To improve the generalization capability and mitigate the overfitting risk, a shrinkage coefficient, also known as the learning rate, is used in the training process to limit the contribution of each weak learner to the output prediction as expressed below:

$$\mathcal{F}_m(\mathcal{X}) = \mathcal{F}_{m-1}(\mathcal{X}) + \gamma_m h_m(x) \quad \text{Eq. 6-6}$$

where γ_m is the learning rate. The number of weak learners and learning rate are amongst the most essential hyperparameters that need to be fine-tuned. A larger number of estimators enhances the prediction accuracy, while excessive estimators may cause overfitting problems. Nevertheless, using low learning rates increases the model's generalization ability and mitigates the potential overfitting (Yang *et al.*, 2020). Immoderate hyperparameters' values could lead to erroneous predictions with poor

generalization ability. Hence, the GBR model should be vigorously tuned as will be discussed later. Scikit-learn library was used to implement the GBR model.

6.3.3.2 Deep Neural Network

Artificial neural networks (ANNs) are a machine learning paradigm that mimics the learning pattern of the biological brain (Meng *et al.*, 2019). ANNs are established based on several connected units referred to as neurons. The simplest ANN is constructed of three layers, i.e., input layer, hidden layer, and output layer, with few neurons in each layer (Liu *et al.*, 2021). Nonetheless, more complex problems and larger datasets can be better analyzed using more sophisticated neural networks with more hidden layers and neurons, typically known as deep neural networks (DNNs).

The input layer consists of neurons corresponding to input feature vectors. There are three main components in each hidden layer including weights, biases, and activation functions as expressed in **Eq. 6-7** below:

$$O(X) = g(\theta^k X + b^k) \quad \text{Eq. 6-7}$$

where X is the input data matrix, θ^k and b^k are the weight matrix and bias vector of the layer k , $O(X)$ is the predictions' vector, and $g(x)$ is the activation function (Abuodeh *et al.*, 2020). The used DNN model is a feed-forward network that uses a backpropagation algorithm to minimize the loss function of the network. Keras library was used to implement the DNN model in this study. The architecture of the network along with the optimization process need to be fine-tuned to carry out robust and generalized predictions as discussed in the next section.

6.3.3.3 Hyperparameter tuning

Bayesian optimization algorithm (BOA) was employed to tune the GBR and DNN models. The BOA is established based on the Bayes theorem expressed by **Eq. 6-8**:

$$p(w | D) = \frac{p(D|w)p(w)}{p(D)} \quad \text{Eq. 6-8}$$

where w is the unseen value, $p(w)$ is the preceding distribution, $p(D | w)$ is the posterior distribution, and $p(w | D)$ is the probability. Bayes rule deploys the prior knowledge to approach the posterior possibility and therefore, BOA uses the previous iterations to find the values for the next iteration. This signifies the efficiency of BOA to find the optimum point in comparison with arbitrary selection in conventional methods such as randomized search optimization. Details on BOA can be found in (Bergstra *et al.*, 2013; Frazier, 2018). In the present study, the Hyperopt library was used to implement BOA coupled with 3-fold cross-validation. Mean squared error (MSE) was monitored as the optimization score. After 100 iterations, the tuned parameters were extracted. Considering a large number of observations in the training data, the search space was narrowed down based on recommendations in the pertinent literature. It is noteworthy that identical hyperparameters were used to train HF and H for both training datasets. **Table 6-2** presents the search space and the tuned values for the GBR and DNN model.

Table 6-2: Search space and tuned hyperparameters of GBR and DNN models

GBR model		
Parameters	Search values	Tuned value
$n_estimators$	[100,500]	300
learning_rate	[0.05, 0.5]	0.3
max_depth	[1,15]	10
min_samples_split	[2,10]	4
DNN model		
Parameters	Search values	Tuned value
number of neurons in each layer	[32, 256]	128
number of layers	[1, 4]	3
activation functions	['ReLU', 'sigmoid', 'tanh']	'ReLU'
optimizer	['SGD', 'Adam']	'Adam'
learning rate	[0.0001, 0.01]	0.005
batch size	[64,1024]	500
epochs	[20,500]	300

6.3.3.4 Evaluation Metrics

The predictive performance of each model developed herein was assessed using several statistical indicators, including the mean absolute error (MAE), root mean squared error (RMSE), and coefficient of determination (R^2) as follows:

$$MSE = \sqrt{\frac{1}{m} \sum_{i=1}^m (Y_i - \hat{Y}_i)^2}, \quad \text{Eq. 6-9}$$

$$MAE = \frac{1}{m} \sum_{i=1}^m |Y_i - \hat{Y}_i|, \quad \text{Eq. 6-10}$$

$$R^2 = 1 - \frac{\sum_{i=1}^m (Y_i - \hat{Y}_i)^2}{\sum_{i=1}^m (Y_i - \bar{Y})^2}, \quad \text{Eq. 6-11}$$

6.3.4 Calculation of apparent activation energy (E_a)

Apparent activation energy of cement-based composites can be calculated using the heat of hydration data obtained from isothermal calorimetry tests (D'aloia & Chanvillard, 2002; Kada-Benameur *et al.*, 2000). For the first time, the modified ASTM C1074 method is coupled with the best developed ML model in this study to calculate the apparent activation energy of the cement-based systems with various levels of MPCM inclusion. For this purpose, the degree of hydration (DOH) of the cementitious system at any given time t is required. DOH of cement, α , is indicative of the cement hydration progress and represents the ratio of the cement grains that have reacted with water. The DOH of cement at any time t , $\alpha(t)$, is calculated using **Eq. 6-12**:

$$\alpha(t) = H(t)/H_c \quad \text{Eq. 6-12}$$

where $H(t)$ is the cumulative heat released from the cement reaction at time t (J/g) and is predicted by the ML model. H_c is the total heat of hydration of cement (J/g). Using Bogue's equation and the proportion of the chemical compositions and phases of the cement given in **Table 5-1**, H_{cem} can be calculated as follows:

$$H_c = 500P_{C_3S} + 260P_{C_2S} + 866P_{C_3A} + 420P_{C_4AF} + 624P_{SO_3} + 1186P_{FreeCa} + 850P_{MgO} \quad \text{Eq. 6-13}$$

where P_i denotes the mass fraction of the i^{th} chemical composition or phase. The cement hydration evolution can be mathematically expressed with different hydration models. Several studies have proposed using a three-parameter exponential function to characterize the hydration progress of the cement paste with time as follows:

$$\alpha(t) = \alpha_u e^{-\left(\frac{\tau}{t}\right)^\beta} \quad \text{Eq. 6-14}$$

where α_u is the maximum DOH, τ is the hydration time parameter, and β is the hydration shape parameter (Poole *et al.*, 2007). The hydration parameters can be obtained by fitting the DOH predicted by the ML model to Eq. 6-14 (Poole *et al.*, 2007; Schindler, 2004; Wirquin *et al.*, 2002). It is noteworthy that based on the modified ASTM C1074 method, the hydration time parameter (τ) was employed to calculate E_a instead of using the equivalent time in the Arrhenius equation. The following steps were implemented to obtain E_a :

- The change in the DOH with time was calculated using **Eqs. 6-12** and **6-13**. The DOH at the given time t was calculated by dividing the cumulative released heat at time t obtained from the best predictive ML model by the total heat of hydration of the cement paste obtained from **Eq. 6-13**.
- The DOH of the MPCM-integrated systems was fitted to the three-parameter hydration model presented in **Eq. 6-14** to solve for α_u , τ , and β using a Bayesian optimization algorithm. The α_u , τ , and β values of each system were computed after 500 optimization iterations for every test temperature. R^2 was monitored as the loss function of the optimization process.
- The average value of α_u and β for each mixture was calculated. Since α_u and β of cementitious materials are independent of the temperature, the final value of τ at each isothermal temperature was recalculated using the average values of α_u and β .
- The negative of the natural logarithm of the hydration time parameter (τ) was plotted versus the inverse of the absolute temperature (in Kelvin) for each mixture.
- The activation energy for each mixture was calculated by multiplying the negative of the slope of $\ln(\tau) - 1/T$ linear line with universal gas constant R ($8.314 \text{ J} \cdot (\text{mol} \cdot \text{K})^{-1}$).

6.4 Results and discussion

This section discusses the prediction performance of the GBR and DNN models trained with both datasets listed in **Table 6-1**, “Train 1” and “Train 2”. Furthermore, the apparent activation energies of diverse MPCM-integrated cementitious composites based on the best predictive model are calculated and thoroughly analyzed.

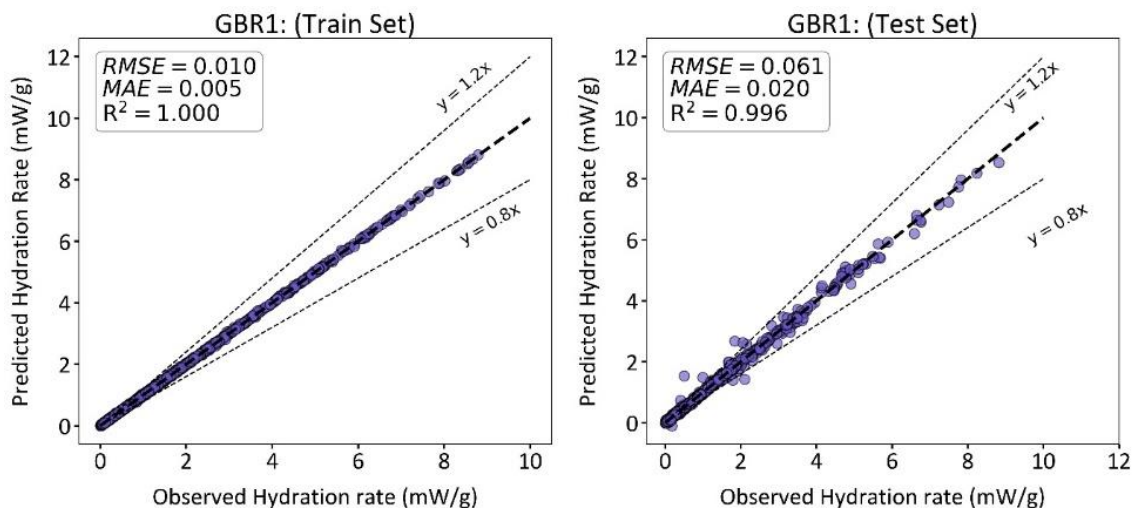
6.4.1 Prediction performance of ML models

The GBR and DNN models were vigorously tuned using the Bayesian optimization approach as explained earlier. The optimized values of hyperparameters listed in **Table 6-2** were extracted using a 3-fold cross validated Bayesian optimization to maximize the prediction accuracy and generalization ability and prevent the likelihood of overfitting to the training set. Thereafter, the GBR and DNN models were trained using the Train 1 and Train 2 datasets, respectively referred to as GBR1, GBR2, DNN1, and DNN2. **Figure 6-2** illustrates the regression fit of GBR1 model for the HF and H predictions. The model achieved a high testing R^2 of 0.9964 and 0.9999 for the HF and H prediction, respectively. To better perceive the prediction accuracy, **Figures 6-3** and **6-4** showcase the actual versus predicted hydration curves obtained from the GBR1 model for the cement-based systems incorporating En28 and En35 at 15°C, respectively. The entire hydration curves obtained from the GBR1 model can be found in **Appendix 1**. The solid lines represent the hydration curves obtained from the experiments, while the scatter points indicate the predictions of the model for the corresponding data points available in the Test-1 dataset. Accordingly, GBR1 was able to accurately predict the time-dependent hydration rate and heat evolution for various systems hydrated at different temperatures.

What is striking in the performance of GBR models is that although this model achieved very high training and testing scores when established using the Train-1 dataset, it surprisingly failed at the testing step when the Train-2 dataset was used for the model development. In other words, when no data observation of the cement-based systems with 15 wt.% of MPCM inclusion (i.e., P15 data entries) was available in the training set, the model could not correctly predict the hydration kinetics of those systems. This emphasizes the highly over-fitted performance of the GBR1 model despite its outstanding training scores. It is noteworthy that retuning of the GBR1 did not further improve its generalization performance and thus, it is concluded that GBR1 lacked the generalization capability and could not interpolate the hydration kinetics of unseen cementitious systems. In contrast to the GBR, DNN models demonstrated a robust performance when trained on either Train-1 or Train-2 datasets. **Figures 6-5** and **6-6** illustrate the regression fit of DNN1 and DNN2 for HF and H prediction, respectively. The actual versus predicted hydration curves of the

cement-based systems incorporating En28, and En35 at 40°C obtained from the DNN1 model are showcased in **Figs. 6-7 and 6-8**. It can be observed that similar to the GBR1, DNN1 achieved outstanding training and testing scores and meticulously predicted the hydration heat flow and cumulative heat of the Test-1 data points for all mixtures. The entire hydration curves obtained from the DNN1 model can be found in **Appendix 1**.

Furthermore, the DNN2 model demonstrated promising accuracy in predicting the hydration kinetics of the cement-based systems incorporating 15 wt.% of MPCMs. The testing R^2 of 0.853 and 0.982 in the prediction of HF and H, respectively, were obtained when the DNN2 model was developed based on the Train-2 dataset. To compare with similar models in the literature, it is noteworthy that Cook *et al.* (Cook *et al.*, 2021) achieved a testing RMSE of 0.331 mW/g and 14.398 J/g for predicting respectively the HF and H of blended cementitious systems using a random forest model. In the current study, testing RMSE of 0.371 mW/g and 14.945 J/g for HF and H predictions were obtained. Moreover, DNN1 and DNN2 indicated less over-fitting towards the training sets in comparison to GBR models. This underscores the superior generalization capability of the deep learning models compared to that of the GBR which fails to capture the hydration pattern of Test-2 data entries.



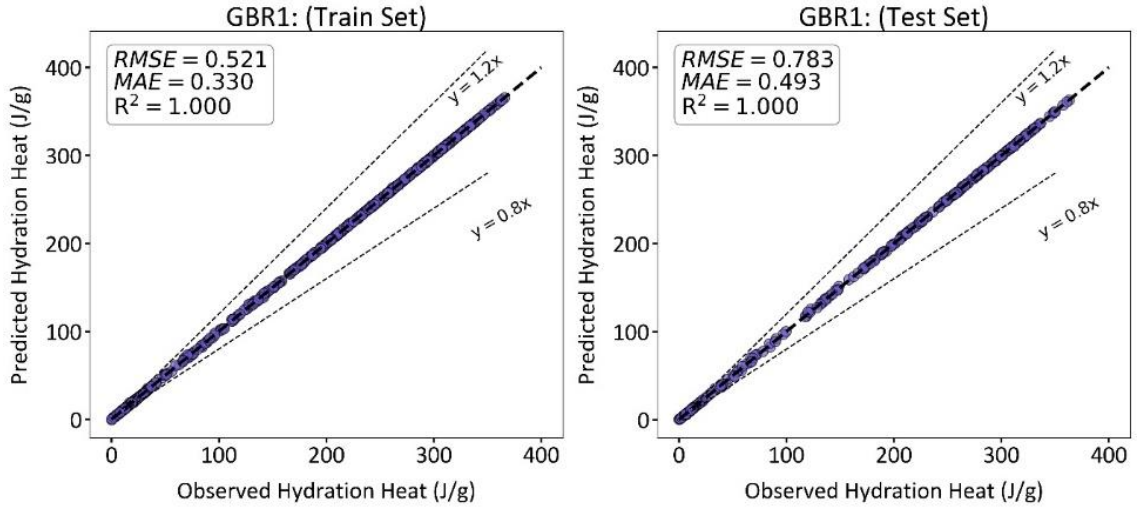


Figure 6-2: GBR1 model for prediction of hydration heat flow and cumulative heat.

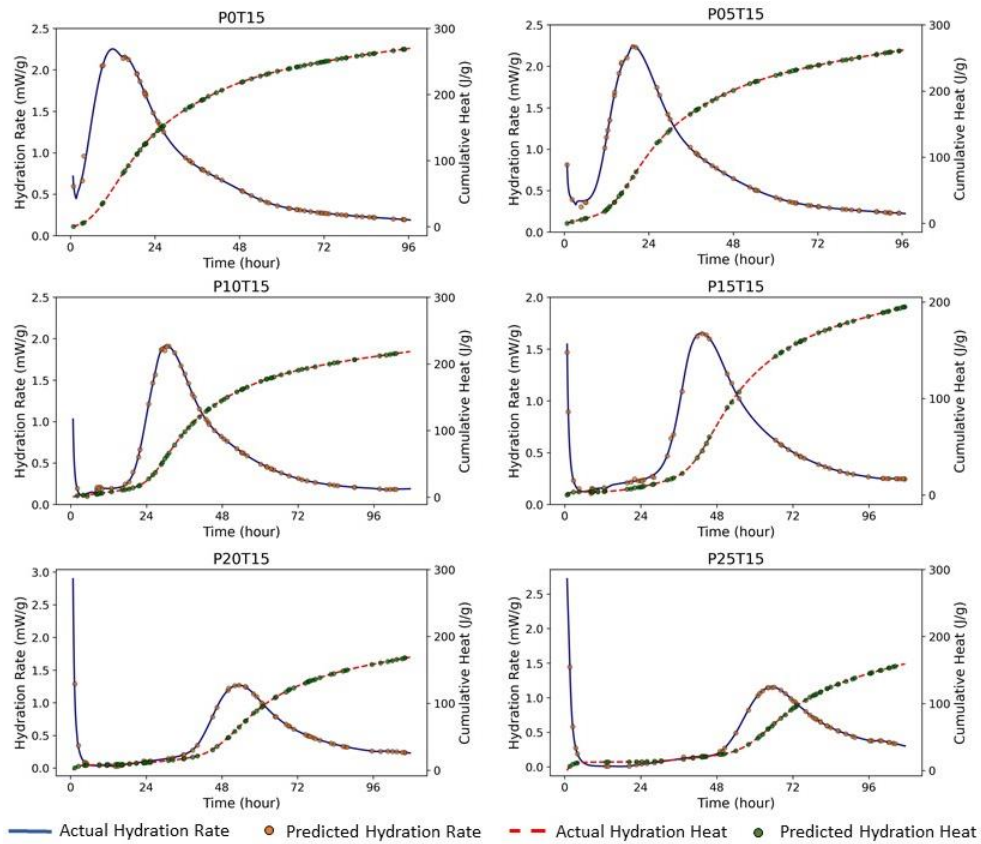


Figure 6-3: Predictions of GBR1 for cement systems incorporating various levels of En28 at 15°C.

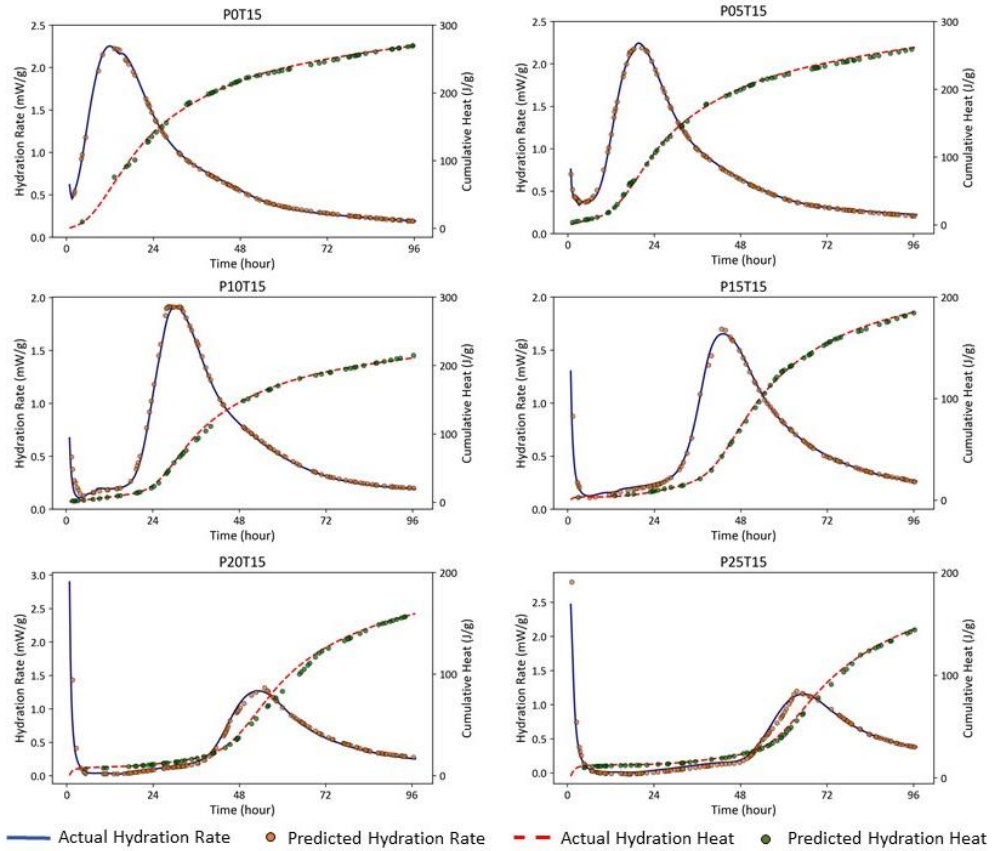
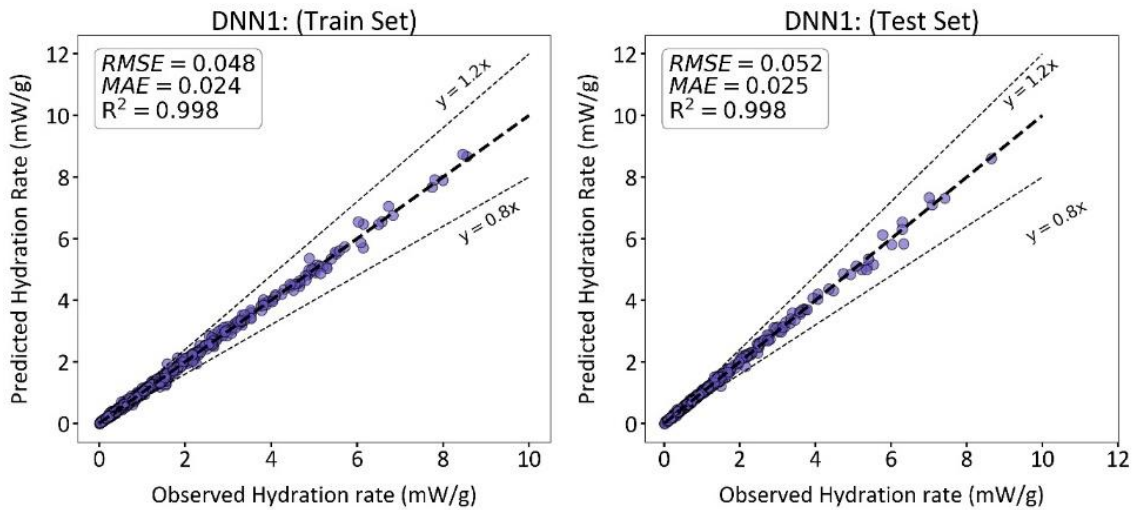


Figure 6-4: Predictions of GBR1 for cement systems incorporating various levels of En35 at 15°C.



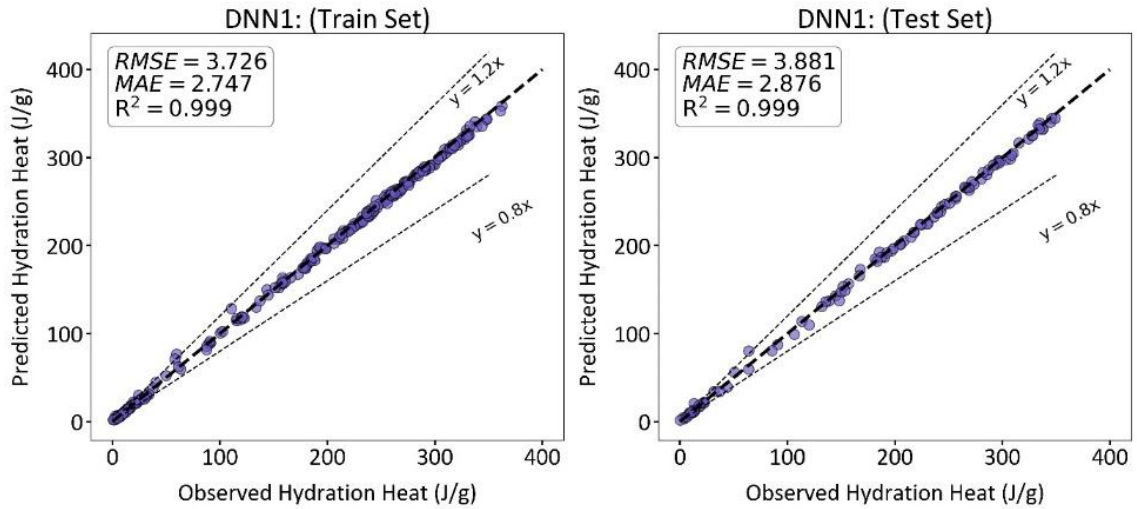


Figure 6-5 : DNN1 model for prediction of hydration heat flow and cumulative heat.

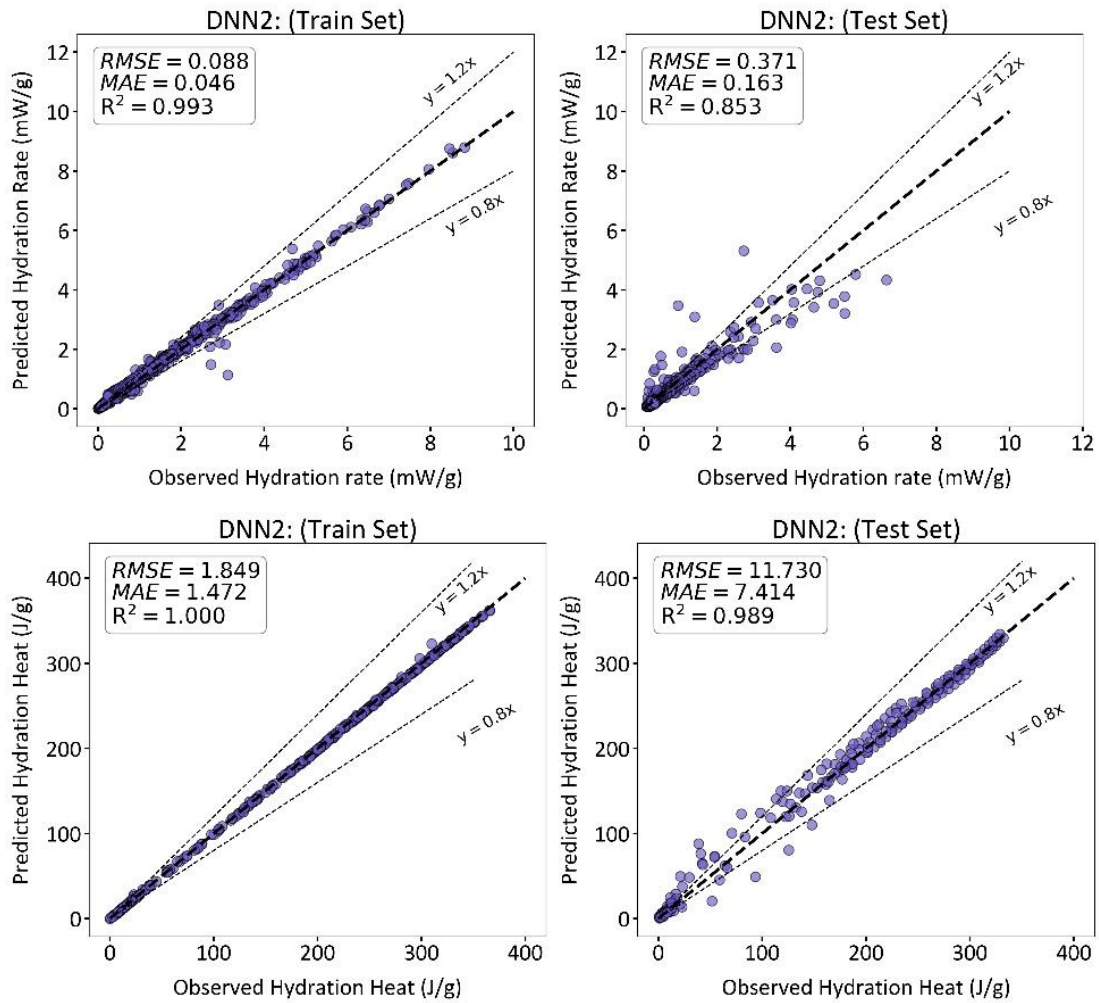


Figure 6-6: DNN2 model for prediction of hydration heat flow and cumulative heat.

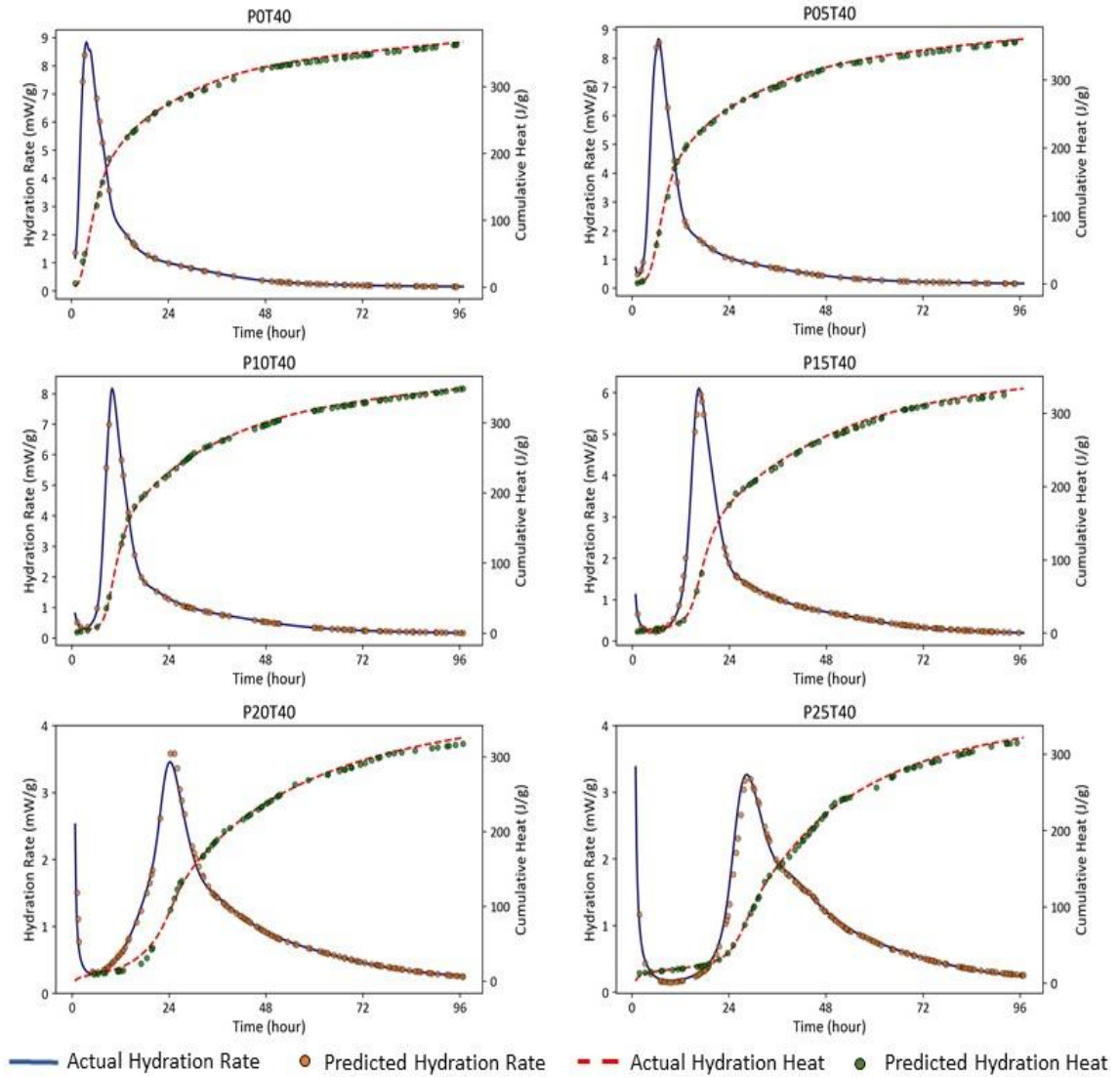


Figure 6-7: Predictions of DNN1 for cement systems incorporating various levels of En28 at 40°C.

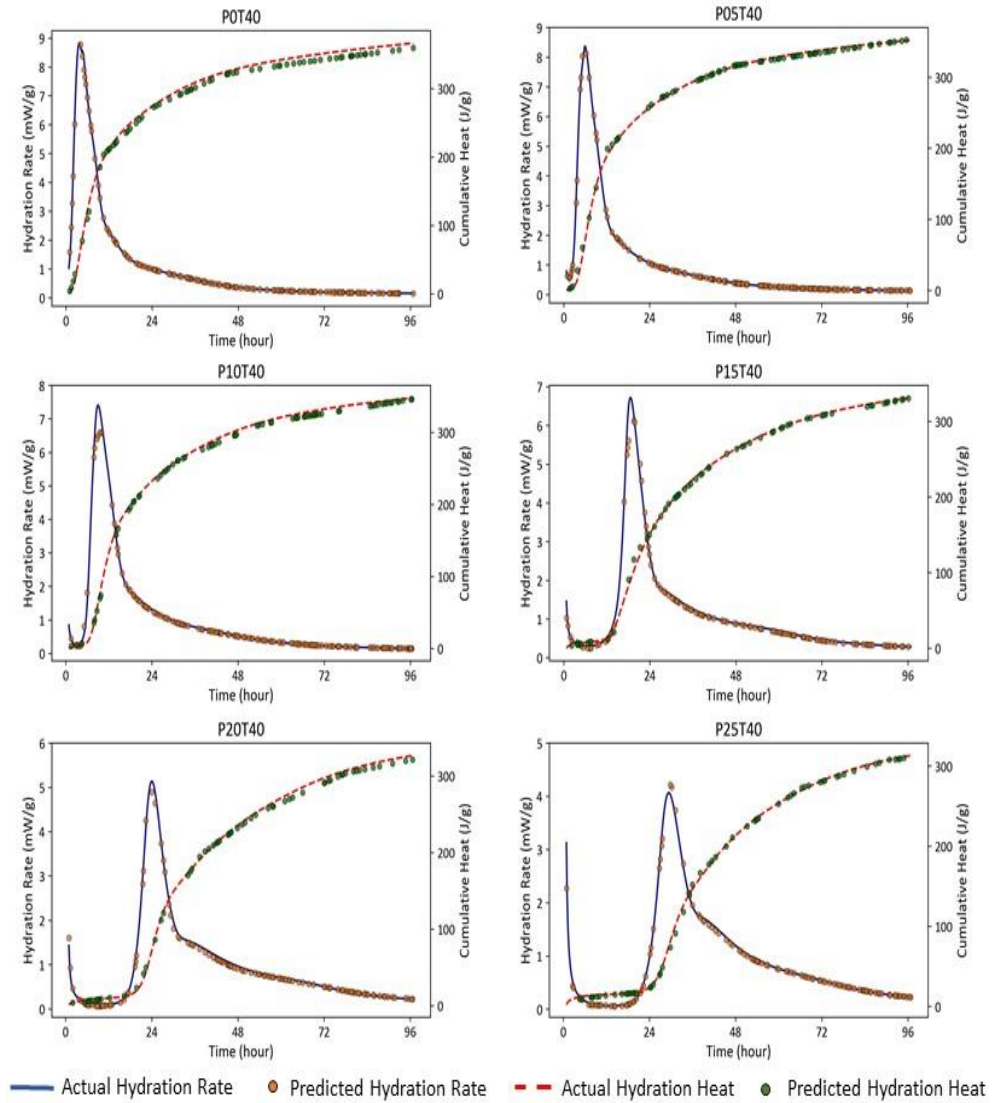
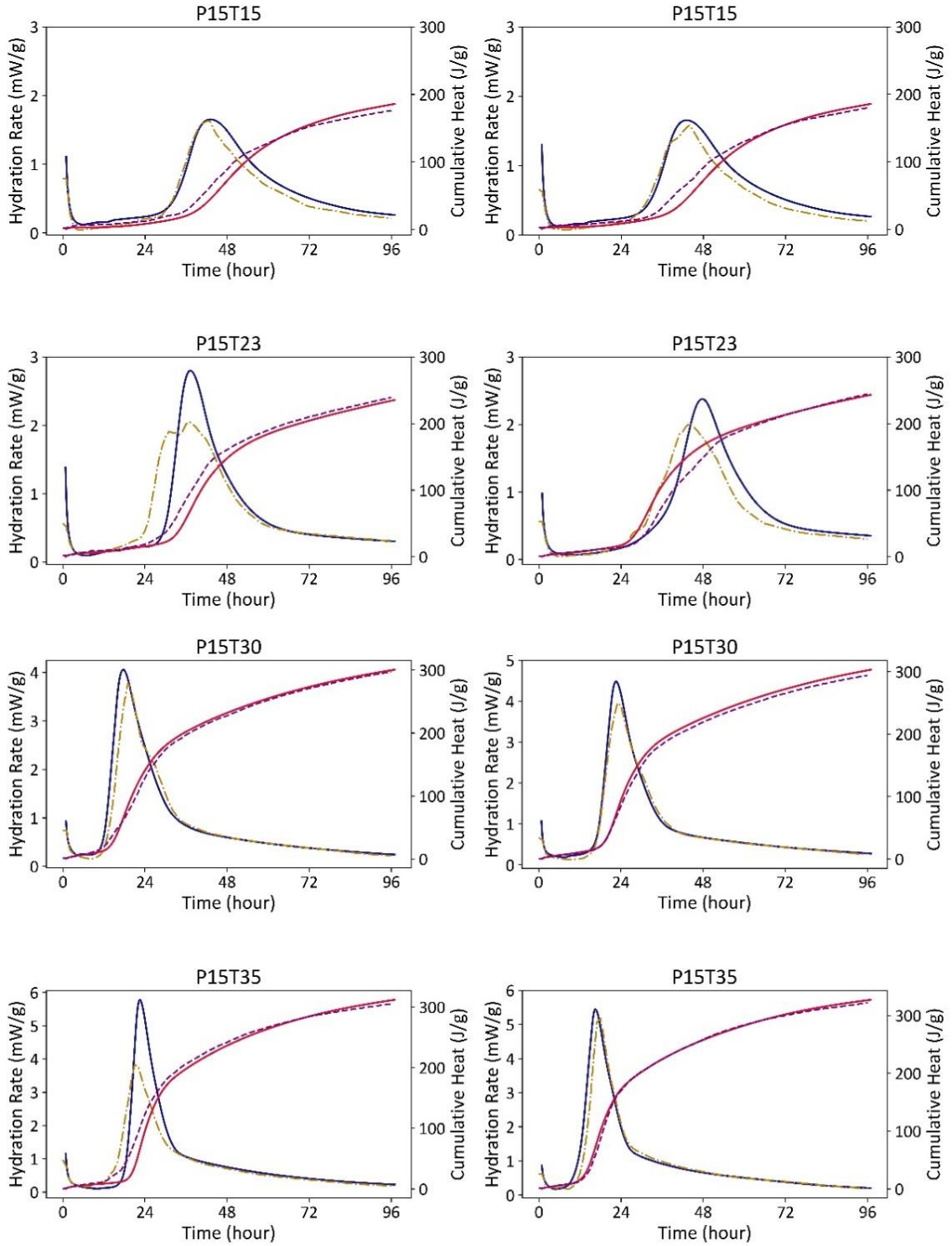


Figure 6-8: Predictions of DNN1 for cement systems incorporating various levels of En35 at 40°C.



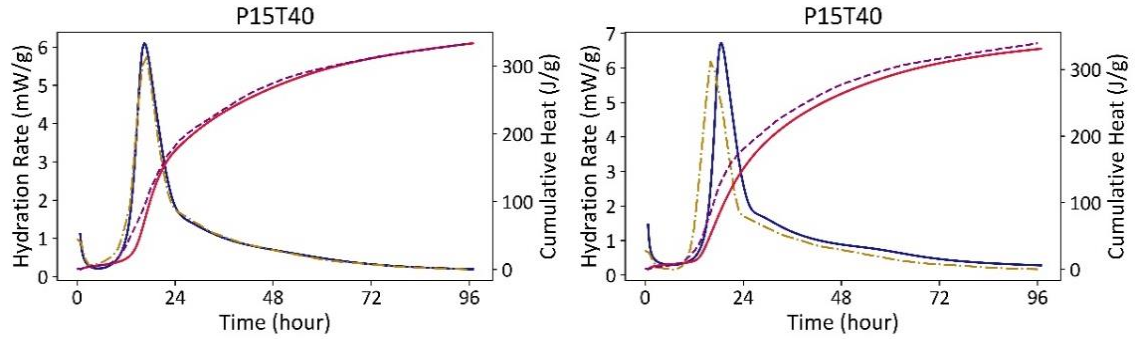


Figure 6-9: HF and H Predictions of DNN2 for cement systems incorporating 15 wt.% En28 (left) and En35 (right) at various temperatures.

6.4.2 Calculation of apparent activation energy

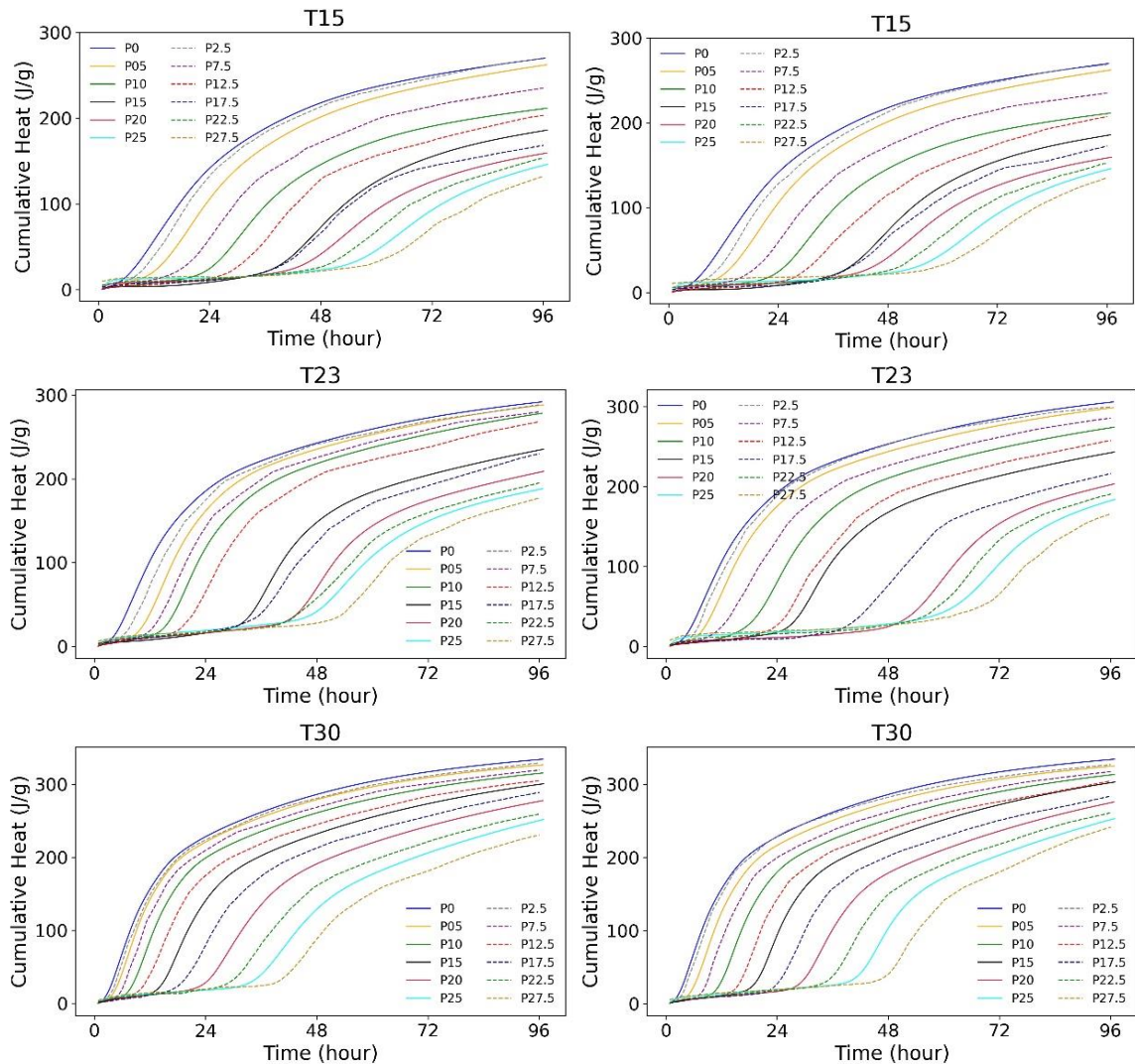
Owing to its outstanding performance in the prediction of the cumulative heat of hydration, DNN2 was employed to generate heat evolution data for diverse cement pastes incorporating En28 and En35. Inclusion levels of 0 to 27.5 wt.% at 2.5% intervals were considered. The time-dependent cumulative heat of those systems was predicted at 15, 23, 30, 35, and 40°C for 96 h. The simulated heat evolution curves are illustrated in **Figure 6-10**. It can be observed that the model demonstrated promising ability in interpolating and extrapolating the heat evolution of mixtures that are not experimentally investigated, i.e., P2.5, P7.5, etc. Although the heat evolution of those mixtures is not compared to experimental measurements, the trend observed in this parametric study suggests that DNN2 successfully captured the underlying pattern in the evolution of hydration heat. Accordingly, the graphs display a gradual decline in the released heat with the increase in the MPCM dosage, a comparable trend previously confirmed in experimental findings (Djamai *et al.*, 2019; Pilehvar *et al.*, 2017; Pilehvar *et al.*, 2020). It can also be observed that increasing the temperature accelerated the hydration kinetics and increased the cumulative released heat at earlier stages.

The DOH of each mixture was calculated based on **Eqs. 6-12** and **6-13** using the heat evolution predictions at any given time t . Thereafter, the apparent activation energy for each mixture was calculated using the procedure described in **Section 6.3.4**. **Tables 6-3** and **6-4** summarize the hydration parameters for the mixtures incorporating En28 and En35, respectively. The results indicate that with the increase in MPCM dosage, the

hydration time (τ) and hydration shape (β) parameters significantly increased. Accordingly, the increase in β indicates a reduction in the DOH of the system at earlier stages of the reaction followed by higher degree at later ages as it can be observed in **Fig. 6-10**. Furthermore, the increase in the τ is indicative of the decelerated hydration reactions and the prolonged induction period. This is probably related to the high water absorption of the MPCMs and the change in the dilution of the cementitious matrix after MPCM addition (Pilehvar *et al.*, 2017). Another potential reason is that MPCM particles tend to wrap around cement grains and thus, fewer nucleation sites were available for the growth of hydration products (Djamai *et al.*, 2019). Furthermore, the increase in τ was greatly correlated to the delay in the setting behavior and mechanical strength development of the cementitious matrix, which is compliant with previous findings in the literature (Fernandes *et al.*, 2014; Padala *et al.*, 2021; Sharifi & Sakulich, 2015).

The hydration time parameter at different temperatures was used to calculate the apparent activation energy of the cementitious systems as listed in **Table 6-5**. Accordingly, the inclusion of MPCMs into the cementitious matrix led to considerable reduction in the apparent activation energy, especially at higher dosages of MPCMs. It is notable that the apparent activation energy was calculated based on the relative change in the cement hydration rate at various temperatures. Hence, this reduction in E_a indicates less sensitivity of the hydration of MPCM-integrated cementitious systems to temperature. One probable reason for this behavior is the latent heat capacity and temperature regulation ability of MPCM particles. Moreover, the incorporation of MPCMs diminished the nucleation sites for precipitation and growth of hydration products. This probably lessened the nucleation and growth mechanism in the hydration process at early ages, and thus reduced the apparent activation energy (Jayapalan *et al.*, 2014). The reduction in E_a implies that the curing temperature had less effect on the mechanical strength gain of the concrete incorporating MPCM inclusions. For instance, the higher curing temperatures did not bring about faster setting and strength development in MPCM-integrated concrete compared to plain concrete. This results in less thermal stress or shrinkage of MPCM-integrated mixtures, which is in great agreement with hypothesis postulated in the open literature (Fernandes *et al.*, 2014; Šavija & Schlangen, 2016).

Figure 6-11 depicts the change in the apparent activation energy with the increase in MPCM dosage. It can be observed that the change in E_a was insignificant at very low dosages of MPCM. However, higher levels of MPCM inclusions caused significant reduction in the apparent activation energy. This is expected since the negative impacts of MPCMs on the cement paste, such as the change in the dilution of cement in the matrix, reduction in the nucleation sites, and hindering the contact of water with the cement grains, are aggravated with the increase in MPCM dosage. In **Fig. 6-12**, the E_a values calculated based on DNN2 predictions were compared to those obtained from the analysis of the experimental measurements (see Chapter 5). It is evidenced that the predictions from the model were very close to the corresponding experimental values with an error in the range of 0.30% to 5.52%, indicating excellent prediction accuracy.



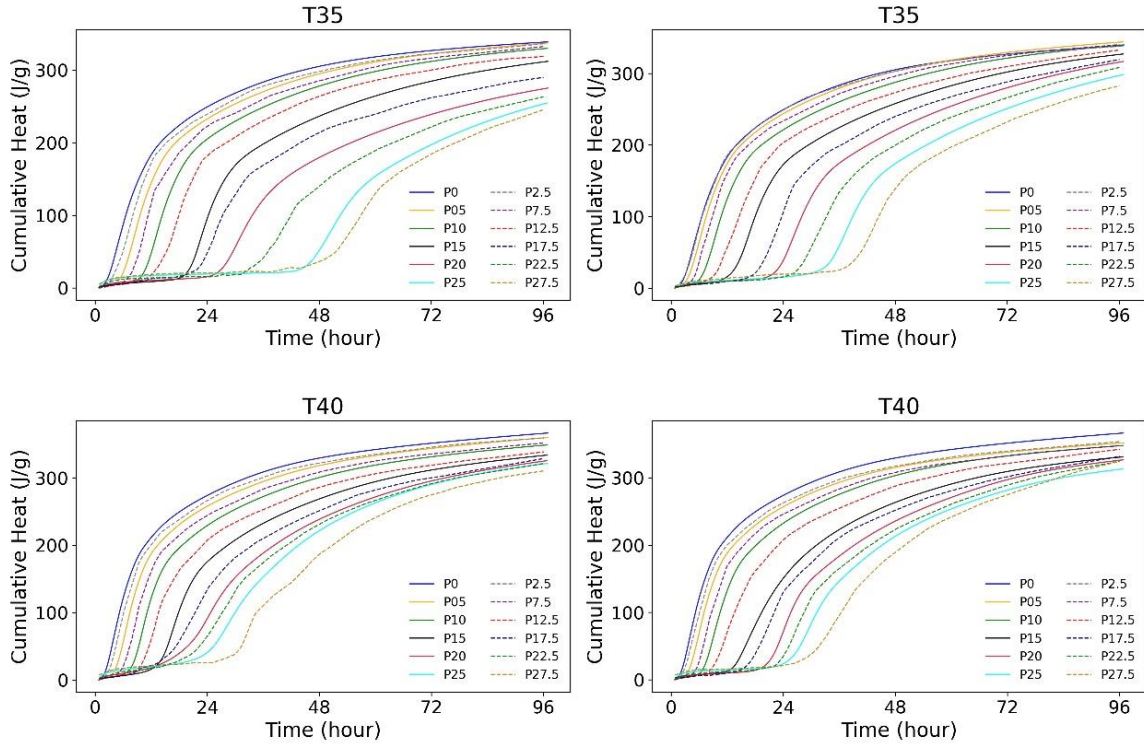


Figure 6-10: Heat evolution curves for various cement systems incorporating En28 (left) and En35 (right) obtained from DNN2 model.

Table 6-3: Hydration parameters for cement-based systems incorporating En28

Mix	T (°C)	Modified ASTM C1074				Mix	T (°C)	Modified ASTM C1074			
		α_u	β	τ (h)	R^2			α_u	β	τ (h)	R^2
P0	15	0.79	0.86	24.93	0.99	P15En28	15	0.61	2.19	54.38	0.94
	23			17.98	0.99		23			37.24	0.99
	30			10.70	0.99		30			21.98	0.99
	35			8.54	0.99		35			22.04	0.98
	40			6.09	0.97		40			17.19	0.95
P2.5En28	15	0.75	1.02	25.69	0.99	P17.5En28	15	0.59	2.29	59.87	0.94
	23			19.22	0.99		23			45.71	0.99
	30			11.31	0.99		30			26.36	0.99
	35			9.51	0.99		35			27.46	0.98
	40			6.82	0.97		40			20.19	0.94
P5En28	15	0.72	1.20	29.32	0.99	P20En28	15	0.57	2.54	65.73	0.94
	23			21.19	0.99		23			53.3	0.98
	30			12.03	0.99		30			32.19	0.99
	35			10.83	0.99		35			33.81	0.99
	40			8.03	0.96		40			23.12	0.94
P7.5En28	15	0.69	1.39	36.36	0.98	P22.5En28	15	0.56	2.74	69.82	0.94
	23			23.20	0.99		23			56.45	0.97
	30			13.17	0.99		30			38.20	0.99
	35			12.24	0.98		35			41.21	0.98
	40			9.34	0.95		40			25.14	0.93

P10En28	15	0.65	1.64	43.60	0.96	P25En28	15	0.56	2.77	75.21	0.94
	23			25.39	0.99		23			60.06	0.96
	30			14.98	0.99		30			44.19	0.99
	35			14.46	0.97		35			50.36	0.96
	40			11.15	0.94		40			27.57	0.93
P12.5En28	15	0.63	1.89	49.11	0.96	P27.5En28	15	0.56	2.85	80.53	0.90
	23			29.80	0.99		23			65.38	0.95
	30			18.01	0.99		30			50.29	0.98
	35			17.60	0.97		35			54.20	0.95
	40			13.77	0.95		40			33.02	0.93

Table 6-4: Hydration parameters for cement pastes incorporating En35

Mix	T (°C)	Modified ASTM C1074				Mix	T (°C)	Modified ASTM C1074			
		α_u	β	τ (h)	R^2			α_u	β	τ (h)	R^2
P0	15	0.79	0.86	25.09	0.99	P15En28	15	0.61	2.21	54.69	0.96
	23			16.78	0.99		23			41.80	0.99
	30			10.13	0.99		30			25.95	0.99
	35			8.04	0.99		35			18.89	0.97
	40			6.19	0.97		40			17.53	0.95
P2.5En28	15	0.75	1.01	26.40	0.99	P17.5En28	15	0.59	2.51	61.09	0.94
	23			17.56	0.99		23			52.62	0.99
	30			11.07	0.99		30			30.61	0.99
	35			8.47	0.99		35			23.19	0.96
	40			6.64	0.98		40			21.49	0.94
P5En28	15	0.73	1.12	29.98	0.99	P20En28	15	0.60	2.59	67.37	0.92
	23			19.54	0.99		23			63.10	0.98
	30			13.39	0.99		30			36.95	0.99
	35			9.39	0.99		35			27.90	0.97
	40			7.96	0.98		40			25.57	0.96
P7.5En28	15	0.7	1.33	34.26	0.98	P22.5En28	15	0.62	2.53	73.52	0.94
	23			21.15	0.99		23			68.62	0.96
	30			15.36	0.99		30			43.70	0.99
	35			10.52	0.98		35			33.37	0.98
	40			9.26	0.97		40			28.72	0.97
P10En28	15	0.67	1.60	41.55	0.96	P25En28	15	0.60	2.73	77.60	0.93
	23			26.09	0.99		23			72.69	0.94
	30			19.99	0.99		30			42.43	0.98
	35			13.93	0.97		35			38.92	0.98
	40			11.05	0.96		40			31.09	0.97
P12.5En28	15	0.64	1.89	49.16	0.97	P27.5En28	15	0.62	2.72	83.30	0.87
	23			33.12	0.99		23			79.7	0.89
	30			23.38	0.99		30			58.35	0.97
	35			16.44	0.97		35			46.59	0.98
	40			14.63	0.95		40			37.35	0.98

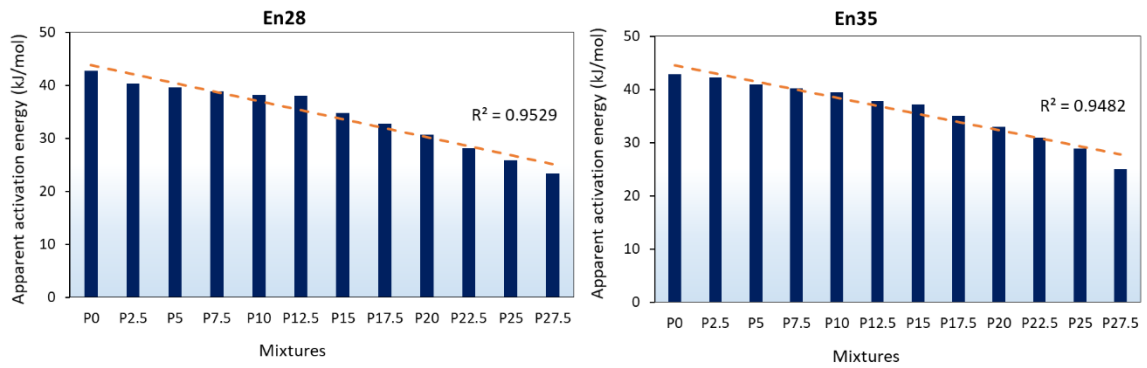


Figure 6-11: Variation in the apparent activation energy with MPCM addition of En28.

Table 6-5: Apparent activation energy of simulated systems

Mixture	Apparent activation energy (kJ/mol)		Mixture	Apparent activation energy (kJ/mol)	
	En28	En35		En28	En35
P0	42.809	42.809	P15	34.83	37.150
P2.5	40.342	42.202	P17.5	32.767	35.055
P5	39.555	40.933	P20	30.727	32.927
P7.5	38.876	40.227	P22.5	28.135	30.882
P10	38.211	39.434	P25	25.829	28.916
P12.5	37.977	37.819	P27.5	23.347	25.071

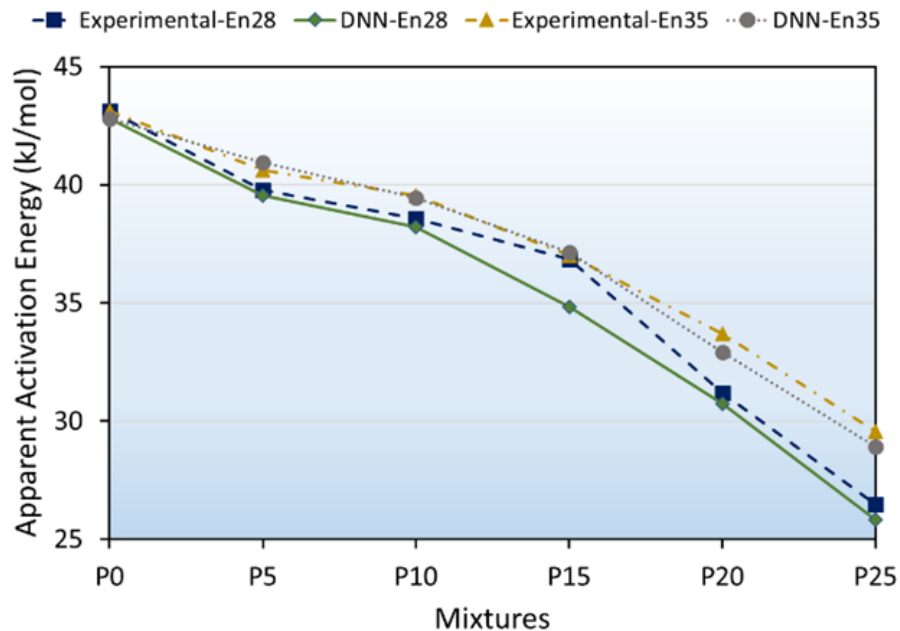


Figure 6-12: Comparison of apparent activation energy obtained from experimental measurements and DNN2 predictions.

6.5 Concluding remarks

This study proposed a deep learning paradigm to calculate the apparent activation energy of cement-based systems incorporating MPCMs using isothermal calorimetry data. Two different data partitioning schemes were adopted to better evaluate the generalization ability of the models in simulating the heat evolution of cement-based systems thus far unseen by the models. It was found that alternative data splitting methods can better reveal the generalization ability of the developed models. Furthermore, results demonstrated that deep learning achieved promising performance in the prediction of the cumulative heat using a large experimental dataset. The predictions were further utilized to calculate the apparent activation energy of diverse cement-based systems with MPCM inclusions. It was evidenced that the inclusion of MPCMs reduced the apparent activation energy which is indicative of lower sensitivity of the hydration reaction to temperature. The obtained results can help better estimate the temperature-related stresses and strains in hydrating concretes with MPCM inclusion. Furthermore, the developed deep learning framework can be coupled with existing compressive strength prediction models to better investigate the strength development of MPCM-integrated cementitious composites.

6.6 References

- Abuodeh, O. R., Abdalla, J. A., & Hawileh, R. A. (2020). Assessment of compressive strength of Ultra-high Performance Concrete using deep machine learning techniques. *Applied Soft Computing*, 95, 106552.
- Aguayo, M., Das, S., Maroli, A., Kabay, N., Mertens, J. C., Rajan, S. D., Sant, G., Chawla, N., & Neithalath, N. (2016). The influence of microencapsulated phase change material (PCM) characteristics on the microstructure and strength of cementitious composites: Experiments and finite element simulations. *Cement and Concrete Composites*, 73, 29-41.
- Agyenim, F., Hewitt, N., Eames, P., & Smyth, M. (2010). A review of materials, heat transfer and phase change problem formulation for latent heat thermal energy storage systems (LHTESS). *Renewable and sustainable energy reviews*, 14(2), 615-628.

Akeiber, H., Nejat, P., Majid, M. Z. A., Wahid, M. A., Jomehzadeh, F., Famileh, I. Z., Calautit, J. K., Hughes, B. R., & Zaki, S. A. (2016). A review on phase change material (PCM) for sustainable passive cooling in building envelopes. *Renewable and sustainable energy reviews*, 60, 1470-1497.

Assi, L., Soltangharai, V., Anay, R., Ziehl, P., & Matta, F. (2018). Unsupervised and supervised pattern recognition of acoustic emission signals during early hydration of Portland cement paste. *Cement and Concrete Research*, 103, 216-225.

Bentz, D. P. (2014). Activation energies of high-volume fly ash ternary blends: Hydration and setting. *Cement and Concrete Composites*, 53, 214-223.

Bergstra, J., Yamins, D., & Cox, D. (2013). Making a science of model search: Hyperparameter optimization in hundreds of dimensions for vision architectures. *International conference on machine learning*,

Bogner, A., Link, J., Baum, M., Mahlbacher, M., Gil-Diaz, T., Lützenkirchen, J., Sowoidnich, T., Heberling, F., Schäfer, T., & Ludwig, H.-M. (2020). Early hydration and microstructure formation of Portland cement paste studied by oscillation rheology, isothermal calorimetry, ¹H NMR relaxometry, conductance and SAXS. *Cement and Concrete Research*, 130, 105977.

Boussaba, L., Foufa, A., Makhlof, S., Lefebvre, G., & Royon, L. (2018). Elaboration and properties of a composite bio-based PCM for an application in building envelopes. *Construction and Building Materials*, 185, 156-165.

Breiman, L. (2017). *Classification and regression trees*. Routledge.

Carette, J., & Staquet, S. (2016). Monitoring and modelling the early age and hardening behaviour of eco-concrete through continuous non-destructive measurements: Part II. Mechanical behaviour. *Cement and Concrete Composites*, 73, 1-9.

Chen, L., Zhang, Y., Wang, L., Ruan, S., Chen, J., Li, H., Yang, J., Mechtcherine, V., & Tsang, D. C. (2022). Biochar-augmented carbon-negative concrete. *Chemical Engineering Journal*, 431, 133946.

Cook, R., Han, T., Childers, A., Ryckman, C., Khayat, K., Ma, H., Huang, J., & Kumar, A. (2021). Machine learning for high-fidelity prediction of cement hydration kinetics in blended systems. *Materials & Design*, 208, 109920.

D'aloia, L., & Chanvillard, G. (2002). Determining the “apparent” activation energy of concrete: E_a —numerical simulations of the heat of hydration of cement. *Cement and Concrete Research*, 32(8), 1277-1289.

Djamai, Z. I., Salvatore, F., Larbi, A. S., Cai, G., & El Mankibi, M. (2019). Multiphysics analysis of effects of encapsulated phase change materials (PCMs) in cement mortars. *Cement and Concrete Research*, 119, 51-63.

Drissi, S., Ling, T.-C., Mo, K. H., & Eddhahak, A. (2019). A review of microencapsulated and composite phase change materials: Alteration of strength and thermal properties of cement-based materials. *Renewable and sustainable energy reviews*, 110, 467-484.

Drissi, S., Mo, K. H., Falchetto, A. C., & Ling, T.-C. (2021). Understanding the compressive strength degradation mechanism of cement-paste incorporating phase change material. *Cement and Concrete Composites*, 124, 104249.

Eddhahak, A., Drissi, S., Colin, J., Caré, S., & Neji, J. (2014). Effect of phase change materials on the hydration reaction and kinetic of PCM-mortars. *Journal of thermal analysis and calorimetry*, 117(2), 537-545.

Faraj, K., Khaled, M., Faraj, J., Hachem, F., & Castelain, C. (2020). Phase change material thermal energy storage systems for cooling applications in buildings: A review. *Renewable and sustainable energy reviews*, 119, 109579.

Fayaz, H., Rahim, N., Hasanuzzaman, M., Nasrin, R., & Rivai, A. (2019). Numerical and experimental investigation of the effect of operating conditions on performance of PVT and PVT-PCM. *Renewable Energy*, 143, 827-841.

Fernandes, F., Manari, S., Aguayo, M., Santos, K., Oey, T., Wei, Z., Falzone, G., Neithalath, N., & Sant, G. (2014). On the feasibility of using phase change materials

(PCMs) to mitigate thermal cracking in cementitious materials. *Cement and Concrete Composites*, 51, 14-26.

Frazier, P. I. (2018). A tutorial on Bayesian optimization. arXiv preprint arXiv:1807.02811.

Friedman, J. H. (2002). Stochastic gradient boosting. *Computational statistics & data analysis*, 38(4), 367-378.

Gomaa, E., Han, T., ElGawady, M., Huang, J., & Kumar, A. (2021). Machine learning to predict properties of fresh and hardened alkali-activated concrete. *Cement and Concrete Composites*, 115, 103863.

Hassan, F., Jamil, F., Hussain, A., Ali, H. M., Janjua, M. M., Khushnood, S., Farhan, M., Altaf, K., Said, Z., & Li, C. (2022). Recent advancements in latent heat phase change materials and their applications for thermal energy storage and buildings: A state of the art review. *Sustainable Energy Technologies and Assessments*, 49, 101646.

He, L., Bai, L., Dionysiou, D. D., Wei, Z., Spinney, R., Chu, C., Lin, Z., & Xiao, R. (2021). Applications of computational chemistry, artificial intelligence, and machine learning in aquatic chemistry research. *Chemical Engineering Journal*, 426, 131810.

[Record #128 is using a reference type undefined in this output style.]

Huang, X., Chen, X., Li, A., Atinafu, D., Gao, H., Dong, W., & Wang, G. (2019). Shape-stabilized phase change materials based on porous supports for thermal energy storage applications. *Chemical Engineering Journal*, 356, 641-661.

Jayapalan, A. R., Jue, M. L., & Kurtis, K. E. (2014). Nanoparticles and apparent activation energy of Portland cement. *Journal of the American Ceramic Society*, 97(5), 1534-1542.

Jose, N. A., Kovalev, M., Bradford, E., Schweidtmann, A. M., Zeng, H. C., & Lapkin, A. A. (2021). Pushing nanomaterials up to the kilogram scale—An accelerated approach for synthesizing antimicrobial ZnO with high shear reactors, machine learning and high-throughput analysis. *Chemical Engineering Journal*, 426, 131345.

Kada-Benameur, H., Wirquin, E., & Duthoit, B. (2000). Determination of apparent activation energy of concrete by isothermal calorimetry. *Cement and Concrete Research*, 30(2), 301-305.

Ke, G., Meng, Q., Finley, T., Wang, T., Chen, W., Ma, W., Ye, Q., & Liu, T.-Y. (2017). Lightgbm: A highly efficient gradient boosting decision tree. *Advances in neural information processing systems*,

Lapeyre, J., Han, T., Wiles, B., Ma, H., Huang, J., Sant, G., & Kumar, A. (2021). Machine learning enables prompt prediction of hydration kinetics of multicomponent cementitious systems. *scientific reports*, 11(1), 1-16.

Li, D., Wang, J., Ding, Y., Yao, H., & Huang, Y. (2019). Dynamic thermal management for industrial waste heat recovery based on phase change material thermal storage. *Applied Energy*, 236, 1168-1182.

Li, G., Hong, G., Dong, D., Song, W., & Zhang, X. (2018). Multiresponsive graphene-aerogel-directed phase-change smart fibers. *Advanced Materials*, 30(30), 1801754.

Li, L., Rong, S., Wang, R., & Yu, S. (2021). Recent advances in artificial intelligence and machine learning for nonlinear relationship analysis and process control in drinking water treatment: A review. *Chemical Engineering Journal*, 405, 126673.

Liu, Y., Zhang, D., Tang, Y., Zhang, Y., Gong, X., Xie, S., & Zheng, J. (2021). Machine Learning-Enabled Repurposing and Design of Antifouling Polymer Brushes. *Chemical Engineering Journal*, 420, 129872.

Lizana, J., Chacartegui, R., Barrios-Padura, A., & Valverde, J. M. (2017). Advances in thermal energy storage materials and their applications towards zero energy buildings: A critical review. *Applied Energy*, 203, 219-239.

Maccarini, A., Hultmark, G., Bergsøe, N. C., & Afshari, A. (2018). Free cooling potential of a PCM-based heat exchanger coupled with a novel HVAC system for simultaneous heating and cooling of buildings. *Sustainable Cities and Society*, 42, 384-395.

Marani, A., & Nehdi, M. L. (2019). Integrating phase change materials in construction materials: Critical review. *Construction and Building Materials*, 217, 36-49.

Marani, A., & Nehdi, M. L. (2020). Machine learning prediction of compressive strength for phase change materials integrated cementitious composites. *Construction and Building Materials*, 265, 120286.

Meng, M., Qiu, Z., Zhong, R., Liu, Z., Liu, Y., & Chen, P. (2019). Adsorption characteristics of supercritical CO₂/CH₄ on different types of coal and a machine learning approach. *Chemical Engineering Journal*, 368, 847-864.

Meuwly, M. (2021). Machine learning for chemical reactions. *Chemical Reviews*, 121(16), 10218-10239.

Nunez, I., Marani, A., Flah, M., & Nehdi, M. L. (2021). Estimating compressive strength of modern concrete mixtures using computational intelligence: A systematic review. *Construction and Building Materials*, 310, 125279.

Padala, S. K., Deshpande, S. J., & Bhattacharjee, B. (2021). Assessment of setting characteristics, water absorption, thermal performance and compressive strength of energy-efficient phase change material (PCM)-ashcrete blocks. *Sādhanā*, 46(2), 1-19.

Pan, W., Li, K., & Teng, Y. (2018). Rethinking system boundaries of the life cycle carbon emissions of buildings. *Renewable and sustainable energy reviews*, 90, 379-390.

Pilehvar, S., Cao, V. D., Szczotok, A. M., Valentini, L., Salvioni, D., Magistri, M., Pamies, R., & Kjønksen, A.-L. (2017). Mechanical properties and microscale changes of geopolymer concrete and Portland cement concrete containing micro-encapsulated phase change materials. *Cement and Concrete Research*, 100, 341-349.

Pilehvar, S., Sanfelix, S. G., Szczotok, A. M., Rodríguez, J. F., Valentini, L., Lanzón, M., Pamies, R., & Kjønksen, A.-L. (2020). Effect of temperature on geopolymer and Portland cement composites modified with Micro-encapsulated Phase Change materials. *Construction and Building Materials*, 252, 119055.

Poole, J. L., Riding, K. A., Folliard, K. J., Juenger, M. C., & Schindler, A. K. (2007). Methods for calculating activation energy for Portland cement. *ACI Materials Journal*, 104(1), 303-311.

Saadoon, T., Gómez-Meijide, B., & Garcia, A. (2019). New predictive methodology for the apparent activation energy and strength of conventional and rapid hardening concretes. *Cement and Concrete Research*, 115, 264-273.

Sakai, Y., & Koga, N. (2022). Kinetics of component reactions in calcium looping appeared during the multistep thermal decomposition of Portland cement under various atmospheric conditions. *Chemical Engineering Journal*, 428, 131197.

Sargam, Y., & Wang, K. (2021). Hydration kinetics and activation energy of cement pastes containing various nanoparticles. *Composites Part B: Engineering*, 216, 108836.

Šavija, B., & Schlangen, E. (2016). Use of phase change materials (PCMs) to mitigate early age thermal cracking in concrete: Theoretical considerations. *Construction and Building Materials*, 126, 332-344.

Schindler, A. K. (2004). Effect of temperature on hydration of cementitious materials. *Materials Journal*, 101(1), 72-81.

Sharifi, N. P., & Sakulich, A. (2015). Application of phase change materials to improve the thermal performance of cementitious material. *Energy and Buildings*, 103, 83-95.

Tafesse, M., & Kim, H.-K. (2019). The role of carbon nanotube on hydration kinetics and shrinkage of cement composite. *Composites Part B: Engineering*, 169, 55-64.

Tanyildizi, H. (2021). Predicting the geopolymerization process of fly ash-based geopolymer using deep long short-term memory and machine learning. *Cement and Concrete Composites*, 123, 104177.

Wirquin, E., Broda, M., & Duthoit, B. (2002). Determination of the apparent activation energy of one concrete by calorimetric and mechanical means: Influence of a superplasticizer. *Cement and Concrete Research*, 32(8), 1207-1213.

Xu, H., Jiang, L., Yuan, A., Lei, Y., Wei, Z., Wang, Y., & Lei, J. (2021). Thermally-stable, solid-solid phase change materials based on dynamic metal-ligand coordination for efficient thermal energy storage. *Chemical Engineering Journal*, 421, 129833.

Yan, Y., Ouzia, A., Yu, C., Liu, J., & Scrivener, K. L. (2020). Effect of a novel starch-based temperature rise inhibitor on cement hydration and microstructure development. *Cement and Concrete Research*, 129, 105961.

Yan, Y., Wang, R., Liu, J., Tang, J., & Scrivener, K. L. (2021). Effect of a liquid-type temperature rise inhibitor on cement hydration. *Cement and Concrete Research*, 140, 106286.

Yang, F., Wang, D., Xu, F., Huang, Z., & Tsui, K.-L. (2020). Lifespan prediction of lithium-ion batteries based on various extracted features and gradient boosting regression tree model. *Journal of Power Sources*, 476, 228654.

Zajac, M., Durdzinski, P., Stabler, C., Skocek, J., Nied, D., & Haha, M. B. (2018). Influence of calcium and magnesium carbonates on hydration kinetics, hydrate assemblage and microstructural development of metakaolin containing composite cements. *Cement and Concrete Research*, 106, 91-102.

Zou, F., Zhang, M., Hu, C., Wang, F., & Hu, S. (2021). Novel CASH/PCE nanocomposites: Design, characterization and the effect on cement hydration. *Chemical Engineering Journal*, 412, 128569.

Chapter 7

7 Multiphysics Study on Cement-Based Composites Incorporating Green Biobased Shape-stabilized Phase Change Materials for Thermal Energy Storage¹

Two types of eco-friendly shape-stabilized phase change materials (SSPCMs) were developed in this study. Biobased PCMs were impregnated into the pore structure of recycled expanded glass granules and coated with silica fume particles using a 4-step vacuum impregnation method. The morphological and thermal properties of the fabricated SSPCMs along with their effects on the hydration, microstructural, mechanical, and thermal properties of cement-based composites were characterized through a set of multiphysics tests including isothermal calorimetry, compressive and tensile strength, capillary water absorption, 3D image analysis of μ -CT scans, and thermoregulating tests. Leak-free impregnation of PCMs into the pore structure of the EG aggregates was achieved, while attaining desirable latent heat capacity. Favorable melting/freezing behavior for application in thermal energy storage (TES) of cement-based building components was demonstrated. The developed SSPCMs can provide considerable TES capacity in cement based materials, which can moderate indoor temperature fluctuations, thus yielding substantial HVAC energy savings.

7.1 Introduction

Latent heat thermal energy storage (LHTES) has emerged in recent years as an expedient technology for efficient energy management and utilization. Buildings are responsible for nearly 40% of the global energy consumption, along with one-third of anthropogenic carbon emissions (Pan *et al.*, 2018). A significant share of the energy consumption in buildings is related to electricity usage, which has dramatically increased over the past decades due to escalating climate change, economic developments, and rising living standards (Palacios *et al.*, 2020). According to several reports in the literature, 40% of the

¹ A version of this chapter is submitted to “*Cement and Concrete Research*” journal, 2022

total energy consumption in buildings is used for cooling, heating, and air conditioning of indoor spaces. Integrating LHTES systems in buildings can enhance energy efficiency, maintain indoor thermal comfort, thus reducing the energy demand for cooling/heating spaces (Hassan *et al.*, 2022).

Phase change materials (PCMs) can be used to develop LHTES-integrated building components. Solid-liquid PCMs with melting/freezing temperatures near room temperature have been used as latent heat storage integrant in building materials. Gypsum and cement-based composites are the most prevalent construction materials for incorporating PCMs (Baetens *et al.*, 2010; Zhang *et al.*, 2004). Numerous research studies in the open literature reported that the inclusion of PCMs in building elements, such as walls and envelopes, improves thermal performance and narrows indoor temperature fluctuations (De Gracia & Cabeza, 2015). For instance, Qu *et al.* (Qu *et al.*, 2021) found that integrating PCMs into building envelopes can effectively reduce the indoor temperature fluctuations and bring about 4.8%-34.8% energy savings depending on the applied climatic condition and the thermophysical properties of the PCM.

The risk of leakage of PCMs after direct incorporation in building materials is problematic in practical applications. Therefore, PCMs need to be properly encapsulated to prevent leakage in the host material during phase transitions. Various encapsulation techniques have been utilized to safely integrate PCMs into building components, including macro-encapsulation, micro-encapsulation, shape-stabilization, and lightweight aggregate (LWA) impregnation as explained in Chapter 2. Using the micro-encapsulation technique, PCMs are typically encapsulated in a polymeric shell (Drissi *et al.*, 2019). Microencapsulated PCMs (MPCMs) have been widely used in cement-based composites. Despite the improvement in the thermal performance of cement mortars and concretes (Pomianowski *et al.*, 2014), MPCMs have been found to be detrimental to mechanical properties. According to previous studies, this adverse effect is attributed to several mechanisms related primarily to the chemical and mechanical incompatibility of MPCMs with the cementitious matrix (Djamai *et al.*, 2019; Drissi *et al.*, 2019; Marani & Nehdi, 2019).

Using an alternative technique, PCMs can be embedded into inorganic porous materials to form shape-stabilized PCMs (SSPCMs) (S. Zhang *et al.*, 2021). SSPCMs have been developed for various applications with a broad range of melting/freezing temperatures and enthalpies (Farnam *et al.*, 2017). Recent findings demonstrated that the fabrication of SSPCMs with desired morphology and enhanced functionality can be a promising and practical solution to manufacture cost-effective LHTES building elements. Yet, concerted research is needed to better investigate the effect of SSPCMs on the mechanical and microstructural properties of cementitious composites.

Composite SSPCMs for use in building materials can be fabricated using various porous LWAs or powders. The vacuum impregnation technique has proven to be an efficient method to incorporate PCMs into the pore structure of the host agent. Memon *et al.* (Memon *et al.*, 2015) reported that the pore structure in LWAs is mostly blocked by air bubbles, and thereby using vacuum impregnation can significantly increase the absorption capacity of the LWAs. They used a synthetic LWA produced from expanded clay with 77% porosity and achieved the encapsulation of paraffin at 70 wt.% in LWAs after the vacuum impregnation (Memon *et al.*, 2015). Several other studies reported the fabrication of leak-free PCM/LWA aggregates using various types of LWAs such as expanded vermiculite (Li, 2021), expanded clay-prepared ceramsite (Y. Zhang *et al.*, 2021), pumice (Sarı *et al.*, 2020), and expanded perlite (Wi *et al.*, 2020).

In addition to LWAs, porous powders with large specific areas can be used to impregnate PCMs. Expanded graphite (EG) has been extensively deployed to develop SSPCMs owing to its high thermal conductivity and good adsorption capacity (He *et al.*, 2016; Ren *et al.*, 2018). More recently, the development of low-cost SSPCMs using solid waste materials has been proposed to further promote environmental protection. Several studies have reported using fly ash to encapsulate various types of organic and inorganic PCMs. Qiu *et al.* (Qiu *et al.*, 2020) used alkali treatment modified fly ash to encapsulate lauric acid. They achieved a latent heat of 65.7 J/g along with good thermal and chemical stability (Qiu *et al.*, 2020). In a similar study, Hekimoglu *et al.* (Hekimoğlu, Nas, Ouikhalfan, Sarı, Kurbetci, *et al.*, 2021) produced fly ash/lauric acid-myritic acid shape-stabilized composites with melting and freezing enthalpy of 45.3 and 44.6 J/g, respectively. The

thermal regulation test indicated that using this composite can reduce the interior temperature of the testing cell by up to 1.90 °C compared to the control cell (Hekimoğlu, Nas, Ouikhalfan, Sarı, Kurbetci, *et al.*, 2021). Comparable results were evidenced by Gu *et al.* (Gu *et al.*, 2021) and Wang *et al.* (Wang *et al.*, 2021). Slag and silica fume (SF) are among other materials deployed for encapsulating PCMs (Gencel, Yaras, *et al.*, 2022; Hekimoğlu, Nas, Ouikhalfan, Sarı, Tyagi, *et al.*, 2021). Hattan *et al.* (Hattan *et al.*, 2021) embedded polyethylene glycol (PEG) into SF particles using the vacuum impregnation technique. With SF:PEG mass ratio of 1.6:1, they achieved a melting and freezing enthalpy of 71.55 and 74.14 J/g, respectively. Thermal performance tests demonstrated that incorporating the developed SSPCM into cement mortar significantly decreased the maximum indoor temperature and moderated temperature fluctuations (Hattan *et al.*, 2021).

Developing green SSPCM composites from renewable and inexpensive resources is of particular importance. Moreover, multi-scale analyses of the mechanical, microstructural, and thermal properties of SSPCM-integrated cementitious composites are necessary for practical applications. Hence the present chapter aims at achieving two goals: i) fabrication of novel green and leak-free SSPCM composites with desirable morphology and thermal properties for developing LHTES-integrated building components; and ii) exploring the effects of the fabricated SSPCMs on the hydration, mechanical, microstructural, and thermal properties of cement-based mortars. For this purpose, two different biobased PCMs, with various melting temperatures, were encapsulated, using a 4-step vacuum impregnation technique, in recycled expanded glass (EG) granules as the carrying agent. Silica fume (SF) was used to coat the PCM-integrated granules to promote adsorption capacity and assure leakage prevention. The morphology, leakage rate, and thermal properties of the SSPCMs were characterized using SEM, DSC, and diffusion-oozing circle tests. Furthermore, the effects of the partial replacement of sand with SSPCMs on the hydration, mechanical, microstructural, and thermal properties of cement-based mortars were investigated using isothermal calorimetry, compressive and tensile strengths, capillary water absorption, micro-computed tomography (μ -CT), and thermoregulating tests.

7.2 Materials and methods

7.2.1 Materials

Two types of green biobased SSPCM composites with different melting temperatures and enthalpies were fabricated in this study. For this purpose, environmentally friendly EG particles were used as the carrying agent. EG particles were produced by blending recycled glass flour with a silicate binder and an expanding agent in a granulating pelletizer. EG granules having 1-2 mm in pore size were used as the carrying agent for SSPCM composites. Two types of biobased PCMs produced by PureTemp (USA) were used as the latent heat component, referred to as PCM 23 and PCM 28. PureTemp PCMs are non-toxic and sustainable chemicals derived from renewable sources such as animal fat and plant oil. **Table 7-1** lists the thermophysical properties of the utilized PCMs. Silica fume with a specific gravity of 2.58 kg/m³ was used for coating EG/PCM composite particles. Ordinary portland cement (OPC) compliant with ASTM C150 guidelines and natural river sand were used for mortar preparation. To adjust the workability of mortars, a polycarboxylate-based high-range water-reducing admixture (HRWRA) was utilized.

Table 7-1: Thermophysical properties of PCM 23 and PCM 28

PCM	Melting temperature (°C)	Melting enthalpy (J/g)	Density (kg/m ³)		Thermal conductivity (W/mK)	
			Liquid	Solid	Liquid	Solid
PCM 23	23	201	830	910	0.15	0.25
PCM 28	28	190	860	950	0.15	0.25

7.2.2 SSPCM Fabrication

Vacuum impregnation has been widely utilized to fabricate leak-free SSPCMs in previous studies (He *et al.*, 2016; Hekimoglu & Sari, 2021). Composite SSPCMs were fabricated using a 4-step vacuum impregnation technique as depicted in **Fig. 7-1**. Accordingly, EG particles were dried in a ventilated oven at 70 °C for 24 h. Afterward, a specified amount of EG was vacuumed in a filtering flask at 60 kPa for 2 h to evacuate the air trapped in the pore structure of EG particles. Subsequently, melted PCM was gradually added to impregnate the pores of EG particles by vacuum force. At this stage, the temperature of the system was kept at 50 °C using a temperature-controlled hot plate to maintain the PCM at the molten state. The vacuum impregnation was continued for 2 h after the addition of

PCM. In the last step, the vacuum process was stopped, and the air was allowed to enter to facilitate the impregnation of liquid PCMs into the pores of EG particles. Meanwhile, SF was gradually added to the EG/PCM composite and stirred for 30 minutes to uniformly coat all PCM-impregnated EG particles. The coated particles were ultimately cooled down, allowing the PCM to solidify inside the EG particles.

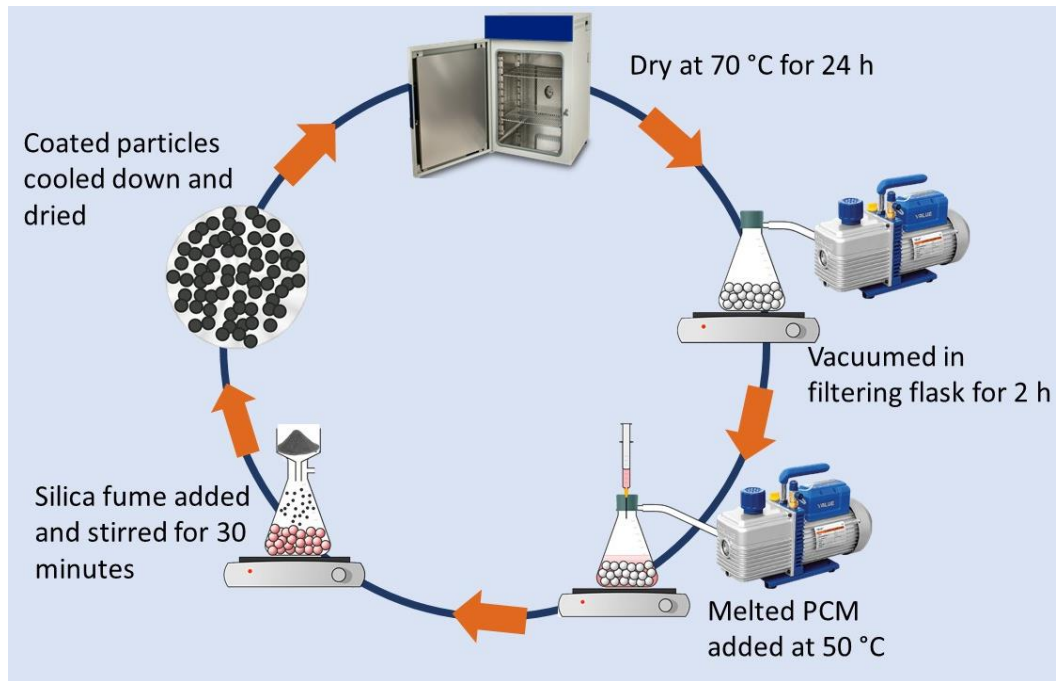


Figure 7-1: Schematic diagram of 4-step vacuum impregnation technique for fabrication of SSPCMs.

The optimum mass ratio of the EG/PCM/SF was experimentally determined for each type of PCM after several trials, followed by leakage tests to ensure the efficient fabrication of leak-free SSPCM particles as explained below. Accordingly, the final mass ratio of EG:PCM:SF was found as 1:0.8:0.4 in the case of PCM 23 and 1:0.9:0.4 in the case of PCM 28. The developed SSPCMs, encapsulating PCM 23 and PCM 28, are referred to as S23 and S28, respectively. **Figure 7-2** shows the appearance of EG, PCM, and SSPCM particles during the fabrication process.

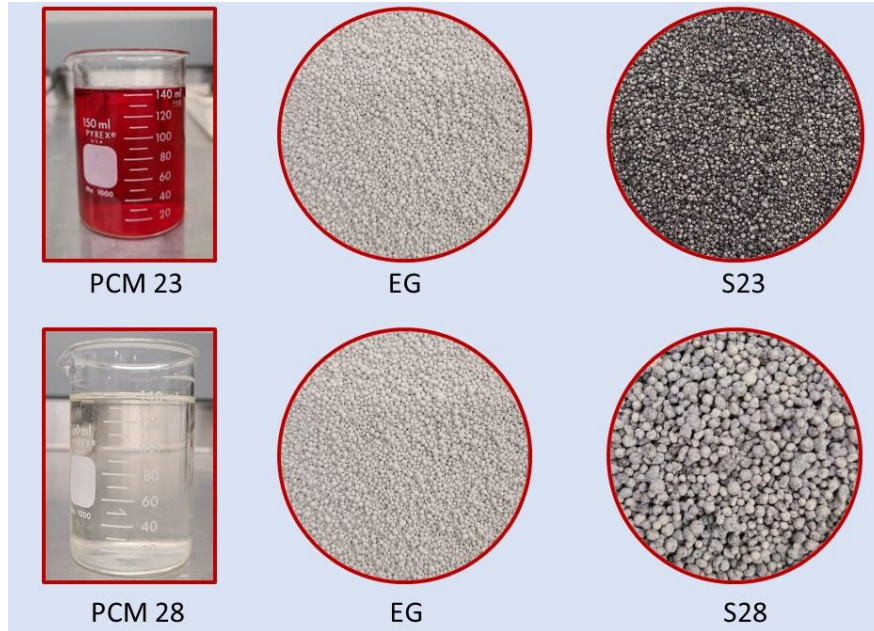


Figure 7-2: Physical appearance of PCMs, EG, and SSPCM particles.

7.2.3 SSPCM characterization

7.2.3.1 Leakage test: Diffusion-oozing circle test

The stability against leakage of SSPCMs was assessed using the diffusion-oozing circle test based on the recommendations given in (Ma *et al.*, 2013; Y. Zhang *et al.*, 2021). Accordingly, 5 grams of SSPCMs were dispersed in circles of 80 mm drawn on qualitative filter papers. The filter paper was then placed in a ventilated oven at 35 and 70 °C for 2 hours. The seepage of SSPCMs was examined by visual inspection of the leakage trace on the filter papers along with the weight loss of SSPCMs after heating. The leakage rate of SSPCMs was calculated using the following equation:

$$R_L = \frac{A-B}{A} \times 100\% \quad \text{Eq. 7-1}$$

where R_L is the leakage rate (%), A is the mass of SSPCM before heating (g), and B is the mass of SSPCM after heating for 2 h (g) (Ding *et al.*, 2020; Qu *et al.*, 2019).

7.2.3.2 Scanning Electron Microscopy

The morphology and microstructure of EG and SSPCM particles were observed using a scanning electron microscope (Hitachi TM 3030Plus). Images were captured with an operating current of 20 μ A and a voltage of 15 kV at various magnifications.

7.2.3.3 Differential Scanning Calorimetry (DSC)

The melting temperatures and enthalpies of the pristine PCMs and SSPCM composites were measured using a differential scanning calorimetry (DSC instruments, METTLER TOLEDO). The DSC test was conducted at a heating/cooling rate of 5 $^{\circ}$ C/min over the temperature range of -10 to 60 $^{\circ}$ C.

7.2.4 Characterization of SSPCM-integrated mortar

7.2.4.1 Isothermal calorimetry

The hydration kinetics of cement pastes incorporating various dosages of SSPCMs were analyzed using an isothermal calorimetry test. A water-to-cement (w/c) ratio of 0.5 was selected and SSPCMs were added at dosages of 0, 10, 20, 30, and 40 % by cement weight. The heat of hydration was measured in an eight-channel microcalorimeter (TAM air, TA Instruments) at 20 ± 0.02 $^{\circ}$ C. **Table 7-2** designates the cement/SSPCM pastes used for isothermal calorimetry tests.

7.2.4.2 Mechanical properties

To investigate the effect of fabricated SSPCMs on the thermomechanical properties of cement mortars, S23 and S28 particles were used as a partial replacement for sand. Accordingly, three groups of mortars were designed including 4 mixtures with SSPCM inclusion, two control mixtures with pure EG particles, and one control mixture with no SSPCM or EG content. **Table 7-3** presents the mixture design of mortar specimens cast for mechanical and thermal experiments. High SSPCM dosages equivalent to 20% and 40% of cement weight were considered to evaluate the correlation between high TES capacity and mechanical strength of the mortars. The mortar specimens were demolded 24 h after casting and kept in a moist room at 20 ± 2 $^{\circ}$ C until the testing age. The compressive strength

was tested using 50 mm cubes at 1, 3, 7, 14, 28, and 56 days, and splitting tensile tests were conducted using 5×10 mm cylinders at 7, 14, and 28 days.

Table 7-2: Cement paste samples used for isothermal calorimetry

Sample	SSPCM dosage (%)	PCM type	Sample	SSPCM dosage (%)	PCM Type
S23-P0	0	-	S28-P0	0	-
S23-P10	10	PCM 23	S28-P10	10	PCM 28
S23-P20	20	PCM 23	S28-P20	20	PCM 28
S23-P30	30	PCM 23	S28-P30	30	PCM 28
S23-P40	40	PCM 23	S28-P40	40	PCM 28

Table 7-3: Mixture design of mortars prepared for thermomechanical tests

Mixture	Cement	Water	Sand	SSPCM/EG	Superplasticizer	PCM Type
C	510	229.5	1535	0	15	-
EG20	510	229.5	1127	102	15	-
EG40	510	229.5	719	204	15	-
S23-P20	510	229.5	1127	102	15	PCM 23
S23-P40	510	229.5	719	204	15	PCM 23
S28-P20	510	229.5	1127	102	15	PCM 28
S28-P40	510	229.5	719	204	15	PCM 28

7.2.4.3 Capillary water absorption

The resistance of mortars to water penetration was investigated using the water absorption test based on ASTM C1585 guidelines. Disk-shaped specimens having a diameter of 100 mm and a height of 50 mm were used for testing. Before the test, all specimens were dried in a ventilated oven at 60 °C until the mass change was less than 0.1%. The curved face of the disks was sealed with silicon to ensure that water can only transport through the circular faces. The specimens were placed in a container with 5-mm deep water. The mass of the specimens was recorded at regular time intervals specified in ASTM C1585 to measure the initial and secondary capillary water absorption. The absorption (I) of specimens was calculated using **Eq. 7-2** below:

$$I = \frac{m_t}{a \times d} \quad \text{Eq. 7-2}$$

where m_t is the mass change in the specimen at time t (g), a is the area of specimen in contact with water (mm^2), and d is the density of water (g/mm^3). The slope of the $I-\sqrt{t}$

curve, known as sorptivity coefficient, was employed to measure the absorption capacity of samples.

7.2.4.4 Micro-computed tomography (μ -CT) scan

The dispersion of the EG and SSPCM particles in the cement mortar matrix along with their effect on the pore structure of the mortar samples were examined using X-ray micro-computed tomography. A Nikon XT-H-225-ST μ CT scanner was employed to scan the 56-day cured mortar specimens listed in **Table 7-3**. High-resolution 2D images of the X-ray projections were used to reconstruct the exterior and interior structure of the scanned samples. The resolution of the 3D images was set to 60 μ m voxels. The scanning was carried out with a voltage of 225 kV, a current of 120 μ A, and a power of 27 Watts. The image segmentation and analysis were performed using Dragonfly 2021.1 software, Object Research Systems (ORS) Inc, Montreal, Canada (available at <http://www.theobjects.com/dragonfly>).

7.2.4.5 Thermoregulating test

The effect of SSPCMs on the TES of cement mortars was studied using a thermoregulating test performed in a walk-in environmental chamber, similar to the test procedure proposed in the literature (Hekimoğlu, Nas, Ouikhalfan, Sarı, Tyagi, *et al.*, 2021; Liu, Lu, *et al.*, 2019; Marani & Madhkhan, 2018, 2021). For this purpose, specimens with dimensions of 30×15×5 cm were placed on top of the extruded polystyrene (XPS) insulation boxes with wall thickness and thermal conductivity of 6 cm and 0.05 W/mK, respectively, as shown in **Fig. 7-3**. A real-time wireless temperature monitoring system provided by Exact Technologies Corporation, Canada, was utilized to record the temperature history of the inner-side surface of the specimens. Two cyclic test scenarios were designed to evaluate the temperature regulating performance of the SSPCM-incorporated specimens. In the first scenario, referred to as a slow thermoregulating test, a temperature profile similar to the hourly ambient temperature of a hot summer day was applied to the outer side surface of the sample for 24 h. In the second approach, a cyclic temperature profile was exerted on specimens. Accordingly, the specimens were kept at the isothermal temperature of $7.5 \pm 0.1^\circ\text{C}$ until their inner-side temperature remained constant. Subsequently, the applied

temperature by the environmental chamber was rapidly increased to and then kept at 42.5 ± 0.1 °C until the temperature of the inner-side surface of all specimens become unchanged. Afterward, the applied temperature was cooled down to 7.5 ± 0.1 °C. This cyclic test scenario is referred to as the rapid thermoregulating test. The temperature history of all specimens was recorded and analyzed to apprehend the effect of SSPCM addition on the thermal performance of mortar specimens.

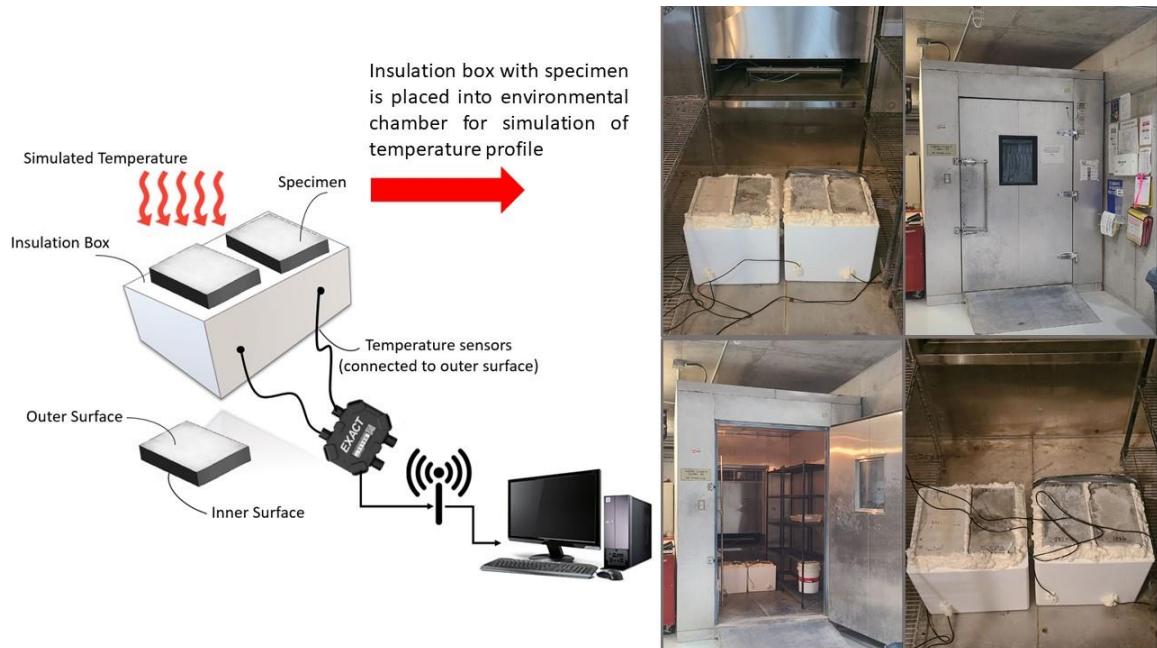


Figure 7-3: Thermoregulating test setup for evaluation of the TES capacity of mortar specimens.

7.3 Results and discussion

7.3.1 Morphology and leakage analysis of SSPCMs

The form stability and leakage rate of TES systems are of particularly great importance in practical applications. In this study, the vacuum impregnation technique was deployed to maximize the absorption capacity of EG particles. **Figure 7-4** shows the SEM images of the surface of EG and the developed SSPCM particles with different magnifications. EG particles have rounded morphology with various macro- and micropores on the surface. The semi-spherical morphology and porous structure of EG aggregates enabled high PCM absorption. Vacuum impregnation further helped evacuate air bubbles from micropores of

the EG particles and enhanced the absorption capacity. **Figures 7-4 (a) and (b)** depict the morphology of S23 and S28 composites coated with SF. It can be observed that major pores of EG particles were impregnated with PCMs and sealed with SF. Coating PCM-impregnated EG particles with silica fume created a sealing layer on the surface of SSPCM particles to absorb excessive PCM leaked from the macropores, as shown in **Fig. 7-4**.

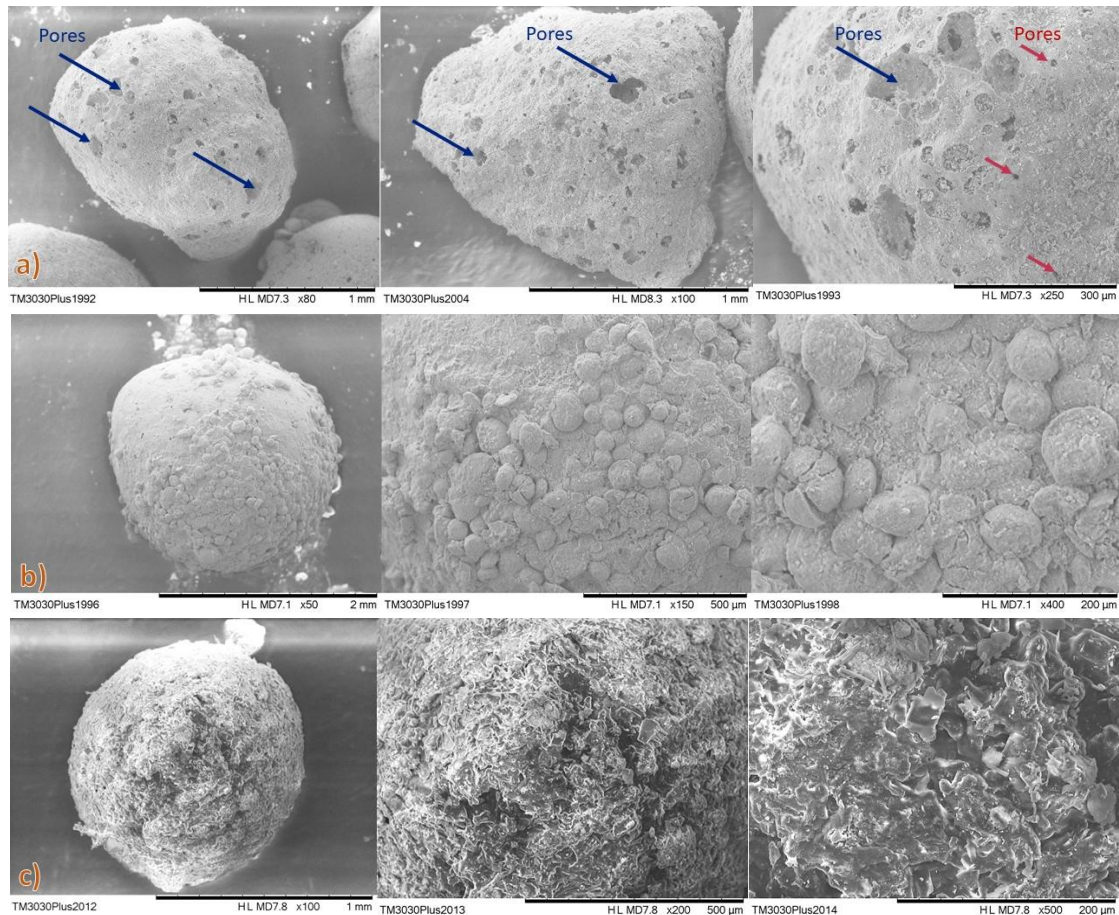


Figure 7-4: SEM images of the surface of a) EG; b) S23; and c) S28 particles.

To better evaluate the leakage behavior of the fabricated SSPCMs, the diffusion-oozing circle test was performed on triplicate samples of SSPCM composites before and after coating with SF. **Figure 7-5** illustrates the leakage trace of SSPCMs after being heated at 35 and 70 °C for two hours. Uncoated SSPCM particles exhibited significant leakage, especially at higher temperatures. In contrast, coating SSPCM particles with SF remarkably prevented the leakage of MPCMs upon melting as measured in **Fig. 7-5 (b)**. No noticeable leakage from coated S23 and S28 particles was detected after being heated at 35 °C. The

leakage rate for both S23 and S28 samples was found to be approximately 1% at 35 °C and 2% at 70 °C. This low leakage rate signifies the excellent encapsulation of PCMs inside the pore structure of EG particles coated with SF.

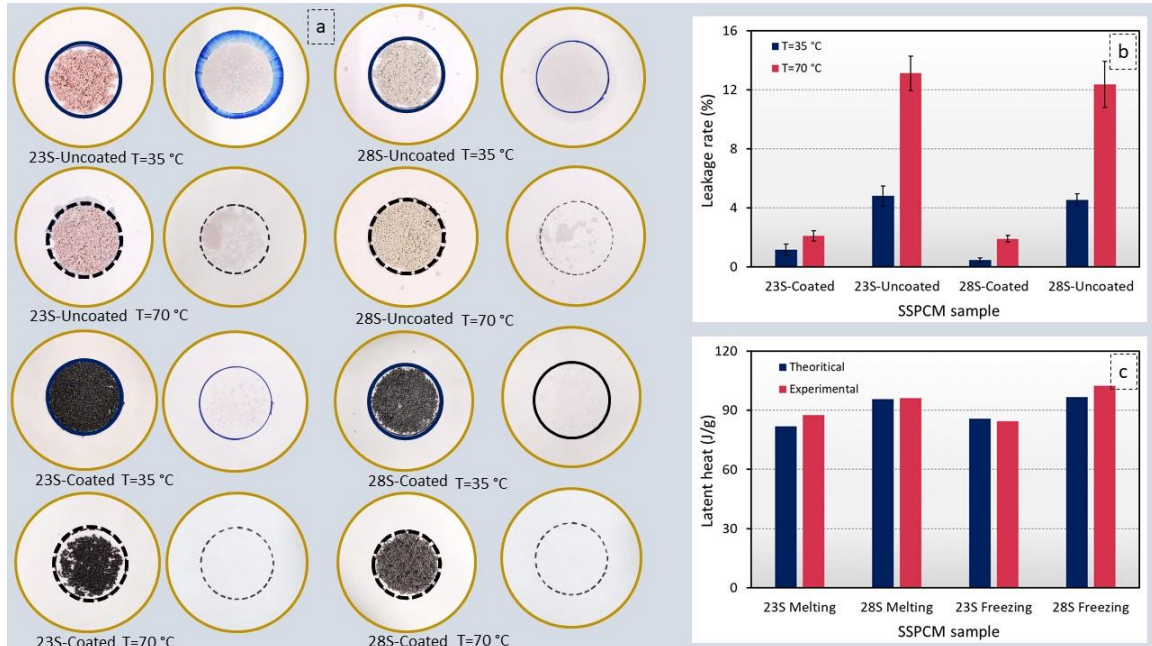


Figure 7-5: a) Diffusion-oozing circle test of SSPCM particles; b) comparison of the leakage rate of S23 and S28; and c) comparison of theoretical and experimental latent heat of S23 and S28.

7.3.2 Thermal properties of SSPCM

The phase change temperatures and enthalpies of pristine PCMs and SSPCMs were measured via the DSC test. **Figure 7-6** depicts the heating/cooling curves of PCM 23, PCM 28, S23, and S28 samples. Endothermic and exothermic peaks associated with the latent heat capacity of PCMs were detected in all specimens. The phase transition behavior of pure PCMs and composite SSPCMs are quantified in **Table 7-4**. It can be observed that the phase transition of PCM 23 started at an onset melting temperature (T_{mo}) of 18.99 °C followed by the peak melting temperature (T_{mp}) of 24.04 °C and finished with an endset melting temperature (T_{me}) of 30.38 °C. In the case of S23, the melting process was observed in a comparatively similar temperature range with a slightly higher peak melting temperature, *i.e.*, 25.57 °C. The solidification process of the PCM 23 occurred at a lower

temperature range, compared to the melting stage, with the onset and peak freezing temperatures of 16.69 and 14.23 °C, respectively. S23 indicated a relatively higher freezing temperature with the onset and peak freezing temperatures of 17.41 °C and 16.49 °C. On the other hand, PCM 28 exhibited a narrower temperature range during the melting and solidification stages compared to PCM 23. The melting process of PCM 28 and S28 started at an onset melting temperature of 28.59 and 27.28 °C, respectively, followed by a peak melting temperature of 31.13 and 32.68 °C. Nevertheless, S28 showed a slightly different freezing point compared to that of PCM 28. Accordingly, the solidification of PCM 28 started at 22.68 °C and ended at 17.31 °C with a peak freezing temperature of 21.24, while the freezing process of S28 started at 22.32 °C, with peak and endset freezing temperatures of 19.04 and 13.08 °C, respectively. The lower freezing point of S28 could be related to the confinement effect of SF that affected the PCM crystallinity (Hekimoğlu, Nas, Ouikhalfan, Sari, Tyagi, *et al.*, 2021; Kang *et al.*, 2015).

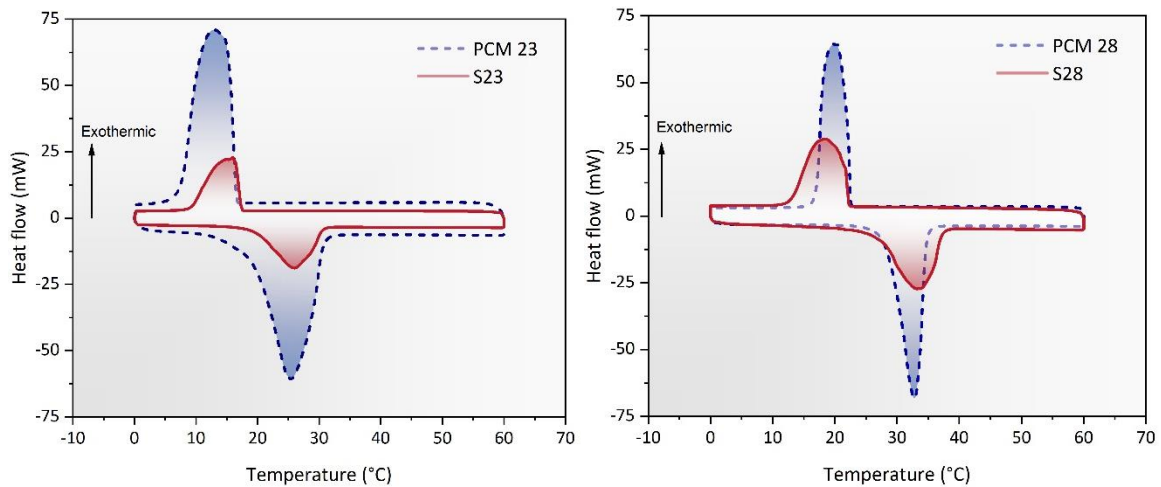
Figure 7-5 (c) compares the experimental latent heat of SSPCM composites obtained from DSC analysis with the theoretical latent heat capacity calculated based on the mass fraction of PCMs in the SSPCM composites. The experimental values were similar to the theoretical values, indicating successful encapsulation of the PCMs in the pore structure of EG and SF particles. Ultimately, melting enthalpies of 87.64 and 96.34 J/g were achieved for the S23 and S28 composites, respectively. **Table 7-5** compares the heat storage capacity of the developed SSPCMs with some similar studies in the literature. It could be realized that S23 and S28 have favorable heat storage properties for applications in buildings to provide TES capacity as will be discussed in subsequent sections.

Table 7-4: Melting/freezing temperatures and enthalpies of PCMs and SSPCMs

Sample	Melting				Freezing			
	T_{mo}	T_{mp}	T_{me}	ΔH_m	T_{fo}	T_{fp}	T_{fe}	ΔH_c
PCM 23	18.99	24.04	30.38	235.77	16.69	14.23	7.86	246.87
S23	19.78	25.57	30.46	87.64	17.41	16.49	9.52	84.52
PCM 28	28.59	31.13	34.39	244.51	22.68	21.24	17.31	247.20
S28	27.28	32.68	37.02	96.34	22.32	19.04	13.08	102.51

Table 7-5: Thermal properties of some SSPCM systems proposed in the literature

Composite	Melting temperature (°C)	Freezing temperature (°C)	Melting enthalpy (J/g)	Ref.
Fly ash/LA-MA	31.1	31.5	45.3	(Hekimoğlu, Nas, <i>et al.</i> , 2021)
Diatomite/paraffin	22.3	24.4	63.9	(Li <i>et al.</i> , 2014)
Fly ash/LA	45.39	40.82	49.71	(Gu <i>et al.</i> , 2021)
Hydrous salts/fly ash	25.3	19.7	106.9	(Liu, Peng, <i>et al.</i> , 2019)
Fly ash/LA	40.8	32.7	65.7	(Qiu <i>et al.</i> , 2020)
SF/biobased PCM	30.87	14.13	103	(Kang <i>et al.</i> , 2015)
Slag/CA	28	26.5	55.5	(Gencil, Yaras, <i>et al.</i> , 2022)
EG/biobased PCM/SF	25.57	16.49	87.64	Current study
EG/biobased PCM/SF	32.68	19.04	96.34	Current study

**Figure 7-6:** DSC curves of PCM 23 and S23 (left), and PCM 28 and S28 (right).

7.3.3 Isothermal calorimetry

The isothermal calorimetry curves of cement pastes incorporating S23 and S28 particles at 20 °C are illustrated in **Fig. 7-7**. It can be observed that the incorporation of SSPCM particles slightly affected the rate of hydration and the cumulative released heat. Two high-intensity peaks related to the hydration of C_3S and C_3A were observed for the plain cement

paste sample. With the addition of SSPCMs, the first peak of hydration slightly decreased and a considerable delay in the second peak was noted. This delay in the peak of the heat flow could be related to the latent heat capacity of the SSPCMs. Nonetheless, the effect of SSPCMs on the hydration rate was more significant in the decelerating segment. In this stage, a rapid decrease in the heat flow rate of the plain cement paste was observed, while the SSPCM addition slowed down the deceleration of the hydration rate. These changes could be attributed to the latent heat capacity of the SSPCM particles, which moderated the released heat during the hydration of cement particles. Comparable effects of polymeric microencapsulated PCMs (MPCMs) on cement hydration have been reported in the literature (Jayalath *et al.*, 2016; Pilehvar *et al.*, 2017). It is to be noted that the addition of MPCMs to cement paste typically prolongs the dormant period, which is related to the high water absorption of MPCMs along with their tendency to wrap around cement particles as observed in Chapter 5. This effect significantly aggravates with the increase in the MPCM dosage (Jayalath *et al.*, 2016). Nevertheless, the incorporation of SSPCMs indicated no considerable change in the dormant period of the cement hydration, demonstrating better compatibility with the cementitious matrix in comparison to MPCMs.

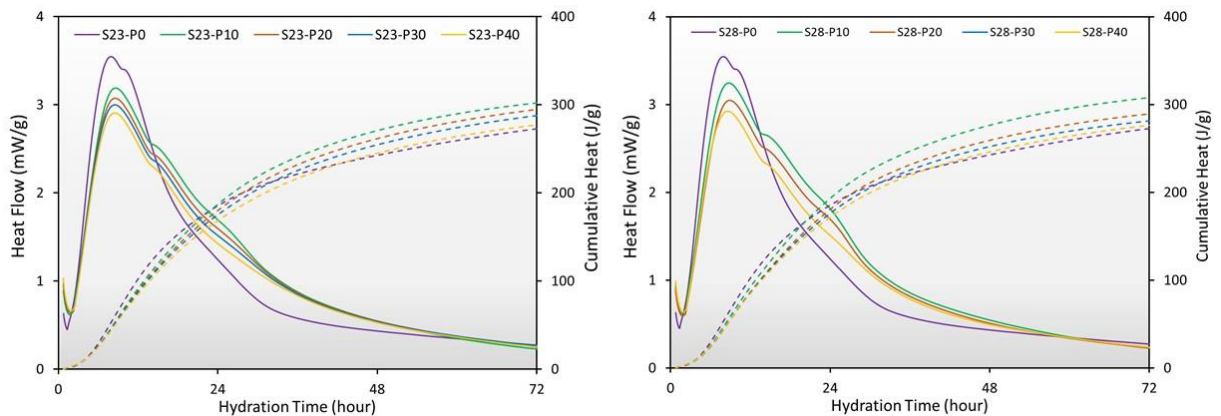


Figure 7-7: Isothermal calorimetry curves of cement pastes in presence of S23 (left) and S28 (right).

7.3.4 Mechanical properties

Although PCMs provide TES capacity in construction materials, such as cement-based composites, they can compromise mechanical properties. The compressive and splitting

tensile strength tests were performed to study the effect of the developed SSPCM additions on the mechanical strength of the mortar mixtures listed in **Table 7-3**. **Figures 7-8 (a) and (b)** illustrate the strength development of mortar specimens with pure EG or SSPCM inclusion equivalent to 20 and 40 wt.% of the cement content, respectively. It could be observed that the compressive strength significantly decreased upon EG and SSPCM addition. Several mechanisms could be related to the reduction of the compressive strength. Firstly, nonstructural EG particles have considerably lower stiffness compared to natural river sand (Balapour *et al.*, 2021). Therefore, partial replacement of sand with SSPCM particles led to a drastic reduction of compressive strength. With the increase in the EG or SSPCM particles dosage, *i.e.*, from 20 to 40 wt.%, the reduction in compressive strength became more prominent, as depicted in **Fig. 7-8 (c)**. The low strength of the lightweight EG or SSPCM particles dominated the strength development of the mortar, especially at later ages.

Another probable reason for the strength reduction is the increased porosity of the cementitious matrix after the addition of the EG and SSPCM particles. As shown in optical microscope images in **Fig. 7-9**, several macropores were evident in various locations of the broken surface of the samples incorporating EG and SSPCM particles. The blue arrays indicate the large pores in the samples and the red arrows show the EG or SSPCM particles. It was observed that with an increase in the dosage of SSPCM or EG particles, the size and number of macropores increased, leading to reduced compressive strength. The increase in the porosity could be related to the morphology (particle shape) and size distribution of the EG and SSPCM particles and thereby, a change in the packing density of the mortar (Gonçalves *et al.*, 2007). Furthermore, the smooth and rounded surfaces of the EG and SSPCM particles led to a weaker connection at the interfacial transition zone (ITZ) with the cement paste. The porosity of each sample can be better analyzed using the μ -CT scan images in **Section 7.3.6**.

It is noted that mixtures with SSPCM inclusion attained higher compressive strength compared to that of the corresponding mixtures with EG inclusion. This is probably related to the higher density of SSPCMs compared to EG particles, along with the stronger bond of SSPCMs with the surrounding cementitious matrix. Owing to the higher density of

SSPCM particles, a smaller volume of fine aggregates was replaced with SSPCMs compared to EG aggregates, which led to slightly higher compressive strength. The tensile strength also indicated a similar trend to the compressive strength where the addition of SSPCM and EG particles resulted in lower strengths. In general, cement mortars containing SSPCMs and EG particles resulted in lower strengths. In general, cement mortars containing SSPCMs indicated a relatively less drastic decrease in the compressive strength compared to mortars with MPCM inclusion reported in the literature (Djamai *et al.*, 2020).

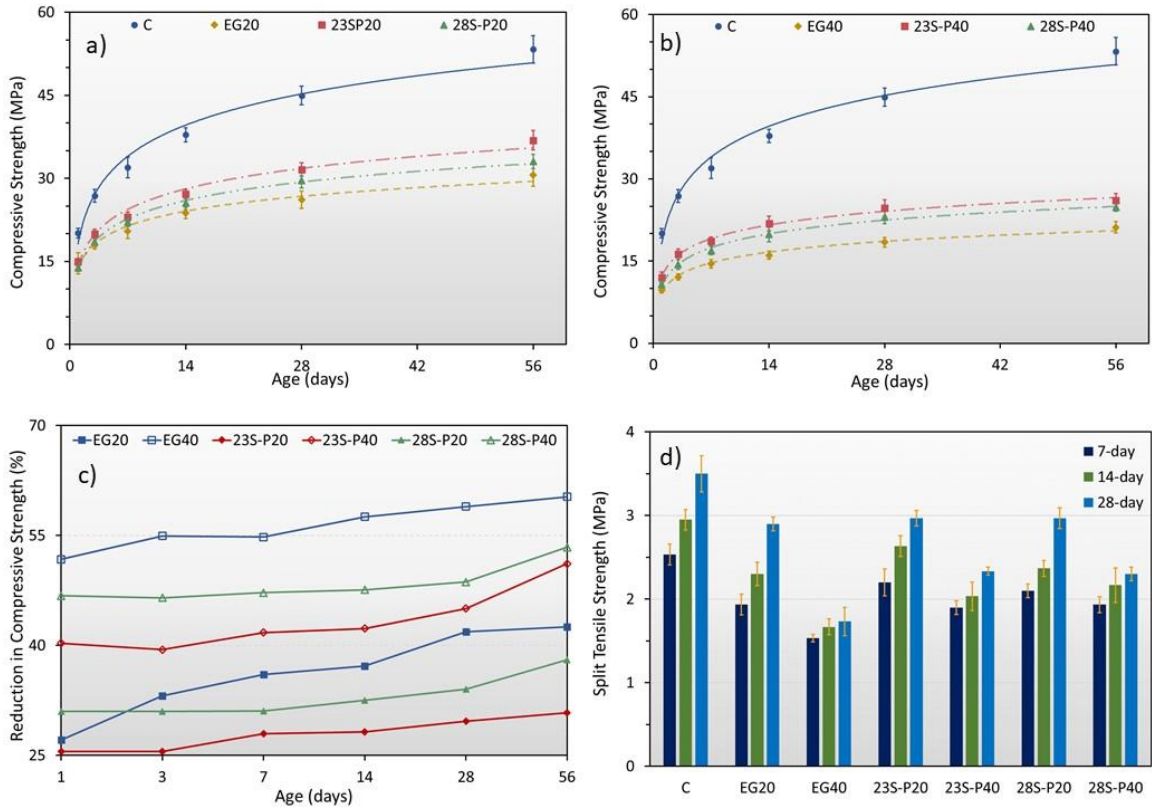


Figure 7-8: Mechanical strength of mortar specimens incorporating EG and SSPCM: a) and b) compressive strength; c) reduction percentage in compressive strength; and d) tensile strength.

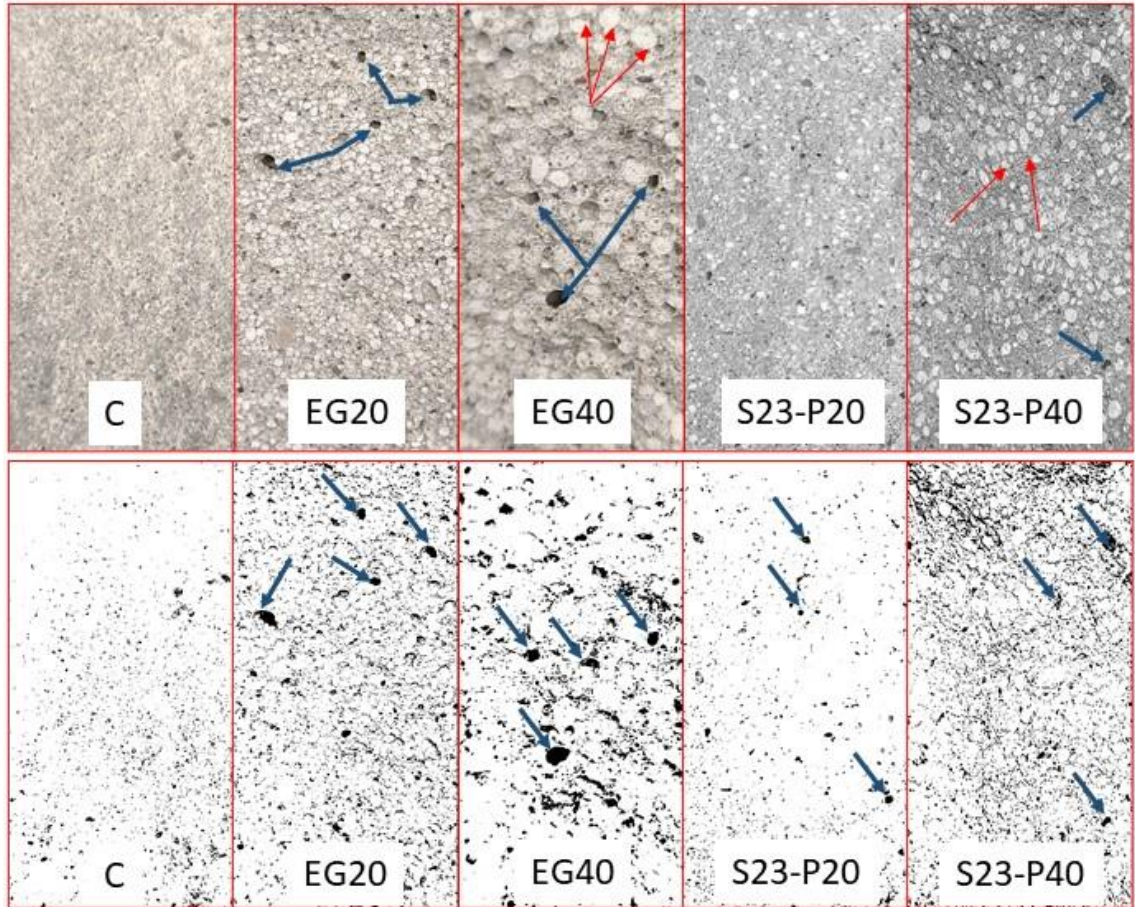


Figure 7-9: Optical and binary images of broken surfaces of specimens. Pores are shown with blue arrays, and EG and SSPCM particles are shown with red arrays.

7.3.5 Capillary water absorption

The capillary water absorption of triplicate mortar specimens after 56 days is depicted in **Fig. 7-10**. The partial replacement of sand with EG and SSPCM particles increased the initial and secondary capillary water absorptions. However, it can be observed that specimens incorporating pure EG particles demonstrated significantly higher water absorption and sorptivity coefficient compared to those incorporating SSPCMs. For instance, the initial sorptivity coefficient of the EG20 sample was 0.005, whereas it was 0.003 and 0.0037 for S23-P20 and S28-P20 specimens, respectively. This could be an indication of the PCMs filling the pore structure of EG particles and thus, reducing the water absorption.

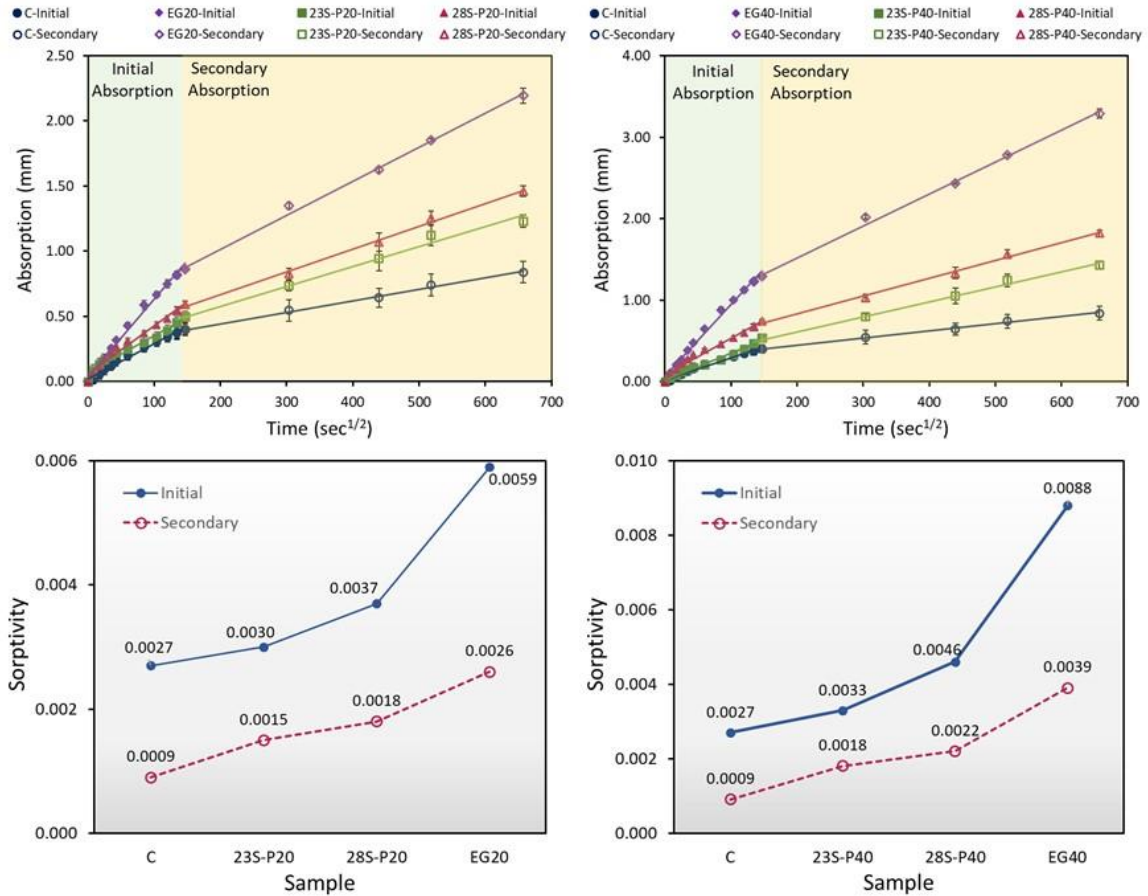


Figure 7-10: Capillary water absorption (top) and sorptivity coefficient (bottom) of mortars incorporating EG and SSPCM particles.

Another interesting observation is that mixtures incorporating S23 exhibited insignificantly higher water absorption and sorptivity coefficient compared to those with S23 inclusion. This might be due to the difference in the porosity induced by the S23 and S28 particles in the surrounding cementitious matrix, which conforms with the results obtained from the compressive strength test. As depicted in **Figs. 7-2** and **4**, S23 and S28 particles had different morphology that could further affect the precipitation of hydration products, microstructural development, and the bond strength between particles and the surrounding mortar at the ITZ. More in-depth investigations on the porosity of the mixtures are provided in the subsequent section.

7.3.6 Micro-computed tomography scan (μ CT scan)

The effect of EG and SSPCM addition on the porosity of the cement mortars listed in **Table 7-3** was quantified using image analysis of 3D μ CT scans. Several remarkable observations can emerge from the pore structure analysis. The segmentation of the scanned samples indicated that the partial replacement of sand with EG or SSPCM particles increased the porosity of the mortar specimens. Accordingly, the porosity of sample C, *i.e.*, with no EG or SSPCM content, was 4.71%, whereas it increased to 11.48% and 22.40% in the EG20 and EG40 samples, respectively. This demonstrates that the addition of pure EG particles led to a drastic increase in the porosity of the mortar samples. On the other hand, the porosity of the 23S-P20 and 23S-P40 samples was calculated as 8.07% and 15.68%, respectively. Therefore, it could be concluded that the addition of SSPCM particles resulted in an increase in the porosity of mortars to a smaller extent compared to EG aggregates. The porosity of S28-P20 and S28-P40 was also found to be 9% and 16.5%, respectively. **Figure 7-11** showcases the reconstructed 3D images and segmentation of the pore structure of the control specimen and the specimens incorporating EG and S23 particles. It is noteworthy that in the case of EG20 and EG40 mixtures, the porosity of the pure EG particles was also included in the porosity measurements. A noticeable finding is that the pore size in specimens with EG particles was relatively larger compared to those of the control specimen and the specimens with S23 particles, especially at 40 wt.% replacement.

The results obtained from the porosity analysis are in conformity with the compressive strength and capillary water absorption measurements explained earlier. For instance, in the case of samples incorporating pure EG aggregates, the compressive strength was significantly lower compared to that of mixtures made with SSPCM inclusions. This is highly correlated to the pore structure of EG20 and EG40 samples that indicated higher porosity than that of 23S-P20, 23SP40, 28S-P20, and 28S-P40 specimens. **Figure 7-12** illustrates the correlation between the compressive strength, sorptivity, and porosity of the mixtures studied herein. It could be observed that a linear inverse correlation between the compressive strength and porosity is evident. This implies that the partial replacement of sand with lightweight EG and SSPCM particles increased the porosity of the mixtures, which is probably related to the change in the packing density of the solid particles. It is

noteworthy that sorptivity also highly depends on the pore structure and pore connectivity of the matrix rather than only the total pore volume. Therefore, further studies are required to better correlate the sorptivity of SSPCM-integrated concrete to the pore structure properties. Furthermore, porous EG and SSPCM particles provide considerably lower stiffness in the matrix, which further decreased the compressive strength. Ultimately, the increased porosity and larger pore size of mixtures made with EG and SSPCM particles increased the capillary water absorption.

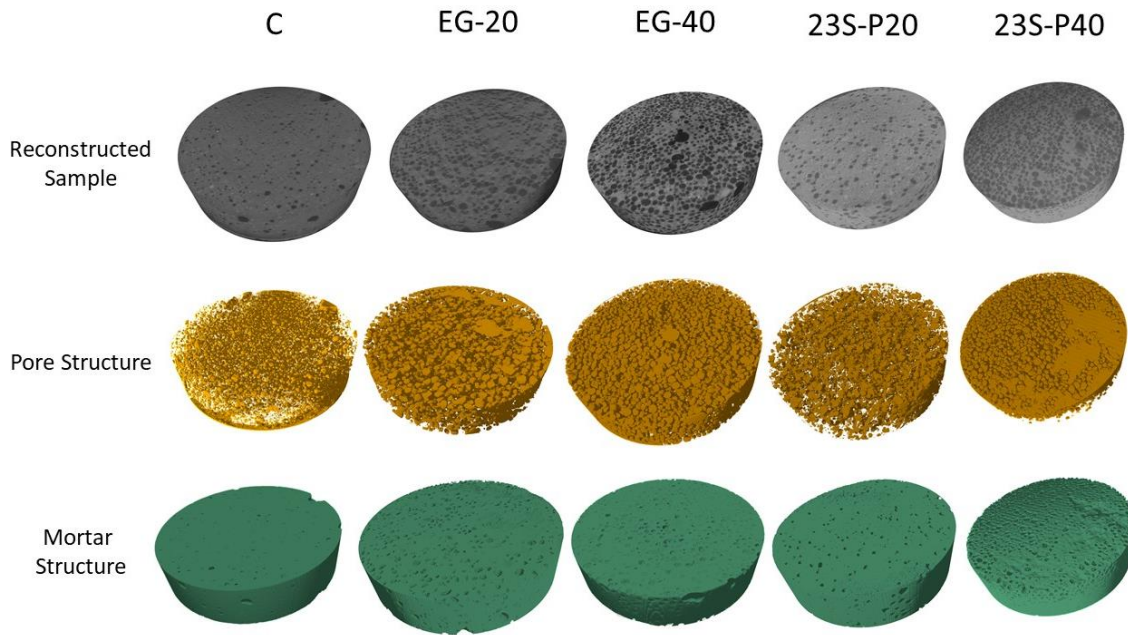


Figure 7-11: Reconstructed 3D scan and segmentation of the pore structure of mortar samples.

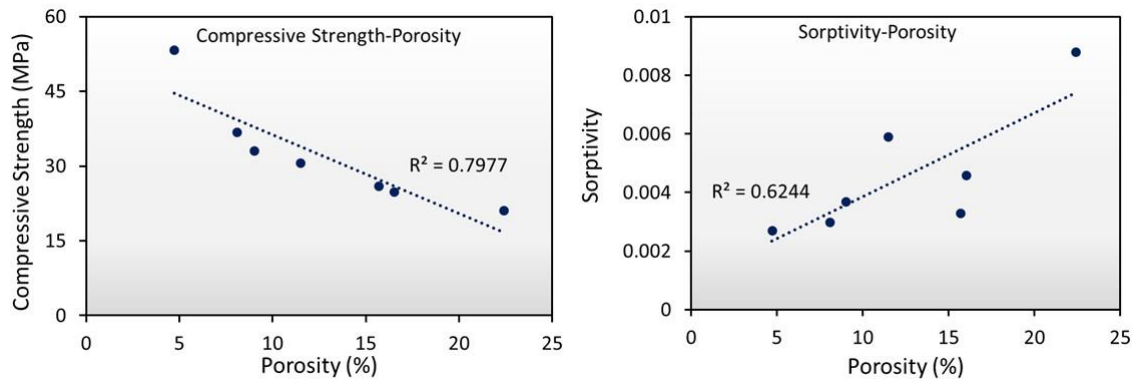


Figure 7-12: Correlation between porosity, sorptivity, and compressive strength.

7.3.7 Thermoregulating performance

The TES capacity and thermoregulating performance of SSPCM-incorporated mortars were investigated using two customized thermal tests as explained earlier. For this purpose, the temperature history of the inner surface of mortar specimens with dimensions of 30×15×5 cm placed on an insulation box was monitored, as schematically shown in **Fig. 7-3**. Two various temperature profiles were applied on the outer surface of the specimens using a walk-in environmental chamber. In the slow test, a temperature profile similar to the hourly ambient temperature of a summer day was simulated and applied to the outer surface of the samples. **Figures 7-13 (a) and (b)** compare the temperature history of the specimens incorporating S23 and S28 under the slow test scenario. Accordingly, the maximum temperature of the inner surface of the specimens incorporating SSPCMs was relatively lower compared to that of the control specimen. A similar trend was also evidenced in the rapid thermoregulating test as depicted in **Figs. 7-14 (a) and (b)**. In the case of the samples with S23 inclusion, the reduction of the inner-side temperature started earlier when the ambient temperature (*i.e.*, the applied temperature profile by the environmental chamber) was above 17°C. In contrast, the reduction in the inner-side temperature of specimens incorporating S28 occurred at a later time when the ambient temperature exceeded 25°C. This is in agreement with the latent heat capacity analysis performed by DSC tests in which the melting process of S23 and S28 particles started at 19°C and 28°C, respectively.

Furthermore, the maximum temperature of the specimen with SSPCM inclusion was considerably shifted off the peak temperature concerning the control sample, as shown in **Fig. 7-13**. For instance, the maximum inner-side temperature of the control sample was 37.5°C, which occurred at 12 h of the test onset. On the other hand, the maximum temperatures of S23-P20 and S23-P40 samples were 36.9°C and 36.3°C, which occurred approximately at time 14 h after the test onset. In the case of the S28-P20 and S28-P40 specimens, the maximum temperatures were 37.1°C and 36.4°C recorded at the time 13.5 h of the test onset.

Another noticeable change in the temperature history of the tested specimens is the delay in the reduction of the inner temperatures of specimens integrating SSPCMs during the

cooling period of the ambient temperature, as can be observed in **Figs. 7-13** and **7-14 (c)** and **(d)**. This is related to the high thermal inertia of the SSPCM-integrated samples, which is indicative of their resistance to temperature change. In other words, the heat transfer rate through the sample is much lower in SSPCM-integrated specimens, especially when the PCM undergoes a phase transition from solid to liquid or vice versa. Therefore, it can be concluded that SSPCM inclusion resulted in remarkably less severe temperature fluctuations in the tested specimens. The hourly difference between inner-side temperatures of the control sample and SSPCM-integrated samples is illustrated in **Figs. 13** and **14 (c)** and **(d)**. It was observed that a maximum reduction of up to 4°C can be achieved when 40 wt.% SSPCMs were incorporated, *i.e.*, 23S-P40 and 28SP40 specimens. It should be noted that the effect of the SSPCM on the thermo-regulating performance of the specimens highly depends on the applied ambient temperature along with the thermal properties of SSPCMs. According to findings in the literature and depending on the climatic conditions, 1°C increase/decrease in the thermostat setting temperature can contribute to approximately 5-15% energy savings on the cooling and heating of the spaces (Gencel, Ustaoglu, *et al.*, 2022; Moon & Han, 2011; Yousefi *et al.*, 2021). Overall, the incorporation of 20 and 40 wt.% of S23 reduced the indoor temperature fluctuations with respect to the control specimen by up to 16.9 and 25.6°C·hour, respectively, during 24 hours of simulation. In the case of S28, the temperature fluctuations were moderated by 14.2 and 23.93 °C·hour when 20 and 40 wt.% SSPCM was utilized, respectively. While further simulations on the energy-saving of cement-based building components incorporating S23 and S28 are needed to determine their energy efficiency more accurately, a 10 to 15% reduction in the energy consumption can be reasonably conceived.

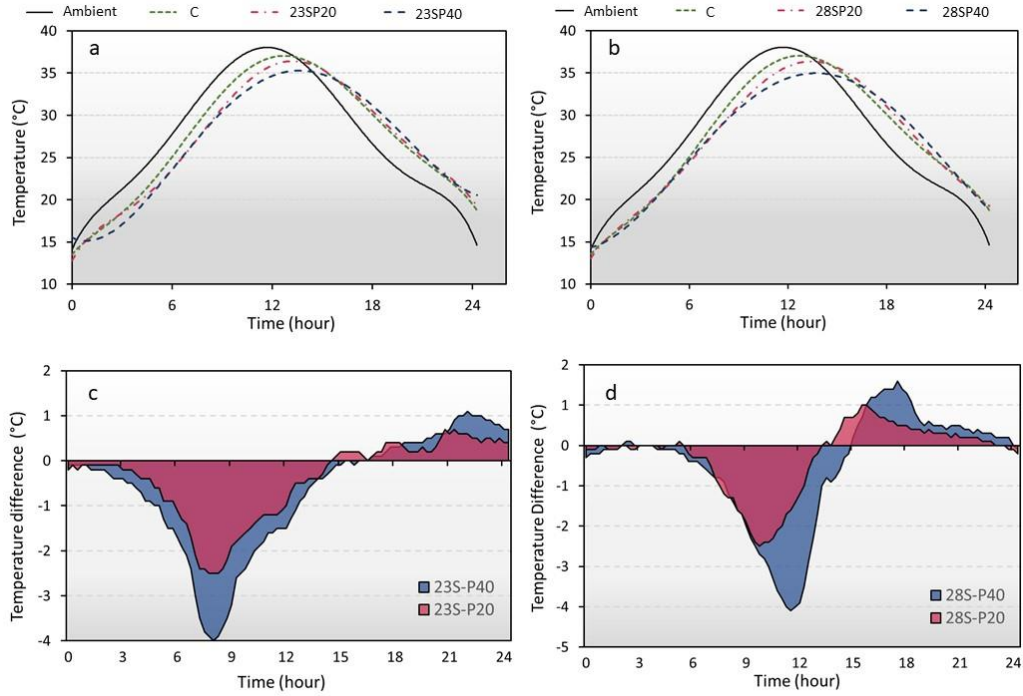


Figure 7-13: Temperature history of specimens under slow thermoregulating test.

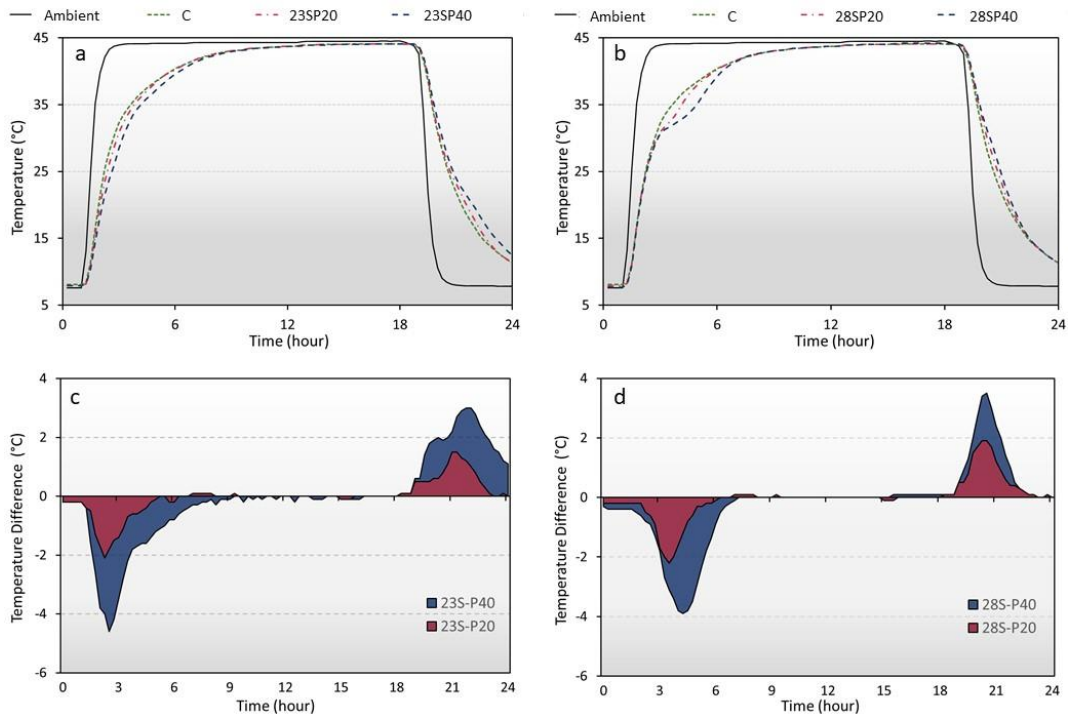


Figure 7-14: Temperature history of specimens under rapid thermoregulating test.

7.4 Concluding remarks

Two types of eco-friendly shape-stabilized phase change materials (SSPCMs) were developed in this study. Biobased PCMs were impregnated into the pore structure of recycled expanded glass granules and coated with silica fume particles using a 4-step vacuum impregnation method. The morphological and thermal properties of the fabricated SSPCMs along with their effect on the hydration, microstructural, mechanical, and thermal properties of cement-based composites were characterized through a set of multiphysics tests. The following conclusions can be drawn after an in-depth analysis of the results:

- Molten PCMs were efficiently encapsulated in porous EG particles. The leakage rate was minimum after coating the surface of PCM-impregnated aggregates with silica fume.
- S23 and S28 particles indicated a favorable melting/freezing behavior for application in thermal energy storage building components having a latent heat of fusion of 87.64 and 96.34 J/g, respectively.
- S23 and S28 particles imparted a insignificant effect on the hydration of cement paste, indicating better compatibility with the cementitious matrix compared to polymeric microencapsulated PCMs.
- Although the compressive strength decreased upon partial replacement of sand with SSPCM particles, a compressive strength of over 30 and 25 MPa could be achieved in samples made with 20 wt.% and 40 wt.% of SSPCM inclusion, respectively.
- μ CT scan and capillary water absorption experiments revealed that the porosity of mixtures increased upon SSPCM addition.
- SSPCMs provide a considerable TES capacity in cement mortars, which helps in moderating temperature fluctuations. Inner-side temperature fluctuations of mortar samples can be reduced by up to 4°C when 40 wt.% SSPCM is used. This can translate into substantial energy savings in buildings.

7.5 References

Baetens, R., Jelle, B. P., & Gustavsen, A. (2010). Phase change materials for building applications: A state-of-the-art review. *Energy and Buildings*, 42(9), 1361-1368.

Balapour, M., Mutua, A. W., & Farnam, Y. (2021). Evaluating the thermal efficiency of microencapsulated phase change materials for thermal energy storage in cementitious composites. *Cement and Concrete Composites*, 116, 103891.

De Gracia, A., & Cabeza, L. F. (2015). Phase change materials and thermal energy storage for buildings. *Energy and Buildings*, 103, 414-419.

Ding, Z., Yang, W., He, F., Jiang, Z., He, R., Fan, J., & Zhang, K. (2020). GO modified EPDM/paraffin shape-stabilized phase change materials with high elasticity and low leakage rate. *Polymer*, 204, 122824.

Djamai, Z. I., Larbi, A. S., Salvatore, F., & Cai, G. (2020). A new PCM-TRC composite: A mechanical and physicochemical investigation. *Cement and Concrete Research*, 135, 106119.

Djamai, Z. I., Salvatore, F., Larbi, A. S., Cai, G., & El Mankibi, M. (2019). Multiphysics analysis of effects of encapsulated phase change materials (PCMs) in cement mortars. *Cement and Concrete Research*, 119, 51-63.

Drissi, S., Ling, T.-C., Mo, K. H., & Eddhahak, A. (2019). A review of microencapsulated and composite phase change materials: Alteration of strength and thermal properties of cement-based materials. *Renewable and sustainable energy reviews*, 110, 467-484.

Farnam, Y., Esmaeeli, H. S., Zavattieri, P. D., Haddock, J., & Weiss, J. (2017). Incorporating phase change materials in concrete pavement to melt snow and ice. *Cement and Concrete Composites*, 84, 134-145.

Gencel, O., Ustaoglu, A., Benli, A., Hekimoğlu, G., Sarı, A., Erdogmus, E., Sutcu, M., Kaplan, G., & Bayraktar, O. Y. (2022). Investigation of physico-mechanical, thermal properties and solar thermoregulation performance of shape-stable attapulgite based composite phase change material in foam concrete. *Solar Energy*, 236, 51-62.

Gencel, O., Yaras, A., Hekimoğlu, G., Ustaoglu, A., Erdogmus, E., Sutcu, M., & Sarı, A. (2022). Cement based-thermal energy storage mortar including blast furnace slag/capric

acid shape-stabilized phase change material: Physical, mechanical, thermal properties and solar thermoregulation performance. *Energy and Buildings*, 111849.

Gonçalves, J., Tavares, L., Toledo Filho, R., Fairbairn, E., & Cunha, E. (2007). Comparison of natural and manufactured fine aggregates in cement mortars. *Cement and Concrete Research*, 37(6), 924-932.

Gu, X., Liu, P., Peng, L., Zhang, Z., Bian, L., & Wang, B. (2021). Low cost, eco-friendly, modified fly ash-based shape-stabilized phase change material with enhanced thermal storage capacity and heat transfer efficiency for thermal energy storage. *Solar Energy Materials and Solar Cells*, 232, 111343.

Hassan, F., Jamil, F., Hussain, A., Ali, H. M., Janjua, M. M., Khushnood, S., Farhan, M., Altaf, K., Said, Z., & Li, C. (2022). Recent advancements in latent heat phase change materials and their applications for thermal energy storage and buildings: A state of the art review. *Sustainable Energy Technologies and Assessments*, 49, 101646.

Hattan, H. A., Madhkhan, M., & Marani, A. (2021). Thermal and mechanical properties of building external walls plastered with cement mortar incorporating shape-stabilized phase change materials (SSPCMs). *Construction and Building Materials*, 270, 121385.

He, Y., Zhang, X., Zhang, Y., Song, Q., & Liao, X. (2016). Utilization of lauric acid-myristic acid/expanded graphite phase change materials to improve thermal properties of cement mortar. *Energy and Buildings*, 133, 547-558.

Hekimoğlu, G., Nas, M., Ouikhalfan, M., Sarı, A., Kurbetci, Ş., Tyagi, V., Sharma, R., & Saleh, T. A. (2021). Thermal management performance and mechanical properties of a novel cementitious composite containing fly ash/lauric acid-myristic acid as form-stable phase change material. *Construction and Building Materials*, 274, 122105.

Hekimoğlu, G., Nas, M., Ouikhalfan, M., Sarı, A., Tyagi, V., Sharma, R., Kurbetci, Ş., & Saleh, T. A. (2021). Silica fume/capric acid-stearic acid PCM included-cementitious composite for thermal controlling of buildings: Thermal energy storage and mechanical properties. *Energy*, 219, 119588.

Hekimoglu, G., & Sarı, A. (2021). Fly ash/octadecane shape-stabilized composite PCMs doped with carbon-based Nanoadditives for thermal regulation applications. *Energy & Fuels*, 35(2), 1786-1795.

Jayalath, A., San Nicolas, R., Sofi, M., Shanks, R., Ngo, T., Aye, L., & Mendis, P. (2016). Properties of cementitious mortar and concrete containing micro-encapsulated phase change materials. *Construction and Building Materials*, 120, 408-417.

Kang, Y., Jeong, S.-G., Wi, S., & Kim, S. (2015). Energy efficient Bio-based PCM with silica fume composites to apply in concrete for energy saving in buildings. *Solar Energy Materials and Solar Cells*, 143, 430-434.

Li, M. (2021). Mechanical and thermal performance assessment of paraffin/expanded vermiculite-diatomite composite phase change materials integrated mortar: Experimental and numerical approach. *Solar Energy*, 227, 343-353.

Li, X., Sanjayan, J. G., & Wilson, J. L. (2014). Fabrication and stability of form-stable diatomite/paraffin phase change material composites. *Energy and Buildings*, 76, 284-294.

Liu, L., Lu, G., Qiu, G., Yue, C., Guo, M., Ji, R., & Zhang, M. (2019). Characterization of novel shape-stabilized phase change material mortar: Portland cement containing $\text{Na}_2\text{SO}_4 \cdot 10\text{H}_2\text{O}$ and fly ash for energy-efficient building. *International Journal of Energy Research*, 43(11), 5812-5823.

Liu, L., Peng, B., Yue, C., Guo, M., & Zhang, M. (2019). Low-cost, shape-stabilized fly ash composite phase change material synthesized by using a facile process for building energy efficiency. *Materials Chemistry and Physics*, 222, 87-95.

Ma, B., Adhikari, S., Chang, Y., Ren, J., Liu, J., & You, Z. (2013). Preparation of composite shape-stabilized phase change materials for highway pavements. *Construction and Building Materials*, 42, 114-121.

Marani, A., & Madhkhan, M. (2018). An innovative apparatus for simulating daily temperature for investigating thermal performance of wallboards incorporating PCMs. *Energy and Buildings*, 167, 1-7.

Marani, A., & Madhkhan, M. (2021). Thermal performance of concrete sandwich panels incorporating phase change materials: An experimental study. *Journal of Materials Research and Technology*, 12, 760-775.

Marani, A., & Nehdi, M. L. (2019). Integrating phase change materials in construction materials: Critical review. *Construction and Building Materials*, 217, 36-49.

Memon, S. A., Cui, H., Lo, T. Y., & Li, Q. (2015). Development of structural–functional integrated concrete with macro-encapsulated PCM for thermal energy storage. *Applied Energy*, 150, 245-257.

Moon, J. W., & Han, S.-H. (2011). Thermostat strategies impact on energy consumption in residential buildings. *Energy and Buildings*, 43(2-3), 338-346.

Palacios, A., Barreneche, C., Navarro, M., & Ding, Y. (2020). Thermal energy storage technologies for concentrated solar power—A review from a materials perspective. *Renewable Energy*, 156, 1244-1265.

Pan, W., Li, K., & Teng, Y. (2018). Rethinking system boundaries of the life cycle carbon emissions of buildings. *Renewable and sustainable energy reviews*, 90, 379-390.

Pilehvar, S., Cao, V. D., Szczotok, A. M., Valentini, L., Salvioni, D., Magistri, M., Pamies, R., & Kjøniksen, A.-L. (2017). Mechanical properties and microscale changes of geopolymer concrete and Portland cement concrete containing micro-encapsulated phase change materials. *Cement and Concrete Research*, 100, 341-349.

Pomianowski, M., Heiselberg, P., Jensen, R. L., Cheng, R., & Zhang, Y. (2014). A new experimental method to determine specific heat capacity of inhomogeneous concrete material with incorporated microencapsulated-PCM. *Cement and Concrete Research*, 55, 22-34.

Qiu, F., Song, S., Li, D., Liu, Y., Wang, Y., & Dong, L. (2020). Experimental investigation on improvement of latent heat and thermal conductivity of shape-stable phase-change materials using modified fly ash. *Journal of Cleaner Production*, 246, 118952.

Qu, Y., Wang, S., Tian, Y., & Zhou, D. (2019). Comprehensive evaluation of Paraffin-HDPE shape stabilized PCM with hybrid carbon nano-additives. *Applied Thermal Engineering*, 163, 114404.

Qu, Y., Zhou, D., Xue, F., & Cui, L. (2021). Multi-factor analysis on thermal comfort and energy saving potential for PCM-integrated buildings in summer. *Energy and Buildings*, 241, 110966.

Ren, Y., Xu, C., Yuan, M., Ye, F., Ju, X., & Du, X. (2018). Ca (NO₃)₂-NaNO₃/expanded graphite composite as a novel shape-stable phase change material for mid-to high-temperature thermal energy storage. *Energy conversion and management*, 163, 50-58.

Sanfeliix, S. G., Zea-García, J. D., Londono-Zuluaga, D., Santacruz, I., Angeles, G., & Kjøniksen, A.-L. (2020). Hydration development and thermal performance of calcium sulphoaluminate cements containing microencapsulated phase change materials. *Cement and Concrete Research*, 132, 106039.

Sari, A., Hekimoğlu, G., Tyagi, V., & Sharma, R. (2020). Evaluation of pumice for development of low-cost and energy-efficient composite phase change materials and lab-scale thermoregulation performances of its cementitious plasters. *Energy*, 207, 118242.

Shi, X., Memon, S. A., Tang, W., Cui, H., & Xing, F. (2014). Experimental assessment of position of macro encapsulated phase change material in concrete walls on indoor temperatures and humidity levels. *Energy and Buildings*, 71, 80-87.

Wang, T., Wang, K., Ye, F., Ren, Y., & Xu, C. (2021). Characterization and thermal properties of a shape-stable Na₂CO₃-K₂CO₃/coal fly ash/expanded graphite composite phase change materials for high-temperature thermal energy storage. *Journal of Energy Storage*, 33, 102123.

Wi, S., Yang, S., Park, J. H., Chang, S. J., & Kim, S. (2020). Climatic cycling assessment of red clay/perlite and vermiculite composite PCM for improving thermal inertia in buildings. *Building and Environment*, 167, 106464.

Yousefi, A., Tang, W., Khavarian, M., & Fang, C. (2021). Development of novel form-stable phase change material (PCM) composite using recycled expanded glass for thermal energy storage in cementitious composite. *Renewable Energy*, 175, 14-28.

Zhang, D., Li, Z., Zhou, J., & Wu, K. (2004). Development of thermal energy storage concrete. *Cement and Concrete Research*, 34(6), 927-934.

Zhang, S., Feng, D., Shi, L., Wang, L., Jin, Y., Tian, L., Li, Z., Wang, G., Zhao, L., & Yan, Y. (2021). A review of phase change heat transfer in shape-stabilized phase change materials (ss-PCMs) based on porous supports for thermal energy storage. *Renewable and sustainable energy reviews*, 135, 110127.

Zhang, Y., Sang, G., Du, X., Cui, X., Zhang, L., Zhu, Y., & Guo, T. (2021). Development of a novel alkali-activated slag-based composite containing paraffin/ceramsite shape stabilized phase change material for thermal energy storage. *Construction and Building Materials*, 304, 124594.

Chapter 8

8 Hydration Kinetics, Mechanical, Microstructural, and Thermal Characterization of Low-carbon Limestone Calcined Clay Cement (LC³) Mortars Incorporating MPCMs¹

Low-carbon ternary limestone calcined clay cement (LC³) binder system can be developed by substituting up to 50% of ordinary portland cement with metakaolin and limestone. This chapter investigates the hydration kinetics, microstructural and strength development, and thermos-regulating performance of LC³ mortars incorporating microencapsulated phase change materials (MPCMs). Isothermal calorimetry measurements indicated that the inclusion of MPCMs prolonged the dormant period and reduced the intensity of hydration peaks. Furthermore, compressive strength decreased upon the addition of MPCMs. Nevertheless, high compressive strength could be achieved when a low water-to-binder (w/b) ratio was used. Image analysis of micro-computed tomography (μ -CT) scans revealed that the porosity of the mortar increased after the integration of MPCMs. Ultimately, It was evidenced that latent heat thermal energy storage (LHTES) LC³ mortars can regulate the indoor temperature fluctuations and thus, reduce the operational energy consumption of buildings.

8.1 Introduction

The built environment, which contains buildings and major civil infrastructures, is a fundamental element of the circular economy and social development due to the consumption of copious materials and energy (Huang *et al.*, 2018). Pertinent research indicated that buildings are responsible for approximately 40% of the global energy consumption along with over one-third of carbon emissions (Sbci, 2009). From a life cycle analysis (LCA) point of view, the energy consumption of the built environment is attributed to two main compartments: i) embodied energy which is used for the construction,

¹ A version of this chapter is in preparation to be submitted to “*Cement and Concrete Research*” Journal.

renovation and rehabilitation, maintenance, and demolition of the built environment; ii) operational energy which is used for operating purposes such as heating, cooling, air conditioning, and ventilation (HVAC), hot water, electricity, etc. (Cabeza *et al.*, 2014). It has been demonstrated that nearly 80% of the total life cycle energy consumption in an occupied building is related to operational energy (Sartori & Hestnes, 2007). This is contrary to the non-occupiable parts of the built environment, including roads, bridges, and other infrastructures, in which 90% of the life cycle energy consumption is attributed to the embodied energy (Huang *et al.*, 2015; Huang *et al.*, 2018; Stephan & Stephan, 2016).

These analyses emphasize the crucial role of the operational and embodied energy consumptions of the built environment in developing practical strategies to mitigate the environmental footprint of the construction sector and tackle climate change. Extensive research has been devoted to exploring viable solutions for reducing the energy consumption of buildings along with lessening the carbon emissions of the built environment (Pomponi & Moncaster, 2016). Accordingly, different research perspectives could be explored including the enhancement of the energy efficiency in consuming sectors, *i.e.*, reducing operational energy (da Cunha & de Aguiar, 2020), and the utilization of alternative low-carbon construction materials, *i.e.*, reducing embodied emissions (Miller *et al.*, 2018; Schneider, 2019).

Latent heat thermal energy storage (LHTES) systems have emerged as a promising approach for increasing the energy efficiency of buildings (Tatsidjodoung *et al.*, 2013; Zhou *et al.*, 2012). Phase change materials (PCMs) are substances that can absorb/release a great deal of thermal energy upon physical phase transition, *e.g.*, solid to liquid, while their temperature remains relatively constant (Tyagi & Buddhi, 2007). PCMs with melting points near room temperature have been widely employed as the latent heat component in various LHTES systems in buildings. For instance, integrating PCMs in HVAC systems could increase energy efficiency and enhance cost and energy savings (Promopattum *et al.*, 2017). PCMs can also be integrated into building components such as roofs, walls, envelopes, etc. Several research studies evidenced that PCM inclusion in such elements alleviates the indoor temperature fluctuations, which in turn reduces the energy

consumption for the heating and cooling of the indoor spaces (Marani & Madhkhan, 2018; Thiele, Jamet, *et al.*, 2015; Thiele, Sant, *et al.*, 2015).

Different techniques can be used to incorporate PCMs into building materials, such as cement-based composites (Marani & Nehdi, 2019). Microencapsulated PCMs (MPCMs) are the most prevalent method in the open literature to incorporate PCMs into cement mortars and concretes (Drissi *et al.*, 2019; Zhao & Zhang, 2011). Accordingly, MPCMs significantly improve the thermal performance of cement-based composites by providing latent heat capacity.

In parallel to the efforts for reducing the energy consumption and carbon footprint of buildings by using PCM-integrated construction materials, paramount research has also been dedicated to developing alternative low-carbon and low-embodied energy building materials in recent years (Cabeza *et al.*, 2013; Coffetti *et al.*, 2022). Concrete is the world's most widely used human-made material and ordinary portland cement (OPC) is the major binder of the manufactured concrete worldwide. However, the high production of the OPC has been identified as an aggravating environmental challenge since it contributed to nearly 7-12% of the total CO_2 emissions in 2020 (Zheng *et al.*, 2021; Zhong *et al.*, 2021). To address this problem, researchers have suggested the employment of alternative low-carbon binder systems such as alkali-activated materials (AAMs) (Provis, 2018), reactive MgO cement (Walling & Provis, 2016), ternary and quaternary cementitious systems (Nehdi, 2001), etc. Blended cements incorporate supplementary cementitious materials (SCMs) as partial replacement for OPC so that the carbon footprint related to clinker production is reduced.

Limestone calcined clay cement (LC^3) is a type of ternary cement system in which nearly 50% of the conventional OPC is replaced with limestone and kaolinitic calcined clays (Zunino & Scrivener, 2022). According to pertinent research studies in the literature, LC^3 systems gain similar strength after 7 days and exhibit higher durability against chloride ions penetration and alkali-silica reaction compared to conventional OPC (Avet & Scrivener, 2018; Nguyen *et al.*, 2020; Zunino & Scrivener, 2021). Meanwhile, using LC^3

can reduce over 30% of the CO_2 emissions per ton of the cement manufactured (Scrivener *et al.*, 2018).

Diverse research in the literature examined the effects of MPCMs on the thermal, mechanical, and microstructural properties of OPC concrete. Yet, the effects of MPCMs on the hydration kinetics and microstructural development of emerging alternative binder systems remain widely unexplored. The current study intends to carry out a novel multi-physics analysis to explore the effects of MPCM addition on the hydration, strength development, microstructure, and thermos-regulating properties of ternary LC³ systems. Purposefully, this chapter proposes the following novelties: i) study of the hydration kinetics and strength development of LC³ systems in presence of two types of MPCMs with different melting temperatures; ii) assessment of the microstructural development of LC³ mortars after MPCM addition, and iii) analysis of the thermo-regulating performance of LC³ systems with and without PCMs. Multiple laboratory experiments are employed to characterize the fabricated mortar specimens as described below.

8.2 Materials and methods

8.2.1 Materials

ASTM C150 Type I OPC, metakaolin, and limestone were used to prepare the ternary LC³ binder system. **Table 8-1** presents the chemical composition of the OPC and metakaolin. Two types of non-formaldehyde bio-based MPCMs having melting temperatures of 28 and 35°C, referred to as En28 and En35, respectively, supplied by Encapsys LLC were used. Natural river sand and a polycarboxylate-based superplasticizer (SP) were also used for making mortar specimens. The thermos-physical properties of En28 and En35 are given in Chapter 5 (see **Table 5-2** and **Figure 5-1**).

Table 8-1: Chemical composition of OPC and metakaolin

OPC			
Components	Proportion (%)	Components	Proportion (%)
Silicon oxide (SiO ₂)	19.6	Free Calcium	1
Aluminum oxide (Al ₂ O ₃)	4.8	Other oxides	-
Ferric oxide (Fe ₂ O ₃)	3.3	Tricalcium silicate (C ₃ S)	55
Calcium oxide (CaO)	61.5	Dicalcium silicate (C ₂ S)	15
Magnesium oxide (MgO)	3	Tricalcium aluminate (C ₃ A)	7
Sulfur trioxide (SO ₃)	3.5	Tetracalcium aluminoferrite (C ₄ AF)	10
Metakaolin			
Components	Proportion (%)	Components	Proportion (%)
Silicon oxide (SiO ₂)	53.5	Free Calcium	-
Aluminum oxide (Al ₂ O ₃)	42.5	Other oxides	-
Ferric oxide (Fe ₂ O ₃)	1.90	Tricalcium silicate (C ₃ S)	-
Calcium oxide (CaO)	0.2	Dicalcium silicate (C ₂ S)	-
Magnesium oxide (MgO)	-	Tricalcium aluminate (C ₃ A)	-
Sulfur trioxide (SO ₃)	0.05	Tetracalcium aluminoferrite (C ₄ AF)	-

8.2.2 Experimental plan

In this chapter, the effects of MPCM addition on the hydration kinetics of LC³ pastes was studied using the isothermal calorimetry (IC) test. The strength development of LC³ mortars incorporating MPCMs was evaluated by compressive strength measurements. The microstructure and porosity of the mortars were further analyzed using scanning electron microscopy coupled with energy-dispersive X-ray spectroscopy (SEM-EDX) and 3D X-ray micro-computed tomography (μ -CT) scans. Ultimately, thermos-regulating tests were performed to evaluate the LTHES capacity of the MPCM-integrated LC³ mortars as explained below.

8.2.2.1 Isothermal calorimetry (IC)

IC tests were employed to study the hydration kinetics of LC³ pastes incorporating En28 and En35. Water-to-binder (w/b) ratios of 0.5 and 0.4 were selected and MPCMs were added at the dosages of 0, 5, 10, and 20% by cement weight. **Table 8-2** summarizes the mixtures prepared for the IC test. The heat of hydration of cement pastes was measured in an eight-channel micro-calorimeter (TAM air, TA Instruments) at three different temperatures including 20, 30, and 40 \pm 0.02 °C. Collectively, 42 isothermal calorimetry tests (14 mixtures at 3 testing temperatures) were conducted to obtain the rate of hydration data. The rate of hydration was recorded every 60 s and normalized per gram of LC³ binder

(mW/g). The calorimetry measurements were performed using an ex-situ mixing procedure of approximately 5 grams of cement paste for 96 h. It is noteworthy that opening the cover and putting the ampoule into the channel can cause a drastic increase in the heat flow for the initial few minutes of the experiments. Thus, the measurements were considered from 0.75 h after the placement of the sample to minimize this error.

Table 8-2: Mixture components of LC³ pastes used for IC tests

Designation	LC ³ (g)	Water (g)	En28 (g)	Designation	LC ³ (g)	Water (g)	En35 (g)
WB04	3	1.2	0	WB04	3	1.2	0
WB04P05En28	3	1.2	0.15	WB04P05En35	3	1.2	0.15
WB04P10En28	3	1.2	0.3	WB04P10En35	3	1.2	0.3
WB04P20En28	3	1.2	0.6	WB04P20En35	3	1.2	0.6
WB05	3	1.5	0	WB05	3	1.5	0
WB05P05En28	3	1.5	0.15	WB05P05En35	3	1.5	0.15
WB05P10En28	3	1.5	0.3	WB05P10En35	3	1.5	0.3
WB05P20En28	3	1.5	0.6	WB05P20En35	3	1.5	0.6

8.2.2.2 Compressive strength

Ten different mixture designs of LC³ mortars were considered for the compressive strength measurements, including two control mixtures without MPCM having w/b ratios of 0.4 and 0.5, four mixtures having w/b ratios of 0.4 and 0.5 and incorporating En28 at the dosages of 10 and 20 wt.% of the binder, and four mixtures with w/b ratios of 0.4 and 0.5 incorporating En35 at the dosages of 10 and 20 wt.% of the binder. MPCMs were added as partial replacement for sand particles. **Table 8-3** summarizes the mixture design of the fabricated mortars. 50-mm mortar cubes were used to cast specimens for compressive strength tests. Specimens were demolded after 24 h and then cured in a moist room at 20 ± 1°C. The compressive strength of triplicate samples was measured at 1, 3, 7, 14, 28, and 56 days of curing.

Table 8-3: Mixture proportions of LC³ mortars used for compressive strength tests

Mixture	Cement (kg/m ³)	Metakaolin (kg/m ³)	Limestone (kg/m ³)	Water (kg/m ³)	Sand (kg/m ³)	MPCM (kg/m ³)	SP (kg/m ³)
WB04	275	150	75	200	1500	0	20
WB05	275	150	75	250	1500	0	15
WB04P10En28	275	150	75	200	1350	50	20
WB04P20En28	275	150	75	200	1200	100	20
WB05P10En28	275	150	75	250	1350	50	15
WB05P20En28	275	150	75	250	1200	100	15
WB04P10En35	275	150	75	200	1350	50	20
WB04P20En35	275	150	75	200	1200	100	20
WB05P10En35	275	150	75	250	1350	50	15
WB05P20En35	275	150	75	250	1200	100	15

8.2.2.3 Microstructural analysis

The microstructure and morphology of the failure surface of the LC³ mortars cured for 28 days were investigated using scanning electron microscopy coupled with energy dispersive X-ray (SEM-EDX). SEM imaging was performed by a Hitachi SU8230 Regulus Ultra High-Resolution Field Emission SEM and Bruker X-Flash EDX detector at an accelerating voltage of 15 kV. Mortar samples with 0 and 20 wt.% MPCM inclusion at w/b ratios of 0.5 and 0.4 were selected for the microstructural analysis.

8.2.2.4 Micro-computed tomography (μ -CT) scan

The distribution of the MPCM particles in the LC³ mortar along with their effect on the pore structure of the matrix were examined using X-ray micro-computed tomography. A Nikon XT-H-225-ST μ CT scanner was employed to scan the 56-day cured mortar specimens listed in **Table 8-3**. High-resolution 2D images of the X-ray projections were used to reconstruct the exterior and interior structure of the scanned samples. The resolution of the 3D images was set to 60 μ m voxels. The scanning was carried out with a voltage of 225 kV, a current of 120 μ A, and a power of 27 Watts. The image segmentation, analysis, and visualizations were performed using the Dragonfly 2021.1 software, Object Research Systems (ORS) Inc., Montreal Canada (more information available at: <http://www.theobjects.com/dragonfly>).

8.2.2.5 Thermo-regulating performance

The effect of En28 and En35 inclusion on the LHTES performance of LC³ mortars was studied using a thermo-regulating test carried out in a walk-in environmental chamber, similar to the test procedure proposed in the literature (Hekimoğlu *et al.*, 2021; Liu *et al.*, 2019; Marani & Madhkhan, 2018, 2021). Mortars with w/b ratio of 0.4 were selected for the thermal performance tests. For this purpose, specimens with dimensions of 30×15×5 cm were placed and sealed on the top of the extruded polystyrene (XPS) insulation boxes with wall thickness and thermal conductivity of 6 cm and 0.05 W/mK, respectively, as shown in **Fig. 8-1**. A real-time wireless temperature monitoring system provided by Exact Technologies Corporation, Toronto, Canada, was utilized to record the temperature history of the inner-side surface of the specimens. For this purpose, a temperature profile similar to the hourly ambient temperature of a hot summer day was applied to the outer side surface of the sample for 24 h. The temperature history of all specimens was recorded and analyzed to apprehend the effect of MPCM addition on the thermal performance of LC³ mortar specimens.

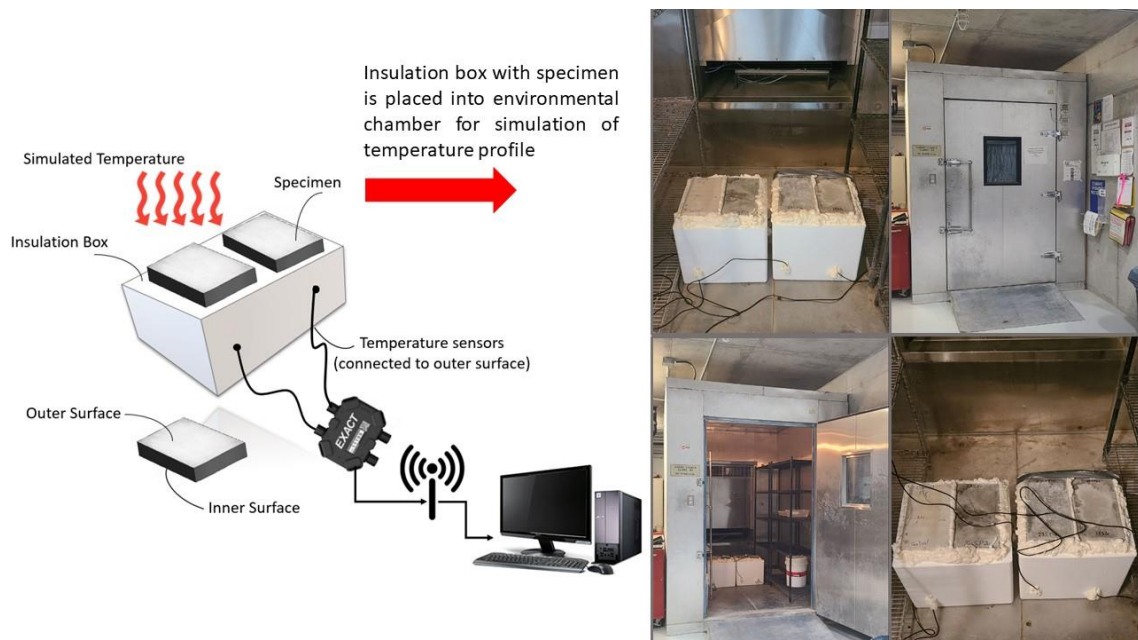


Figure 8-1: Thermo-regulating test setup for evaluation of the TES capacity of mortar specimens.

8.3 Results and discussion

8.3.1 Analysis of hydration kinetics using IC test

Calorimetry curves of LC³ systems incorporating En28 and En35 are illustrated in **Figs. 8-2** and **8-3**, respectively. Two distinct hydration peaks are evident at earlier hydration times of LC³ systems without MPCM addition. The first gentle peak is mostly related to the hydration of the silicate phases in the OPC. The second and sharper peak is mostly related to the alumina available in the metakaolin (Shah *et al.*, 2020; Sharma *et al.*, 2021; Vance *et al.*, 2013). Furthermore, a third but low-intensity peak associated with the formation of carbo-aluminates can also be observed (Parashar & Bishnoi, 2021). The addition of MPCMs exerted significant changes in the hydration patterns of the LC³ systems. It could be observed that the MPCM inclusion resulted in a longer induction period, especially at higher dosages. For instance, the acceleration period of the pure LC³ system with the w/b ratio of 0.5 measured at 20°C began approximately 3 hours after starting the test. In contrast, in the case of samples with 10 and 20 wt.% of En28 inclusion (*i.e.*, WB05P10En28 and WB05P20En28), the start of the acceleration period occurred 6.5 hours and 11 hours after the start of the test, respectively. Additionally, the intensity of the hydration peaks decreased significantly in the presence of the MPCM particles. The maximum rate of hydration along with the time to reach the maximum hydration rate are given in **Table 8-4**. It could be understood that the addition of MPCMs generally caused a delay in the hydration peaks and diminished the maximum rate of hydration. Such effects were previously observed in OPC and alkali-activated systems (Jayalath *et al.*, 2016; Pilehvar *et al.*, 2017; Pilehvar *et al.*, 2020).

The longer dormant period of MPCM-integrated systems and lower-intensity peaks could be related to several mechanisms. Firstly, the addition of hydrophilic polymer MPCMs with high water absorption affects the dilution of the system along with the degree of the reaction of the OPC (Fernandes *et al.*, 2014). This also reduces the amount of accessible water for the hydration process. Furthermore, MPCM particles indicate a tendency to wrap around cement grains and prevent their contact with water. This decreases the nucleation sites for the precipitation and growth of the hydration products (Djamai *et al.*, 2019). It is noteworthy that the results obtained from IC tests at higher temperatures suggest the

accelerated hydration of silicate and aluminate phases, especially at lower dosages of MPCMs, as indicated in **Figs. 8-2** and **8-3** and **Tables 8-4** and **8-5**. For instance, the maximum hydration rate of mixtures with a w/b ratio of 0.4 containing En35 at 0 and 20 wt.% tested at 40°C was increased by 69% and 77% compared to the testing temperature of 20 °C.

Table 8-4: Hydration parameters of LC³ pastes incorporating En28

<i>w/b = 0.4</i>								
Temp. (°C)	<i>R_{max}</i>				<i>T_{Rmax}</i>			
	P0	P05	P10	P20	P0	P05	P10	P20
20	4.86	4.40	3.35	1.43	13.59	15.45	19.05	33.12
30	8.42	7.10	5.69	3.31	7.35	9.04	10.90	17.48
40	13.11	10.22	8.65	4.73	4.49	5.27	5.85	10.66
<i>w/b = 0.5</i>								
Temp. (°C)	<i>R_{max}</i>				<i>T_{Rmax}</i>			
	P0	P05	P10	P20	P0	P05	P10	P20
20	5.81	4.76	4.10	1.73	14.42	16.7	20.07	31.33
30	8.42	6.83	6.22	3.49	7.34	10.23	11.32	17.43
40	10.23	9.83	7.68	5.17	5.65	5.85	7.21	9.61

Table 8-5: Hydration parameters of LC³ pastes incorporating En35

<i>w/b = 0.4</i>								
Temp. (°C)	<i>R_{max}</i>				<i>T_{Rmax}</i>			
	P0	P05	P10	P20	P0	P05	P10	P20
20	4.86	4.06	3.14	1.58	13.59	16.65	22.18	32.68
30	8.42	5.73	5.15	2.39	7.35	10.40	11.90	20.56
40	13.11	9.66	6.67	4.39	4.49	5.50	6.88	10.40
<i>w/b = 0.5</i>								
Temp. (°C)	<i>R_{max}</i>				<i>T_{Rmax}</i>			
	P0	P05	P10	P20	P0	P05	P10	P20
20	4.08	4.26	3.45	1.60	14.42	16.98	20.84	30.45
30	8.03	6.14	5.01	2.59	9.22	10.82	11.34	20.69
40	10.23	8.28	6.75	4.48	5.65	6.25	7.44	10.29

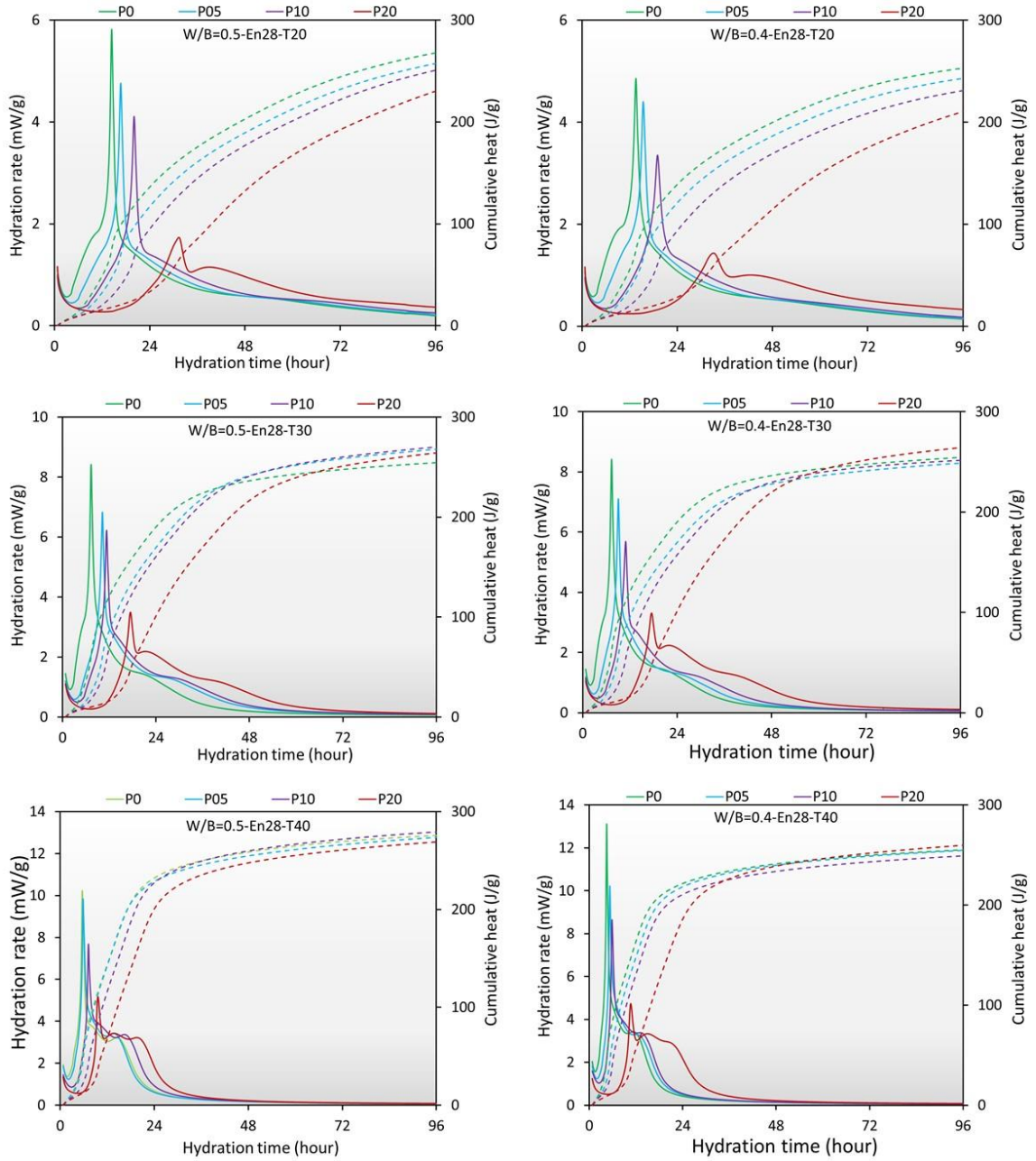


Figure 8-2: Isothermal hydration curves of LC³ pastes incorporating En28.

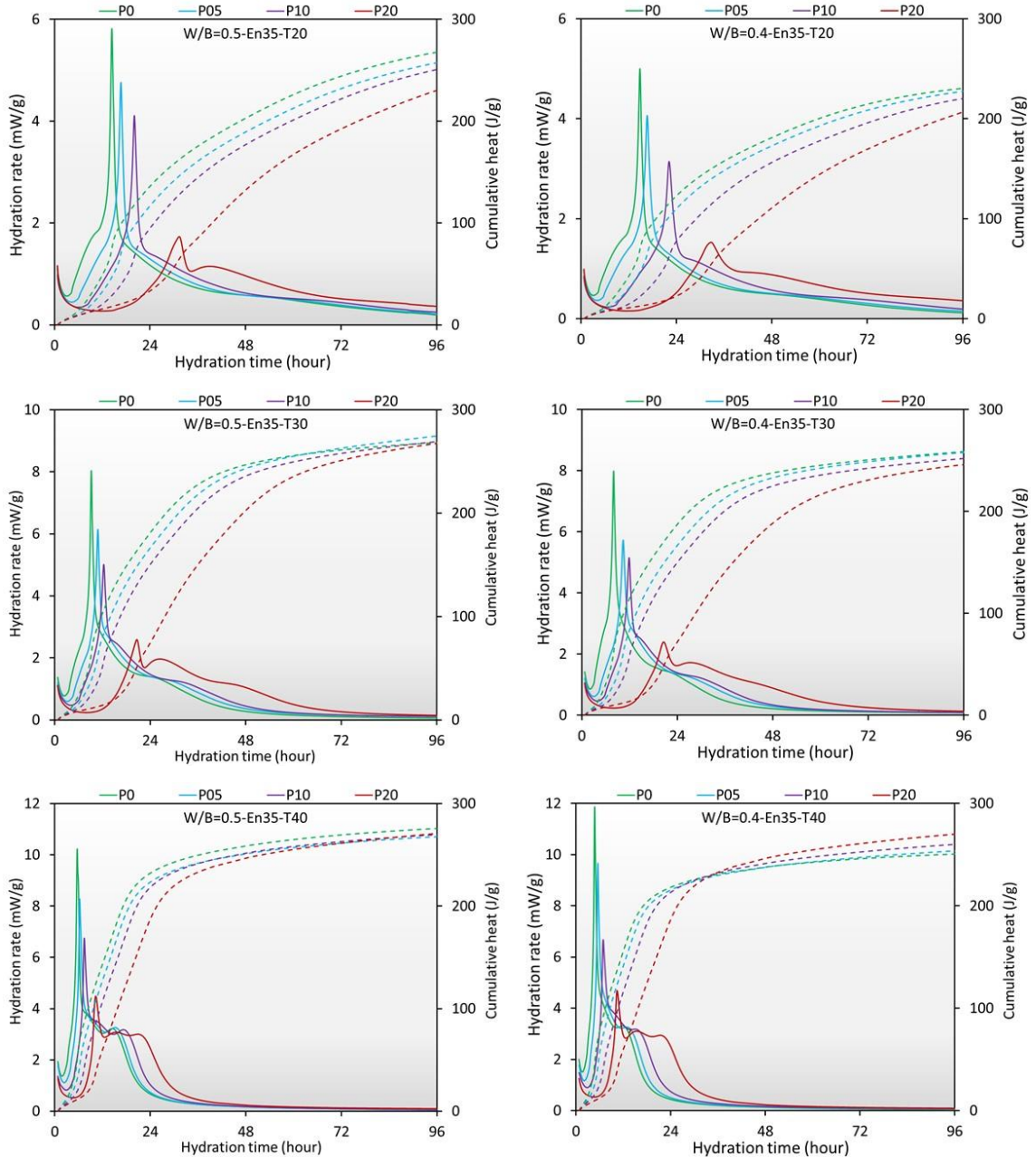


Figure 8-3: Isothermal hydration curves of LC³ pastes incorporating En35.

8.3.2 Effect of MPCMs on compressive strength

Figure 8-4 indicates the strength development of mixtures listed in **Table 8-3**. Accordingly, the replacement of fine aggregates with MPCM particles led to a decrease in the compressive strength of LC³ mortars, especially at higher dosages of MPCMs. Comparable reduction in compressive strength for OPC mortars and concretes after the

addition of MPCMs has been widely reported in the literature (Balapour *et al.*, 2021; Drissi *et al.*, 2019; Drissi *et al.*, 2021; Pilehvar *et al.*, 2017; Pilehvar *et al.*, 2020). The primary reason for this reduction in compressive strength is the soft effect of microcapsules (Balapour *et al.*, 2021; Fernandes *et al.*, 2014). MPCMs are fabricated of soft polymeric shells with a stiffness significantly lower than that of fine aggregates, which provides no remarkable resistance against applied loads. Another reason for the reduction in the compressive strength is the weak bond between MPCMs and the surrounding matrix (Djamai *et al.*, 2019). It can be observed in SEM images (see **Section 8.3.3.**) that weak connections and in some cases, large gaps, are evident at the interfacial transition zone (ITZ) between the MPCM particles and LC³ matrix. Additionally, MPCMs' shells deform during the mixing and casting stages of the mortar and probably during melting/freezing cycles. Such deformations further compromise their bond connection to the mortar and induce porosity in the matrix, leading to significant strength loss.

It is noteworthy that the incorporation of MPCMs exerted considerable delay in the strength gain of mortars, especially at higher levels of MPCMs. For instance, the compressive strength of specimens incorporating MPCMs at 20 wt.% of the binder was below 2 MPa after 24 hours. This is in agreement with observations drawn from IC measurements where MPCM inclusion prolonged the dormant period and postponed the maximum rate of hydration. The peak of hydration of cementitious materials is highly correlated to their setting behavior and strength development. The change in the rate of strength development can be clearly observed in the curves shown in **Fig. 8-4.**

Another interesting observation that emerged from the compressive strength results is that when w/b ratio of 0.5 was used, specimens with En28 inclusion attained a higher compressive strength compared to those with En35 at both 10 and 20 wt.% dosages. Nevertheless, this trend was not observed when w/b ratio of 0.4 was used, and specimens made with En28 and En35 microcapsules achieved comparable compressive strength. This could be related to the better filling of pores with hydration products at lower w/b ratios owing to the contribution of the filler effect of metakaolin. The microstructural analysis and porosity of the specimens are further discussed in **Sections 8.3.3 and 8.3.4.**

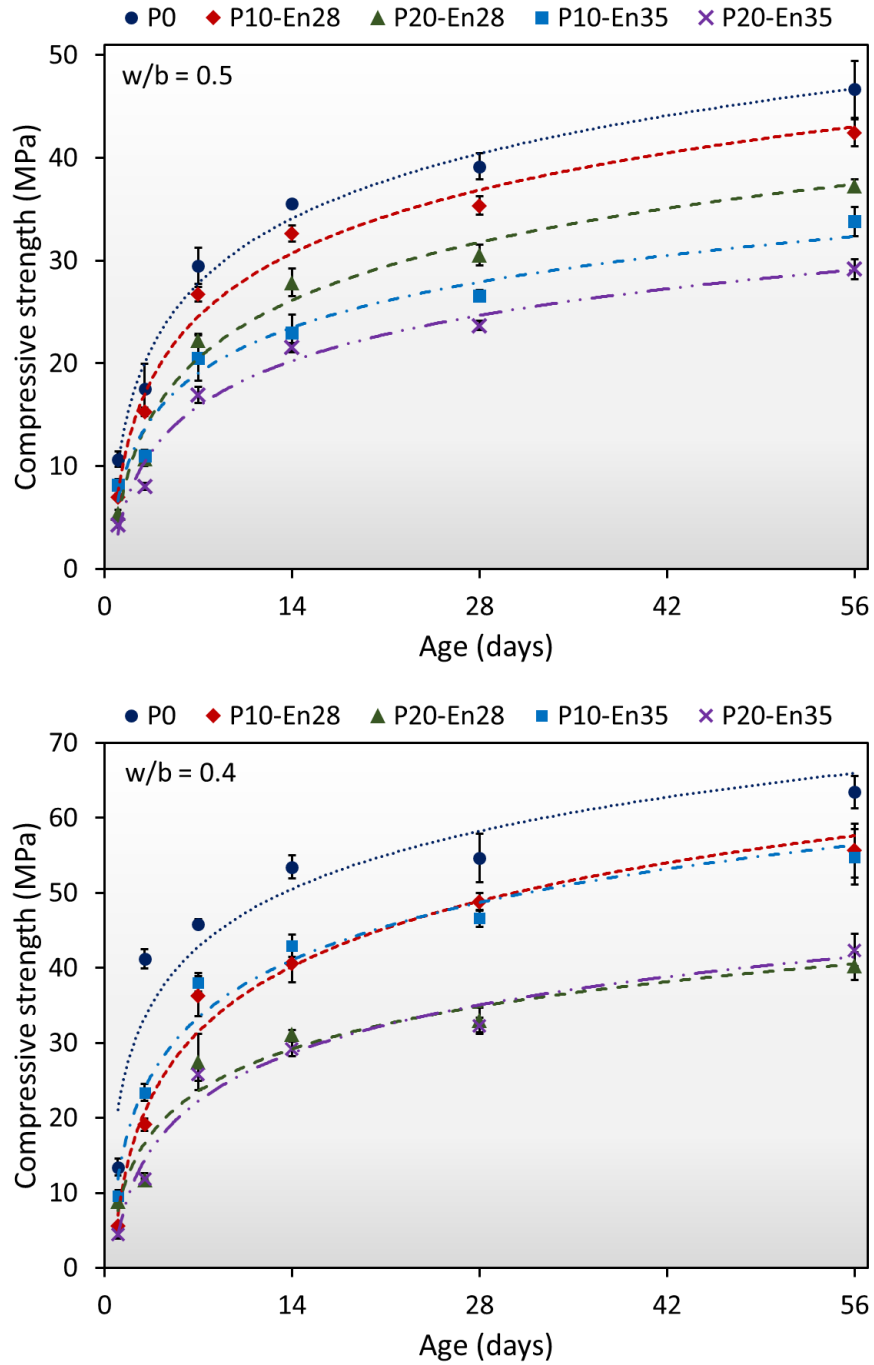


Figure 8-4: Strength development of MPCM-integrated LC³ mortars at w/b ratios of 0.5 (top) and 0.4 (bottom).

8.3.3 Microstructural analysis using SEM-EDX

Figures 8-5 and **8-6** depict SEM images of failure surfaces of mortar specimens made with En28 and En35 inclusions, respectively. Mixtures with 0 and 20 wt.% MPCM inclusions are selected for the analysis. It can be observed that MPCMs exhibited irregular shapes with manifest deformations. The wrinkled microcapsules with the dented surface could affect the packing density of the mixture and increase the porosity of the surrounding matrix. Additionally, the smooth surface of the polymeric microcapsules' shells hinders a strong bond connection with the mortar. As indicated with blue arrows in **Figs. 8-5** and **8-6**, various spots are identified where a gap is evident at the ITZ between the MPCMs and the mortar. This could further initiate microcracking and the loss of compressive strength. The decrease of nucleation sites available for the precipitation and growth of hydration products around the MPCM particles is also a potential reason for the gap and weak bond between the LC³ mortar and MPCM granules.

Comparing the SEM images of specimens containing En28 with those incorporating En35 suggests that En28 particles are better dispersed within the LC³ matrix. This might indicate that when En28 was used, more nucleation sites for the precipitation of hydration products were available. Therefore, the induced porosity is relatively lower in the surrounding mortar when En28 was utilized, especially at the w/b ratio of 0.5. Moreover, comparing the SEM images of specimens with w/b ratios of 0.5 and 0.4 suggests the potential increase of the hydration products around the microcapsules. Although such an explanation conforms to strength development analysis, SEM images alone cannot confirm the effect of w/b ration on the porosity induced by MPCM inclusions. Therefore, EDX analysis along with pore structure analysis using μ CT scan can better clarify the aforementioned observations.

Table 8-6 summarizes the elemental analysis of the hydration products obtained from SEM-EDX analysis. The carbon content was higher in samples with MPCM inclusion, which is probably due to the polymeric shells of the microcapsules. The elemental analysis revealed that in the WC04En35P20 sample, the Ca content increased by approximately 22% compared to that for the WC04En35P20 sample. This could be related to the higher

precipitation of CSH when a lower w/b ratio was used, which is in conformity with compressive strength results.

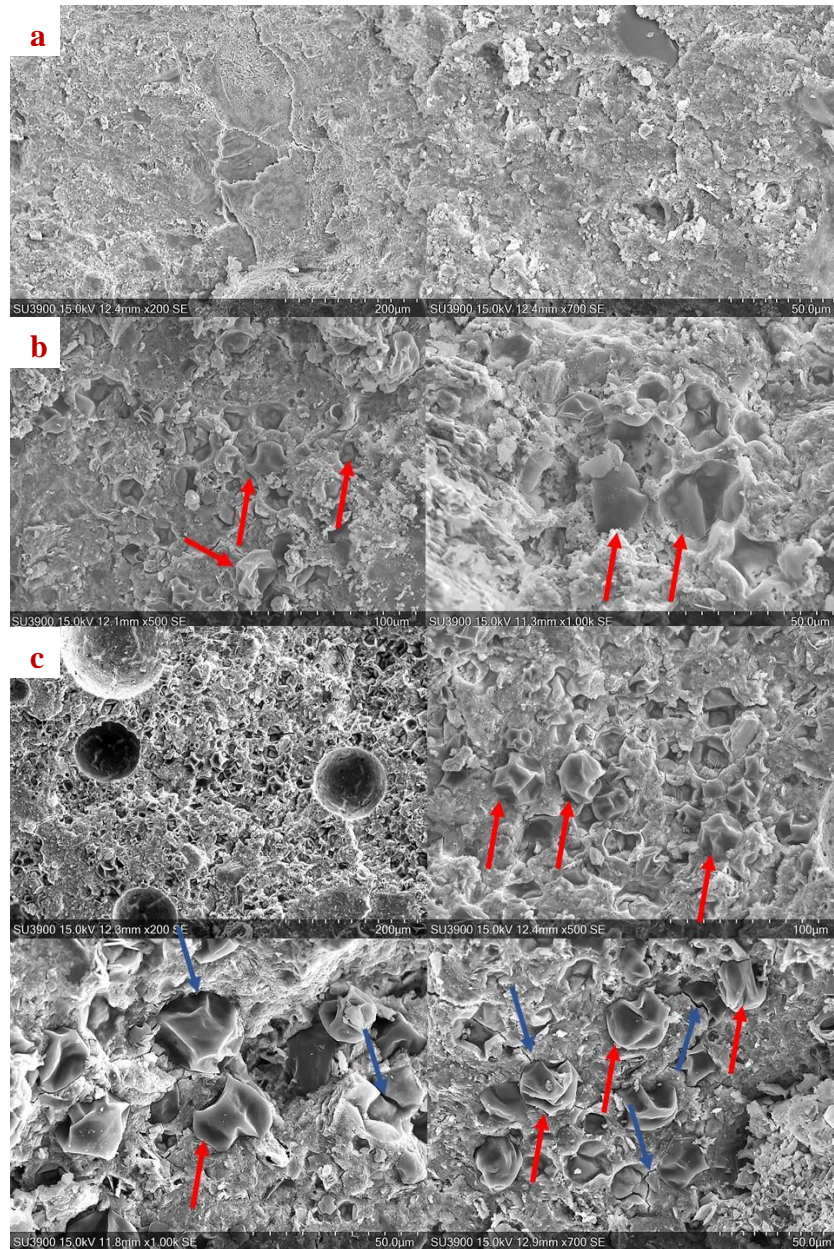


Figure 8-5: SEM images of mortars made with w/b ratio of 0.5: a) No MPCM inclusion; b) 20% En28 inclusion; and c) 20% En35 inclusion.

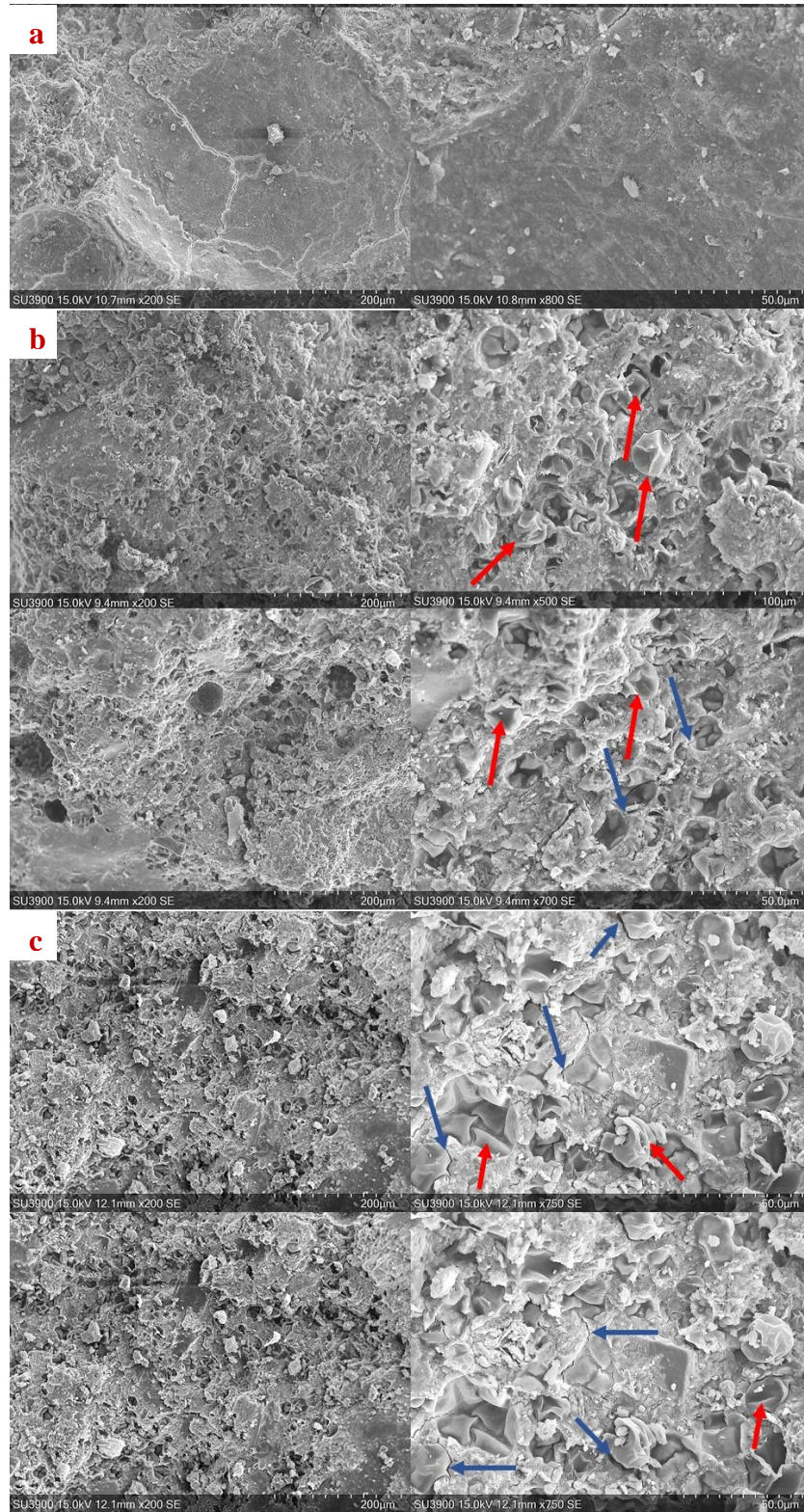


Figure 8-6: SEM images of mortars made with w/b ratio of 0.5: a) No MPCM inclusion; b) 20% En28 inclusion; and c) 20% En35 inclusion.

Table 8-6: EDX analysis of hydration products

Sample	C	Al	Si	Ca	Al/Ca	Si/Ca
WB04	15.23±1.04	5.47±0.28	9.28±1.16	18.68±1.65	0.29±0.02	0.50±0.11
WB04P20En28	24.53±1.06	4.44±0.87	9.53±1.82	18.32±1.53	0.24±0.06	0.52±0.10
WB04P20En35	25.10±0.82	4.34±0.39	7.72±1.28	19.18±1.49	0.22±0.01	0.41±0.09
WB05	14.54±1.10	5.04±1.02	9.85±0.71	19.37±1.10	0.26±0.06	0.51±0.06
WB05P20En28	24.8±1.85	4.4±0.127	8.8±1.22	15.2±1.23	0.28±0.01	0.58±0.10
WB05P20En35	26.8±1.04	4.7±0.17	8.3±1.25	15.7±1.59	0.30±0.04	0.54±0.14

8.3.4 Porosity analysis with μ -CT scan

The porosity of the LC³ mortars listed in **Table 8-3** was examined using the reconstructed 3D images obtained from μ -CT scan analysis. **Figure 8-7** showcases typical 2D slices along with the segmentation of samples with the w/b ratio of 0.4 containing 0, 10, and 20 wt.% of En28, *i.e.*, WB04, WB04P10En28, WB04P20En28. Due to the low level of X-ray attenuation of the organic MPCMs' shells, the discrimination between air voids and MPCM particles is relatively based on their morphology. Air voids tend to form spherical shapes, whereas MPCMs have irregular morphology because of the potential agglomeration. After image segmentation and porosity analysis, it was observed that the addition of MPCMs resulted in increased porosity of the surrounding matrix. Accordingly, the total volume of pores in WB04, WB04P10En28, WB04P20En28 samples were 3.49, 5.07, and 6.76%, respectively. This demonstrates an increase of porosity with the increase in MPCM dosage. WB04P10En35 and WB04P20En35 also indicated comparable porosity percentages of 5.10 and 6.52%, respectively. This is in excellent agreement with the compressive strength measurements discussed earlier.

Furthermore, samples with a higher w/b ratio had higher porosity contents. The volume of pores in the WB04, WB04P10En28, WB04P20En28 specimens was, 5.13, 8.6, and 9.22%, respectively, which is higher compared to specimens with w/b of 0.4. Another interesting finding is that in contrast to samples with w/b ratio of 0.4, the porosity of mixtures with En35 inclusion was higher compared to those with En28 inclusion when the w/b ratio was 0.5. Samples WB04P10En35 and WB04P20En35 had a total pore volume of 10.14 and 11.87%, respectively. The porosity analysis confirmed that MPCM addition induced porosity in the LC³ mortars, which led to a loss of compressive strength. This porosity highly depends on the type of microcapsules, their compatibility with the surrounding

mortar, and the w/b ratio of the paste. **Figure 8-8** displays the 3D pore structure of WB04, WB04P10En28, and WB04P20En28 samples. Significantly larger pore structures are evident in samples with MPCM inclusion.

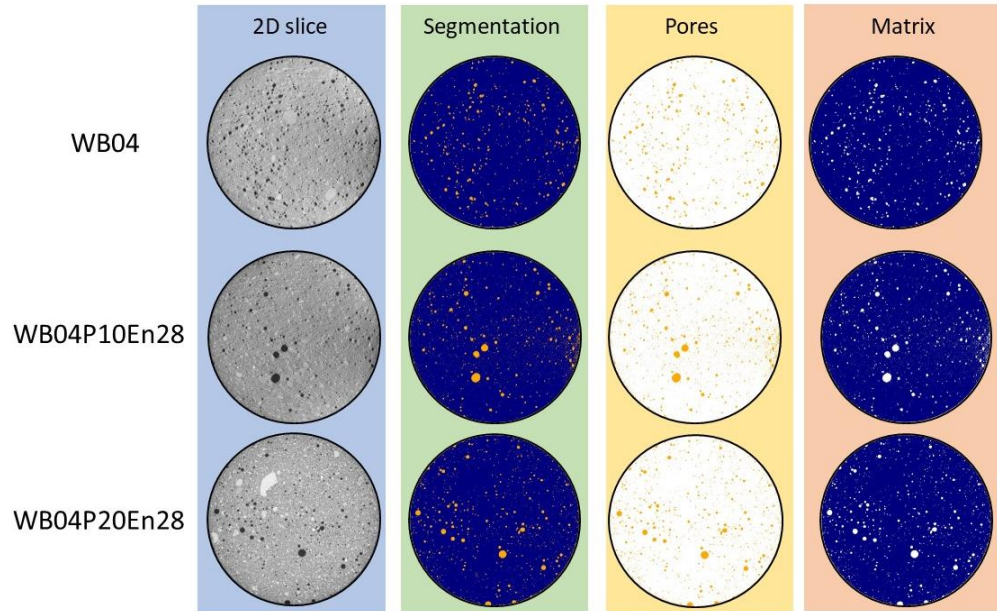


Figure 8-7: Image segmentation for porosity analysis of mortar samples.

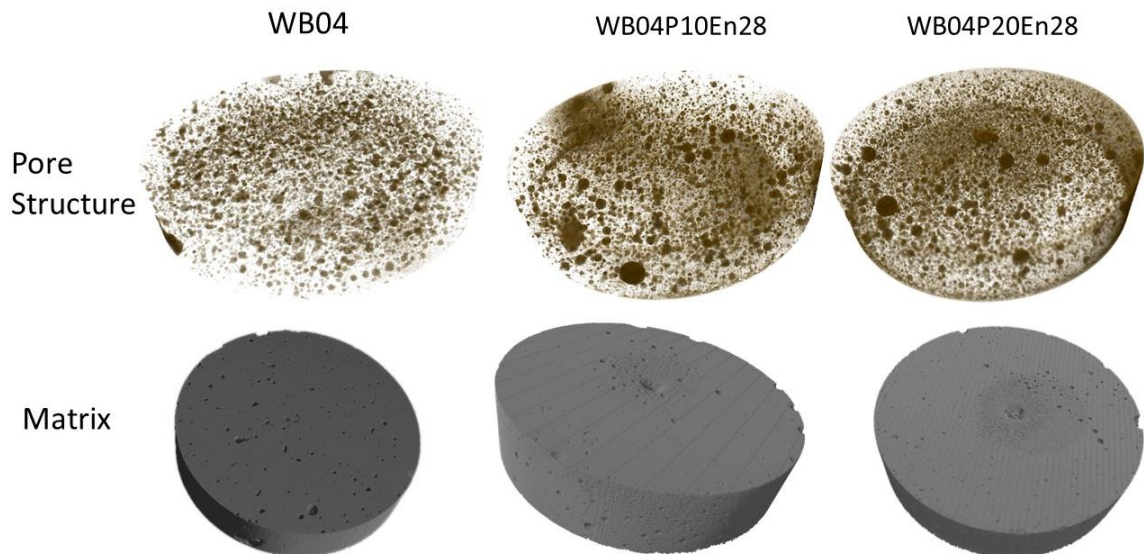


Figure 8-8: 3D pore structure of samples obtained from μ -CT scan analysis.

8.3.5 Thermo-regulating performance

Figure 8-9 illustrates the temperature history of the inner-side surface of specimens under the applied ambient temperature. It can be observed that the addition of MPCMs reduced the maximum inside temperature owing to its latent heat capacity. The analysis of the results indicates that a maximum reduction of the inside temperature up to 2.2 and 3.5°C was achieved in specimens containing 10 and 20 wt.% of En28, respectively. The hourly temperature difference of the inner-side surface of these specimens with respect to the control specimen (*i.e.*, WB04) is shown in **Fig. 8-9 (b)**. For instance, after 9.5 hours from the start of the test, the inner temperature of the control specimen was 33.5°C, whereas it was 30°C for the specimen made with 20 wt.% En28 inclusion (P20En28), indicating a 3.5°C reduction. Furthermore, the addition of En28 shifted the on-peak maximum indoor temperature for 2h to the off-peak period. A less drastic reduction of the inside temperature was also evidenced during the cooling phase of the applied temperature profile, as can be observed in **Fig. 8-9**.

Comparable temperature regulation performance was evidenced in specimens incorporating En35. However, the temperature reduction started at higher temperatures due to the higher melting temperature of the En35 compared to En28 as shown in **Figs. 8-9 (b)** and **(d)**. Overall, the addition of 10 and 20 wt.% of En28 mitigated the indoor temperature fluctuations with respect to the control specimen by up to 16.67 and 25.85°C·hour, respectively, during 24 hours of simulation. In the case of En35, the temperature fluctuations were moderated by 13.1 and 18.2 °C·hour when 10 and 20 wt.% MPCM was utilized, respectively. It should be noted that the effect of the MPCMs on the thermo-regulating performance of the specimens highly depends on the applied ambient temperature along with the melting temperature of MPCMs. Hence, although En28 and En35 particles have similar latent heat capacities, using En28 resulted in better thermo-regulating performance under the applied temperature profile.

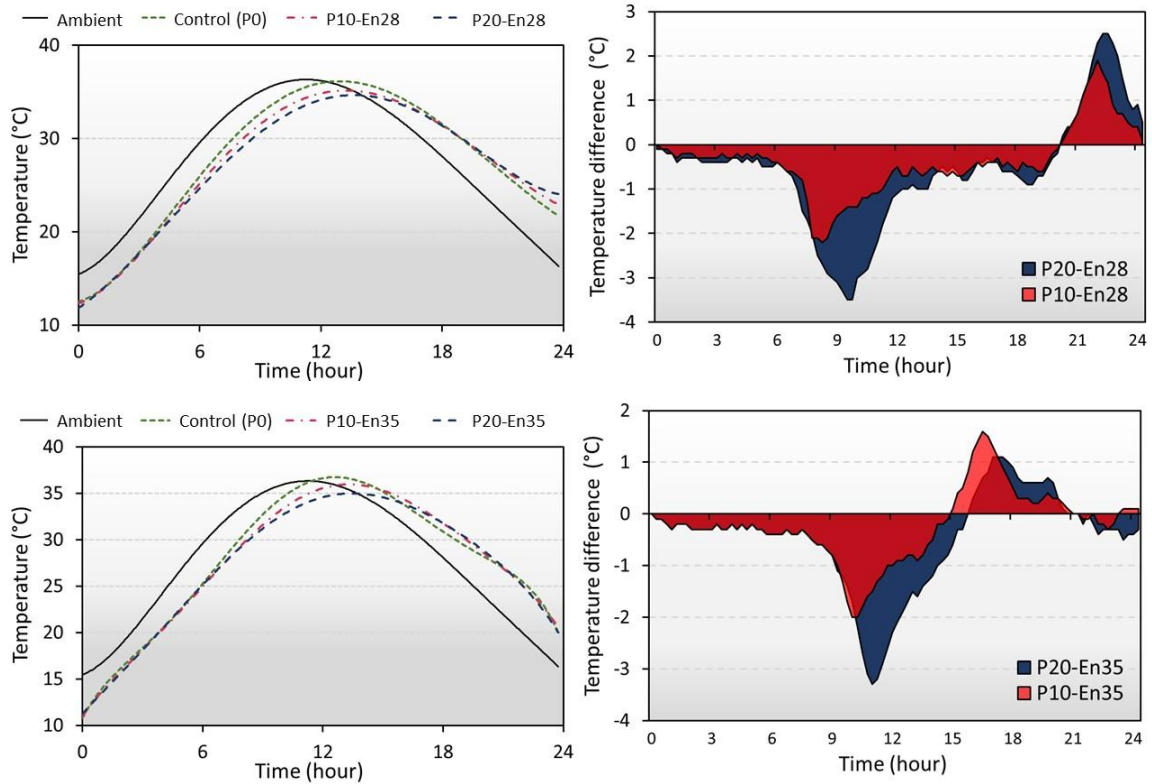


Figure 8-9: Thermo-regulating performance of specimens incorporating En28 (top) and En35 (bottom) inclusion.

8.4 Concluding remarks

This chapter investigates the addition of bio-based non-formaldehyde MPCMs with different thermos-physical properties on the hydration kinetics, strength and microstructural development, and thermo-regulating performance of ternary LC³ mortars. The isothermal calorimetry measurements revealed that the incorporation of MPCMs prolonged the dormant period and reduced the maximum hydration rate, which was reflected in significant delays in the strength development of the mortar. Moreover, the compressive strength decreased after the addition of MPCMs due to their soft effect along with the porosity they induce in the matrix. The microstructural analysis indicates that using lower w/b ratios refines porosity of the matrix and compensates for the strength loss caused by the MPCM addition. Ultimately, the thermo-regulating tests infer that samples with 20 wt% of MPCM inclusion can moderate the temperature fluctuations by 3.5°C, thus reducing the energy consumption of HVAC systems. Therefore, developing LHTES- LC³

systems can significantly reduce the operational and embodied carbon emissions of buildings and promote the resilience and sustainability of the built environment.

8.5 References

Avet, F., & Scrivener, K. (2018). Investigation of the calcined kaolinite content on the hydration of Limestone Calcined Clay Cement (LC3). *Cement and Concrete Research*, 107, 124-135.

Balapur, M., Mutua, A. W., & Farnam, Y. (2021). Evaluating the thermal efficiency of microencapsulated phase change materials for thermal energy storage in cementitious composites. *Cement and Concrete Composites*, 116, 103891.

Cabeza, L. F., Barreneche, C., Miró, L., Morera, J. M., Bartolí, E., & Fernández, A. I. (2013). Low carbon and low embodied energy materials in buildings: A review. *Renewable and sustainable energy reviews*, 23, 536-542.

Cabeza, L. F., Rincón, L., Vilariño, V., Pérez, G., & Castell, A. (2014). Life cycle assessment (LCA) and life cycle energy analysis (LCEA) of buildings and the building sector: A review. *Renewable and sustainable energy reviews*, 29, 394-416.

Coffetti, D., Crotti, E., Gazzaniga, G., Carrara, M., Pastore, T., & Coppola, L. (2022). Pathways towards sustainable concrete. *Cement and Concrete Research*, 154, 106718.

da Cunha, S. R. L., & de Aguiar, J. L. B. (2020). Phase change materials and energy efficiency of buildings: A review of knowledge. *Journal of Energy Storage*, 27, 101083.

Djamai, Z. I., Salvatore, F., Larbi, A. S., Cai, G., & El Mankibi, M. (2019). Multiphysics analysis of effects of encapsulated phase change materials (PCMs) in cement mortars. *Cement and Concrete Research*, 119, 51-63.

Drissi, S., Ling, T.-C., Mo, K. H., & Eddhahak, A. (2019). A review of microencapsulated and composite phase change materials: Alteration of strength and thermal properties of cement-based materials. *Renewable and sustainable energy reviews*, 110, 467-484.

Drissi, S., Mo, K. H., Falchetto, A. C., & Ling, T.-C. (2021). Understanding the compressive strength degradation mechanism of cement-paste incorporating phase change material. *Cement and Concrete Composites*, 124, 104249.

Fernandes, F., Manari, S., Aguayo, M., Santos, K., Oey, T., Wei, Z., Falzone, G., Neithalath, N., & Sant, G. (2014). On the feasibility of using phase change materials (PCMs) to mitigate thermal cracking in cementitious materials. *Cement and Concrete Composites*, 51, 14-26.

Hekimoğlu, G., Nas, M., Ouikhalfan, M., Sarı, A., Tyagi, V., Sharma, R., Kurbetci, Ş., & Saleh, T. A. (2021). Silica fume/capric acid-stearic acid PCM included-cementitious composite for thermal controlling of buildings: Thermal energy storage and mechanical properties. *Energy*, 219, 119588.

Huang, L., Bohne, R. A., Bruland, A., Jakobsen, P. D., & Lohne, J. (2015). Life cycle assessment of Norwegian road tunnel. *The International Journal of Life Cycle Assessment*, 20(2), 174-184.

Huang, L., Krigsvoll, G., Johansen, F., Liu, Y., & Zhang, X. (2018). Carbon emission of global construction sector. *Renewable and sustainable energy reviews*, 81, 1906-1916.

Jayalath, A., San Nicolas, R., Sofi, M., Shanks, R., Ngo, T., Aye, L., & Mendis, P. (2016). Properties of cementitious mortar and concrete containing micro-encapsulated phase change materials. *Construction and Building Materials*, 120, 408-417.

Liu, L., Lu, G., Qiu, G., Yue, C., Guo, M., Ji, R., & Zhang, M. (2019). Characterization of novel shape-stabilized phase change material mortar: Portland cement containing $\text{Na}_2\text{SO}_4 \cdot 10\text{H}_2\text{O}$ and fly ash for energy-efficient building. *International Journal of Energy Research*, 43(11), 5812-5823.

Marani, A., & Madhkhan, M. (2018). An innovative apparatus for simulating daily temperature for investigating thermal performance of wallboards incorporating PCMs. *Energy and Buildings*, 167, 1-7.

Marani, A., & Madhkhan, M. (2021). Thermal performance of concrete sandwich panels incorporating phase change materials: An experimental study. *Journal of Materials Research and Technology*, 12, 760-775.

Marani, A., & Nehdi, M. L. (2019). Integrating phase change materials in construction materials: Critical review. *Construction and Building Materials*, 217, 36-49.

Miller, S. A., John, V. M., Pacca, S. A., & Horvath, A. (2018). Carbon dioxide reduction potential in the global cement industry by 2050. *Cement and Concrete Research*, 114, 115-124.

Nehdi, M. (2001). Ternary and quaternary cements for sustainable development. *Concrete International*, 23(4), 36-44.

Nguyen, Q. D., Kim, T., & Castel, A. (2020). Mitigation of alkali-silica reaction by limestone calcined clay cement (LC3). *Cement and Concrete Research*, 137, 106176.

Parashar, A., & Bishnoi, S. (2021). Hydration behaviour of limestone-calcined clay and limestone-slag blends in ternary cement. *RILEM Technical Letters*, 6, 17-24.

Pilehvar, S., Cao, V. D., Szczotok, A. M., Valentini, L., Salvioni, D., Magistri, M., Pamies, R., & Kjønksen, A.-L. (2017). Mechanical properties and microscale changes of geopolymer concrete and Portland cement concrete containing micro-encapsulated phase change materials. *Cement and Concrete Research*, 100, 341-349.

Pilehvar, S., Sanfelix, S. G., Szczotok, A. M., Rodríguez, J. F., Valentini, L., Lanzón, M., Pamies, R., & Kjønksen, A.-L. (2020). Effect of temperature on geopolymer and Portland cement composites modified with Micro-encapsulated Phase Change materials. *Construction and Building Materials*, 252, 119055.

Pomponi, F., & Moncaster, A. (2016). Embodied carbon mitigation and reduction in the built environment—What does the evidence say? *Journal of environmental management*, 181, 687-700.

Promoppatum, P., Yao, S.-C., Hultz, T., & Agee, D. (2017). Experimental and numerical investigation of the cross-flow PCM heat exchanger for the energy saving of building HVAC. *Energy and Buildings*, 138, 468-478.

Provis, J. L. (2018). Alkali-activated materials. *Cement and Concrete Research*, 114, 40-48.

Sartori, I., & Hestnes, A. G. (2007). Energy use in the life cycle of conventional and low-energy buildings: A review article. *Energy and Buildings*, 39(3), 249-257.

Sbci, U. (2009). Buildings and climate change: Summary for decision-makers. United Nations Environmental Programme, Sustainable Buildings and Climate Initiative, Paris, 1-62.

Schneider, M. (2019). The cement industry on the way to a low-carbon future. *Cement and Concrete Research*, 124, 105792.

Scrivener, K., Avet, F., Maraghechi, H., Zunino, F., Ston, J., Hanpongpun, W., & Favier, A. (2018). Impacting factors and properties of limestone calcined clay cements (LC3). *Green Materials*, 7(1), 3-14.

Shah, V., Parashar, A., Mishra, G., Medepalli, S., Krishnan, S., & Bishnoi, S. (2020). Influence of cement replacement by limestone calcined clay pozzolan on the engineering properties of mortar and concrete. *Advances in Cement Research*, 32(3), 101-111.

Sharma, M., Bishnoi, S., Martirena, F., & Scrivener, K. (2021). Limestone calcined clay cement and concrete: A state-of-the-art review. *Cement and Concrete Research*, 149, 106564.

Stephan, A., & Stephan, L. (2016). Life cycle energy and cost analysis of embodied, operational and user-transport energy reduction measures for residential buildings. *Applied Energy*, 161, 445-464.

Tatsidjodoung, P., Le Pierrès, N., & Luo, L. (2013). A review of potential materials for thermal energy storage in building applications. *Renewable and sustainable energy reviews*, 18, 327-349.

Thiele, A. M., Jamet, A., Sant, G., & Pilon, L. (2015). Annual energy analysis of concrete containing phase change materials for building envelopes. *Energy conversion and management*, 103, 374-386.

Thiele, A. M., Sant, G., & Pilon, L. (2015). Diurnal thermal analysis of microencapsulated PCM-concrete composite walls. *Energy conversion and management*, 93, 215-227.

Tyagi, V. V., & Buddhi, D. (2007). PCM thermal storage in buildings: A state of art. *Renewable and sustainable energy reviews*, 11(6), 1146-1166.

Vance, K., Aguayo, M., Oey, T., Sant, G., & Neithalath, N. (2013). Hydration and strength development in ternary portland cement blends containing limestone and fly ash or metakaolin. *Cement and Concrete Composites*, 39, 93-103.

Walling, S. A., & Provis, J. L. (2016). Magnesia-based cements: a journey of 150 years, and cements for the future? *Chemical Reviews*, 116(7), 4170-4204.

Zhao, C.-Y., & Zhang, G. H. (2011). Review on microencapsulated phase change materials (MEPCMs): fabrication, characterization and applications. *Renewable and sustainable energy reviews*, 15(8), 3813-3832.

Zheng, C., Zhang, H., Cai, X., Chen, L., Liu, M., Lin, H., & Wang, X. (2021). Characteristics of CO₂ and atmospheric pollutant emissions from China's cement industry: A life-cycle perspective. *Journal of Cleaner Production*, 282, 124533.

Zhong, X., Hu, M., Deetman, S., Steubing, B., Lin, H. X., Hernandez, G. A., Harpprecht, C., Zhang, C., Tukker, A., & Behrens, P. (2021). Global greenhouse gas emissions from residential and commercial building materials and mitigation strategies to 2060. *Nature Communications*, 12(1), 1-10.

Zhou, D., Zhao, C.-Y., & Tian, Y. (2012). Review on thermal energy storage with phase change materials (PCMs) in building applications. *Applied Energy*, 92, 593-605.

Zunino, F., & Scrivener, K. (2021). The reaction between metakaolin and limestone and its effect in porosity refinement and mechanical properties. *Cement and Concrete Research*, 140, 106307.

Zunino, F., & Scrivener, K. (2022). Microstructural developments of limestone calcined clay cement (LC3) pastes after long-term (3 years) hydration. *Cement and Concrete Research*, 153, 106693.

Chapter 9

9 Summary, Conclusions, and Recommendations for Future Work

This chapter summarizes the major findings of the current study. Concluding remarks are distinctly outlined and recommendations for future work are provided to overcome the limitations of the present research.

9.1 Summary and conclusions

Enhancing the thermal energy storage (TES) capacity of buildings is of particularly great concern due to escalating worldwide energy demand. Integrating phase change materials (PCMs) into concrete provides latent heat capacity and therefore, moderates the indoor temperature fluctuation in buildings, thus prompting enhanced thermal comfort and considerable energy savings. Nevertheless, the addition of PCMs into concrete could influence its engineering properties, which requires concerted research investigations.

Chapter 2 identifies four primary methods for incorporating PCMs into building materials including microencapsulated PCMs (MPCMs), shape-stabilized PCMs (SSPCMs), lightweight aggregate (LWA) impregnation, and macro-encapsulation. The major findings, drawbacks, limitations for each method were vigorously discussed and future research needs were recognized.

In Chapter 3, a preliminary dataset was compiled and powerful machine learning models were developed to predict the compressive strength of MPCM-integrated cement-based composites with reasonable accuracy. Furthermore, the crucial variables affecting the compressive strength were identified. Accordingly, the MPCM and fine aggregate contents, curing age, and cement content indicated high importance, while the curing temperature was found to be less influential. The thermos-physical properties of MPCMs also seemed to affect the strength gain mechanism.

In Chapter 4, a novel deep learning data synthesizing technique based on an updated version of the experimental dataset was employed to enrich the data points for training

robust ML models. Moreover, a mixture optimization paradigm validated with laboratory tests was developed to propose a mixture design approach for cement-based mortars and concretes for the first time.

Chapter 5 investigates, for the first time, the effects of MPCMs on the apparent activation energy of cement-based composites using isothermal calorimetry and compressive strength measurements. Results demonstrated that the addition of MPCMs decreases the apparent activation energy, indicating less sensitivity of the strength development to temperature. The apparent activation energy of MPCM-integrated mortars and concretes can help better evaluate the temperature gradients and thermal stresses in hardening concrete.

Chapter 6 deploys deep learning modeling techniques to simulate the hydration kinetics of MPCM-integrated cement-based composites. It was observed that the deep learning model outperformed the gradient boosting ensemble in accurately extrapolating the hydration kinetics. The apparent activation energy of diverse cement-based systems was calculated based on deep learning predictions, which were in great conformity with experimental results.

An eco-friendly SSPCM for integrating TES in building materials was fabricated in Chapter 7. Bio-based PCMs were vacuum impregnated in recycled expanded glass granules and sealed with silica fume powder. Results indicated leak-free performance along with favorable melting temperatures and latent heat capacities of the developed SSPCMs for energy saving in buildings. Thermo-regulating analyses suggested maximum reduction of the indoor temperature up to 4°C in specimens with SSPCMs inclusions. Nevertheless, the strength measurements and microstructural analysis of mortars indicated lower compressive strength due to the increased porosity after the addition of SSPCMs.

Ultimately, in Chapter 8, MPCMs were added to limestone calcined clay (LC³) mortars to develop a low-carbon latent heat TES (LHTES) system. MPCMs affected the hydration kinetics by reducing the peak of hydration and delaying the acceleration period. Although MPCMs increased the porosity and reduced the compressive strength, lowering the water-to-binder ratio significantly refined the pore structure and prompted higher compressive strength. The thermos-regulating test also suggested reducing the indoor temperature

fluctuation by 3.5°C after MPCM addition, thus improving the energy saving in buildings along with reducing embodied carbon emissions.

9.2 Contributions to the state-of-the-art

Extensive numerical and laboratory experiments performed in this study provide the following significant contributions to the existing knowledge in the field:

- An up-to-date experimental dataset on the mixture design of cement mortars and concretes incorporating various types MPCMs was collected.
- Machine learning models were developed, for the first time, to predict the compressive strength of MPCM-integrated cementitious composites and identify the most influential design variables.
- Tabular generative adversarial networks (TGAN) were employed to generate numerous synthetic and credible data to compensate the low number of available experimental data.
- A novel ternary machine learning framework was proposed, for the first time, to optimize the mixture design of cement mortars and concretes incorporating various commercially available MPCMs.
- The apparent activation energy of cement-based composites incorporating MPCMs was calculated using isothermal calorimetry and compressive strength measurements to better understand the temperature sensitivity of such composites.
- The correlation between the melting temperature of MPCMs and curing temperature of concrete was explored.
- Eco-friendly SSPCMs suitable for thermal energy storage applications in buildings were developed using commercially available recycled aggregates and biobased PCMs in Canada.

- Novel low-carbon limestone calcined clay cement composites incorporating MPCMs were developed, for the first time, to simultaneously reduce the embodied and operational environmental footprint and carbon emissions of buildings.

9.3 Research limitations

Despite the promising contributions achieved in the current study, several limitations were recognized that need to be addressed in future work as follows:

- There is clear lack of available experimental data on the diverse engineering properties of MPCM-integrated concretes such as slump. The mixture design of concretes should be optimized considering workability, environmental, and energy saving aspects, in addition to the mechanical performance requirements taken into account in this study.
- The effects of MPCMs with similar melting temperatures, but different latent heat enthalpies, on the strength development of cement-based composites should be investigated.
- The correlation between the energy saving capacity and mechanical strength of concretes incorporating various types of MPCMs should be benchmarked.
- The economic benefits of MPCM-integrated concretes considering the cost of MPCMs compared to conventional ingredients of concrete should be calculated.
- Life cycle analyses need to be carried out to better understand the environmental and cost saving effects of the developed low-carbon thermal energy storage composites.

9.4 Recommendations for future research

The major findings of this research along with the existing limitations point to the following research ideas for potential future research:

- The mixture optimization in the current research was carried out considering the objective of maximum latent heat capacity content with specific compressive strength requirements. As experimental data becomes more available in the future, the optimization can further be improved by including the fresh properties of MPCM-integrated mortars and concretes, such as slump.
- Machine and deep learning methods demonstrated outstanding capability in modeling some of the engineering characteristics of the MPCM-integrated cement based-systems. Nevertheless, more comprehensive data are required to further correlate their mechanical strength with the energy storage capacity.
- The calculation of the apparent activation energy in this research provides an opportunity for numerical simulation of the semi-adiabatic temperature rise in mass concrete elements. The effects of MPCMs on the thermal stress and strain development in mass concrete can now be better estimated using the activation energy values obtained herein.
- More extensive experimental efforts are needed to evaluate various engineering properties of low-carbon LHTES systems such as LC³-LHTES concrete developed in this study. Integrating low-carbon alternative binders with LHTES materials can further promote sustainability and reduce the operational and embodied emissions of major infrastructures.
- Life cycle analysis (LCA) and life cycle cost analysis (LCCA) are needed to better illustrate the long-term energy and cost-saving of LHTES-integrated cementitious materials.
- For the broader application of PCMs in the construction industry, it is crucial to develop new encapsulation techniques that are more compatible with cementitious matrices, and thus can improve mechanical performance.

Appendix A

The actual hydration heat curves versus predicted values obtained from the GBR1 and DNN1 models developed in Chapter 6 for all cement-based systems are illustrated in **Figs. A-1 to A-20**. The simulated systems include En28 and En35 microencapsulated PCMs. The isothermal calorimetry tests were conducted at 15, 23, 30, 35, and 40°C. The systems are designated as PxTy where x denotes the inclusion percentage of MPCMs and y indicates the testing temperature.

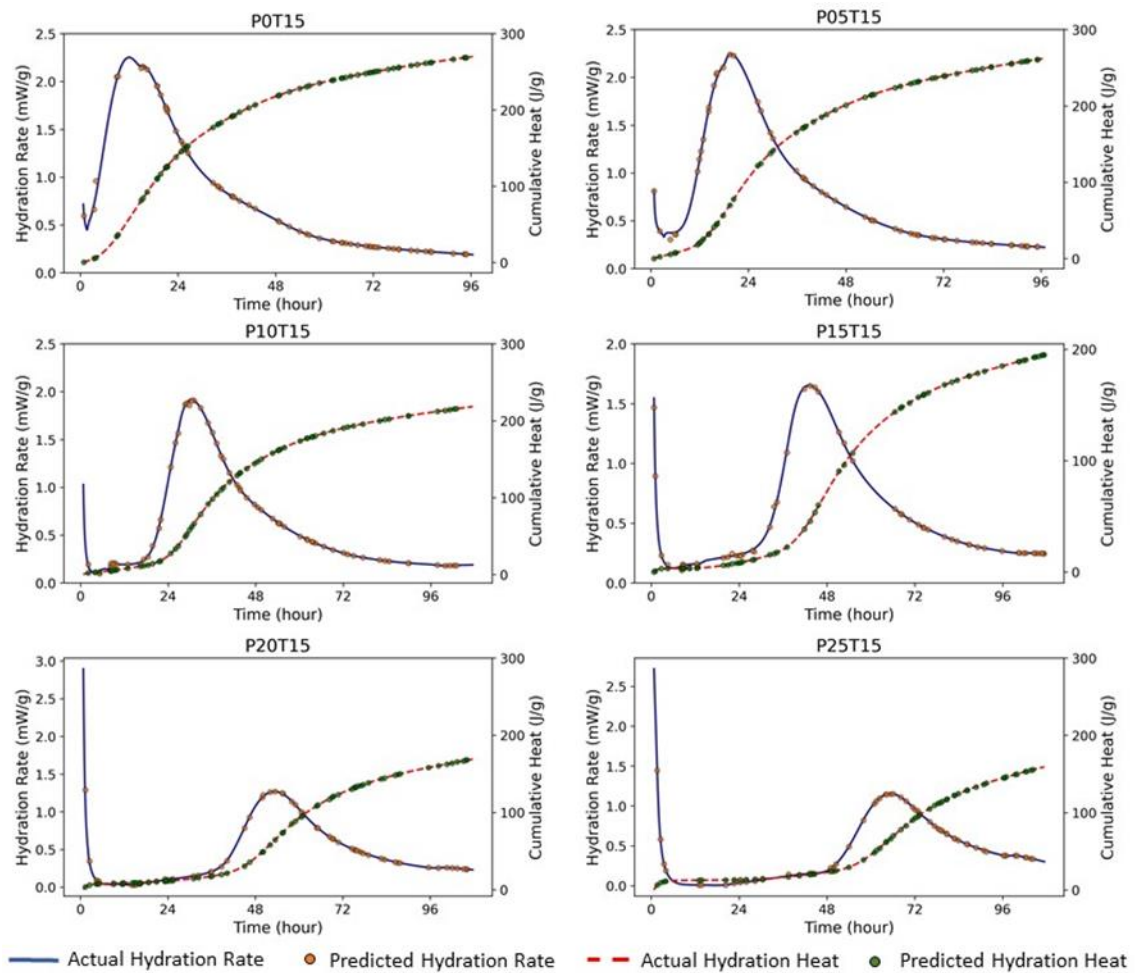


Figure A-1: Predictions of GBR1 for cement systems incorporating various levels of En28 at 15°C.

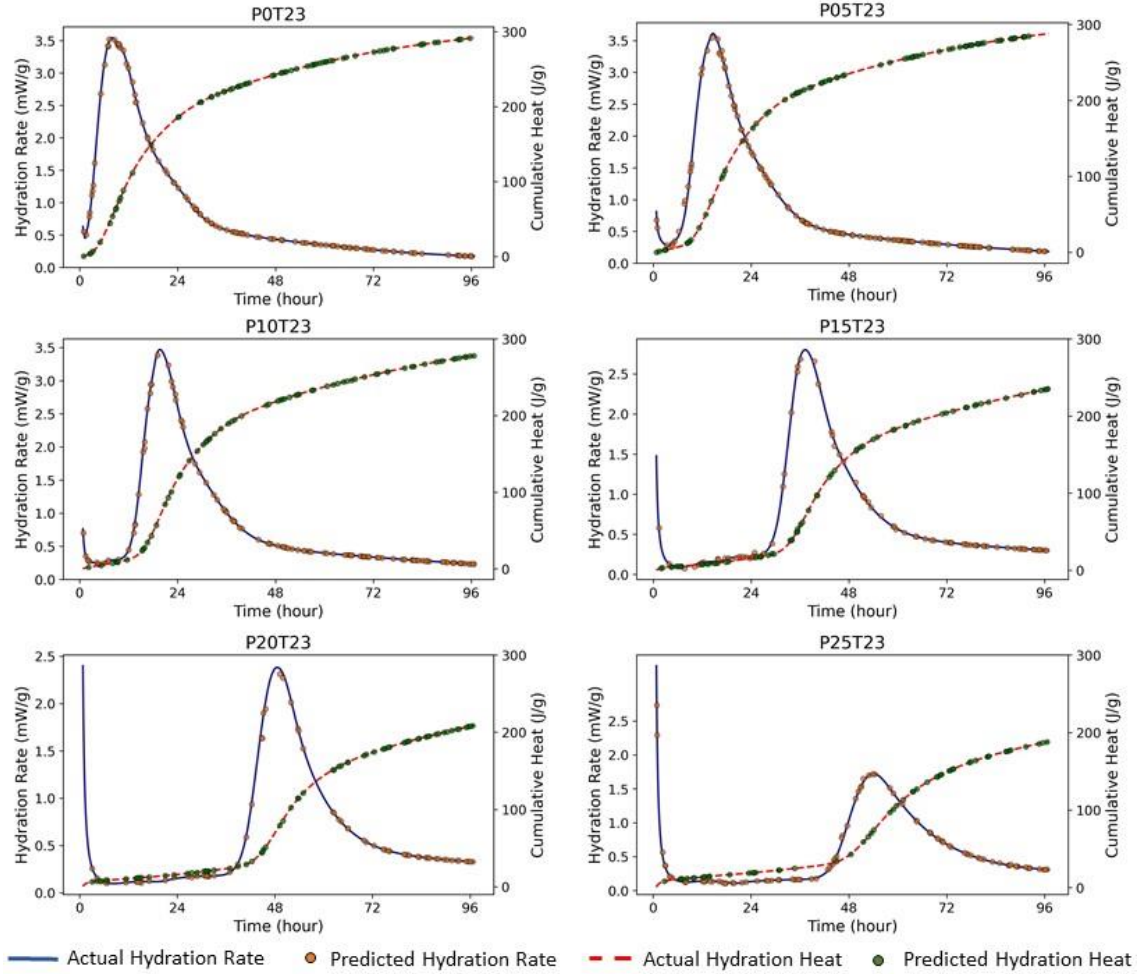


Figure A-2: Predictions of GBR1 for cement systems incorporating various levels of En28 at 23°C.

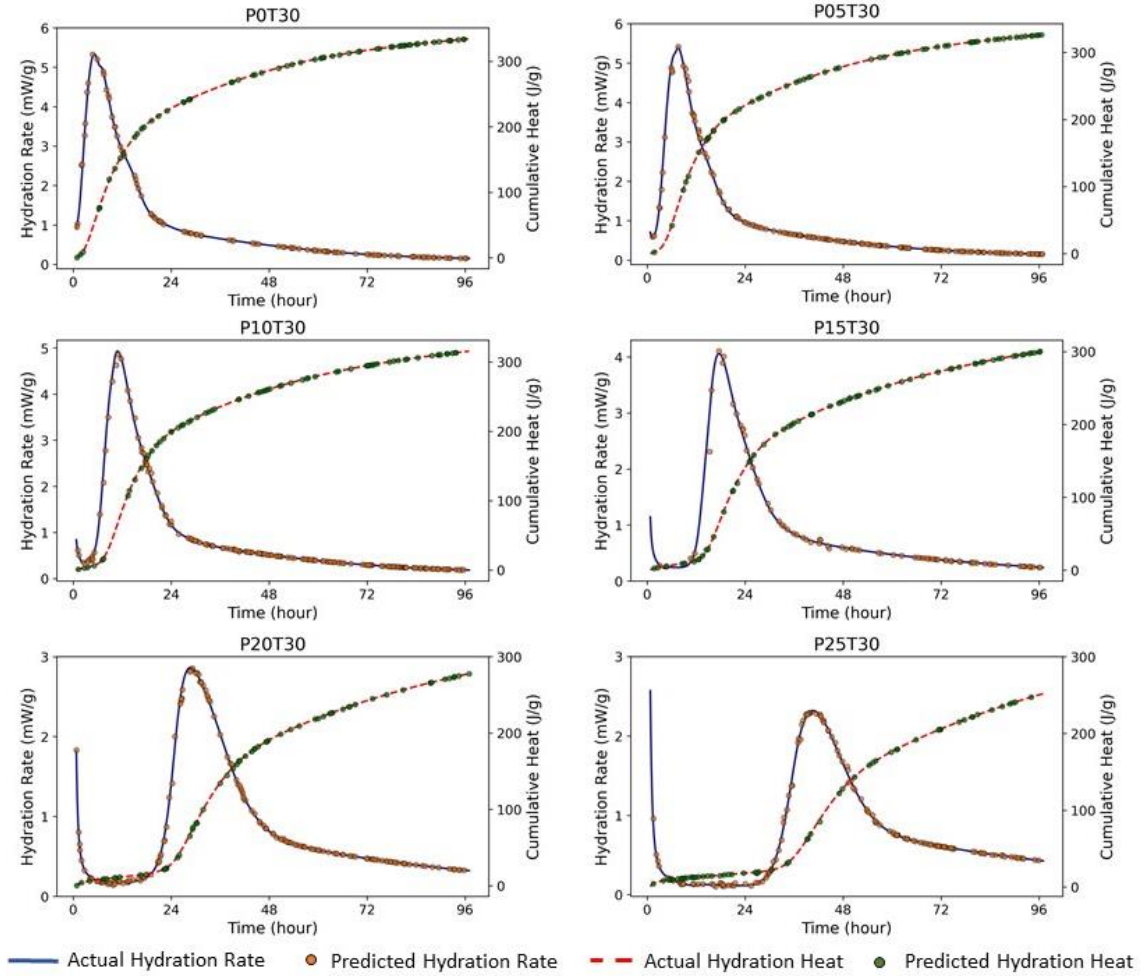


Figure A-3: Predictions of GBR1 for cement systems incorporating various levels of En28 at 30°C.

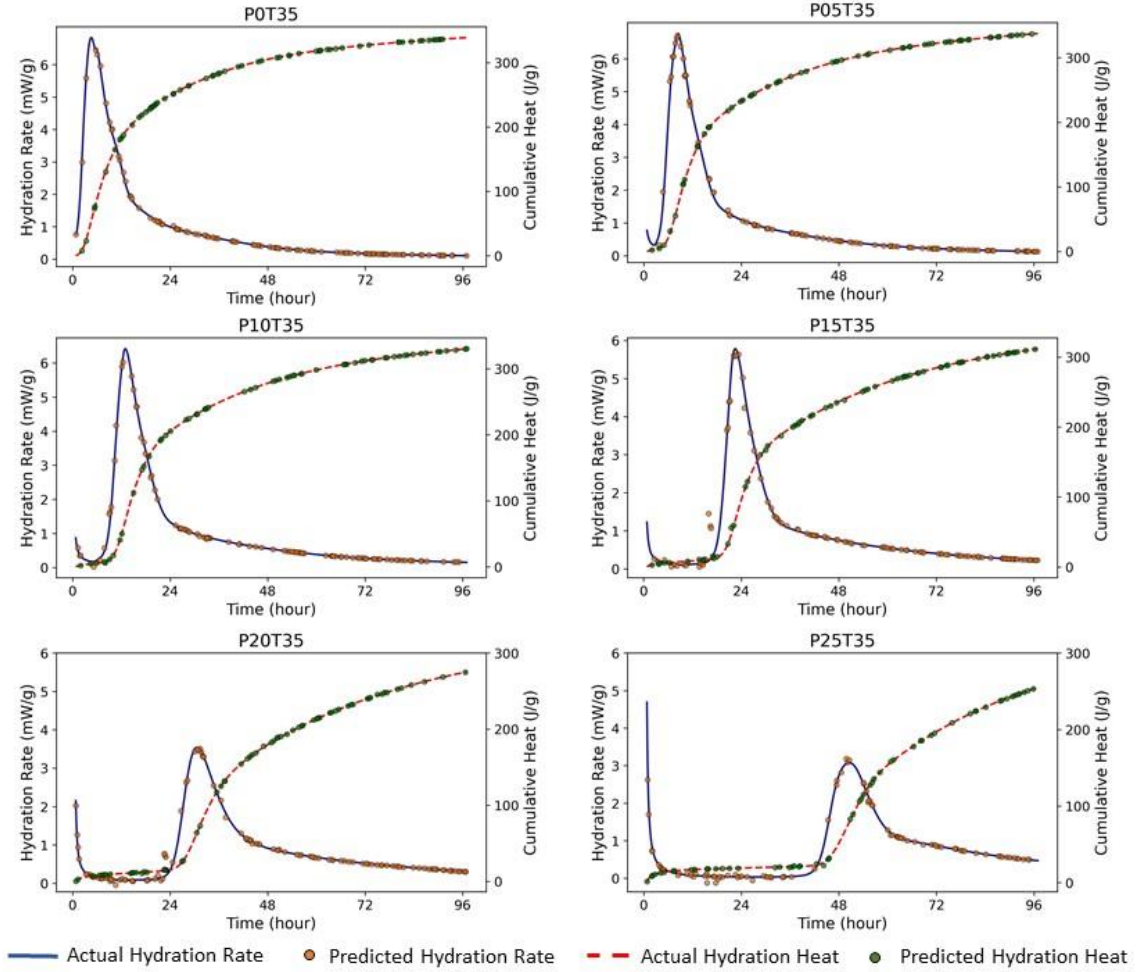


Figure A-4: Predictions of GBR1 for cement systems incorporating various levels of En28 at 35°C.

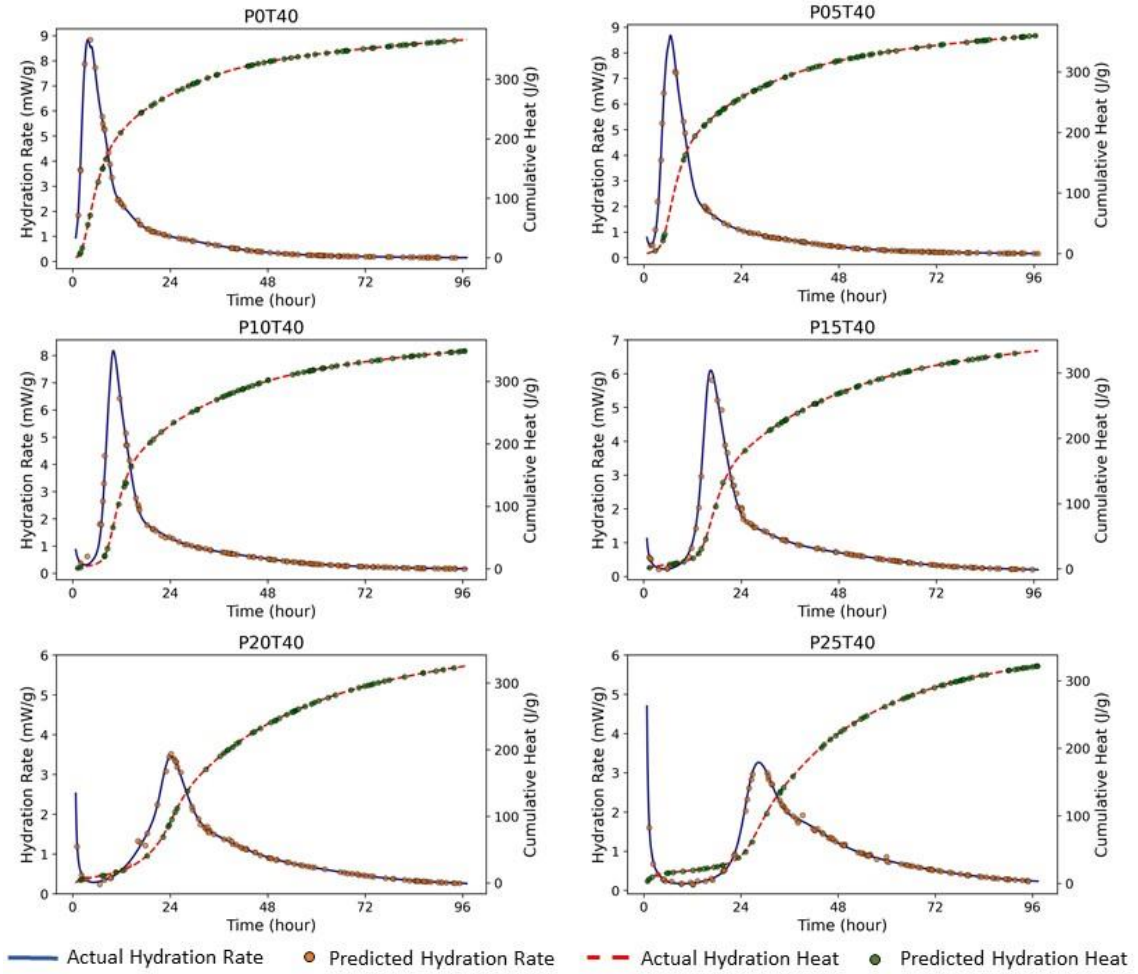


Figure A-5: Predictions of GBR1 for cement systems incorporating various levels of En28 at 40°C.

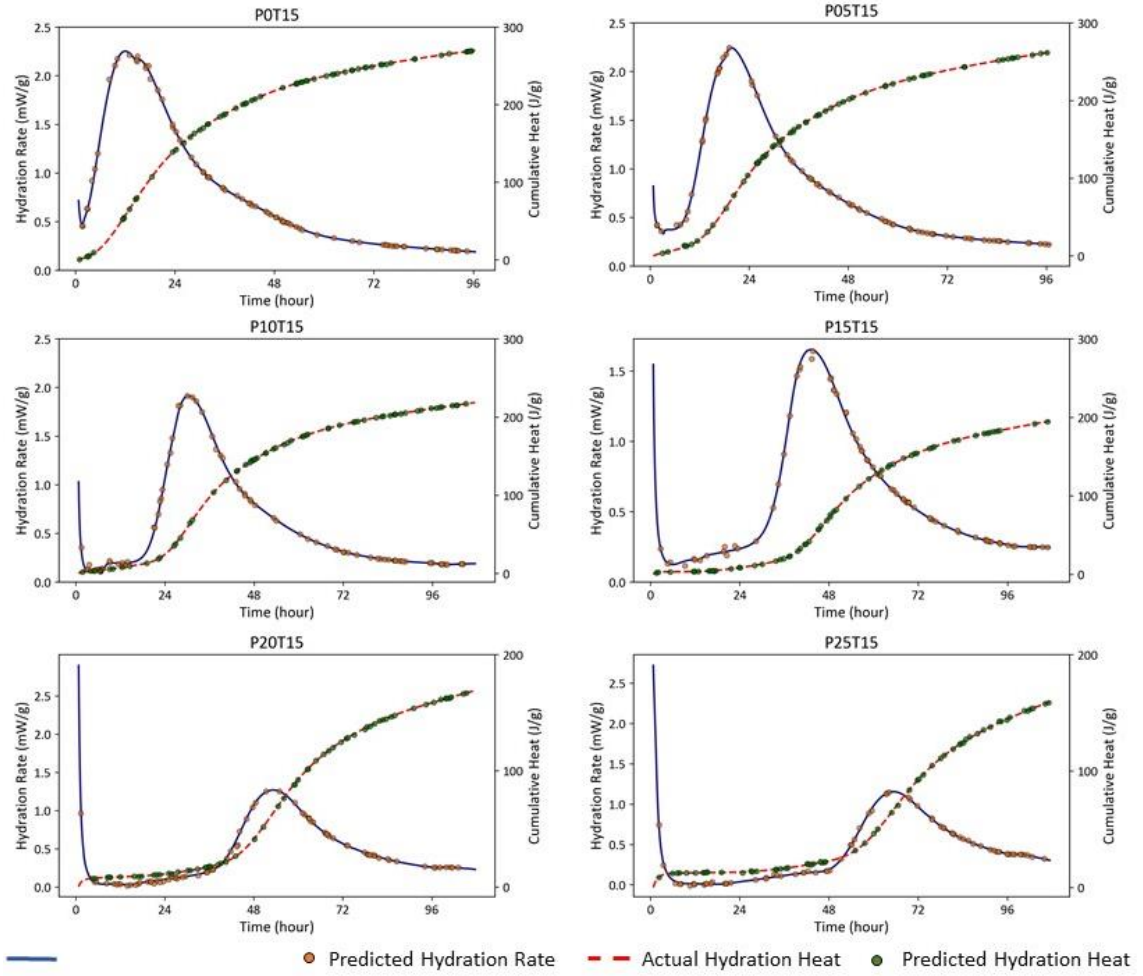


Figure A-6: Predictions of GBR1 for cement systems incorporating various levels of En35 at 15°C.

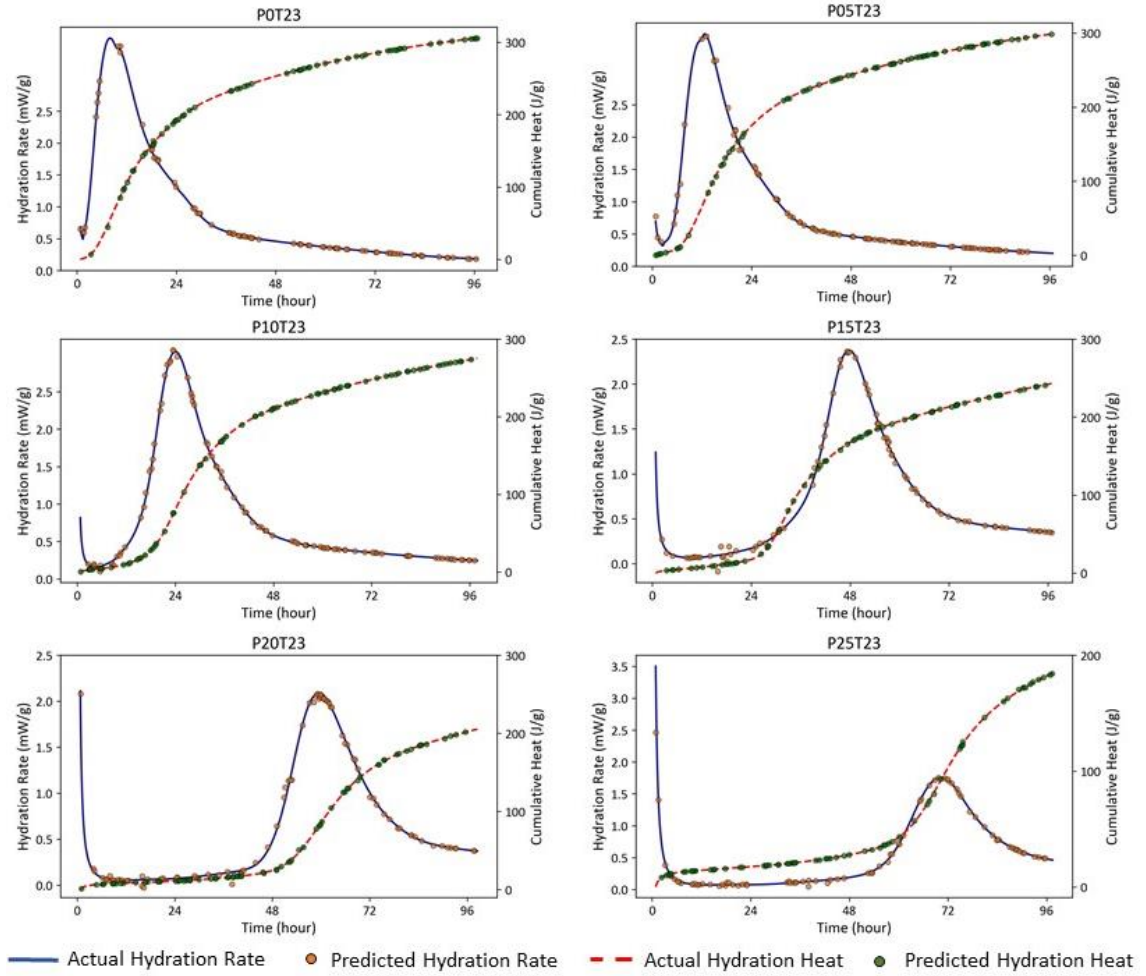


Figure A-7: Predictions of GBR1 for cement systems incorporating various levels of En35 at 23°C.

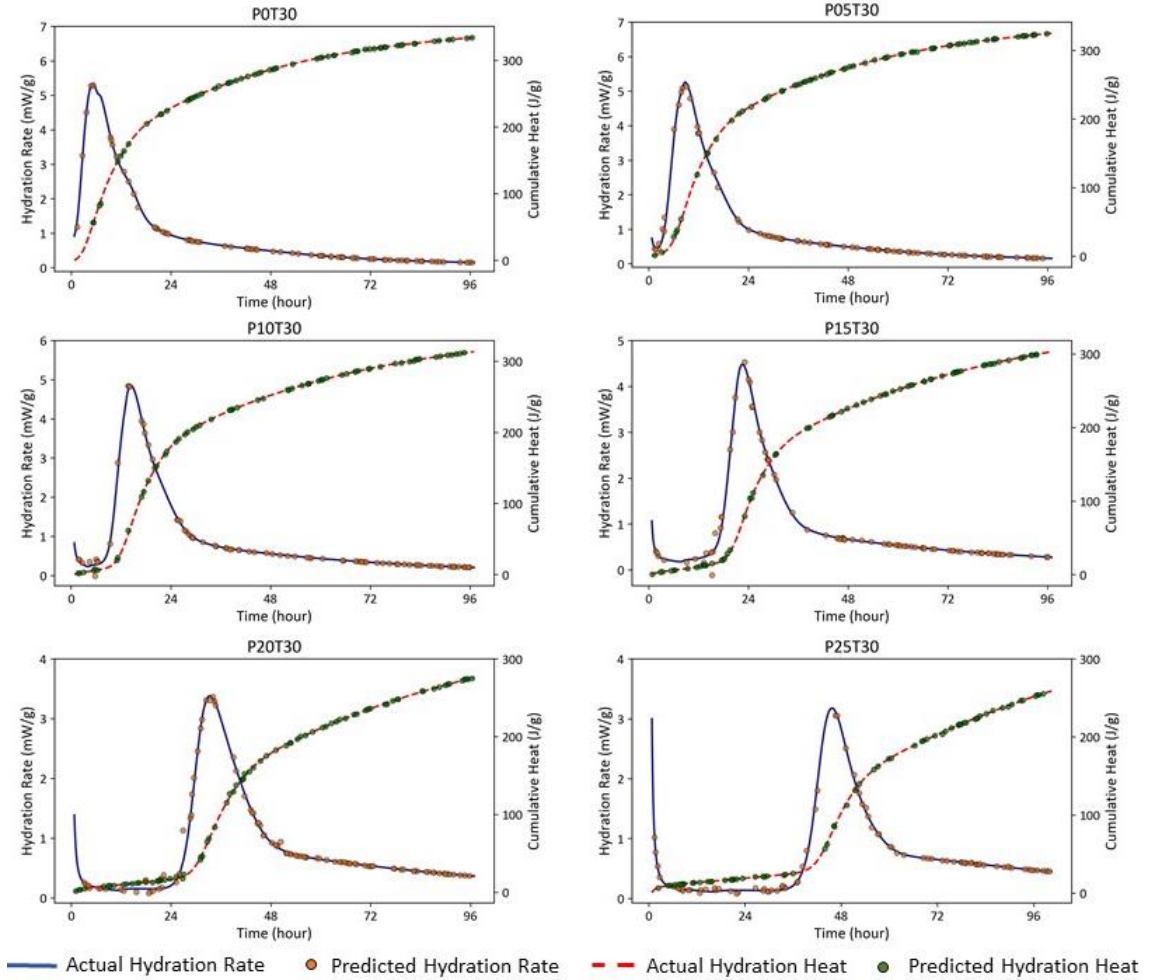


Figure A-8: Predictions of GBR1 for cement systems incorporating various levels of En35 at 30°C.

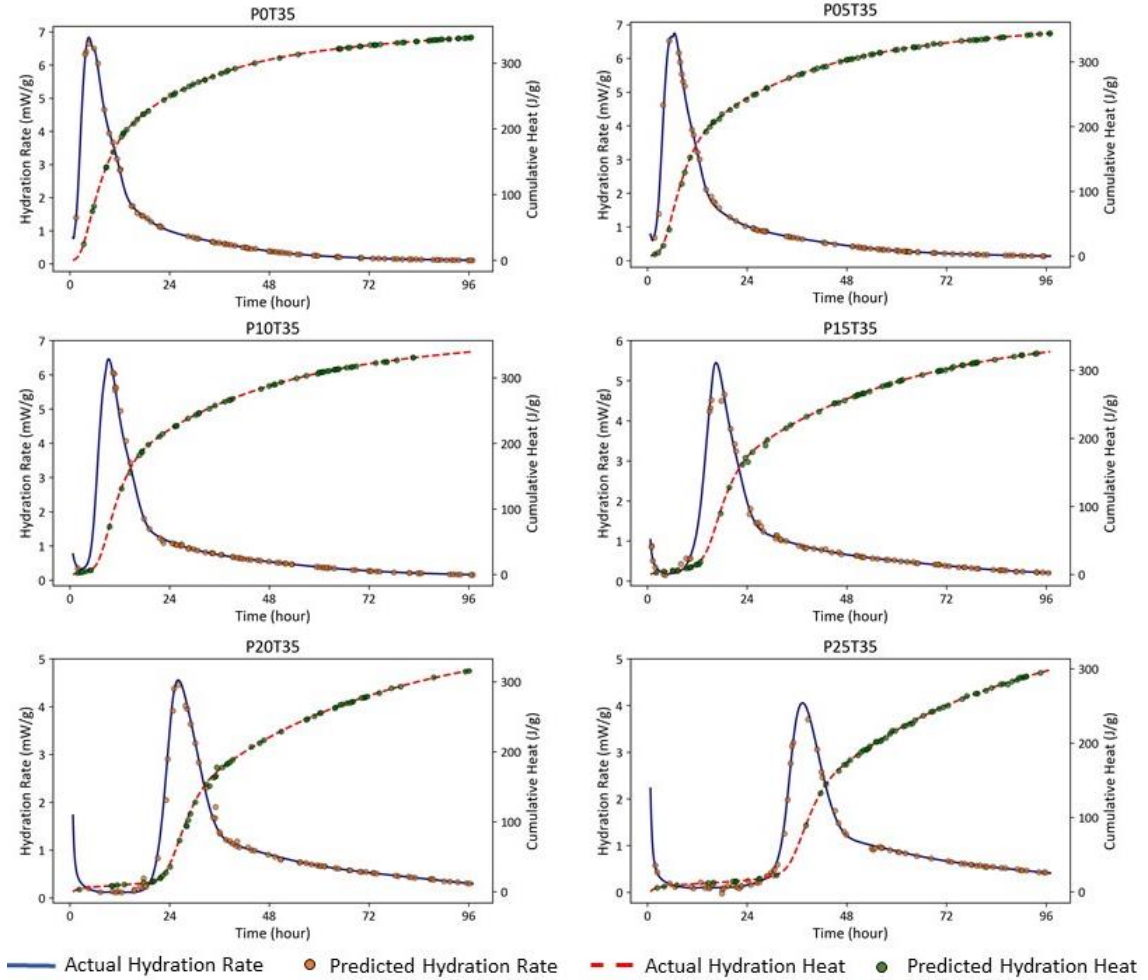


Figure A-9: Predictions of GBR1 for cement systems incorporating various levels of En35 at 35°C.

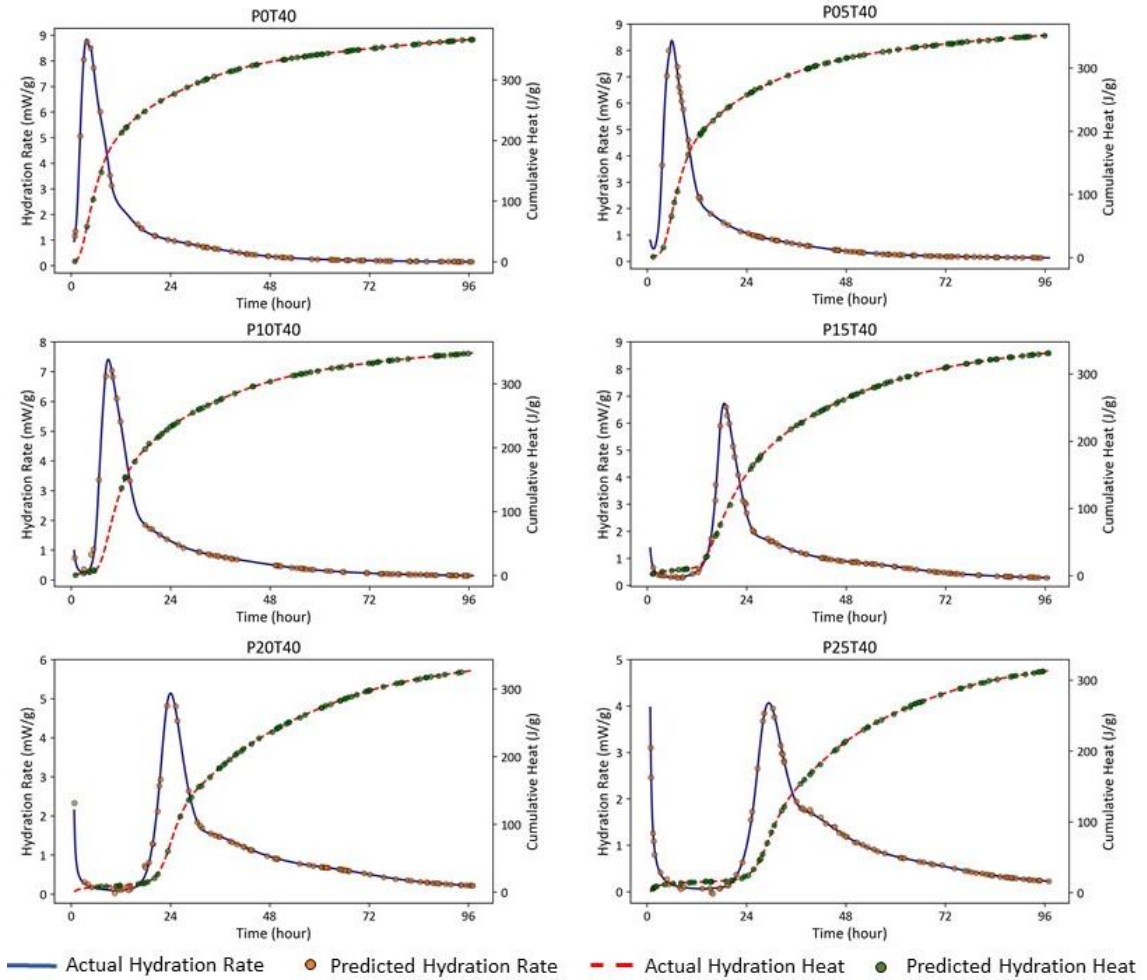


Figure A-10: Predictions of GBR1 for cement systems incorporating various levels of En35 at 40°C.

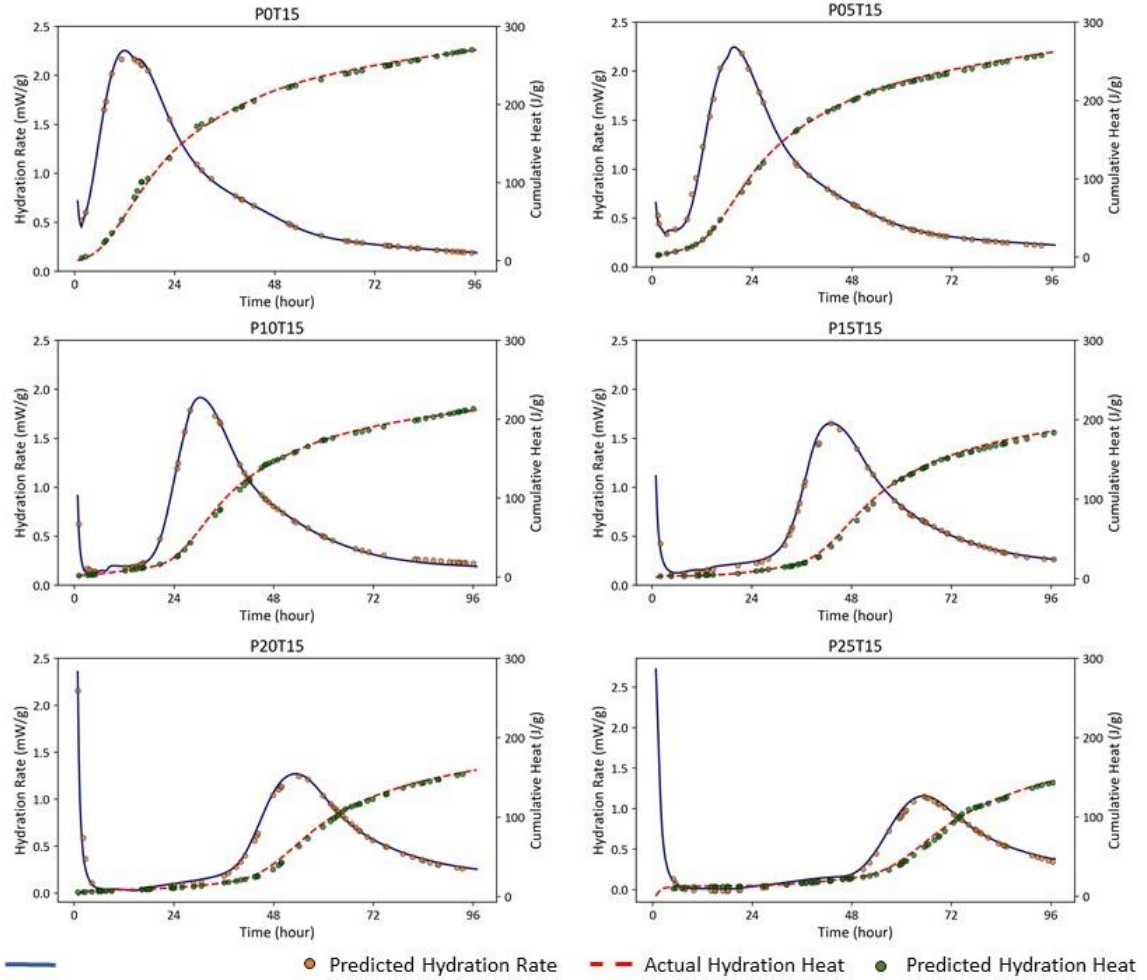


Figure A-11: Predictions of DNN1 for cement systems incorporating various levels of En28 at 15°C.

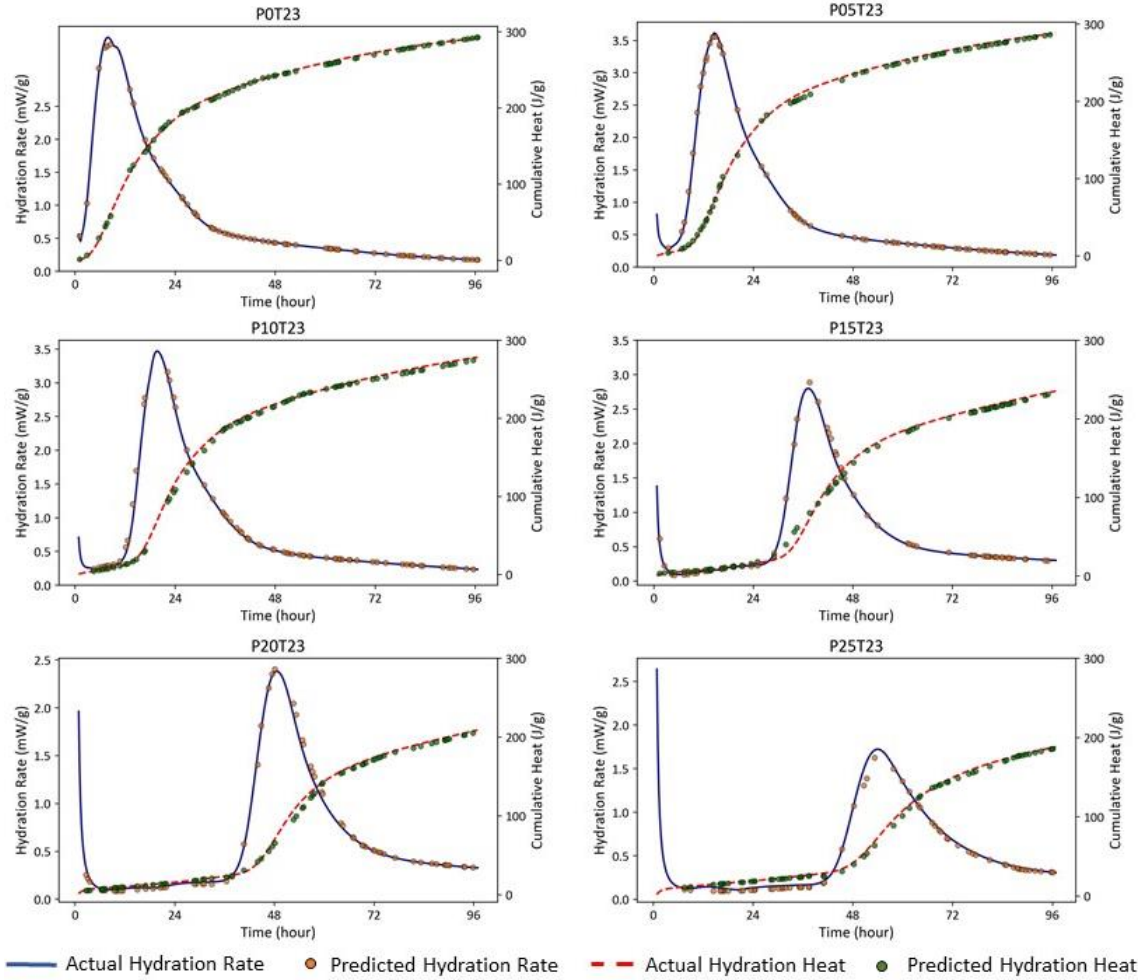


Figure A-12: Predictions of DNN1 for cement systems incorporating various levels of En28 at 23°C.

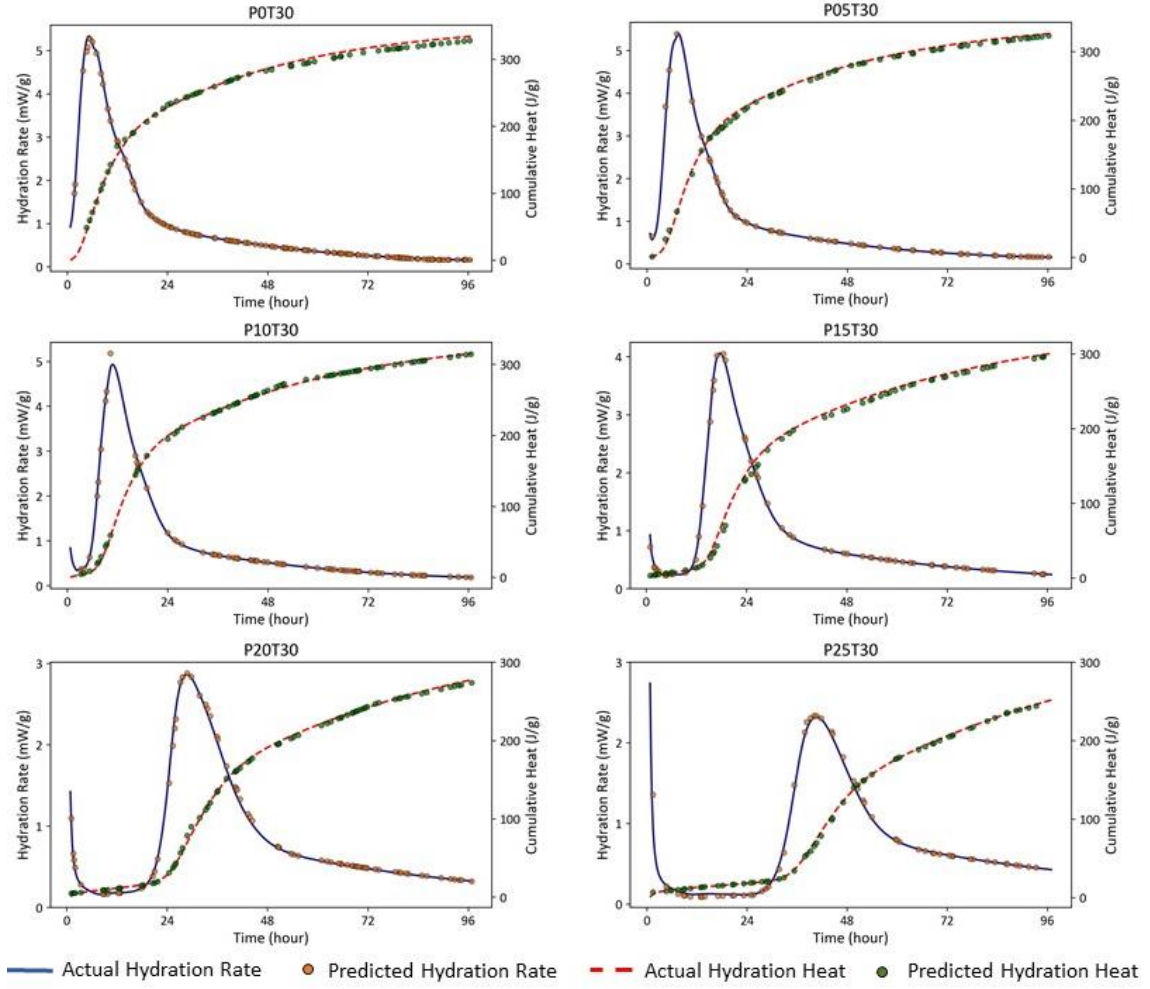


Figure A-13: Predictions of DNN1 for cement systems incorporating various levels of En28 at 30°C.

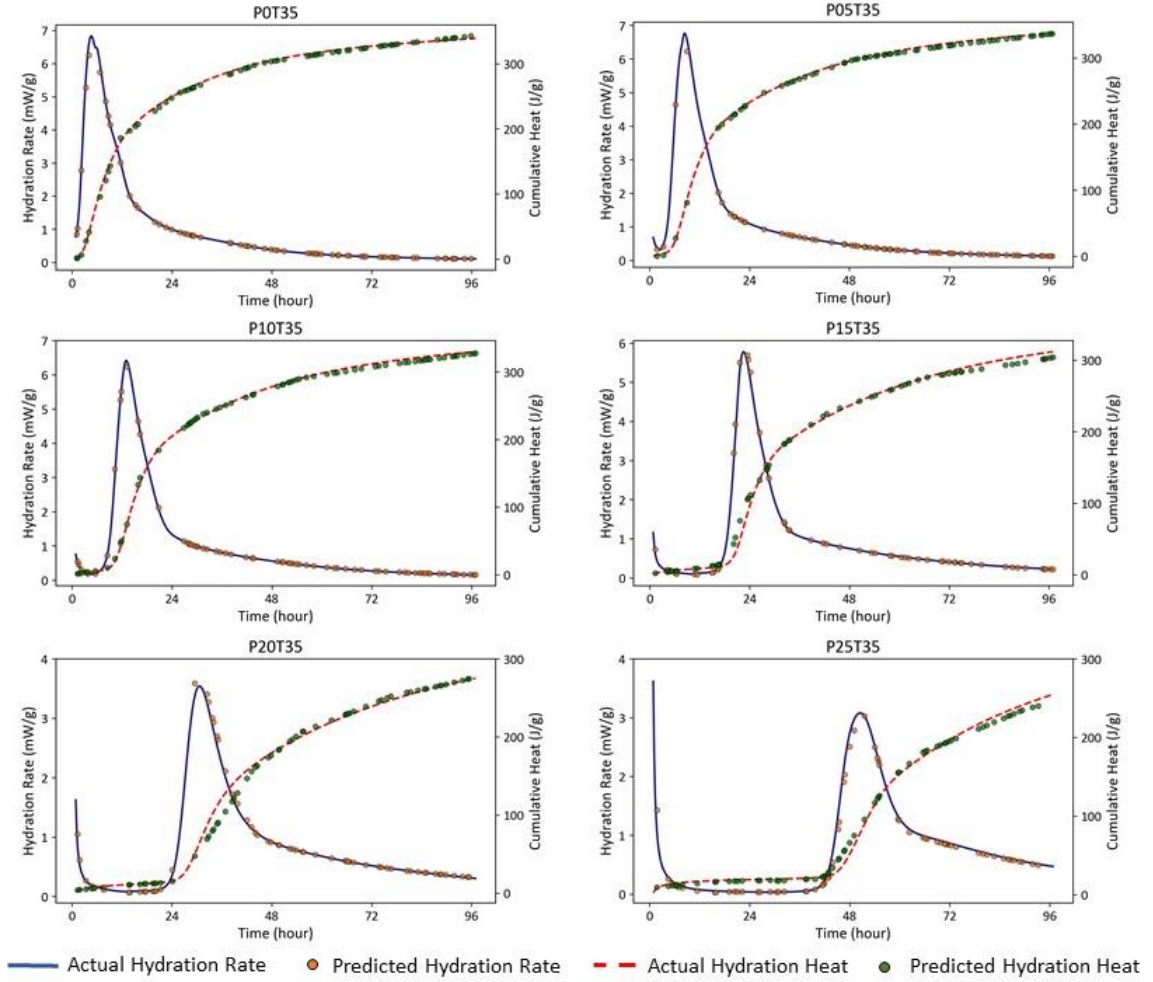


Figure A-14: Predictions of DNN1 for cement systems incorporating various levels of En28 at 35°C.

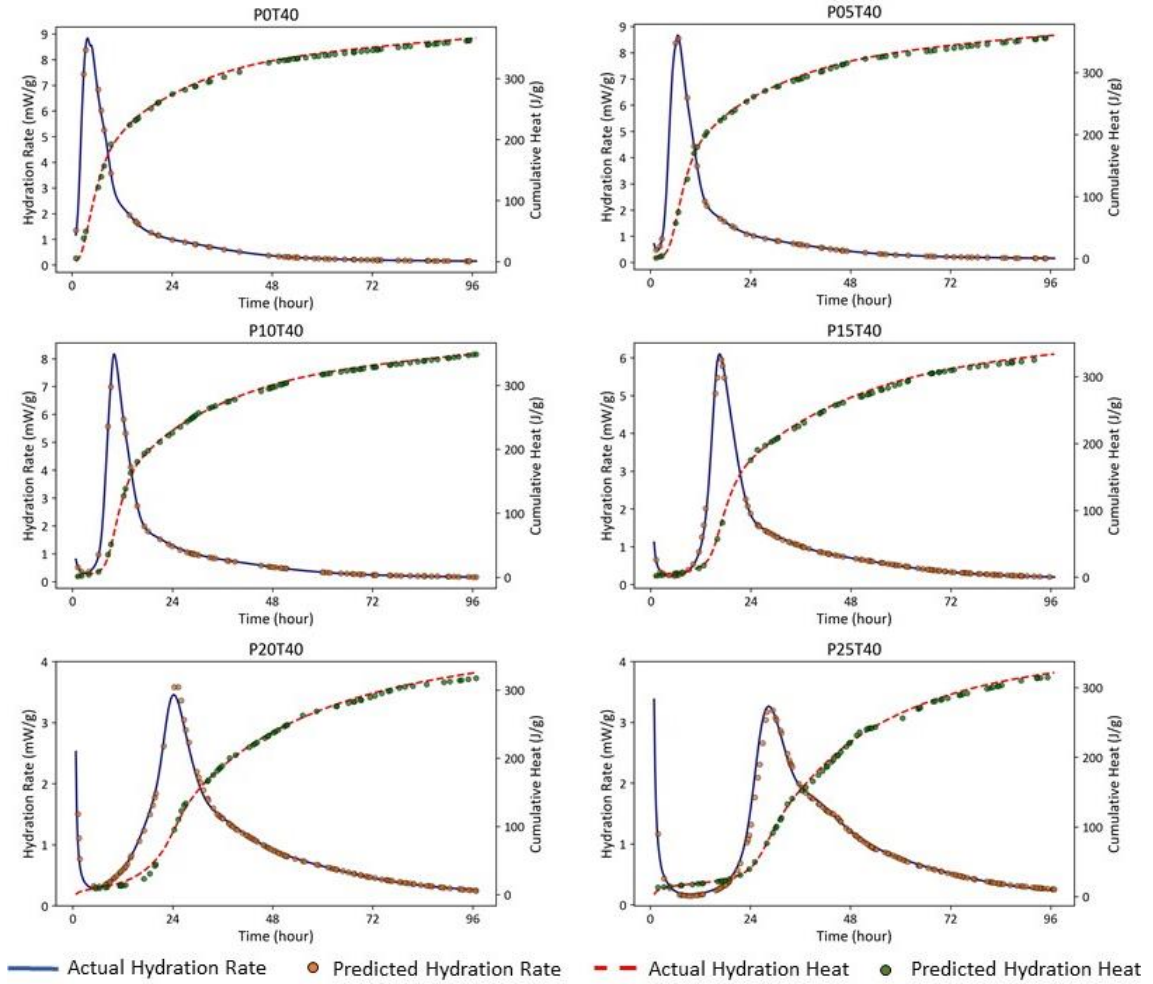


Figure A-15: Predictions of DNN1 for cement systems incorporating various levels of En28 at 40°C.

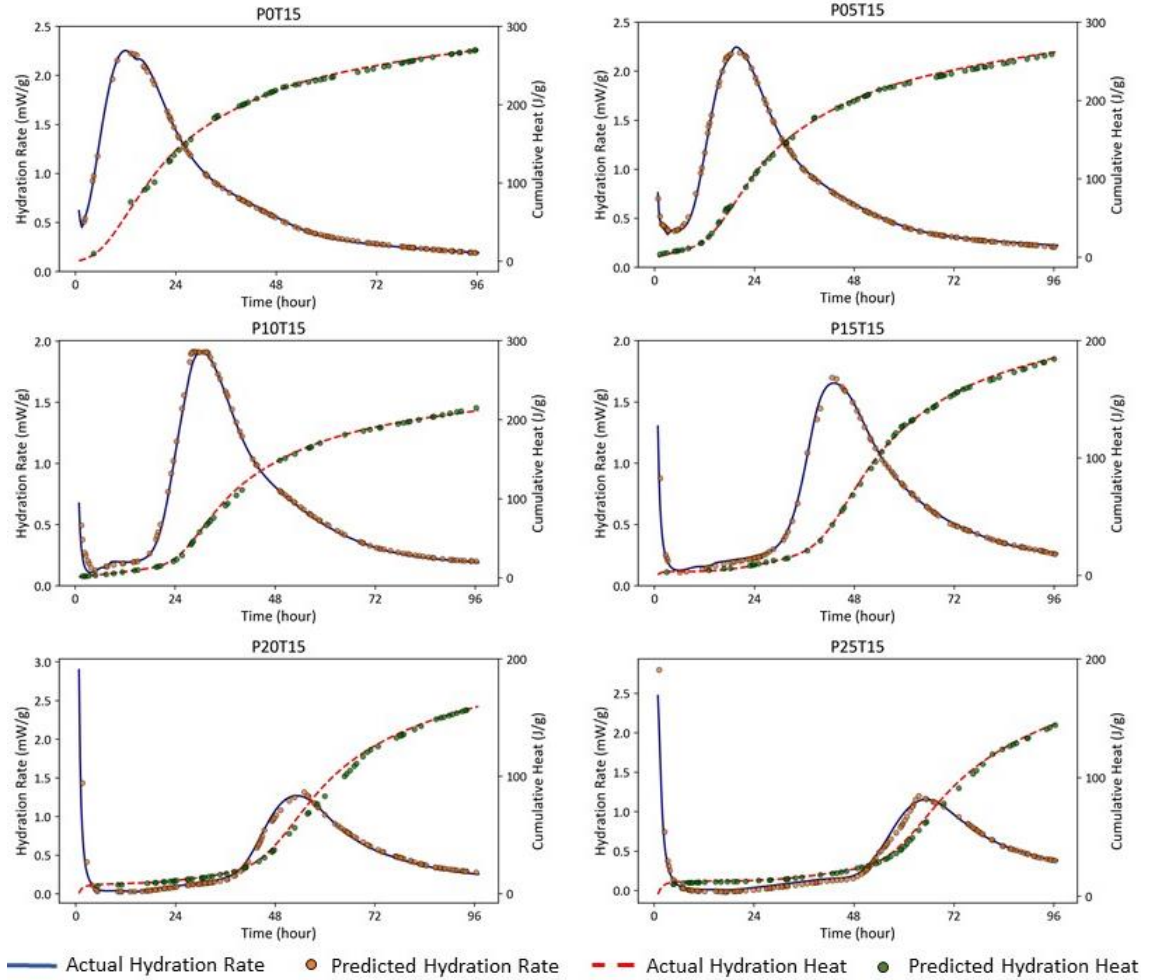


Figure A-16: Predictions of DNN1 for cement systems incorporating various levels of En35 at 15°C.

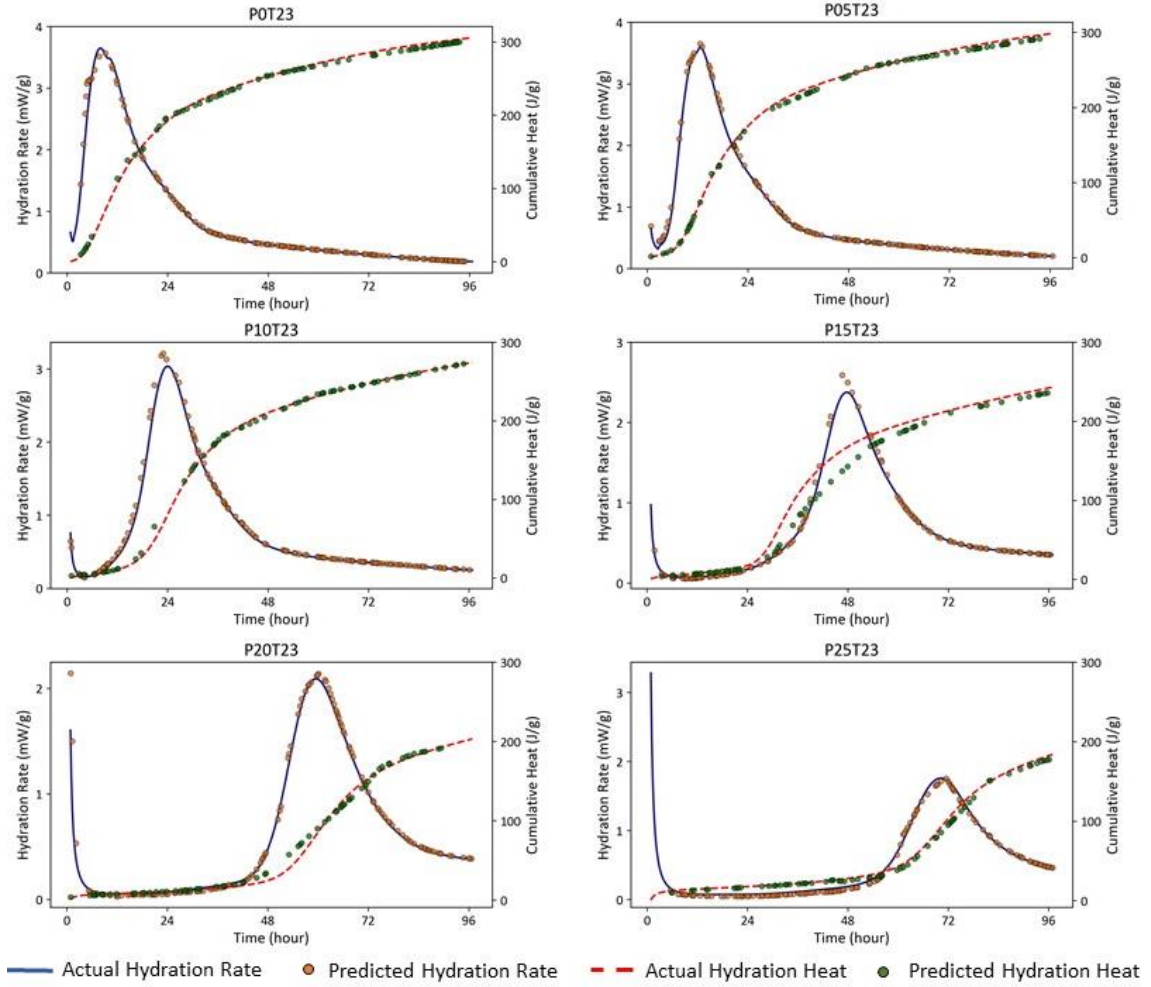


Figure A-17: Predictions of DNN1 for cement systems incorporating various levels of En35 at 23°C.

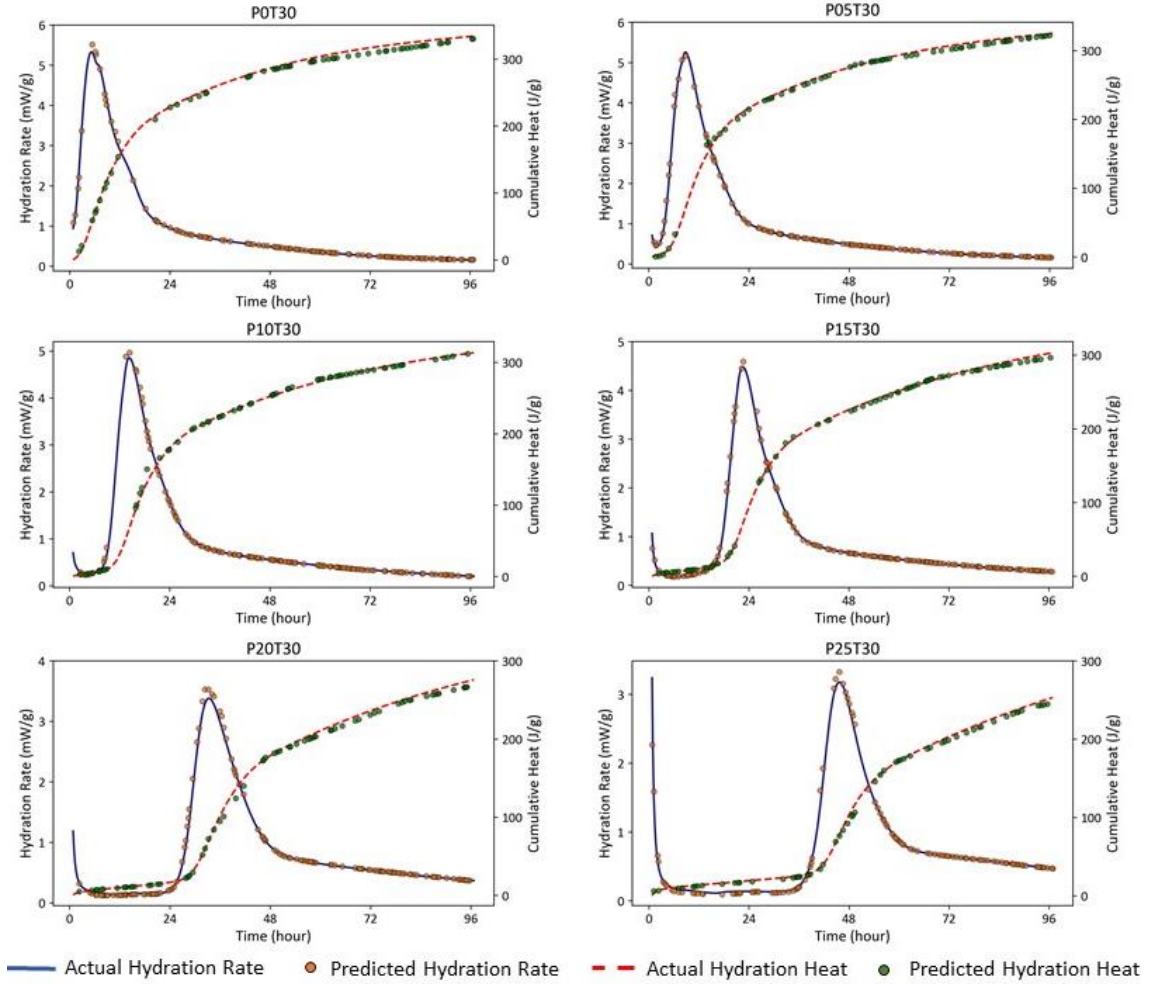


Figure A-18: Predictions of DNN1 for cement systems incorporating various levels of En35 at 30°C.

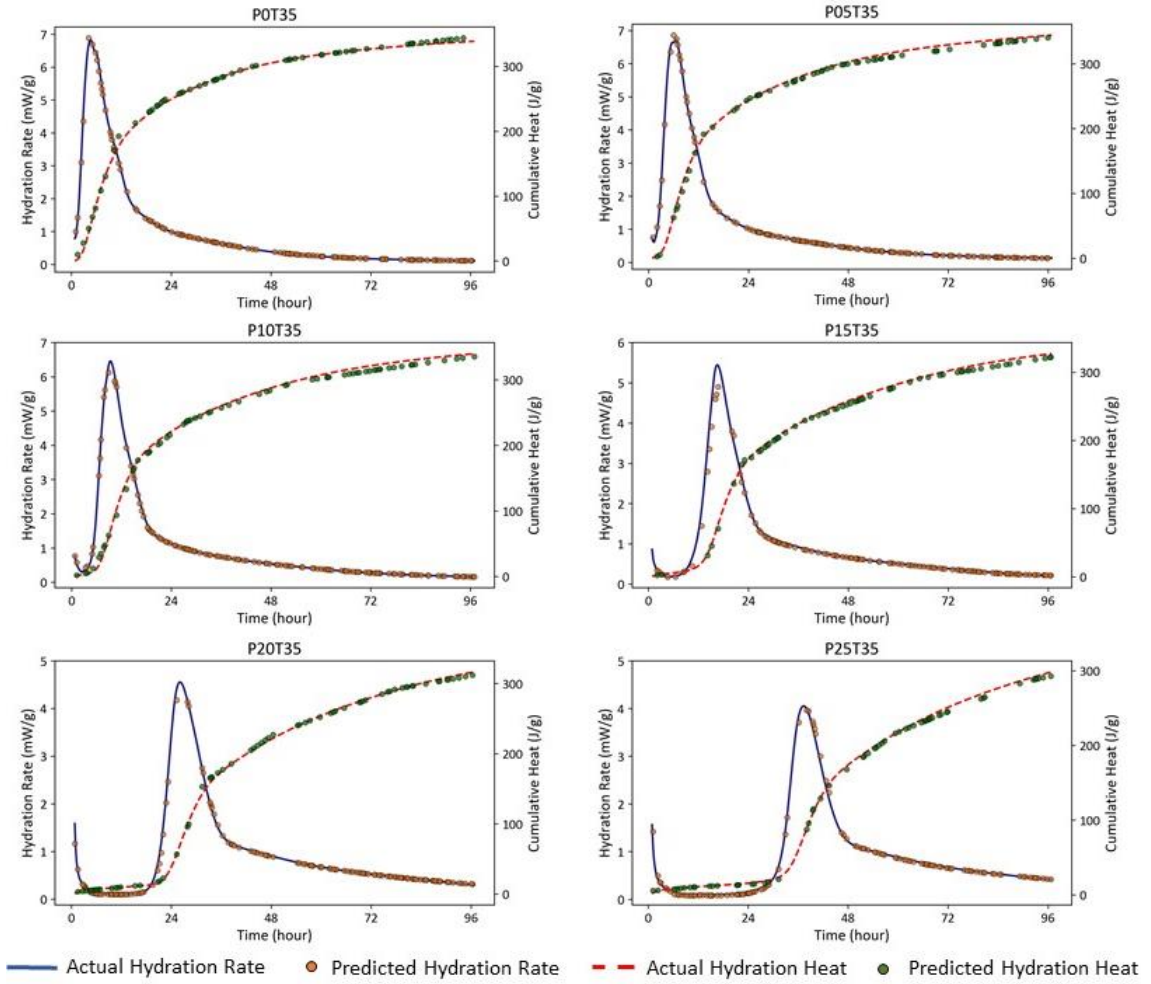


Figure A-19: Predictions of DNN1 for cement systems incorporating various levels of En35 at 35°C.

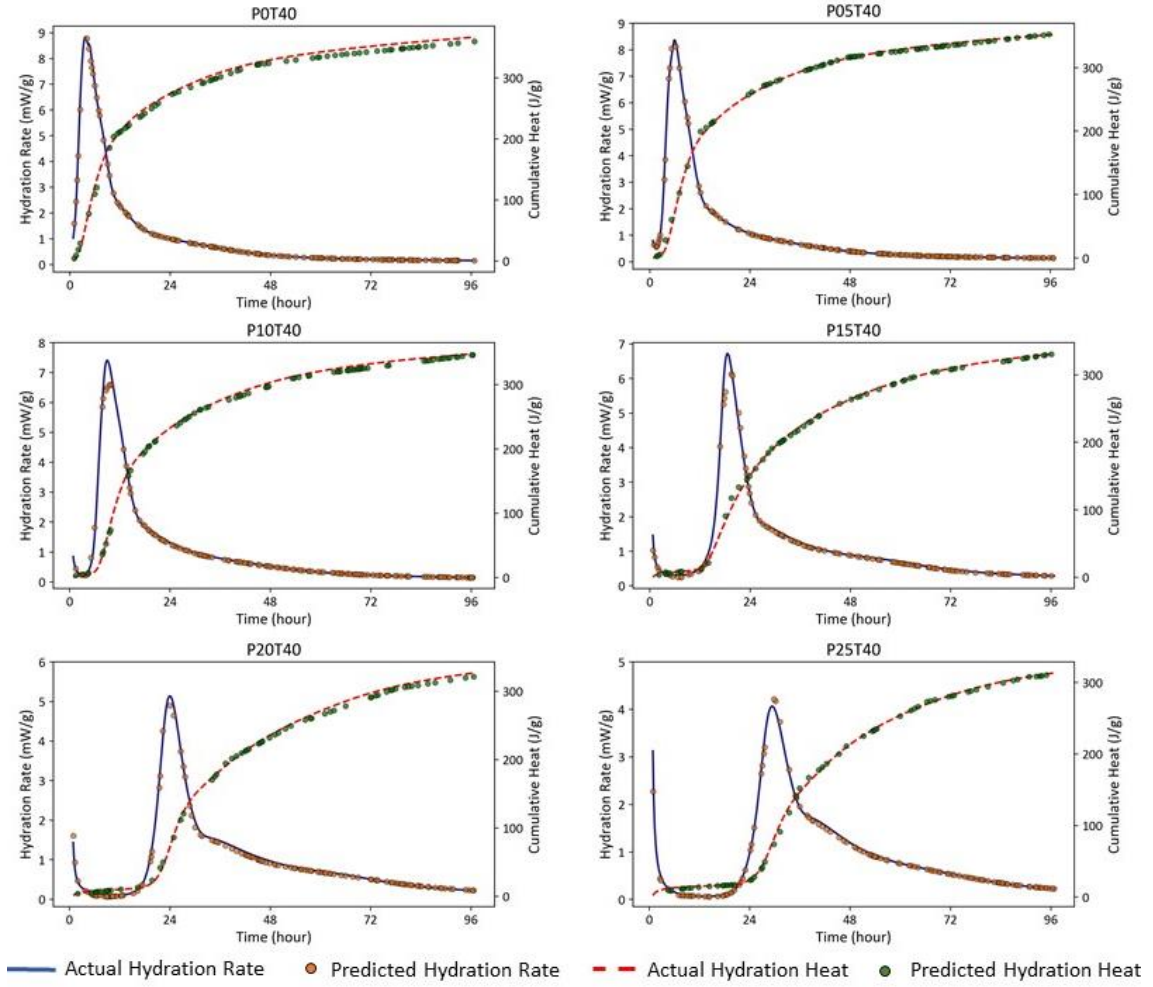


Figure A-20: Predictions of DNN1 for cement systems incorporating various levels of En35 at 40°C.

Appendix B

Table B-1: Collected data for developing machine learning models

No.	Tm	Lm	PCM	PCM_D	C_type	C	W	FA	CA	SP	Age	T	fc
2	28	98	18	900	2	434	192	1004	705	5.6	7	20	46
3	28	98	36	900	2	434	192	951	705	5.6	7	20	35
4	28	98	72	900	2	434	192	846	705	5.6	7	20	26
5	28	98	0	900	2	434	192	1057	705	5.6	7	40	53
6	28	98	18	900	2	434	192	1004	705	5.6	7	40	48
7	28	98	36	900	2	434	192	951	705	5.6	7	40	44
8	28	98	72	900	2	434	192	846	705	5.6	7	40	30
9	28	98	0	900	2	434	192	1057	705	5.6	28	20	61
10	28	98	18	900	2	434	192	1004	705	5.6	28	20	57
11	28	98	36	900	2	434	192	951	705	5.6	28	20	50
12	28	98	72	900	2	434	192	846	705	5.6	28	20	35
13	28	98	0	900	2	434	192	1057	705	5.6	28	40	73
14	28	98	18	900	2	434	192	1004	705	5.6	28	40	63
15	28	98	36	900	2	434	192	951	705	5.6	28	40	56
16	28	98	72	900	2	434	192	846	705	5.6	28	40	39
17	24	120	0	750	1	480	264	1575	0	0	3	23	32
18	24	120	106	750	1	480	264	1440	0	0	3	23	27
19	24	120	0	750	1	480	264	1575	0	0	7	23	38
20	24	120	106	750	1	480	264	1440	0	0	7	23	33
21	24	120	0	750	1	480	264	1575	0	0	28	23	51
22	24	120	106	750	1	480	264	1440	0	0	28	23	43
23	25	159	0	900	1	650	260	1119	0	0	1	23	23
24	25	159	6	900	1	667	266.8	1091	0	0	1	23	24
25	25	159	12	900	1	684	273.6	1060	0	0	1	23	28
26	25	159	19	900	1	702	280.8	1027	0	0	1	23	26
27	25	159	26	900	1	721	288.4	993	0	0	1	23	25
28	25	159	0	900	1	650	260	1119	0	0	3	23	34
29	25	159	6	900	1	667	266.8	1091	0	0	3	23	34
30	25	159	12	900	1	684	273.6	1060	0	0	3	23	38
31	25	159	19	900	1	702	280.8	1027	0	0	3	23	36
32	25	159	26	900	1	721	288.4	993	0	0	3	23	35
33	25	159	0	900	1	650	260	1119	0	0	7	23	38
34	25	159	6	900	1	667	266.8	1091	0	0	7	23	44
35	25	159	12	900	1	684	273.6	1060	0	0	7	23	44
36	25	159	19	900	1	702	280.8	1027	0	0	7	23	43
37	25	159	26	900	1	721	288.4	993	0	0	7	23	41
38	25	159	0	900	1	650	260	1119	0	0	28	23	48
39	25	159	6	900	1	667	266.8	1091	0	0	28	23	57

40	25	159	12	900	1	684	273.6	1060	0	0	28	23	60
41	25	159	19	900	1	702	280.8	1027	0	0	28	23	57
42	25	159	26	900	1	721	288.4	993	0	0	28	23	51
43	26	100	0	900	1	650	260	1119	0	0	1	23	23
44	26	100	6	900	1	667	266.8	1091	0	0	1	23	18
45	26	100	12	900	1	684	273.6	1060	0	0	1	23	18
46	26	100	19	900	1	702	280.8	1027	0	0	1	23	17
47	26	100	26	900	1	721	288.4	993	0	0	1	23	18
48	26	100	0	900	1	650	260	1119	0	0	3	23	35
49	26	100	6	900	1	667	266.8	1091	0	0	3	23	29
50	26	100	12	900	1	684	273.6	1060	0	0	3	23	28
51	26	100	19	900	1	702	280.8	1027	0	0	3	23	27
52	26	100	26	900	1	721	288.4	993	0	0	3	23	27
53	26	100	0	900	1	650	260	1119	0	0	7	23	40
54	26	100	6	900	1	667	266.8	1091	0	0	7	23	32
55	26	100	12	900	1	684	273.6	1060	0	0	7	23	33
56	26	100	19	900	1	702	280.8	1027	0	0	7	23	29
57	26	100	26	900	1	721	288.4	993	0	0	7	23	29
58	26	100	0	900	1	650	260	1119	0	0	28	23	48
59	26	100	6	900	1	667	266.8	1091	0	0	28	23	42
60	26	100	12	900	1	684	273.6	1060	0	0	28	23	39
61	26	100	19	900	1	702	280.8	1027	0	0	28	23	33
62	26	100	26	900	1	721	288.4	993	0	0	28	23	32
63	25	85	0	350	1	450	249.8	1238	0	0	7	23	35
64	25	85	5.1	350	1	450	249	1201	0	0	7	23	26
65	25	85	8.4	350	1	450	248.5	1176	0	1	7	23	24
66	25	85	16.9	350	1	450	247.3	1114	0	2	7	23	30
67	25	85	25.3	350	1	450	246	1052	0	2.8	7	23	27
68	25	85	33.8	350	1	450	244.8	990	0	2.5	7	23	29
69	25	85	59.1	350	1	450	241.1	805	0	2.5	7	23	20
70	25	85	96.2	350	1	450	235.6	532	0	2.5	7	23	19
71	25	85	0	350	1	450	249.8	1238	0	0	28	23	44
72	25	85	5.1	350	1	450	249	1201	0	0	28	23	32
73	25	85	8.4	350	1	450	248.5	1176	0	1	28	23	26
74	25	85	16.9	350	1	450	247.3	1114	0	2	28	23	37
75	25	85	25.3	350	1	450	246	1052	0	2.8	28	23	30
76	25	85	33.8	350	1	450	244.8	990	0	2.5	28	23	34
77	25	85	59.1	350	1	450	241.1	805	0	2.5	28	23	25
78	25	85	96.2	350	1	450	235.6	532	0	2.5	28	23	23
79	25	85	0	350	1	294.3	154.67	837	1008.8	4.0875	7	23	43
80	25	85	22.56	350	1	294.3	154.18	814	1008.8	4.905	7	23	28
81	25	85	67.7	350	1	294.3	153.36	769	1008.8	6.54	7	23	16
82	25	85	112.815	350	1	294.3	152.38	724	1008.8	11.445	7	23	13

83	25	85	0	350	1	294.3	154.67	837	1008.8	4.0875	28	23	57
84	25	85	22.56	350	1	294.3	154.18	814	1008.8	4.905	28	23	47
85	25	85	67.7	350	1	294.3	153.36	769	1008.8	6.54	28	23	22
86	25	85	112.815	350	1	294.3	152.38	724	1008.8	11.445	28	23	20
87	26	160	0	900	1	370	210	802	985	0	28	20	52
88	26	160	11.8	900	1	370	210	767	985	0	28	20	39
89	26	160	23	900	1	370	210	734	985	0	28	20	29
90	26	160	65.3	900	1	370	210	610	985	0	28	20	16
91	26	160	103.3	900	1	370	210	499	985	0	28	20	10
92	18	100	0	900	1	524	234	951	638	2.6	28	23	44
93	18	100	24	900	1	511	228	927	622	2.6	28	23	44
94	18	100	71	900	1	486	218	882	592	2.4	28	23	29
95	18	100	102	900	1	447	223	817	548	6.8	28	23	25
96	21	85	0	350	1	510	255	1530	0	0	28	20	61
97	21	85	5.1	350	1	507	254	1521	0	0	28	20	56
98	21	85	10.1	350	1	504	252	1513	0	0	28	20	53
99	21	85	15	350	1	501	251	1504	0	0	28	20	48
100	21	85	24.8	350	1	496	248	1488	0	0	28	20	48
101	21	85	48.3	350	1	483	241	1448	0	0	28	20	43
102	21	85	5.1	350	1	510	255	1515	0	0	28	20	54
103	21	85	10.2	350	1	510	255	1500	0	0	28	20	52
104	21	85	15.3	350	1	510	255	1485	0	0	28	20	50
105	21	85	25.5	350	1	510	255	1455	0	0	28	20	46
106	21	85	51	350	1	510	255	1380	0	0	28	20	42
107	16	184	5.1	800	1	507	254	1521	0	0	28	20	61
108	16	184	15	800	1	501	251	1504	0	0	28	20	52
109	16	184	24.8	800	1	496	248	1488	0	0	28	20	53
110	16	184	48.3	800	1	483	241	1448	0	0	28	20	47
111	20	113	5.1	800	1	507	254	1521	0	0	28	20	61
112	20	113	15	800	1	501	251	1504	0	0	28	20	54
113	20	113	24.8	800	1	496	248	1488	0	0	28	20	52
114	20	113	48.3	800	1	483	241	1448	0	0	28	20	47
115	25	185	5.1	800	1	507	254	1521	0	0	28	20	61
116	25	185	15	800	1	501	251	1504	0	0	28	20	52
117	25	185	24.8	800	1	496	248	1488	0	0	28	20	51
118	25	185	48.3	800	1	483	241	1448	0	0	28	20	47
119	28	175	0	900	1	390	285	1517	0	0	28	20	20
120	28	175	213	900	1	341	307	883	0	0	28	20	13
121	28	175	0	900	1	348	209	903	864	0	28	20	52
122	28	175	190	900	1	366	225	593	567	0	28	20	10
123	28	175	0	900	1	450	183	1673	0	13.5	28	20	61
124	28	175	263	900	1	450	213	900	0	13.5	28	20	16
125	28	175	199	900	1	450	194	1099	0	13.5	28	20	23

126	28	175	133	900	1	450	189	1300	0	13.5	28	20	30
127	28	175	0	900	1	439	188	1088	604	34.2	28	20	54
128	28	175	234	900	1	439	214	386	604	13.2	28	20	8
129	28	175	117	900	1	439	201	737	604	23.7	28	20	21
130	28	175	78	900	1	439	196	854	604	27.2	28	20	31
131	25	100	0	915	1	450	203.2	965	706.7	3.1	28	23	74
132	25	100	23.3	915	1	450	207.4	893	706.7	3.1	28	23	52
133	25	100	70	915	1	450	211.5	795	706.7	2.4	28	23	35
134	25	100	113.7	915	1	450	248.4	795	706.7	2.9	28	23	21
135	29	185	0	900	1	350	200	630	1160	0	7	25	18
136	29	185	10.66	900	1	350	200	599	1160	0	7	25	15
137	29	185	21.32	900	1	350	200	567	1160	0	7	25	15
138	29	185	31.97	900	1	350	200	536	1160	0	7	25	17
139	29	185	42.63	900	1	350	200	504	1160	0	7	25	15
140	29	185	0	900	1	350	200	630	1160	0	28	25	21
141	29	185	10.66	900	1	350	200	599	1160	0	28	25	19
142	29	185	21.32	900	1	350	200	567	1160	0	28	25	18
143	29	185	31.97	900	1	350	200	536	1160	0	28	25	18
144	29	185	42.63	900	1	350	200	504	1160	0	28	25	16
145	29	185	0	900	1	350	200	630	1160	0	7	25	18
146	29	185	10.66	900	1	350	200	630	1160	0	7	25	13
147	29	185	21.32	900	1	350	200	630	1160	0	7	25	11
148	29	185	31.97	900	1	350	200	630	1160	0	7	25	12
149	29	185	42.63	900	1	350	200	630	1160	0	7	25	10
150	29	185	0	900	1	350	200	630	1160	0	28	25	21
151	29	185	10.66	900	1	350	200	630	1160	0	28	25	16
152	29	185	21.32	900	1	350	200	630	1160	0	28	25	13
153	29	185	31.97	900	1	350	200	630	1160	0	28	25	13
154	29	185	42.63	900	1	350	200	630	1160	0	28	25	13
155	28	98	0	900	2	471.1	235.6	957	705	4.8	1	20	32
156	28	98	0	900	2	471.1	235.6	957	705	4.8	7	20	46
157	28	98	0	900	2	471.1	235.6	957	705	4.8	14	20	49
158	28	98	0	900	2	471.1	235.6	957	705	4.8	28	20	54
159	28	98	64.3	900	2	471.1	235.6	766	705	4.8	1	20	17
160	28	98	64.3	900	2	471.1	235.6	766	705	4.8	7	20	24
161	28	98	64.3	900	2	471.1	235.6	766	705	4.8	14	20	27
162	28	98	64.3	900	2	471.1	235.6	766	705	4.8	28	20	30
163	24	96	64.3	900	2	471.1	235.6	766	705	4.8	1	20	15
164	24	96	64.3	900	2	471.1	235.6	766	705	4.8	7	20	24
165	24	96	64.3	900	2	471.1	235.6	766	705	4.8	14	20	27
166	24	96	64.3	900	2	471.1	235.6	766	705	4.8	28	20	30
167	28	98	0	900	2	471.1	235.6	957	705	4.8	1	40	37
168	28	98	0	900	2	471.1	235.6	957	705	4.8	7	40	53

169	28	98	0	900	2	471.1	235.6	957	705	4.8	14	40	66
170	28	98	0	900	2	471.1	235.6	957	705	4.8	28	40	72
171	28	98	64.3	900	2	471.1	235.6	766	705	4.8	1	40	17
172	28	98	64.3	900	2	471.1	235.6	766	705	4.8	7	40	26
173	28	98	64.3	900	2	471.1	235.6	766	705	4.8	14	40	32
174	28	98	64.3	900	2	471.1	235.6	766	705	4.8	28	40	35
175	24	96	64.3	900	2	471.1	235.6	766	705	4.8	1	40	21
176	24	96	64.3	900	2	471.1	235.6	766	705	4.8	7	40	31
177	24	96	64.3	900	2	471.1	235.6	766	705	4.8	14	40	36
178	24	96	64.3	900	2	471.1	235.6	766	705	4.8	28	40	43
179	28	102	0	694	1	536	214	750	857	1.6	7	23	42
180	28	102	69	694	1	467	214	653	747	5.4	7	23	26
181	28	102	139	694	1	398	214	557	636	9.4	7	23	17
182	28	102	208	694	1	329	214	460	526	18.8	7	23	10
183	28	102	69	694	1	536	214	485	857	8	7	23	33
184	28	102	139	694	1	536	214	220	857	13.4	7	23	18
185	28	102	0	694	1	536	214	750	857	1.6	7	40	41
186	28	102	69	694	1	467	214	653	747	5.4	7	40	20
187	28	102	139	694	1	398	214	557	636	9.4	7	40	13
188	28	102	208	694	1	329	214	460	526	18.8	7	40	8
189	28	102	69	694	1	536	214	485	857	8	7	40	32
190	28	102	139	694	1	536	214	220	857	13.4	7	40	18
191	28	102	0	694	1	536	214	750	857	1.6	28	23	45
192	28	102	69	694	1	467	214	653	747	5.4	28	23	29
193	28	102	139	694	1	398	214	557	636	9.4	28	23	19
194	28	102	208	694	1	329	214	460	526	18.8	28	23	12
195	28	102	69	694	1	536	214	485	857	8	28	23	35
196	28	102	139	694	1	536	214	220	857	13.4	28	23	18
197	28	102	0	694	1	536	214	750	857	1.6	28	40	45
198	28	102	69	694	1	467	214	653	747	5.4	28	40	20
199	28	102	139	694	1	398	214	557	636	9.4	28	40	13
200	28	102	208	694	1	329	214	460	526	18.8	28	40	8
201	28	102	69	694	1	536	214	485	857	8	28	40	33
202	28	102	139	694	1	536	214	220	857	13.4	28	40	21
203	25	160	0	900	1	582	282.3	1535	0	0	28	20	70
204	25	160	99	900	1	545	317	1438	0	0	28	20	46
205	25	160	186.5	900	1	513	348	1352	0	0	28	20	29
206	25	160	263	900	1	483	377.5	1273	0	0	28	20	21
207	23	148	0	800	2	500	275	1419	0	15	28	23	29
208	23	148	184.9	800	2	500	255	925	0	15	28	23	18
209	23	148	257.7	800	2	500	280	644	0	15	28	23	12
210	23	148	292.9	800	2	500	300	488	0	15	28	23	11
211	23	148	0	800	1	500	255	1471	0	15	28	23	44

212	23	148	184.9	800	1	500	255	925	0	15	28	23	19
213	23	148	252.9	800	1	500	290	632	0	15	28	23	16
214	23	148	290.2	800	1	500	305	484	0	15	28	23	14
215	22	200	0	700	2	500	325	1279	0	15	28	10	20
216	22	200	32.2	700	2	500	275	1290	0	15	28	10	18
217	22	200	62.2	700	2	500	250	1244	0	15	28	10	18
218	22	200	90.3	700	2	500	225	1204	0	15	28	10	19
219	22	200	0	700	2	500	325	1279	0	15	28	25	19
220	22	200	32.2	700	2	500	275	1290	0	15	28	25	17
221	22	200	62.2	700	2	500	250	1244	0	15	28	25	18
222	22	200	90.3	700	2	500	225	1204	0	15	28	25	19
223	22	200	0	700	2	500	325	1279	0	15	28	40	21
224	22	200	32.2	700	2	500	275	1290	0	15	28	40	19
225	22	200	62.2	700	2	500	250	1244	0	15	28	40	19
226	22	200	90.3	700	2	500	225	1204	0	15	28	40	19
227	23	55	0	980	1	575	172.5	912	711	5	7	23	50
228	23	55	13.5	980	1	572	171.5	907	707	5	7	23	48
229	23	55	26.15	980	1	558	172.5	885	690	5.8	7	23	44
230	23	55	38.2	980	1	543	179.5	860	670	6.95	7	23	36
231	23	55	50.5	980	1	484	191	888	690	5.8	7	23	32
232	23	55	62.5	980	1	255	160.5	876	752	6	7	23	12
233	23	55	0	980	1	575	172.5	912	711	5	28	23	55
234	23	55	13.5	980	1	572	171.5	907	707	5	28	23	51
235	23	55	26.15	980	1	558	172.5	885	690	5.8	28	23	49
236	23	55	38.2	980	1	543	179.5	860	670	6.95	28	23	43
237	23	55	50.5	980	1	484	191	888	690	5.8	28	23	39
238	23	55	62.5	980	1	255	160.5	876	752	6	28	23	20
239	23	55	0	980	1	575	172.5	912	711	5	60	23	60
240	23	55	13.5	980	1	572	171.5	907	707	5	60	23	55
241	23	55	26.15	980	1	558	172.5	885	690	5.8	60	23	51
242	23	55	38.2	980	1	543	179.5	860	670	6.95	60	23	49
243	23	55	50.5	980	1	484	191	888	690	5.8	60	23	42
244	23	55	62.5	980	1	255	160.5	876	752	6	60	23	20

Curriculum Vitae

Name:	Afshin Marani
Post-secondary Education and Degrees:	<p>Isfahan University of Technology (IUT) Isfahan, Iran 2009-2014 B.Sc.</p> <p>Isfahan University of Technology (IUT) Isfahan, Iran 2014-2017 M.Sc.</p> <p>The University of Western Ontario London, Ontario, Canada 2018-2022 Ph.D.</p>
Honours and Awards:	<p>Mitacs Elevate Thematic Postdoctoral Fellowship 2022-2023, 2023-2024</p> <p>Bartlett Graduate Scholarship in Structural Engineering 2021</p> <p>Flight 752 Memorial Graduate Scholarship in Engineering and Science 2011</p> <p>Graduate Fellowship Western University Doctoral Fellowship 2018-2022</p> <p>Western Graduate Research Scholarship (WGRS) Doctoral Fellowship 2018-2022</p>
Related Work Experience	<p>Teaching Assistant The University of Western Ontario 2019-2022</p> <p>Teaching Assistant Isfahan University of Technology (IUT) 2014-2017</p>

Journal Publications:

- [14] **Marani, A.**, & Nehdi, M. L. (2022). Predicting shear strength of FRP-reinforced concrete beams using novel synthetic data driven deep learning. *Engineering Structures*, 257, 114083.
- [13] Zhang, L. V., Suleiman, A. R., Allaf, M. M., **Marani, A.**, Tuyan, M., & Nehdi, M. L. (2022). Crack self-healing in alkali-activated slag composites incorporating immobilized bacteria. *Construction and Building Materials*, 326, 126842.
- [12] Tanyildizi, H., **Marani, A.**, Türk, K., & Nehdi, M. L. (2022). Hybrid deep learning model for concrete incorporating microencapsulated phase change materials. *Construction and Building Materials*, 319, 126146.
- [11] Zhang, L. V., **Marani, A.**, & Nehdi, M. L. (2022). Chemistry-informed machine learning prediction of compressive strength for alkali-activated materials. *Construction and Building Materials*, 316, 126103.
- [10] Zhang, L. V., Nehdi, M. L., Suleiman, A. R., Allaf, M. M., Gan, M., **Marani, A.**, & Tuyan, M. (2021). Crack self-healing in bio-green concrete. *Composites Part B: Engineering*, 227, 109397.
- [9] Nunez, I., **Marani, A.**, Flah, M., & Nehdi, M. L. (2021). Estimating compressive strength of modern concrete mixtures using computational intelligence: A systematic review. *Construction and Building Materials*, 310, 125279.
- [8] Wong, L. S., **Marani, A.**, & Nehdi, M. L. (2021). Gradient Boosting Coupled with Oversampling Model for Prediction of Concrete Pipe-Joint Infiltration Using Designwise Data Set. *Journal of Pipeline Systems Engineering and Practice*, 12(3), 04021015.
- [7] **Marani, A.**, & Madhkhan, M. (2021). Thermal performance of concrete sandwich panels incorporating phase change materials: An experimental study. *Journal of Materials Research and Technology*, 12, 760-775.

- [6] Hattan, H. A., Madhkhan, M., & **Marani, A.** (2021). Thermal and mechanical properties of building external walls plastered with cement mortar incorporating shape-stabilized phase change materials (SSPCMs). *Construction and Building Materials*, 270, 121385.
- [5] **Marani, A.**, & Nehdi, M. L. (2020). Machine learning prediction of compressive strength for phase change materials integrated cementitious composites. *Construction and Building Materials*, 265, 120286.
- [4] **Marani, A.**, Jamali, A., & Nehdi, M. L. (2020). Predicting Ultra-High-Performance Concrete Compressive Strength Using Tabular Generative Adversarial Networks. *Materials*, 13(21), 4757.
- [3] Nunez, I., **Marani, A.**, & Nehdi, M. L. (2020). Mixture Optimization of Recycled Aggregate Concrete Using Hybrid Machine Learning Model. *Materials*, 13(19), 4331.
- [2] **Marani, A.**, & Nehdi, M. L. (2019). Integrating phase change materials in construction materials: Critical review. *Construction and Building Materials*, 217, 36-49.
- [1] **Marani, A.**, & Madhkhan, M. (2018). An innovative apparatus for simulating daily temperature for investigating thermal performance of wallboards incorporating PCMs. *Energy and Buildings*, 167, 1-7.

Conference Proceedings:

- [5] Marani, A., & Nehdi, M. L. (2021). Application of artificial neural networks in prediction of compressive strength of PCM-integrated concretes. *CSCE Materials and Mechanics Specialty Annual Conference*, 10 p.
- [4] Marani, A., Zhang, L. V., & Nehdi, M. L. (2021). Experimental study on effect of micro-encapsulated PCM

addition on cement hydration. CSCE Materials and Mechanics Specialty Annual Conference, 9 p.

[3] Zhang, L. V., Suleiman, A. R., Marani, A., & Nehdi, M. L. (2021). Effect of various temperatures and relative

humidity on crack self-healing in fiber-reinforced mortars incorporating crystalline additives. CSCE Materials and Mechanics Specialty Annual Conference, 9 p.

[2] Zhang, L. V., Suleiman, A. R., Marani, A., & Nehdi, M. L. (2021). Comparative study on self-healing behavior of alkali-activated composites and cement-based materials.

[1] Marani, A., & Madhkhan, M. (2017) Application Effects of Polyethylene Glycol 600 in Concrete Sandwich Panels. 2nd International and 6th National Conference on Modern Materials and Structures in Civil Engineering, Yazd, Iran.

Under Review and in Preparation:

[5] **Marani, A.**, Zhang, L. V., & Nehdi, M. L. (2022), “Design of concrete incorporating microencapsulated phase change materials for clean energy: a ternary machine learning approach”, In preparation, **to be submitted to** Engineering Applications of Artificial Intelligence.

[4] **Marani, A.**, Zhang, L. V., & Nehdi, M. L. (2022), “Activation energy of concrete incorporating phase change materials”, **under review** in Cement and Concrete Composites, Elsevier.

[3] **Marani, A.**, Geranfar, E., & Nehdi, M. L. (2022), “Deep learning-assisted calculation of apparent activation energy for cement-based composites incorporating microencapsulated phase change materials” **to be submitted to** Construction and Building Materials, Elsevier

[2] **Marani, A.**, Zhang, L. V., & Nehdi, M. L. (2022), “Multiphysics Study on Cement-Based Composites Incorporating Green Biobased Shape-stabilized Phase Change Materials for Thermal Energy Storage” **under revision in** Journal of Cleaner Production, Elsevier

[1] **Marani, A.**, & Nehdi, M. L. (2022), “Hydration Kinetics and Microstructural Development of Ternary Limestone Calcined Clay Cement (LC³) Composites Incorporating Phase Change Materials” **In preparation**, to be submitted to Cement and Concrete Research, Elsevier.